

ABSTRACT

JI, CHUNYANG. Characterizing Seismic Wave Attenuation via the High-Frequency Spectral Decay Parameter Kappa: Effects of Near-Surface Sedimentary Deposits on Uncertainty and Applications in Geotechnical Earthquake Engineering. (Under the direction of Dr. Ashly Cabas).

The effects of local soil conditions on the intensity of earthquake ground motions have long been recognized. Numerical modeling of site effects, known as site response, requires the characterization of subsurface conditions including dynamic properties of the sedimentary deposit, such as the shear wave velocity, V_s , and damping. Site-specific probabilistic seismic hazard analysis (PSHA) for critical civil infrastructure incorporates site effects into hazard evaluations, which requires knowledge of attenuation properties of shallow and deep geologic structures at the site of interest. Multiple attenuation metrics exist, from laboratory-based damping ratios (commonly used in geotechnical engineering) to the seismic quality factor, Q , and the high-frequency spectral decay parameter kappa, κ , which are more often used in engineering seismology. However, their potential relationships, and best practices for their implementation in various earthquake engineering analysis remain poorly understood.

κ is computed as the slope of the high-frequency decaying portion of an FAS plotted in log-linear space, which makes it an observable parameter from ground motion recordings, but not a measurable parameter in the field. Thus, previous studies have focused on investigating the uncertainties in κ calculations and the physics behind it. While previous studies have provided evidence of the variation in the site-specific component of kappa, κ_0 , with local site conditions, little is known about the sources of variation in κ (per record) and κ_0 at a single site. Moreover, most of the previous studies on κ focus on the linear-elastic regime, even though nonlinear soil behavior has often been responsible for increasing the damage potential of strong ground motions. Finally, the contributions of shallow and deeper geologic structures to κ and κ_0 values

are still poorly understood, yet necessary for the robust implementation of κ in future generations of GMMs, and site-specific PSHA.

To overcome these issues, improve the robustness of κ estimations, and broaden its applications in research and practice, this work focuses on studying the sources of variability in κ . First, a framework to identify, classify, and separate the potential effects that could bias κ estimates at a given station (i.e., within-station variability in κ) is proposed. By studying the influence of ground motion directionality and ground motion selection criteria (e.g., range of allowable focal depths) using the Japanese ground motion database, KiK-net, the significance of the within-station variability in κ is quantified. Second, the influence of soil nonlinearity on κ is studied with strong ground motions from KiK-net. It is found that soil nonlinearity can affect κ and κ_0 , but this influence is station-dependent. Key assumptions underlying the classic κ model are also discussed namely, (1) the flat earthquake source spectrum above the corner frequency, (2) frequency-independent Q, and (3) negligible site response (i.e., amplification) in high frequencies. Finally, the influence of deeper geologic structures in κ and κ_0 is studied via coda wave analysis using ground motions from California and nearby regions. A new ground motion database including earthquakes in or near California from 1999 to 2021 is created. Variations among κ_r and κ_0 estimated with the entire time series (i.e., including all waveforms), S-wave and coda wave windows are computed and compared. A better agreement between all κ_0 values is obtained for stiffer sites. However, conflicting trends are observed at softer sites, which will require further research. Overall, this work presents investigations of the computation process of κ , sources of variability at single sites, behavior beyond the linear-elastic regime, and contributions from deeper geologic structures. Collectively, these findings will advance the state-of-the-art in the characterization and modeling of near-surface seismic wave attenuation.

© Copyright 2021 by Chunyang Ji

All Rights Reserved

Characterizing Seismic Wave Attenuation via the High-Frequency Spectral Decay Parameter
Kappa: Effects of Near-Surface Sedimentary Deposits on Uncertainty and Applications in
Geotechnical Earthquake Engineering

by
Chunyang Ji

A dissertation submitted to the Graduate Faculty of
North Carolina State University
in partial fulfillment of the
requirements for the degree of
Doctor of Philosophy

Civil Engineering

Raleigh, North Carolina
2021

APPROVED BY:

Dr. Ashly Cabas Mijares
Committee Chair

Dr. Mervyn Kowalsky

Dr. Brina Montoya

Dr. DelWayne Bohnenstiehl

Dr. Fabrice Cotton
External Member

DEDICATION

To my beloved parents Xuehong and Shijie, and my lovely sister Chunlai, who give me unconditional supports.

BIOGRAPHY

Chunyang Ji is from China. She received a bachelor's degree in Civil Engineering from Shenzhen University, and a Master of Science in Structural Engineering from University of Southern California. After that, she switched to geotechnical engineering with the focus of seismic hazard analysis. She started to pursue her Ph.D.'s degree at North Carolina State University under the supervision of Dr. Ashly Cabas.

ACKNOWLEDGMENTS

Four years ago, I thought it would be a long and hard journey to achieve my Ph.D.'s degree. However, when I sit down and write this last piece of my dissertation, I feel that time goes fast, and I enjoy every day at NC State as a Ph.D. student.

First, I would love to give my deepest gratitude to my supervisor Dr. Ashly Cabas. She is an amazing advisor. Her patience, wisdom, passions to research, and kindness always inspire me to explore new topics and learn new skills. She also creates a lot of opportunities to support me to collaborate with excellent researchers from other institutions and explore topics I am interested in. Dr. Cabas has a magic power that can help me to release my negative emotions and can redirect me to the right track. Meeting and discussing with her are the most enjoyable time for me each week. She is my advisor, role model, friend, and family. Meanwhile, I am truly grateful to Dr. Fabrice Cotton at GFZ and University of Potsdam. His comments and suggestions always hit the points, which helps me to improve my work. I also appreciate his service on my committee. I thank Dr. Mervyn Kowalsky, Dr. Brina Montoya, and Dr. DelWayne Bohnenstiehl on serving on my committee.

Meanwhile, I would love to appreciate my colleagues from all over the world! I am grateful to my friends at GFZ Dr. Marco Pilz, who gives me incredible helps continuously, and Dr. Dino Bindi, who helped me to complete my first work about seismic hazard. I give grateful thanks to Dr. Fabian Bonilla from IFSTTAR and Dr. Céline Gelis from IRSN. It is an amazing and enjoyable experience to work with them, which not only teaches me how to do research but also what research is. I want to thank Dr. Albert Kottke from PG&E, who provides great supports and encouragements. I also appreciate Dr. Eric Thompson from USGS, who shares his expertise generously. I feel blessed to know and work with all of them.

I would like to thank my friends from our GeoQuake research lab, Ishika Nawrin Chowdhury, Thomas Na, Maria Ramos Sepulveda, Cristina Lorenzo-Velasquez, Nancy Ingabire Abayo, Cassie Gann, Sugandha Singh, and Mona Doostmohammadibueini. I also want to thank friends from Geotechnical Engineering, Zahra Faeli, Qianwen Liu, Pegah Ghasemi, Azmayeen Shahriar, Rowshon Jadid, Jinung Do, Jenny Vaugh, and Ashkan Nafisi. There are also special thanks to my special friends, Qingyu Hu and Rui Du, who shared, are sharing, and will share all the excellent moments.

Finally, big thanks to my family. My parents give me unconditional supports. They always support each big decision I made at the important point. My sister is the best listener of my sadness, happiness, and nonsense. I cannot be here without them.

TABLE OF CONTENTS

| | |
|--|------------|
| TABLE OF CONTENTS | VII |
| LIST OF TABLES | X |
| LIST OF FIGURES | XI |
| CHAPTER 1. INTRODUCTION | 1 |
| 1.1. Background of κ | 1 |
| 1.2. Research problems | 3 |
| 1.3. Objectives and research tasks..... | 5 |
| 1.4. Documents layout..... | 6 |
| CHAPTER 2. WITHIN-STATION VARIABILITY IN KAPPA: EVIDENCE OF DIRECTIONALITY EFFECTS..... | 8 |
| 2.1. Abstract | 8 |
| 2.2. Introduction | 9 |
| 2.3. Uncertainty and Variability in κ | 11 |
| 2.4. Database Description and Study sites | 16 |
| 2.5. Methods..... | 19 |
| 2.5.1. Estimation of κ_r and κ_0 | 19 |
| 2.5.2. Ground Motion Directionality | 23 |
| 2.6. Results and Discussion..... | 24 |
| 2.6.1. Directionality effects on κ_r and κ_0 estimations | 24 |
| 2.6.2. Earthquake type and focal depth effects on κ_r , κ_R , and κ_0 estimations | 31 |
| 2.7. Conclusions | 34 |
| 2.8. Data and Resources | 37 |
| CHAPTER 3. EFFECTS OF NONLINEAR SOIL BEHAVIOR ON KAPPA (κ): OBSERVATIONS FROM THE KIK-NET DATABASE..... | 38 |
| 3.1. Abstract | 38 |
| 3.2. Introduction | 39 |
| 3.3. Background | 40 |
| 3.4. Conceptual basis for the interpretation of κ beyond the linear-elastic regime..... | 44 |
| 3.5. Database description | 46 |
| 3.6. Method | 49 |
| 3.6.1. Identification of the onset of nonlinearity | 49 |
| 3.6.2. Linear, transitional, and nonlinear datasets | 51 |
| 3.6.3. κ_{r_AS} estimates..... | 56 |
| 3.6.4. κ_0 -model | 60 |
| 3.7. Results and Discussion..... | 63 |
| 3.7.1. Effects of soil nonlinearity on empirical κ_{r_AS} | 63 |
| 3.7.2. Effects of soil nonlinearity on the empirical κ_0 -model..... | 65 |
| 3.7.3. Effects of soil nonlinearity on predicted near-surface attenuation | 73 |
| 3.8. Conclusions | 78 |
| 3.9. Data and Resources | 82 |

| | |
|---|------------|
| CHAPTER 4. VARIABILITY IN KAPPA: CONTRIBUTIONS FROM THE COMPUTATION PROCEDURE | 83 |
| 4.1. Abstract | 83 |
| 4.2. Introduction | 84 |
| 4.3. Methods | 86 |
| 4.4. Results and discussions | 88 |
| 4.5. Conclusions | 95 |
| CHAPTER 5. A DESIGNSAFE GROUND MOTION DATABASE FOR CALIFORNIA. 97 | |
| 5.1. Abstract | 97 |
| 5.2. Introduction | 97 |
| 5.3. Ground motion database..... | 100 |
| 5.3.1. Earthquake and ground motion selection | 100 |
| 5.3.2. Automated ground motion processing | 102 |
| 5.4. Overview of processed ground motions | 103 |
| 5.5. Site database | 106 |
| 5.5.1. V_s and V_p dataset and profiles | 107 |
| 5.5.2. Predominate frequency | 109 |
| 5.5.3. Site-specific κ_0 values | 110 |
| 5.6. Station and waveform metrics..... | 113 |
| 5.7. Summary | 113 |
| CHAPTER 6. VARIABILITY IN KAPPA (κr) ESTIMATED WITH CODA WAVES FOR CALIFORNIA | 116 |
| 6.1. Abstract | 116 |
| 6.2. Introduction | 117 |
| 6.3. Methods | 118 |
| 6.4. Results and discussions | 121 |
| 6.5. Conclusions | 125 |
| CHAPTER 7. SITE-SPECIFIC NEAR-SURFACE ATTENUATION ESTIMATED WITH CODA WAVES..... | 127 |
| 7.1. Abstract | 127 |
| 7.2. Introduction | 128 |
| 7.3. Database description | 130 |
| 7.4. Method | 132 |
| 7.4.1. Seismic phase windowing..... | 132 |
| 7.4.2. Estimations of κ | 134 |
| 7.5. Discussion and Conclusions..... | 139 |
| 7.6. Limitations of this work and future research directions..... | 144 |
| CHAPTER 8. CONCLUSIONS AND FUTURE WORK | 145 |
| 8.1. Conclusions | 145 |
| 8.1.1. Within-station variability in κ | 145 |
| 8.1.2. Effects of soil nonlinearity on κ | 146 |
| 8.1.3. Coda wave and κ | 146 |

| | |
|--|------------|
| 8.2. Limitations and Future work | 147 |
| 8.2.1. Soil nonlinearity and κ | 147 |
| 8.2.2. Coda wave and κ for California | 148 |
| REFERENCES..... | 152 |
| APPENDICES..... | 170 |
| Appendix A: Supplementary Material for Chapter 2 | 171 |
| Appendix B: Supplementary Material for Chapter 3 | 178 |

LIST OF TABLES

| | |
|---|-----|
| Table 2.1. Selected station information | 18 |
| Table 2.2. Station information and statistical parameters for $\Delta\kappa(\theta)$ | 29 |
| Table 3.1. Local soil conditions, number of ground motions per dataset, predetermined fixed-frequency bandwidth and thresholds for shear strain index, I_γ at all study sites..... | 48 |
| Table 3.2. Ground motion datasets constructed via alternative approaches (AP1 to AP4) explored in this study to implement the κ_0 -model. | 62 |
| Table 3.3. Site-specific κ_0 values obtained from different dataset definitions at stations FKSH14 and MYGH10..... | 68 |
| Table 3.4. T-test results for κ_{0_pred} values estimated with linear and nonlinear datasets defined by AP3 (which includes records categorized as transitional into the nonlinear dataset). | 77 |
| Table 4.1. Site information for the selected KiK-net stations..... | 87 |
| Table 5.1. Summary of ground motion screening criteria and processing using with USGS gmprocess toolkit. | 101 |
| Table 5.2. Major information included in this dataset | 115 |
| Table 6.1. Variability in κr_{coda} as a function of the coda wave durations and coda wave onset for the selected GMs at SB.GVDA..... | 121 |
| Table A. 1. Estimated κ -values along with the corresponding earthquake type and depth at each selected station..... | 171 |
| Table B. 1. κ_0 -model estimated with datasets defined by AP1, AP2, AP3 and AP4..... | 197 |
| Table B. 2. Average and standard derivation of κ_{0_pred} values for surface linear and nonlinear datasets. | 199 |

LIST OF FIGURES

| | |
|--|----|
| Figure 1.1. Illustration of the κr computation. Ground motion recorded at IBRH20 from KiK-net. f_c refers to the corner frequency, f_1 and f_2 are the minimum and maximum frequencies considered in the calculation of κr . Details of the selected ground motion are shown in the textbox..... | 2 |
| Figure 2.1. Logic tree for the estimation of κ_0 values. The highlighted branches are explored in this work..... | 12 |
| Figure 2.2. Locations of each selected Japanese station in this study. | 17 |
| Figure 2.3. Selection of f_1 and f_2 on the Fourier acceleration amplitude spectrum corresponding to a surface record at station IBRH20. f_c refers to the corner frequency as estimated by the Brune (1970) model with stress drop of 3.0 MPa for active crustal events. | 20 |
| Figure 2.4. Comparison between κ_{r_AS} (from the whole FAS) and $\kappa_{r_AS_SW}$ (from the S-wave window FAS) corresponding to our ten study sites. r_1 is the ratio computed by $\kappa_{r_AS}/\kappa_{r_AS_SW}$. The dash line represents a ratio of 1.0. The circles depict the mean r_1 of all observed records, and the error bars indicate the +/- standard derivation of all observed ratios at each site of interest..... | 22 |
| Figure 2.5. Example of $\kappa_{r_AS_ROT}$ variations. (a) Shear wave velocity profile at FKSH19, (b) comparison between $\kappa_{r_AS_ROT}$ and rotation angle at surface and borehole for one record, and (c) the FAS for rotated components with θ of 80° and 160°. The dark solid and dash lines show the smoothen FAS to emphasize the differences between rotated FASs. The select ground motion was a shallow active crustal event recorded at FKSH19 (site class: D) with seismic moment magnitude of 4.4, azimuth of 19o, and epicentral distance of 117 km (recorded on 07/26/2003 (UT)).. | 25 |
| Figure 2.6. Comparison between mean κ_{r_AS} of rotated motions (i.e., $\kappa_{r_AS_mean}$) and mean κ_{r_AS} of two recorded horizontal component (i.e., $\kappa_{r_AS_ave}$) at selected stations along with the corresponding standard derivation at (a) borehole and (b) ground surface. r_2 corresponds to the ratio $\kappa_{r_AS_ave}/\kappa_{r_AS_mean}$. The dash line indicates an r_2 equal to 1.0, and the circles depict the mean r_2 across all records considered per station. The error bars indicate the +/- standard deviation of all r_2 computed at each site of interest..... | 26 |
| Figure 2.7. Variability of $\Delta\kappa(\theta)$ at the stations of interest and the corresponding site information. The solid lines represent the mean of all $\Delta\kappa(\theta)$ across all records per rotation angle, while the gray circles depict $\Delta\kappa(\theta)$ obtained for each record and multiple rotation angles. H_{800} refers to depth to a horizon with velocity V_s of 800 m/s or more. | 28 |

| | |
|---|----|
| Figure 2.8. Comparison of $\text{mean}(\Delta\kappa(\theta))$ and $\Delta\kappa_0$ at each station. $\Delta\kappa_0$ is the difference between surface and borehole κ_0 estimated from empirical regressions on as-recorded horizontal components. The error bar (within-station variability) represents ± 1 standard derivation of $\Delta\kappa(\theta)$ at each station. The horizontal solid line presents the mean of $\Delta\kappa(\theta)$ across all stations, and the dash lines indicate the ± 1 standard derivation of $\Delta\kappa(\theta)$ across all considered stations (between-station variability)..... | 30 |
| Figure 2.9. Comparisons of κ_0 (at the ground surface and at depth), κ_R , and $\Delta\kappa_0$ values for different earthquake types at each station. | 32 |
| Figure 2.10. Comparisons of κ_0 (at the ground surface and at depth), κ_R , and $\Delta\kappa_0$ (the difference between surface and borehole κ_0) values for different focal depth groups at each station. Groups 1, 2 and 3 consider focal depths of less than 35 km, from 35 to 70 km, and more than 70 km, respectively. | 33 |
| Figure 2.11. Comparisons of κ_0 (at the ground surface and at depth), κ_R , and $\Delta\kappa_0$ (the difference between surface and borehole κ_0) values estimated with ACRsh dataset, and Group 1. Group 1 includes the events with focal depth less than 35 km (which includes both ACRsh and SZintra events)..... | 34 |
| Figure 3.1. Comparisons between a weak and a strong ground motion recorded at FKSH14 ($V_{s30} = 237$ m/s). The M_w and R_e are 4 and 15 km for the low-intensity ground motion, while 5.1 and 15 km for the high-intensity ground motion. The frequency window ([10.05, 30] Hz) applied in this plot is picked manually. The left and right columns correspond to analyses conducted on the horizontal components H_1 and H_2 , respectively. The color version of this figure is available only in the electronic version of this article..... | 43 |
| Figure 3.2. (a) Locations of selected Japanese recording stations in this study, and (b) magnitude and distance distribution of selected ground motions. | 47 |
| Figure 3.3. Hyperbolic models fitted to observed $\text{PGA}_{\text{rotD50}}$ and $I_{\gamma,0}$ data at four study sites. The V_{s30} for IBRH16, IBRH17, IBRH20, and IWTH21 are 626, 301, 244, and 521 m/s, respectively..... | 50 |
| Figure 3.4. Surface $\text{PGA}_{\text{rotD50}}$ against $I_{\gamma,0}$ at MYGH10 ($V_{s30} = 348$ m/s). The red dot-dashed lines present the linear ($I_{\gamma,0,l}$) and transitional ($I_{\gamma,0,t}$) thresholds for $I_{\gamma,0}$. The color version of this figure is available only in the electronic version of this article..... | 52 |
| Figure 3.5. G/G_{max} versus $I_{\gamma,0}$ at study sites. The G_{max} is computed from the average values of $\left(\frac{\text{PGA}_{\text{rotD50}}}{\text{PGV}_{\text{rotD50}}/V_{s,0}} \right)$ for records with $I_{\gamma,0}$ less than 0.001%. The colors represent $\text{PGA}_{\text{rotD50}}$ values (in units of m/s^2). The color version of this figure is only | |

- available in the electronic version of this article. The color version of this figure is available only in the electronic version of this article..... 55
- Figure 3.6. Comparisons of individual κ_r estimates from our automated algorithm, $\kappa_{r,auto}$, and the fixed frequency band method, κ_{r_AS} at FKSH14 ($V_{s30} = 237$ m/s) for surface (left) and borehole (right) records. The color version of this figure is available only in the electronic version of this article. 58
- Figure 3.7. Surface κ_{r_AS} estimates and their corresponding PGA_{rotD50} , $I_{\gamma,0}$ and R_e values for selected ground motions recorded at (a) FKSH14 ($V_{s30} = 237$ m/s) and (b) MYGH10 ($V_{s30} = 348$ m/s). Different colors represent varying epicentral distances per record, and the size of markers indicate the corresponding PGA_{rotD50} . The color version of this figure is only available in the electronic version of this article. The color version of this figure is available only in the electronic version of this article..... 64
- Figure 3.8. κ_0 -model at FKSH14 ($V_{s30} = 237$ m/s) from datasets defined by (a) AP1, which only considers the linear and nonlinear datasets, (b) AP2, where transitional records are included as part of the linear dataset, (c) AP3, where transitional records are included as part of the nonlinear dataset, and (d) AP4, where the linear, transitional, and nonlinear datasets are considered separately. The color version of this figure is only available in the electronic version of this article. 66
- Figure 3.9. κ_0 -model at MYGH10 ($V_{s30} = 348$ m/s) with datasets defined by: (a) AP1, which only considers the linear and nonlinear datasets, (b) AP2, where transitional records are included as part of the linear dataset, (c) AP3, where transitional records are included as part of the nonlinear dataset, and (d) AP4, where the linear, transitional, and nonlinear datasets are considered separately. The color version of this figure is available only in the electronic version of this article. 67
- Figure 3.10. Ratio of $\kappa_{0_nl_sur}/\kappa_{0_lin_sur}$ at study sites estimated using the dataset definitions based on AP3 (left panel) and AP4 (right panel) against to V_{s5} , V_{s10} , and V_{s30} . The color version of this figure is available only in the electronic version of this article..... 71
- Figure 3.11. Estimated surface κ_{0_pred} and their corresponding ground shaking intensity and in situ deformation characterized by PGA_{rotD50} and $I_{\gamma,0}$, respectively at (a) FKSH14 ($V_{s30} = 237$ m/s) and (b) MYGH10 ($V_{s30} = 348$ m/s). Both, the color and the size of markers represent varying PGA_{rotD50} values. Triangles and circles represent the linear and nonlinear datasets defined by AP3. The red dashed lines depict the local regression model based on the κ_{0_pred} and $I_{\gamma,0}$ data. The color version of this figure is only available in the electronic version of this article. The color version of this figure is available only in the electronic version of this article..... 75
- Figure 3.12. Observed distribution of κ_{0_pred} at (a) FKSH14 ($V_{s30} = 237$ m/s) and (b) MYGH10 ($V_{s30} = 348$ m/s) for the linear and nonlinear datasets. The red lines

| | |
|--|-----|
| depict the theoretical probability density function (PDF) fitted with a Gaussian distribution. The color version of this figure is available only in the electronic version of this article..... | 76 |
| Figure 4.1. Example of κ_r estimate for a ground motion observed at a KiK-net station (IBRH20). Depicted f_1 and f_2 correspond to the range of frequencies where the linear decay of the spectrum is used for the computation of κ_r . The f_1 and f_2 are selected manually in this case to illustrate the computation of κ_r . f_c refers to the corner frequency of the corresponding event..... | 85 |
| Figure 4.2. The effects of frequency band selection on κ_{r_AS} estimates at (a) FKSH19 for H_1 , (b) FKSH19 for H_2 , (c) AICH17 for H_1 , and (d) AICH17 for H_2 | 90 |
| Figure 4.3. Example ground motion for surface κ_{r_AS} estimates and the corresponding ETF of two orthogonal horizontal components. This event was observed at FKSH19 on December 31, 2002 (UT). The seismic moment magnitude (M_w) is 4.3, the focal depth is 35 km, the epicentral distance is 82 km and the azimuth is 124° | 92 |
| Figure 4.4. Example ground motions at FKSH19 with negative κ_{r_AS} estimates. (a) and (b) are FAS corresponding to the H_1 and H_2 recorded components at the ground surface, (c) and (d) present the empirical transfer function (ETF) computed using the surface and borehole records at the site for the H_1 and H_2 components, respectively, (e) and (f) depict the FAS corresponding to the borehole H_1 and H_2 recorded components. The ground motions depicted here are associated with a seismic event recorded on June 11, 2011 (UT). The corresponding seismic moment magnitude (M_w) is 3.7, the focal depth is 58 km, the epicentral distance is 48 km and the azimuth is 116° | 94 |
| Figure 5.1. Location of (a) earthquake epicenters and (b) ground motion recording stations included in DSGM-CA database..... | 105 |
| Figure 5.2. Distribution of ground motions included in datasets DSGM-CA-P1 and DSGM-CA-P2..... | 105 |
| Figure 5.3. Distribution of epicentral distance, magnitude and PGArrotD50 for all records in this work..... | 106 |
| Figure 5.4. Comparisons of (a) PGArrotD50 and (b) PGVrotD50 for duplicated records included in DSGM-CA-P1 and DSGM-CA-P2..... | 106 |
| Figure 5.5. (a) Location of recording station used in this work along with available V_s measured profiles, (b) Comparison of the distribution of proxy-based V_{s30} values and their counterparts from measured V_s in the field..... | 108 |
| Figure 5.6. Locations of UCLA VSPDB stations included DSGM-CA database. The red dots depict the UCLA VSPDB V_{s30} values from measurements at stations in California; green and blue circles indicate the UCLA VPDB locations where V_p | |

and V_s profiles are available in California, respectively, and the black circles show the location of HVSR measurements from the UCLA VPDB database. 109

Figure 5.7. An example ground motion for κr computation. This ground motion was recorded at NC.MCO from a 2020 Mw 4.6 earthquake in Bodie, California. 111

Figure 5.8. (a) Location of stations with site-specific κ_0 values in California and nearby regions, and (b) relationship between entire time series- and S-wave-based κ_0 values with proxy-based V_{s30} at selected stations within this DSGM-CA database. 113

Figure 6.1. (a) Location of SB.GVDA and observed earthquakes, and (b) shear-wave velocity profile at SB.GVDA. 119

Figure 6.2. Variations of κr_{coda} with coda wave durations at SB.GVDA for (a) NS and (b) EW component. The dots show the mean estimate of κr_{coda} estimated from coda windows with potential durations, the error bars represent the corresponding σ_{κ} , and marker colors show the PGA per horizontal component. 120

Figure 6.3. Illustrations of coda duration influence on $\kappa_{(r_coda)}$ estimates with example GMs (NS component). Three coda windows with different durations are determined with the same onset, and the corresponding FAS and $\kappa_{(r_coda)}$ values are plotted (bottom). (a) and (b) are observed from event ci37701544, (c) and (d) are from event ci10370141. 122

Figure 6.4. Variations of κr_{coda} with coda wave onset selections at SB.GVDA for (a) NS and (b) EW component. The dots show the mean estimate of κr_{coda} estimates with all moving coda window, the error bars represent the corresponding standard deviation, and marker colors show the PGA per horizontal component. 124

Figure 6.5. Variations of $\kappa_{(r_coda)}$ with coda wave onset at SB.GVDA for NS (left) and EW (right) component. The dots show the mean estimate of κr_{coda} estimated from coda windows with different start times, the error bars represent the corresponding standard deviation, and marker colors show the PGA per horizontal component. 125

Figure 7.1. Locations of ground motion recording stations selected for κr and κ_0 calculations in this study. 132

Figure 7.2. An example record to illustrate the seismic wave phase windowing used in this study. This ground motion was recorded at NC.MCO from a 2020 M_w 4.6 earthquake in Bodie, California. 133

Figure 7.3. Example of (a) Error I-1 and (b) I-2 in ground motions at stations CE.54428 and RE.FRNT, respectively. These ground motions correspond to a 2020 Mw 4.6 earthquake in Bodie, California, and epicentral distances of 53 and 143 km. 135

| | |
|---|-----|
| Figure 7.4. Examples of Errors II-1 and II-2 identified in ground motions at stations CE.55157 and NC.MDH. These ground motions correspond to a 2020 Mw 4.6 earthquake in Bodie, California and epicentral distances of 36 and 52 km. The (B) acceleration time series, and the corresponding (c) ETS FAS and (e) coda FAS is east-west component at CE.55157. The (b) acceleration time series, and the corresponding (e) ETS FAS and (f) coda FAS is east-west component at NC.MDH..... | 137 |
| Figure 7.5. An example record for κr_{ets} , κr_{sw} , and κr_{coda} computations. This ground motion is observed at site NC.MCO from a 2020 earthquake with M_w of 4.6. The thin black line shows the ETS FAS, the red dash line is the SW FAS, and the gray line presents the coda FAS..... | 138 |
| Figure 7.6. Comparisons between (a) κr_{ets} and κr_{coda} and (b) κr_{sw} and κr_{coda} datasets, which includes all ground motions observed at the 113 stations with more than 5 suitable records in this work. | 140 |
| Figure 7.7. Comparisons between site-specific κ_0 and USGS proxy-based V_{s30} | 141 |
| Figure 7.8. Comparisons among κ_0_{ets} , κ_0_{sw} , and κ_0_{coda} values across different V_{s30} -based groups. The stations are grouped using USGS proxy-based V_{s30} values. Group 1 includes the stations with USGS proxy-based V_{s30} less than 360 m/s (a and b), group 2 includes the stations with USGS proxy-based V_{s30} between 360 and 700 m/s (c and d), and group 3 includes the stations with USGS proxy-based V_{s30} more than 700 m/s (e and f)..... | 143 |
| Figure 8.1. Distribution of ground motions for different error types. The patches of lines present the motions included in DSGM-CA P1, and the dot patches presents the motion from DSGM-CA P2 (see Chapter 7 for more details on the composition of the database)..... | 150 |
| Figure 8.2. Histogram for the number of ground motions with κ values per station. | 151 |
| Figure A. 1. Comparison between source-to-site azimuth and rotation angle corresponding to the maximum $\kappa_{r_AS_ROT}$ (θ_{max}) calculated from borehole and surface records at the selected stations..... | 174 |
| Figure A. 2. Comparisons between $\kappa_{r_AS_ave}$ and $\kappa_{r_AS_mean}$ at selected stations: (a) the results at borehole, and (b) the data at surface. The colors represent the difference between κ_{r_AS} estimated from two as-recorded borehole horizontal components. The solid line provides the 1:1 correlation reference between $\kappa_{r_AS_ave}$ and $\kappa_{r_AS_mean}$, and the colors indicate the differences between $\kappa_{r_AS_H1}$ and $\kappa_{r_AS_H2}$ computed from as-recorded horizontal components. $\kappa_{r_AS_mean}$ is the mean values of all $\kappa_{r_AS_ROT}$ for each record, and $\kappa_{r_AS_ave}$ is the arithmetic average of two as-recorded horizontal component values..... | 175 |

| | |
|--|-----|
| Figure B. 1. Surface PGA_{rotD50} against $I_{\gamma,0}$ at the studied stations. The dashed lines represent the linear and transitional thresholds of $I_{\gamma,0}$ | 179 |
| Figure B. 2. Relationship between surface κ_{r_AS} estimates and ground shaking intensities at the studied sites. Different colors illustrate epicentral distances per record, and the sizes of markers represent the corresponding PGA_{rotD50} | 185 |
| Figure B. 3. Correlations between surface κ_{0_pred} and ground shaking intensities at studied sites. At each site, both colors and sizes of markers present the corresponding PGA_{rotD50} values. The triangle and circles depict linear and nonlinear datasets defined by AP3, respectively. The red dashed-lines indicate the trend between κ_{0_pred} and $I_{\gamma,0}$ as determined by a local regression model..... | 191 |

CHAPTER 1. INTRODUCTION

1.1. Background of κ

The high-frequency spectral decay parameter kappa (κ_r) was proposed by Anderson and Hough (1984) to describe the linear decay of shear-wave (S-wave) Fourier Amplitude Spectrum (FAS) in log-linear scale (see example in Figure 1.1). There are three assumptions applied to the classic κ_r definition, namely (1) the earthquake source can be modelled with an ω^2 model (Haendel et al. 2020) where the source spectrum is flat above the earthquake's corner frequency, (2) the seismic quality factor, Q (Knopoff, 1964), is frequency-independent and (3) the total site response is almost flat in high frequencies (i.e., no significant amplification or de-amplification). Anderson (1991) tried to separate the total κ_r observed from FAS into a site-specific component κ_0 , and a path attenuation component, $\kappa_R(R)$, which is a function of source-to-site distance, R. The linear κ_r distance-dependency model, is provided below:

$$\kappa_r = \kappa_0 + R \times \kappa_R \quad (1.1)$$

where the path contribution is modelled as $\kappa_R(R) = R \times \kappa_R$, with units of s/km, and R is the source-to-site distance measure (e.g., epicentral or rupture distance). The influence of earthquake source on κ_r is trivial with the ω^2 earthquake source model and often neglected (e.g., Ktenidou et al., 2014, Van Houtte et al., 2011, Cabas et al. 2017). The frequency-independent Q assumption enables the linear distance-dependency model as it assumes a single value of κ_R to be valid over the range of distances considered, and over the range of frequencies used in the κ_r calculation per record. Values of Q, however, are not frequency-independent (e.g., Aki, 1980), so this assumption is still highly debated in the literature. Anderson and Hough (1984) indicated that κ_r may consider only anelastic attenuation, which is frequency-independent. This limitation is further discussed as part of this PhD work.

The site-specific component, κ_0 , captures the attenuation experienced by seismic waves as they propagate directly through the soil deposits below the site of interest (Ktenidou et al. 2013). Thus, site-specific κ_0 received attention and popularity from both geotechnical engineering and seismological communities because its performance in characterizing the site effects and capturing near-surface attenuation. Site-specific κ_0 can be used to adjust ground motion models (GMMs) from host to target regions or to characterize the attenuation properties of shallow and deep geologic structures in site-specific seismic hazard analysis for critical facilities such as nuclear power plants (Rodriguez-Marek et al. 2014, Cabas and Rodriguez-Marek 2017).

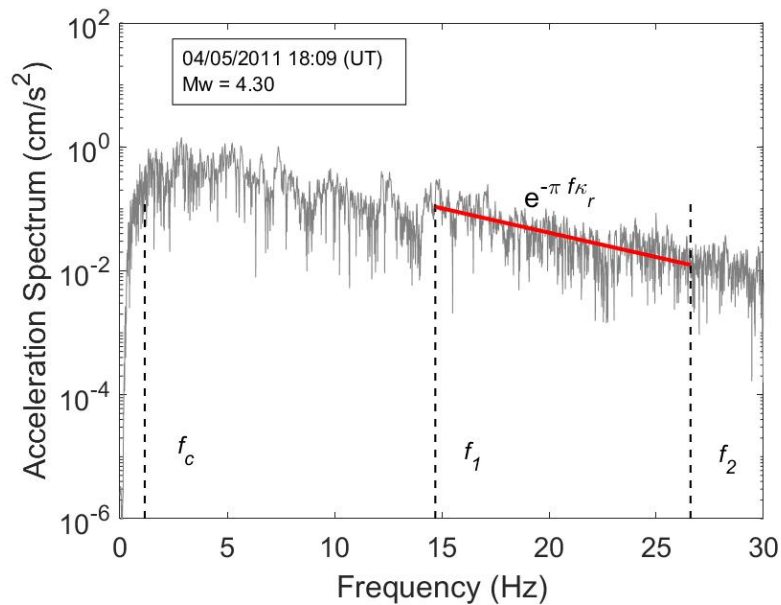


Figure 1.1. Illustration of the κ_r computation. Ground motion recorded at IBRH20 from KiK-net. f_c refers to the corner frequency, f_1 and f_2 are the minimum and maximum frequencies considered in the calculation of κ_r . Details of the selected ground motion are shown in the textbox.

1.2. Research problems

Despite the consensus about the ability of site-specific κ_0 to characterize and parameterize near-surface attenuation, the unveiled physics behind κ_r and the still large variability in κ_r and site-specific κ_0 hinder their applications in engineering practices. Thus, a comprehensive and well-developed understanding for uncertainties in κ_r and site specific κ_0 is the prerequisite for κ -related studies such as (1) the exploration of correlations between site-specific κ_0 and site conditions, (2) the incorporation of site-specific κ_0 as a site proxy to refine GMMs and site-specific hazard assessment, and (3) the development attenuation models or maps in local or regional scales with κ .

The overarching goal of this work is to characterize and parameterize site-specific near-surface attenuation with κ_0 , and well-constrained κ_r and site-specific κ_0 estimates are essential to achieve such goal. Thus, this dissertation focuses on the identification and exploration of uncertainties and variabilities in κ_r and site-specific κ_0 caused by multiple factors. The relationship between κ_0 values and site parameters have been studied frequently (e.g., correlation between κ_0 and V_{s30} ; Van Houtte et al., 2014). However, there is no widely accepted correlations available. Meanwhile, the high variability associated with site-specific κ_0 is a long-standing issue. Thus, starting from constraining the variability and uncertainty in site-specific κ_0 at a given station, a framework of within-station variability in κ_0 is proposed to identify and discuss all potential factors that influence κ_0 , which can be summarized as follows:

- *Soil linearity and nonlinearity*: The soft soil is subjected to nonlinear behavior when strong ground motions occur.
- *Estimation method for κ_0* : κ_0 can be computed either by statistical regression of individual κ_r against distance, or directly measured from the site's transfer function

or a ground motion's response spectrum. Currently, the most used approach is to calculate κ_0 by fitting a simplified linear distance-dependency model.

- *Estimation methods for κ_r* : the individual κ_r value is measured from an FAS. The classic approach is the acceleration spectrum approach used by Anderson and Hough (1984). Besides, there are also other approaches such as the displacement spectrum approach (Biasi and Smith 2001). However, the κ_r values computed with different approaches are not directly comparable (Ktenidou et al. 2014). The variabilities in κ_r can be transferred to κ_0 .
- *Dataset selections*: The selection of the ground motion dataset with considerations of ground motion azimuths, source-to-site distances, earthquake type, focal depths, and intensity can affect the robustness of κ_r directly, and bias κ_0 .
- *Record processing*: The signal processing protocol governs the quality of records. Meanwhile, different seismic wave windows (e.g., S-wave or P-wave) could be used for κ_r estimations with different applications.
- *Spectrum processing*: κ_r is highly affected by the selection of the frequency band that is used to fit the linear decay trend in FAS and to compute κ_r .

The scope of this work covers (1) the effect of ground motion directionality and dataset selection on within station variability in κ_0 within elastic linear regime, (2) the influence of soil nonlinearity on κ , and (3) the variabilities of κ_0 estimated with different wave phases to explore the contributions from deeper geologic structures to κ .

1.3. Objectives and research tasks

The overarching goal of this work is to characterize the site-specific near-surface attenuation by identifying, understanding, and quantifying the variabilities in κ_r and site-specific κ_0 . The influence of the near-surface soil layers and deeper geologic structures, input motion intensity and computation procedure on κ_r and site-specific κ_0 are studied. Specifically, the following research tasks are included in this work:

1. Investigation of the effects of ground motion directionality, earthquake depth and type on κ_r and site-specific κ_0 in the linear elastic regime and within a given station, A framework to explain within-station variability in κ_0 is developed.
2. Evaluation of the correlation between κ and soil nonlinearity, which explores if κ can capture the onset of soil nonlinearity and how κ_r and site-specific κ_0 change with nonlinearity.
3. Identification of the sources of variability and limitations of the original κ_r model defined by Anderson and Hough (1984).
4. Creation of a ground motion database for California (and nearby regions) with earthquakes that occurred from 1999 to 2021.
5. Computation of κ_r and site-specific κ_0 with different seismic wave phases and quantify their corresponding variability. This task focuses on the uncertainties in κ_r estimated with coda waves.
6. Quantification of near-surface attenuation characterized by coda wave for California.

1.4. Documents layout

This dissertation focuses on the investigation the variability in κ_r and site-specific κ_0 and the effects of the near-surface sedimentary deposits. Eight chapters are included in this work.

Chapter 1 provides a background introduction, motivation of this work, and objectives of this dissertation.

Chapter 2 is entitled “Within-station variability in kappa: Evidence of directionality effects” by Ji, C., Cabas, A., Cotton, F., Pilz, M. and Bindi, D. This work was published on the Bulletin of the Seismological Society of America in 2020.

Chapter 3 is entitled “Effects of Nonlinear Soil Behavior on Kappa (κ): Observations from the KiK-Net Database” by Ji, C., Cabas, A., Bonilla, L.F. and Gelis, C. It was published on the Bulletin of the Seismological Society of America in 2021.

Chapter 4 is a conference paper entitled “Variability in kappa: contributions from the computation procedure” by Ji, C., Cabas, A., Bonilla, L.F. and Gelis, C., which was accepted for publication in the 2022 Geo-Congress proceedings, to take place in Charlotte, North Carolina.

Chapter 5 is a data paper entitled “A DesignSafe Ground Motion Database for California” by Ji, C., Cabas, A., Kottke, A. and Pilz, M.. It will be submitted to Earthquake Spectra for publication.

Chapter 6 is a conference paper entitled “Variability in kappa (κ_r) estimated with coda waves for California” by Ji, C., Cabas, A., Pilz, M. and Kottke, A., which is under review. It was submitted to the 4th International Conference on Performance-based Design in Earthquake Geotechnical Engineering (PBD-IV) in Beijing.

Chapter 7 is entitled “Site-specific near-surface attenuation estimated with coda waves,” by Ji, C., Cabas, A., Pilz, M. and Kottke, A. It will be submitted to the Bulletin of the Seismological Society of America for publication.

Chapter 8 summarizes the conclusions and limitations of this work and outlines future research tasks and directions based on the contributions from this dissertation.

CHAPTER 2. WITHIN-STATION VARIABILITY IN KAPPA: EVIDENCE OF DIRECTIONALITY EFFECTS

Based on the paper published on Bulletin of the Seismological Society of America:

Ji, C., Cabas, A., Cotton, F., Pilz, M. and Bindi, D., 2020. Within-station variability in kappa: Evidence of directionality effects. Bulletin of the Seismological Society of America, 110(3), pp.1247-1259.

2.1. Abstract

One of the most commonly used parameters to describe seismic attenuation is the high-frequency spectral decay parameter Kappa (κ_r), yet the physics behind it remain little understood. A better understanding of potential factors that lead to large scatter in estimated values of κ_r constitutes a critical need for ground motion modeling and seismic hazard assessment at large. Most research efforts to date have focused on studying the site-to-site and model-to-model variability of κ , but the uncertainties in individual κ_r estimations associated with different events at a selected site (which we refer to as the within-station variability of κ_r) remain uncharacterized. As a direct corollary, obtaining robust estimates of the site-specific component, κ_0 , and their corresponding interpretation become a challenge. To understand the sources of the variability observed in κ_r (and κ_0) at a single site, we select ten Japanese Kiban-Kyoshin network (KiK-net) downhole arrays and investigate the systematic contributions from ground motion directionality. We observe that κ_r estimated from a single horizontal component is orientation-dependent. In addition, the influence of ground motion directionality is a function of local site conditions. We propose an orientation-independent κ_r value, which is not affected neither by ground motion directionality nor the events' azimuths. Additionally, we find that focal depth of events used in κ_r calculations affects the estimation of the regional attenuation component κ_R , which in turn influences the within-station variability in the κ_0 -model.

2.2. Introduction

The characterization of attenuation at various scales (from regional to local) constitutes a critical component in the prediction of ground motions, site response analysis and seismic hazard assessments. Thus, understanding ground motion characteristics at high frequencies has become a research focus in recent studies (e.g., Mayor et al. 2018; Parolai 2018). The high-frequency decay parameter, κ , was proposed by Anderson and Hough (1984) to characterize linear decay of the shear-waves (S-wave) Fourier acceleration amplitude spectrum (FAS) in log-linear scale in the high-frequency range. In general, individual estimations of κ values, hereafter referred to as κ_r , are decomposed into a site-specific component, κ_0 , a generalized distance-dependency component, $\widetilde{\kappa}_R$, and a source component, κ_s (Ktenidou et al. 2014).

The site-specific component, κ_0 , captures the attenuation taking place directly below the site of interest (Ktenidou et al. 2013), but further investigation is required to define the depth of the geologic profile that contributes toward the κ_0 resulting at the ground surface. Ground motion models and their adjustments from host to target regions have used estimates of κ_0 to characterize the effects of high frequency attenuation (e.g., Van Houtte et al. 2011, Campbell 2003, Ktenidou et al. 2014). Moreover, knowledge of κ_0 benefits the identification of epistemic uncertainties to remove the ergodic assumption in site-specific probabilistic seismic hazard analysis (PSHA), which is crucial for the seismic design of critical facilities such as nuclear power plants (Rodriguez-Marek et al. 2014, Cabas and Rodriguez-Marek 2017). Deciphering the physics behind empirical estimates of κ_0 requires understanding the site's contribution to the overall attenuation. Decoupling local and regional attenuation mechanisms will facilitate the development of physics-based ground motion simulations and non-ergodic ground motion prediction equations (GMPEs).

Previous studies have investigated the correlation between κ_0 and other site parameters, such as the time-averaged shear-wave velocity of the top 30 m subsoil (V_{s30}) (e.g., Van Houtte et al. 2011, 2014, Ktenidou et al. 2015, Cabas et al. 2017), but large uncertainties in κ_r estimations (which also affect the computation of κ_0) impose difficulties to unveil the physical meaning of κ_0 (Perron et al. 2017). An understanding of the sources of variability affecting κ_r and κ_0 constitutes a crucial step toward robust and sustainable applications of κ_0 in earthquake engineering practice.

The variability of κ has been studied through different lenses in the last decade, from model-to-model variability (e.g., Ktenidou et al. 2014, Edwards et al. 2015, Perron et al. 2017), user-to-user variability (e.g., Edwards et al. 2015, Douglas et al. 2010), to site-to-site variability (e.g., Van Houtte et al. 2011, 2014, Cabas et al. 2017). Some have investigated the variability in κ_r and κ_0 estimates when utilizing a single methodology, but incorporating alternative assumptions throughout the implementation (e.g., Ktenidou et al. 2013). Other efforts have focused on understanding the correlation (or lack thereof) among different methods to obtain κ_0 (e.g., Ktenidou et al. 2014, Perron et al. 2017). Whilst, the variability of κ_0 as a function of site conditions have been extensively studied for multiple regions, including Japan, Greece, France and the US (e.g., Douglas et al. 2010, Laurendeau et al. 2013, Ktenidou et al. 2015, Cabas et al. 2017, Parolai 2018).

The objective of this study is to characterize the within-station variability of κ_0 . Ten stations from the Japanese database, KiK-net, are investigated. Their corresponding National Earthquake Hazards Reduction Program (NEHRP) site class classification varies from B (rock) to D (stiff soils). First, we introduce a framework to evaluate aleatory variability and epistemic uncertainty in κ_r and κ_0 . Then, we focus on individual values of κ_r calculated following the

traditional approach by Anderson and Hough (1984) at the ten study sites, and investigate how ground motion directionality affects the estimation of κ_r . Finally, we explore the influence of earthquake type and focal depth on the estimates of κ_R and κ_0 . Within one selected station, we find that values of κ_R and κ_0 are affected by repeatable contributions from the path, with these path effects being more significant for κ_R .

2.3. Uncertainty and Variability in κ

Empirical data from multiple seismic events and recording stations are used to construct ground motion models (GMM) that can describe the distribution of ground motion in terms of a median and a logarithmic standard deviation, σ (Al Atik et al. 2010). The aleatory variability in the ground motion, represented by σ has proven to exert a strong influence on hazard estimates, especially at low annual exceedance frequencies (Bommer and Abrahamson 2006, Al Atik et al., 2010, Rodriguez-Marek et al., 2014). Defensible reductions in σ are desirable not only because of their ultimate effect on PSHA, but also because they result from a clear separation of aleatory variability (which is theoretically irreducible) and epistemic uncertainty (which can be reduced with the collection of new data, Rodriguez-Marek et al. 2014). In pursuit of defensible reductions in σ , repeatable source, path, and/or site contributions can be identified at a single site and invoke the nonergodic assumption. The ergodic assumption implies that the temporal distribution of ground motions at a given site is equivalent to the spatial distribution of ground motions across many sites (given the same causal parameters, Kuehn et al. 2019).

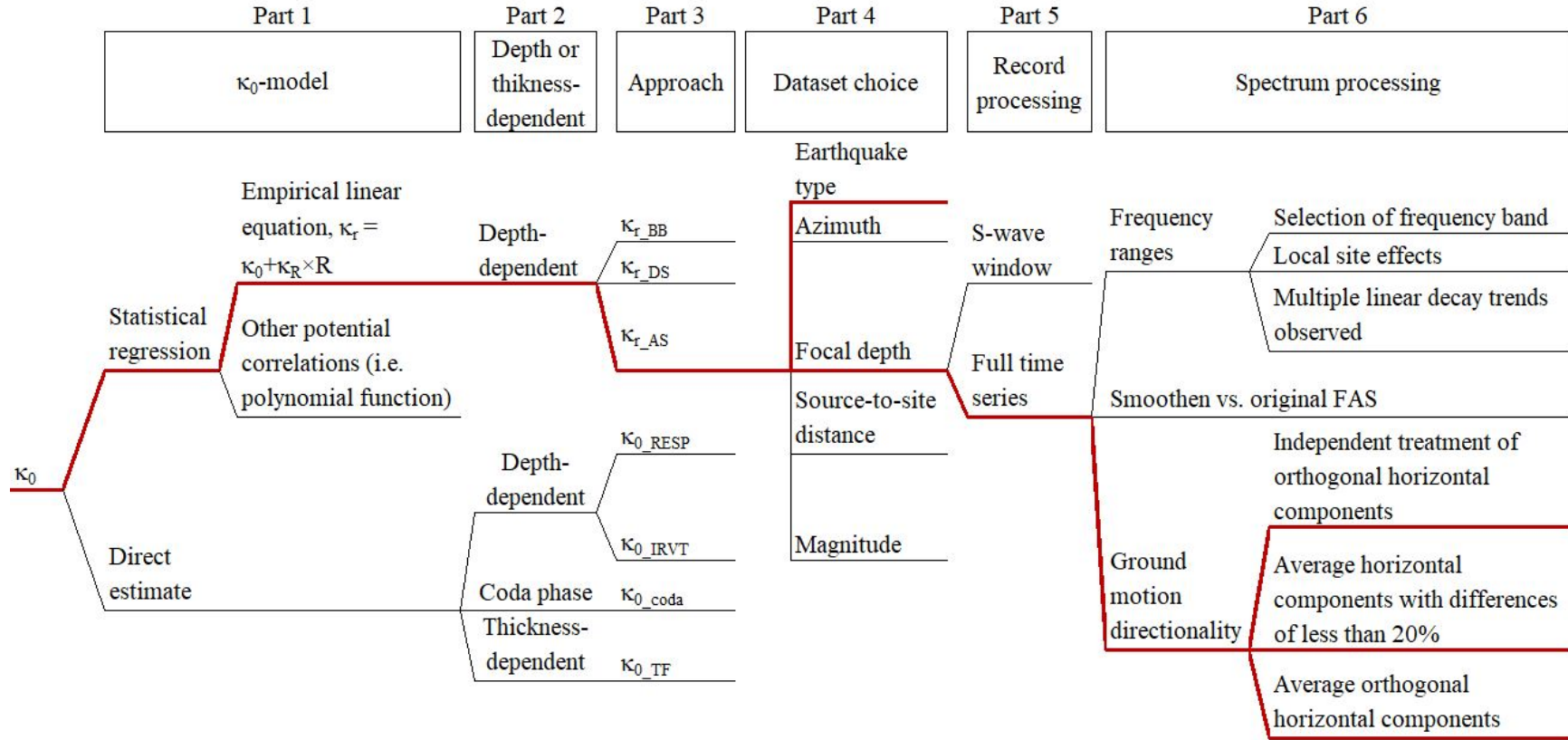


Figure 2.1. Logic tree for the estimation of κ_0 values. The highlighted branches are explored in this work.

In this study, we focus on identifying repeatable site and path contributions to the observed variability in κ_r , κ_R and κ_0 . Drawing parallels to the residual analysis process in ground motion modeling, this work aims to provide a characterization of the within-station variability in κ_r and κ_0 estimates, which can further support the development of the site-term parameterization in nonergodic GMMs. Baltay et al. (2017) provided evidence of a correlation between κ_0 values and the average site residual, using small-magnitude ground motion data recorded at ten stations from the ANZA network. Estimates of κ_0 could inform predictions of station-specific site residuals in partially nonergodic GMMs “to improve our physical understanding of the site term at specific stations” (Baltay et al. 2017). We select a subset of recordings at selected stations from the KiK-net database to identify and quantify systematic, repeatable contributions to κ_r , κ_R and κ_0 estimates; hereafter referred to as within-station variability in κ .

Approaches to estimate κ_0 can be classified into two types, namely direct estimates and empirical estimates from statistical regressions. Factors that introduce variability in κ_0 estimates for each type are grouped into six categories with considerations of model selections, database choices and record processing protocols as shown in Figure 2.1. The latter provides a framework to investigate epistemic uncertainties in κ_0 estimates for the linear elastic regime only. Further research is required should soil nonlinearity be triggered. The description of each category depicted in is presented below.

- Part 1 κ_0 -model

The commonly used statistical regression approach is based on a linear distance-dependent model, where κ_0 represents the site-specific component, while κ_R refers to the regional attenuation. Values of κ_0 and κ_R are obtained via empirical linear regression of κ_r following the Anderson and Hough (1984) method. Alternatively, direct estimates of κ_0 can be obtained

from the site properties (e.g., measurements of κ_0 in the high frequency decay of a transfer function, Drouet et al. 2010) without the definition of the κ_0 - linear regression model. The choice of a linear regression as opposed to other possible functional forms has been mostly based on the simplicity of the model and observed fit to the empirical data (Ktenidou et al 2013).

- Part 2 depth-dependency

The measured κ_0 values can be depth-dependent or thickness-dependent based on the approach selected for the respective calculations. Values of κ_0 provide an estimate of attenuation directly below the depth at which the ground motions are recorded. Different κ_0 values are typically obtained at different depths within a site profile (e.g., Ktenidou et al 2015). Values of site-specific κ_0 have also been proposed to represent the contribution of a specific soil column with a given thickness (e.g., Campbell 2009).

- Part 3 approach choice

Previous studies show that various κ calculation approaches will result in different individual κ_r values (for the same ground motion), and ultimately different κ_0 estimates (e.g., Ktenidou et al 2014). Understanding the suitability of each method in consideration of the available records and site conditions is relevant to reduce uncertainties in κ estimations. In Figure 2.1, κ_{r_BB} , κ_{r_DS} and κ_{r_AS} refer to individual values of κ from the broadband method (Ktenidou et al., 2016), the displacement method (Biasi and Smith, 2001), and the acceleration spectrum method (Anderson and Hough 1984), respectively. Direct measurement approaches also shown in Figure 2.1 include estimations of κ_0 from the response spectrum, κ_{0_RESP} (Silva and Darragh 1995), utilizing inverse random vibration theory, κ_{0_IRVT} (Al Atik et al 2014), and from the site's transfer function, κ_{0_TF} (Drouet et al 2010).

- Part 4 dataset choice

Choosing an appropriate dataset can reduce the within-station variability in κ_0 by constraining the uncertainties associated with individual κ_r values. In general, only magnitude, source-to-site distance, and type of seismicity are used to select appropriate ground motions for kappa calculations. However, we hypothesize that considering the events' azimuth, and focal depths can provide insights on other sources of within-station variability.

- Part 5 record processing

The variability associated with record processing refers to differences stemming from the usage of the S-wave window or the whole time series to calculate κ_r values. Anderson and Hough (1984) originally introduced the calculation of κ_{r_AS} as the linear decay of the S-wave FAS in the high frequency range. However, varying selections of the S-wave window can introduce additional scatter in κ_r for the same event (Douglas et al. 2010, Cabas et al. 2017, Xu et al. 2019). This additional variability may be caused by the assumed duration of the selected S-wave window or by the explicit consideration of the direct S-wave only or the direct S-wave window and coda/surface waves. Values of κ_{r_AS} estimated from the S-wave window could be significantly biased by scattering effects, except when intrinsic attenuation is dominant (Parolai et al. 2015, Pilz and Fah 2017, Parolai 2018, Pilz et al. 2019).

- Part 6 spectrum processing

The estimation of κ_{r_AS} is significantly sensitive to the selection of frequency ranges, including: (1) the length of the frequency band; (2) local site conditions such as site-amplification peaks (Parolai and Bindi 2004); and (3) the presence of multiple linear decay trends in the high frequency range of the FAS. Using smoothen FAS instead of the original

FAS also introduces differences for κ_r estimates. Additionally, there is variability resulting from different approaches to treat recorded horizontal components. For instance, (a) treating orthogonal horizontal components independently (Dimitriu et al. 2001), (b) averaging κ_{r_AS} values estimated from as-recorded horizontal components if differences in these κ_{r_AS} values are less than 20% (Ktenidou et al. 2013), and (c) averaging κ_{r_AS} values estimated from as-recorded horizontal components without consideration of the corresponding differences in individual κ_{r_AS} .

We would like to emphasize that the ultimate influence of the aforementioned sources of variability is usually station-dependent, although the logic tree and framework described in Figure 2.1 can be implemented at any site. Thus, the significance of each branch is unique for a given site, which results in a better characterization of the within-station variability at the site. In this paper, we only focus on the branches highlighted in Figure 2.1. The Anderson and Hough (1984) method is used to investigate systematic contributions to the variability in κ_r (hereafter referred to as κ_{r_AS}) and κ_0 . We investigate the within-station variability caused by (1) the dataset choice (part 4) based on earthquake types and focal depths, and (2) spectrum processing (part 6) by understanding the contributions of ground motion directionality.

2.4. Database Description and Study sites

We use the Japanese Kiban-Kyoshin network (KiK-net) database (see Data and Resources Section), which is a strong-motion seismograph network uniformly deployed at more than 600 locations in Japan and able to provide high-quality data at various site classes. KiK-net has a pair of seismographs at each station, one located on the ground surface, and the other one in a borehole together with high-sensitivity (Hi-net) seismographs. The depth of each borehole

sensor is typically between 100 m and 200 m. Instrumental sampling frequencies are 100 Hz or 200 Hz. Wave velocity profiles (for both P-wave and S-wave) at each station are measured by downhole PS logging, and the corresponding files are available on the KiK-net website (see Data and Resources). The orientations of orthogonal ground surface sensors are north-south and east-west. However, difficulties during installation and regular maintenance at some stations may have changed the orientations of borehole sensors (Aoi et al. 2004, Aoi et al. 2011). The azimuths of borehole sensors at each KiK-net station are available on the Hi-net website (see Data and Resources). The entire dataset and flatfile used in this paper is built and compiled with an automated protocol by Dawood et al. (2016). The seismic moment magnitude M_w , focal depth, epicenter location and focal mechanism information are obtained from the NIED moment tensor solution available at the broadband seismography network (F-net) catalogue.

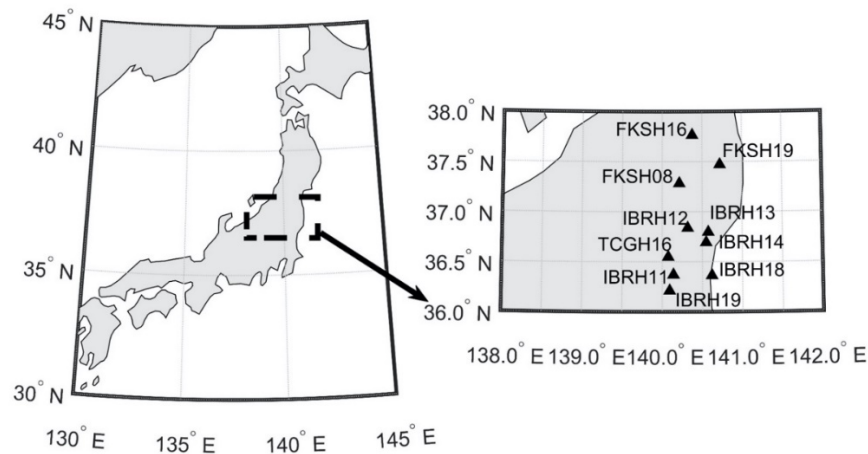


Figure 2.2. Locations of each selected Japanese station in this study.

In this paper, recorded horizontal components at the ground surface and at depth are used. The criteria for selection of ground motions and stations include: (1) epicentral distances less than 150 km; (2) M_w larger than 4.0; (3) peak ground acceleration (PGA) values at the surface

less than 0.01 g (to avoid effects of soil nonlinearity); (4) at least 50 available records complying with requirements (1) to (3) per study site; (5) the signal-to-noise ratio (SNR) larger 3.0 over the frequency ranges for κ_{r_AS} estimation. Moreover, the ability of shear-wave velocity profiles measured by downhole logging at KiK-net stations to describe actual site conditions has been questioned in the past (Wu et al. 2017). 2D/3D wave propagation could be significant at some KiK-Net stations because of the edge-generated surface waves, topographic effects and focusing effects. However, the potential for site scattering effects can be reduced as we considered KiK-Net sites with reliable shear wave velocity (V_s) profiles that meet the 1D wave propagation assumptions based on the results from Pilz and Cotton (2019). Thus, ten stations corresponding to various site classes (NEHRP site class from B to D) are selected in this study. Key characteristics pertaining these study sites are provided in Figure 2.2 and Table 2.1.

Table 2.1. Selected station information

| Station Name | Station Latitude | Station Longitude | * V_{s30} | †Hole Depth | †† H_{800} | Borehole Sensor Azimuth | §NEHRP Site Class |
|--------------|------------------|-------------------|-------------|-------------|--------------|-------------------------|-------------------|
| | degree | degree | m/s | m | m | degree | |
| FKSH08 | 37.28 | 140.22 | 562.50 | 105 | 8 | -3 | C |
| FKSH16 | 37.76 | 140.38 | 531.61 | 300 | 180 | 1 | C |
| FKSH19 | 37.47 | 140.73 | 338.06 | 100 | 20 | -4 | D |
| IBRH11 | 36.37 | 140.14 | 242.49 | 103 | 30 | 0 | D |
| IBRH12 | 36.83 | 140.32 | 485.71 | 200 | 20 | -3 | C |
| IBRH13 | 36.79 | 140.58 | 335.37 | 100 | 34 | 2 | D |
| IBRH14 | 36.69 | 140.55 | 829.12 | 100 | 10 | -1 | B |
| IBRH18 | 36.36 | 140.62 | 558.56 | 504 | 30 | 0 | C |
| IBRH19 | 36.21 | 140.09 | 692.31 | 210 | 2 | -1 | C |
| TCGH16 | 36.54 | 140.08 | 213.20 | 112 | NaN | -2 | D |

* V_{s30} : the time-averaged shear-wave velocity of the top 30 m subsoil

†Hole-depth: the depth of borehole sensor relative to the ground surface

†† H_{800} : depth to a horizon with velocity V_s of 800 m/s or more

§NEHRP Site Class: National Earthquake Hazards Reduction Program (NEHRP) site class classification

2.5. Methods

2.5.1. Estimation of κ_r and κ_0

We use the acceleration spectrum approach (Anderson and Hough, 1984) to estimate κ_{r_AS} . The slope of the linear decay, $-\pi\kappa_{r_AS}$, of the acceleration FAS in the high frequency range using log-linear coordinates is calculated for each horizontal component of the selected records. A weighted robust least square linear regression with Bisquare function over a manually selected high-frequency range ($[f_1, f_2]$) (see Figure 2.3 as an example). The minimum difference between f_1 and f_2 is 8 Hz. Following the recommendations of Ktenidou et al. (2013), f_1 is larger than the corresponding earthquake source-corner frequency (f_c), computed by Equation (2.1). (Brune, 1970, 1971):

$$f_c = 4.9 \times 10^4 \beta \left(\frac{\Delta\sigma}{M_0} \right)^{\frac{1}{3}} \quad (2.1)$$

Where f_c is in Hz, β is the shear-wave velocity near the source with units of km/s, $\Delta\sigma$ is the stress drop in MPa, and M_0 is the seismic moment in N·m. In this article, β is assumed to be 3.6 km/s (Pei et al. 2009). The value of $\Delta\sigma$ is assumed to be 3 MPa for crustal earthquakes and 5.5 MPa for subduction zone events (Nakano et al. 2015). Moreover, because the instrument's response is approximately flat below 30 Hz (which is close to the response of a three-pole Butterworth filter with a cutoff frequency of 30 Hz), we restrict f_2 to be less than 30 Hz (Aoi et al. 2004, Fujiwara et al. 2004, Oth et al. 2011, Laurendeau et al, 2013, Cabas et al. 2017).

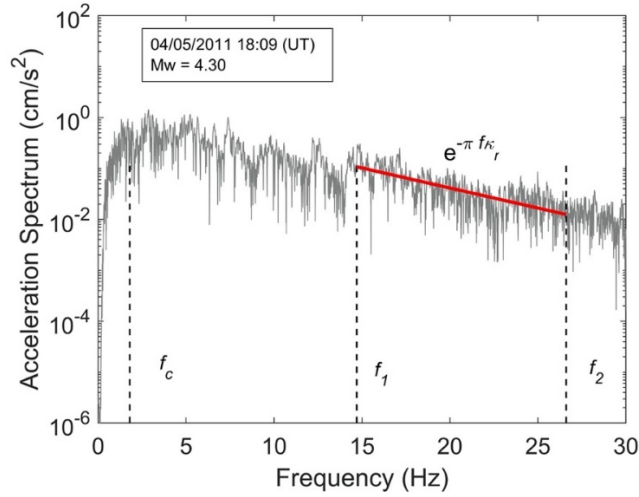


Figure 2.3. Selection of f_1 and f_2 on the Fourier acceleration amplitude spectrum corresponding to a surface record at station IBRH20. f_c refers to the corner frequency as estimated by the Brune (1970) model with stress drop of 3.0 MPa for active crustal events.

The S-wave window is often used to estimate κ_{r_AS} . Previous studies have picked the direct S-wave manually assuming a minimum duration of 5 sec for small/nearby events and 20 sec for large/far events (Ktenidou et al. 2013). Whilst, others have included the coda wave within the selected S-wave window for records where the coda wave cannot be separated clearly (Anderson and Hough 1984). Differences in κ_{r_AS} (computed by the acceleration spectrum approach using the whole time series) and $\kappa_{r_AS_SW}$ (computed by the acceleration spectrum approach using manually selected S-wave windows, following Anderson and Hough (1984)) are compared for records from shallow crustal earthquakes used in this study (see Figure 2.3). The same frequency range, f_1 and f_2 , is applied to each record to avoid bias from frequency range selections. The ratio, $r_1 = \kappa_{r_AS}/\kappa_{r_AS_SW}$, is computed at each study site to represent the differences between κ_{r_AS} and $\kappa_{r_AS_SW}$ in Figure 2.4. Values of $\kappa_{r_AS_SW}$ are generally larger than κ_{r_AS} at the study sites (i.e., r_1 is generally less than 1.0). Scattering effects can help explain

observed lower κ_{r_AS} values from the whole time series. When intrinsic attenuation is strong at a given site, higher frequencies can be removed more efficiently resulting in a steep slope in the S-wave FAS (Parolai et al. 2015). The full time series is composed of the direct S-waves, but also scattered waves from the redistribution of the seismic waves' energy. The latter can modify the slope in the FAS at high frequencies producing a biased κ_{r_AS} , which generally is lower.

Moreover, the S-wave window dominates the spectrum at surface and the downgoing waves could more affect the borehole time series. Thus, more variations between κ_{r_AS} and $\kappa_{r_AS_SW}$ at depth are observed. Because the differences between $\kappa_{r_AS_SW}$ and κ_{r_AS} are less than 20% for most of the selected ground motions used in this study, we choose the full time series to estimate κ_{r_AS} values. Further guidance in the selection of the S-wave window for kappa calculations can provide meaningful insights to reduce the between-station variability in kappa.

We choose the linear κ_0 -model introduced by Anderson (1991) and follow the nomenclature proposed by Ktenidou et al. (2013) to estimate the site component κ_0 :

$$\kappa_{r_AS} = \kappa_0 + \kappa_R \cdot R_{epic} \quad (2.2)$$

Where the κ_{r_AS} , and κ_0 are expressed in units of time (s), κ_R in units of s/km, and R_{epic} is the epicentral distance in km. This κ_0 -model assumes a unique source-to-site path for each record, and a homogeneous, frequency-independent seismic quality factor, Q (Knopoff 1964). Thus, we only select events with epicentral distances less than 150 km to minimize the potential for multiple source-to-site ray paths per record. The assumption of a unique Q -value allows for the calculation of κ_R (following the linear model in Equation (2.2)), which describes regional attenuation. Japan has varying Q -values across the region, with lower Q -values in the central Japanese island and higher Q -values on the east coast (Pei et al. 2009, Nakano et al. 2015). The low Q - and high Q -value regions are separated by Japan's volcanic belt. Thus, we avoid using

records that cross the volcanic belt during their propagation path from source to site based on the attenuation classification map provided by Nakano et al. (2015). The κ_0 -model in Equation (2.2) is also based on the assumption that the source contribution is negligible (Ktenidou et al. 2014, Van Houtte et al. 2011). For the selected KiK-net stations, the path component, κ_R , is constrained to be the same for both surface and borehole records because the regional attenuation contributions should be identical when analyzing individual stations (Ktenidou et al. 2013, 2015, Cabas et al. 2017). We use the maximum likelihood method to model κ_{r_AS} with the constrained κ_R based on Equation (2.2).

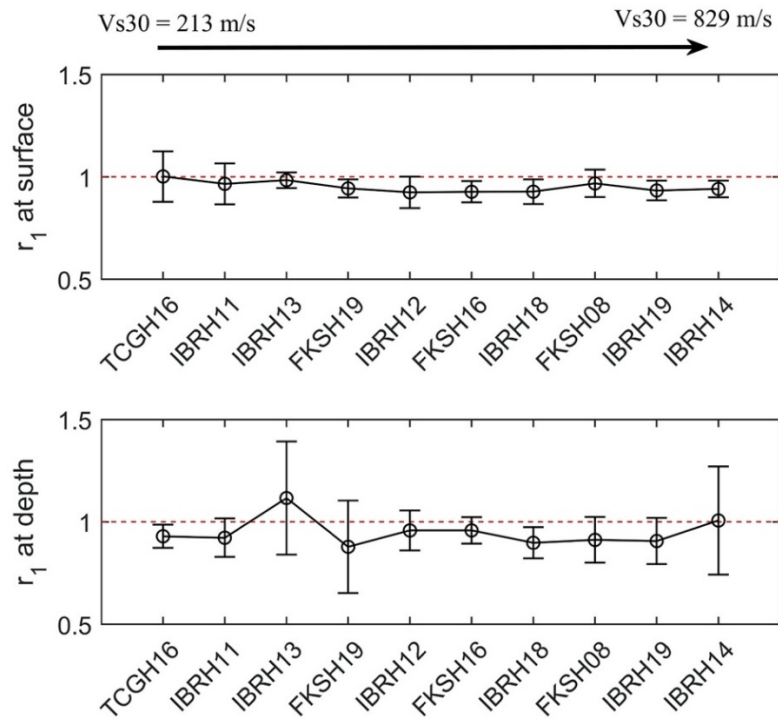


Figure 2.4. Comparison between κ_{r_AS} (from the whole FAS) and $\kappa_{r_AS_SW}$ (from the S-wave window FAS) corresponding to our ten study sites. r_1 is the ratio computed by $\kappa_{r_AS}/\kappa_{r_AS_SW}$. The dash line represents a ratio of 1.0. The circles depict the mean r_1 of all observed records, and the error bars indicate the +/- standard derivation of all observed ratios at each site of interest.

2.5.2. Ground Motion Directionality

A recorded ground motion at a specific site can vary depending on sensor orientation (Boore et al. 2006). This lack of uniformity of ground motions in all possible orientations is known as ground motion directionality. Two as-recorded horizontal orthogonal components of each selected ground motion are rotated to study the influence of ground motion directionality on the estimation of κ_{r_AS} . All records are rotated using the following equations (Boore et al. 2006, Boore 2010):

$$a_{ROT_1}(t; \theta) = a_1(t) \cos(\theta) + a_2(t) \sin(\theta) \quad (2.3)$$

$$a_{ROT_2}(t; \theta) = -a_1(t) \sin(\theta) + a_2(t) \cos(\theta) \quad (2.4)$$

Where $a_1(t)$ and $a_2(t)$ are the as-recorded acceleration time series, $a_{ROT_1}(t; \theta)$ and $a_{ROT_2}(t; \theta)$ are the rotated motions with the corresponding rotation angle θ . The κ_{r_AS} values computed from the corresponding FAS of rotated motions are referred to as $\kappa_{r_AS_ROT}$. In this article, we only rotate one single horizontal component ($a_1(t)$ or $a_2(t)$) from 0° to 180° (i.e., non-redundant angles) with increments of 10° to investigate the influence of ground motion directionality on κ_{r_AS} .

Considering that the frequency range ($[f_1, f_2]$) to estimate κ_{r_AS} is selected visually for each event, a large number of calculations is required for $\kappa_{r_AS_ROT}$ estimations. Thus, we propose a semi-automatic algorithm to compute $\kappa_{r_AS_ROT}$. First, we select the frequency range based on visual inspection of the as-recorded motion from a given event (at a given site). Then, a common frequency range is selected for the pair of recorded horizontal components and applied to all the corresponding rotated motions from that same event at that station. The main advantage of the proposed procedure, beyond the optimization of the computational process, is that it

avoids the introduction of additional uncertainties stemming from the frequency range selection. The performance of the proposed semi-automatic algorithm is evaluated by visually inspecting the rotated FAS plots and the corresponding frequency range.

The influence of ground motion directionality on the attenuation contributed by the soil column, hereafter referred to as $\Delta\kappa(\theta)$, is also investigated. $\Delta\kappa(\theta)$ is calculated as follows, assuming the κ_R value remains unchanged:

$$\begin{aligned}\Delta\kappa(\theta) &= \kappa_{r_AS_ROT_sur}(\theta) - \kappa_{r_AS_ROT_bore}(\theta) \\ &= (\kappa_{0_ROT_sur}(\theta) + \kappa_R \times R_{epic}) - (\kappa_{0_ROT_bore}(\theta) + \kappa_R \times R_{epic}) \\ &= \Delta\kappa_{0_ROT}(\theta)\end{aligned}\tag{2.5}$$

It should be noted that errors in the azimuth of borehole sensors (i.e., sensors not oriented in the true NS or EW directions) could propagate through the estimation of $\Delta\kappa(\theta)$, which means that values of θ at the surface and at depth may not be consistent. The errors in the azimuth are observed at eight selected sites, and the maximum borehole sensor deflection is 4° (shown in Table 1). Thus, we correct the borehole record orientation with the azimuth of borehole sensors provided by Hi-net before the borehole horizontal component is rotated.

2.6. Results and Discussion

2.6.1. Directionality effects on κ_r and κ_0 estimations

A variation of $\kappa_{r_AS_ROT}$ with rotation angle is observed for both surface and borehole records at all stations. Figure 2.5 presents an example of the relationship between $\kappa_{r_AS_ROT}$ and rotation angles at FKSH19. The corresponding FAS of the rotated components are also presented (i.e., with rotation angle of 80° and 160°) for comparison purposes, depicting changes of the

decay in the high-frequency range. The standard derivations corresponding to $\kappa_{r_AS_ROT_sur}$, and $\kappa_{r_AS_ROT_bore}$ are 0.0109 s and 0.0041 s, respectively.

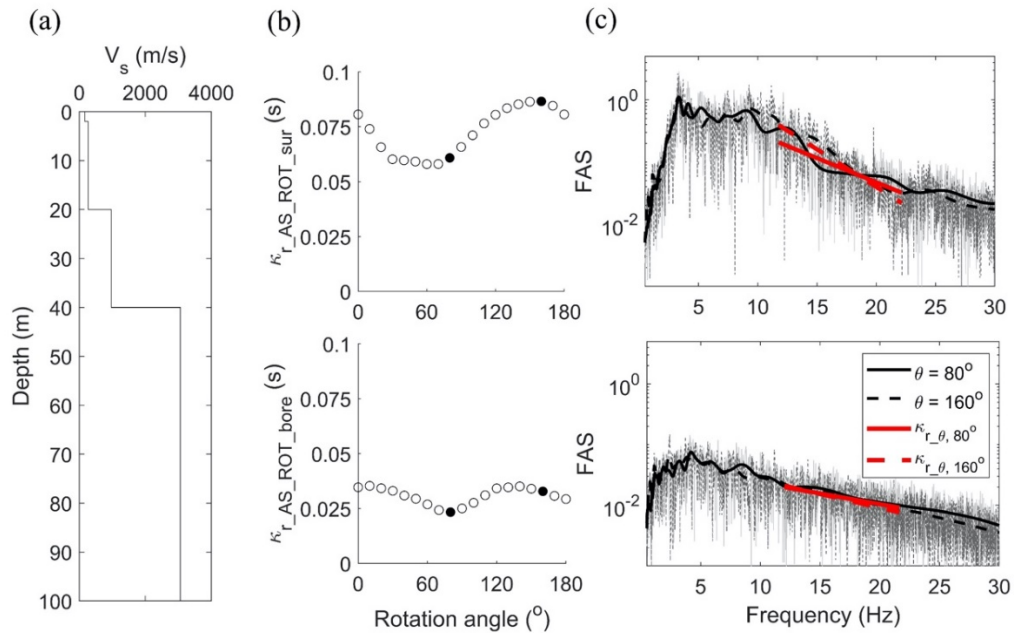


Figure 2.5. Example of $\kappa_{r_AS_ROT}$ variations. (a) Shear wave velocity profile at FKSH19, (b) comparison between $\kappa_{r_AS_ROT}$ and rotation angle at surface and borehole for one record, and (c) the FAS for rotated components with θ of 80° and 160° . The dark solid and dash lines show the smoothen FAS to emphasize the differences between rotated FASs. The select ground motion was a shallow active crustal event recorded at FKSH19 (site class: D) with seismic moment magnitude of 4.4, azimuth of 190° , and epicentral distance of 117 km (recorded on 07/26/2003 (UT)).

Figure 2.5 illustrates that the variation of $\kappa_{r_AS_ROT}$ at the surface is more significant than at depth, which is also observed for the majority of records across all stations. We then investigate the influence of the event azimuth on the maximum $\kappa_{r_AS_ROT}$ observed and its corresponding rotation angle. The rotation angle associated with the maximum $\kappa_{r_AS_ROT}$ is

hereafter referred to as θ_{\max} . A correlation between θ_{\max} and the azimuth of each record at the surface and at depth is not found. The corresponding comparison between event azimuth and θ_{\max} for each study site is presented in Figure A.1 of the electronic supplement to this article, which supports our hypothesis that the maximum $\kappa_{r_AS_ROT}$ is affected by the local site condition rather than the event azimuth.

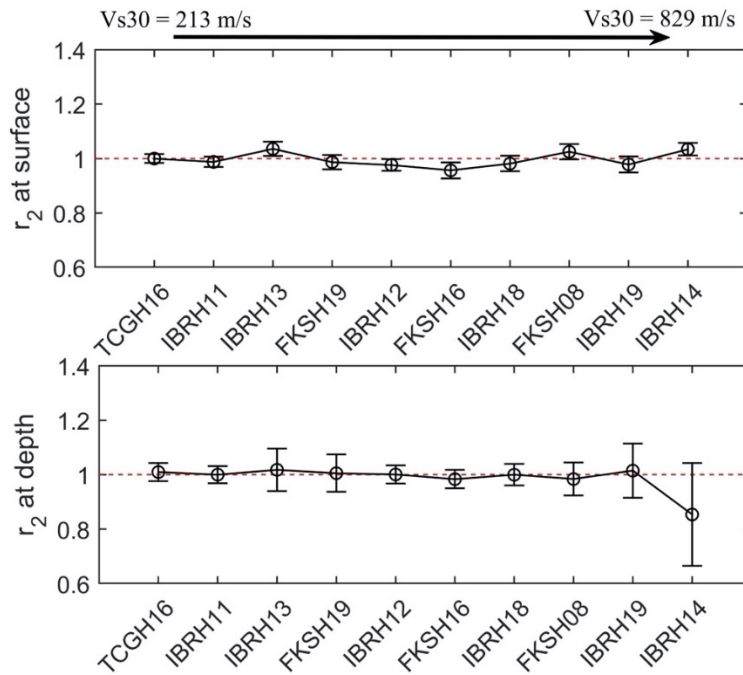


Figure 2.6. Comparison between mean κ_{r_AS} of rotated motions (i.e., $\kappa_{r_AS_mean}$) and mean κ_{r_AS} of two recorded horizontal component (i.e., $\kappa_{r_AS_ave}$) at selected stations along with the corresponding standard derivation at (a) borehole and (b) ground surface. r_2 corresponds to the ratio $\kappa_{r_AS_ave}/\kappa_{r_AS_mean}$. The dash line indicates an r_2 equal to 1.0, and the circles depict the mean r_2 across all records considered per station. The error bars indicate the \pm standard deviation of all r_2 computed at each site of interest.

The mean of all $\kappa_{r_AS_ROT}$ for each record, $\kappa_{r_AS_mean}$, and the average of $\kappa_{r_AS_H1}$ and $\kappa_{r_AS_H2}$ from the corresponding as-recorded horizontal components, $\kappa_{r_AS_ave}$, are compared in Figure 2.6 by means of the ratio, $r_2 = \kappa_{r_AS_ave}/\kappa_{r_AS_mean}$. Figure 2.6 demonstrates that the

differences between $\kappa_{r_AS_mean}$ and $\kappa_{r_AS_ave}$ values at the ground surface are small; the maximum average of surface r_2 across the ten study sites is 1.04 (at IBRH13; $V_{s30} = 335$ m/s) and the minimum average is 0.96 (at FKSH16; $V_{s30} = 532$ m/s). However, at station IBRH14 ($V_{s30} = 829$ m/s), the differences of borehole $\kappa_{r_AS_mean}$ and $\kappa_{r_AS_ave}$ values are relatively large, with an average r_2 of 0.85 and a standard derivation of r_2 equal to 0.19. A closer inspection of the empirical transfer function (ETF) at this station reveals that κ_{r_AS} estimates at IBRH14 could be affected by the site-amplification in high frequencies, which can help explain observed differences between $\kappa_{r_AS_mean}$ and $\kappa_{r_AS_ave}$. The corresponding ETFs at IBRH13, FKSH08, FKSH16, and FKSH19 also show varying site-amplification in the high frequency range. Differences between $\kappa_{r_AS_mean}$ and $\kappa_{r_AS_ave}$ for all study sites are also presented in Figure A.2 (available in the electronic supplement to this article). In Figure A.2, the different colors indicate the differences between $\kappa_{r_AS_H1}$ and $\kappa_{r_AS_H2}$, which shows the discrepancy between two horizontal components will not affect $\kappa_{r_AS_ROT}$ and $\kappa_{r_AS_mean}$. Considering the similarity observed between values of $\kappa_{r_AS_mean}$ and $\kappa_{r_AS_ave}$ for multiple ground motions and across study sites, an orientation-independent κ_r value for one recorded event at a given station can be estimated from the average of $\kappa_{r_AS_H1}$ and $\kappa_{r_AS_H2}$ computed from as-recorded orthogonal horizontal components directly. In the following sections, we use $\kappa_{r_AS_ave}$ (also denoted as κ_{r_AS} for simplicity) as the representative value for each pair of orthogonal horizontal components.

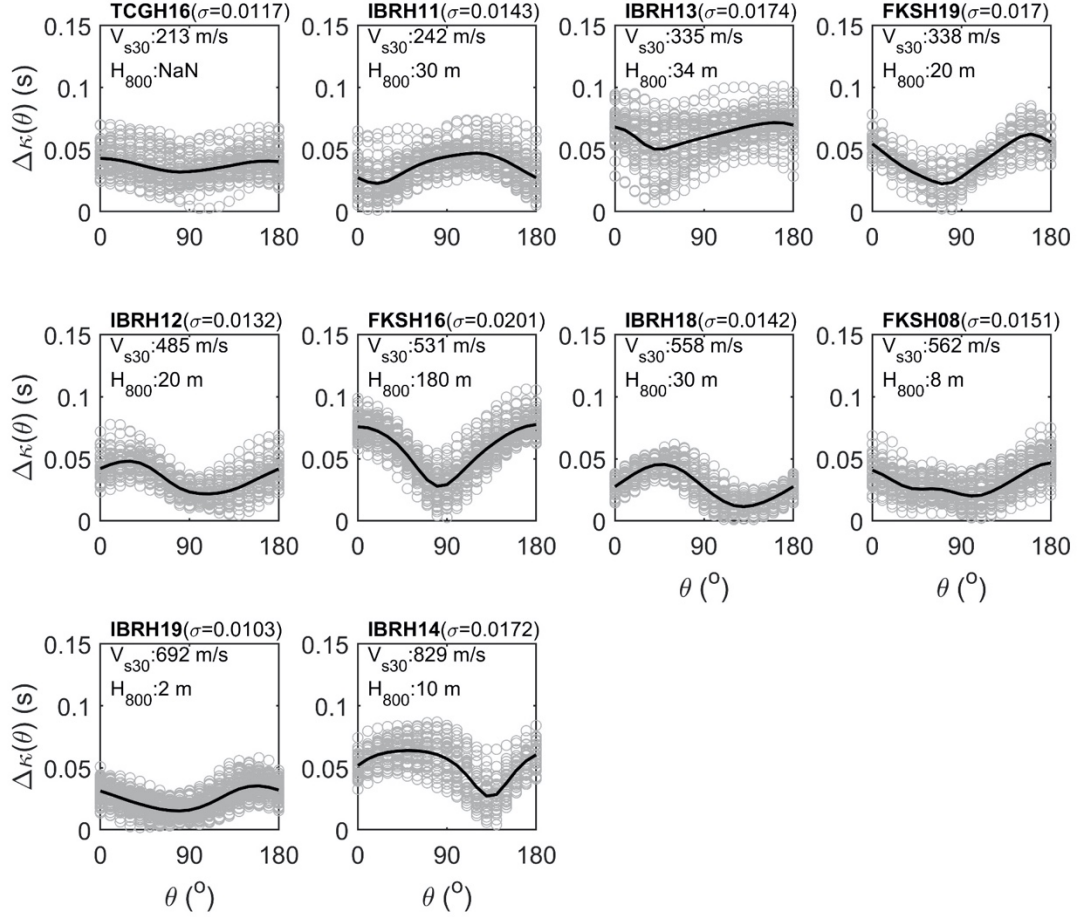


Figure 2.7. Variability of $\Delta\kappa(\theta)$ at the stations of interest and the corresponding site information. The solid lines represent the mean of all $\Delta\kappa(\theta)$ across all records per rotation angle, while the gray circles depict $\Delta\kappa(\theta)$ obtained for each record and multiple rotation angles. H_{800} refers to depth to a horizon with velocity V_s of 800 m/s or more.

The effects of ground motion directionality on $\Delta\kappa(\theta)$ (Equation (2.5)) are also explored to investigate how the orientation of ground motion can affect the seismic attenuation taking place throughout the soil column. Figure 2.7 and Table 2.2 show the variations of $\Delta\kappa(\theta)$ at the sites of interest. First, we observe that the seismic attenuation contributed by the soil column is affected by ground motion directionality. Second, there seems to be a systematic variation with directionality unique to each site, with the maximum $\Delta\kappa(\theta)$ generally corresponding to the same

rotation angle across different ground motions at each station. Kotha et al. (2019) proved that the contribution of radiation pattern to the ground shaking characteristics would be weak and random in the high frequency range. Thus, we hypothesize that the influence of ground motion directionality on the high-frequency parameter κ is station-dependent and not affected by the earthquake source. Moreover, the maximum σ for $\Delta\kappa(\theta)$ is observed at FKSH16, which has a thick soil column (hole-depth of 300 m, and $H_{800} = 180$ m) and a $V_{s30} = 532$ m/s. The minimum σ value is found at IBRH19 with H_{800} of 2 m, V_{s30} of 692 m/s and hole-depth of 210 m. However, a strong correlation between σ and H_{800} or V_{s30} or hole depth is not evident across all study sites. Different site parameters (or a combination of existing ones) with considerations of shallow and deeper geologic structures are required to further detect potential correlations between site conditions and variability in $\Delta\kappa_0$ due to ground motion directionality.

Table 2.2. Station information and statistical parameters for $\Delta\kappa(\theta)$

| Station Name | *Hole Depth | $\dagger H_{800}$ | $\dagger\dagger V_{s,\text{mean}}$ | $\S \sigma(\Delta\kappa(\theta))$ | $\parallel_{\text{mean}}(\Delta\kappa(\theta))$ | **NEHRP Site Class |
|--------------|-------------|-------------------|------------------------------------|-----------------------------------|---|--------------------|
| | m | m | m/s | s | s | |
| IBRH14 | 100 | 10 | 1601.44 | 0.0172 | 0.0525 | B |
| IBRH19 | 210 | 2 | 1792.68 | 0.0103 | 0.0249 | C |
| FKSH08 | 105 | 8 | 936.59 | 0.0151 | 0.0310 | C |
| IBRH18 | 504 | 30 | 1522.67 | 0.0142 | 0.0279 | C |
| FKSH16 | 300 | 180 | 841.95 | 0.0201 | 0.0566 | C |
| IBRH12 | 200 | 20 | 967.53 | 0.0132 | 0.0341 | C |
| FKSH19 | 100 | 20 | 842.76 | 0.0170 | 0.0422 | D |
| IBRH13 | 100 | 34 | 793.95 | 0.0174 | 0.0620 | D |
| IBRH11 | 103 | 30 | 649.92 | 0.0143 | 0.0366 | D |
| TCGH16 | 112 | NaN | 369.34 | 0.0138 | 0.0369 | D |

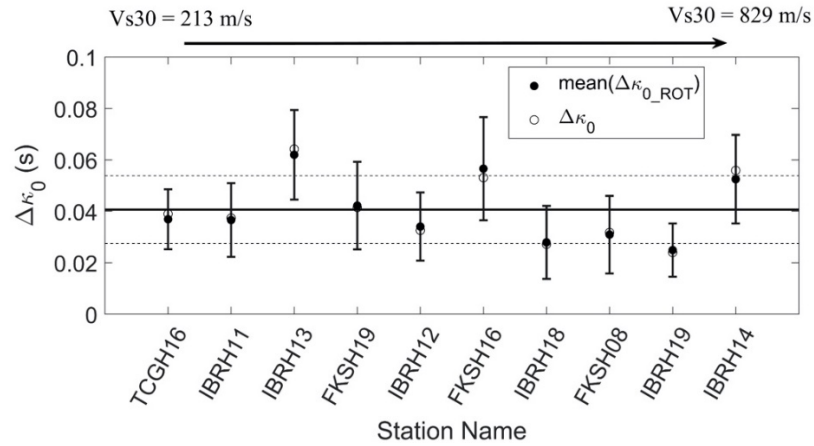


Figure 2.8. Comparison of $\text{mean}(\Delta\kappa(\theta))$ and $\Delta\kappa_0$ at each station. $\Delta\kappa_0$ is the difference between surface and borehole κ_0 estimated from empirical regressions on as-recorded horizontal components. The error bar (within-station variability) represents ± 1 standard derivation of $\Delta\kappa(\theta)$ at each station. The horizontal solid line presents the mean of $\Delta\kappa(\theta)$ across all stations, and the dash lines indicate the ± 1 standard derivation of $\Delta\kappa(\theta)$ across all considered stations (between-station variability).

Finally, we compare the mean of all $\Delta\kappa(\theta)$ values with the difference between surface and borehole κ_0 values (hereafter referred to as $\Delta\kappa_0$) from empirical linear regressions conducted on as-recorded horizontal components (i.e., averaging as-recorded κ_{r_AS} values for each pair) at each station (Figure 2.8). Mean values of $\Delta\kappa(\theta)$ shown in Figure 2.8 are only slightly higher than the corresponding $\Delta\kappa_0$ values, which indicates that the mean of two as-recorded κ_{r_AS} values can lead to an orientation-independent estimation of $\Delta\kappa_0$. Figure 2.8 also provides a comparison of the within-station and between-station variability of $\Delta\kappa(\theta)$. For most stations considered in this study (i.e., FKSH08, IBRH14, IBRH12, FKSH19, IBRH18, IBRH13 and IBRH11), the within-station variability in $\Delta\kappa(\theta)$ is comparable and sometimes more significant, which evidences the need for a more rigorous consideration of the within-station variability in κ_0 estimates. We note

that the observed larger within-station variabilities in $\Delta\kappa(\theta)$ at IBRH13, IBRH14, FKSH08, and FKSH19 can be influenced by site-amplification effects at these sites in the high frequency. The latter can induce bias in the resulting κ values. The quantification of the within-station variability in κ will result in more reliable κ_0 estimates, which can inform empirical correlations with local site conditions.

2.6.2. Earthquake type and focal depth effects on κ_r , κ_R , and κ_0 estimations

In this section, we investigate the influence of earthquake type and focal depth on average κ_{r_AS} from as-recorded components, regional attenuation, as captured by κ_R , and κ_0 estimations. The algorithm proposed by Garcia et al. (2012) is used herein to classify earthquake types as: (1) shallow active crustal, ACRsh (if the hypocentral depth is less than 35 km), (2) deep active crustal, ACRde (if the hypocentral depth is larger than 35 km), (3) subduction zone intraslab, SZintra (with minimum focal depth of 15 km), and (4) subduction zone interface, SZinter, earthquakes (with minimum focal depth of 70 km).

Values of $\Delta\kappa_0$, κ_{0_sur} , κ_{0_bore} , and κ_R at the selected ten stations are computed for different datasets categorized by earthquake type, and shown in Figure 2.9. It should be noted that the limited number of ACRde events did not allow for the derivation of the corresponding κ_0 and κ_R for this particular dataset. A few negative values of κ_R and κ_0 values are obtained at some stations for some of the datasets, which could be caused by the lack of available events for each earthquake type at specific epicentral distance ranges. For example, ACRsh events recorded at IBRH11 only have epicentral distances in the range of 50 to 150 km. Hence, those cases were not included in Figure 2.9. The resulting κ_0 and κ_R values demonstrate that different seismicity types lead to varying estimates of the κ_R component (i.e., the slope of κ_0 -model), which in turn

affects the estimated site-specific κ_0 component (i.e., the intersect in the y-axis at zero epicentral distance). Records from subduction and active crustal earthquakes will be affected by different wave propagation paths, which is reflected in the variability in the path-component κ_R .

Variations in $\Delta\kappa_0$ values at selected stations are relatively small for the different datasets considered, which supports previous research indicating the site-specific nature of $\Delta\kappa_0$ values that is not affected by the focal depth (i.e., the difference between κ_{0_sur} and κ_{0_bore} represents the seismic attenuation taking place throughout the local soil column, Cabas et al. 2017).

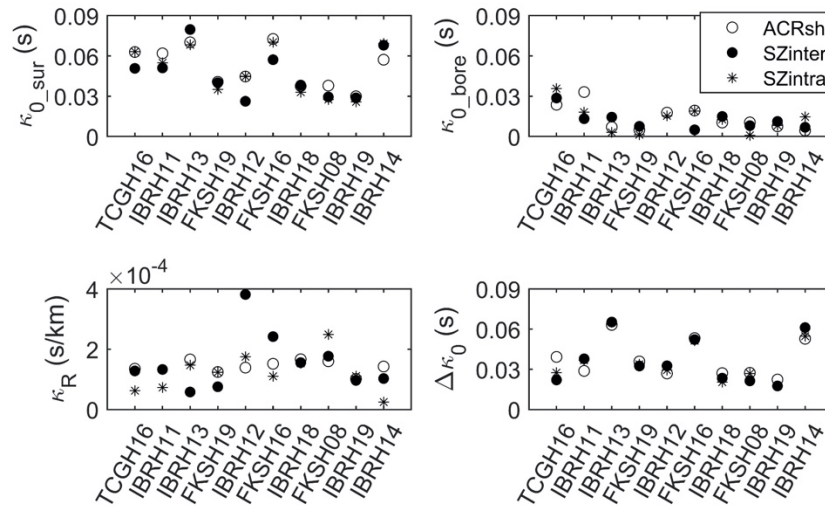


Figure 2.9. Comparisons of κ_0 (at the ground surface and at depth), κ_R , and $\Delta\kappa_0$ values for different earthquake types at each station.

The influence of focal depth on the estimations of κ_0 and κ_R is investigated by separating into three groups with focal depths of: (1) less than 35 km (which includes both ACRsh and SZintra events), (2) from 35 km to 70 km (which includes the ACRde and SZintra events), and (3) more than 70 km (which includes the ACRde and SZinter events). A correlation between κ_R

values and focal depth is not observed, but κ_R values show less variation when grouped by focal depth (regardless of earthquake type) than by earthquake type as seen in Figure 2.10.

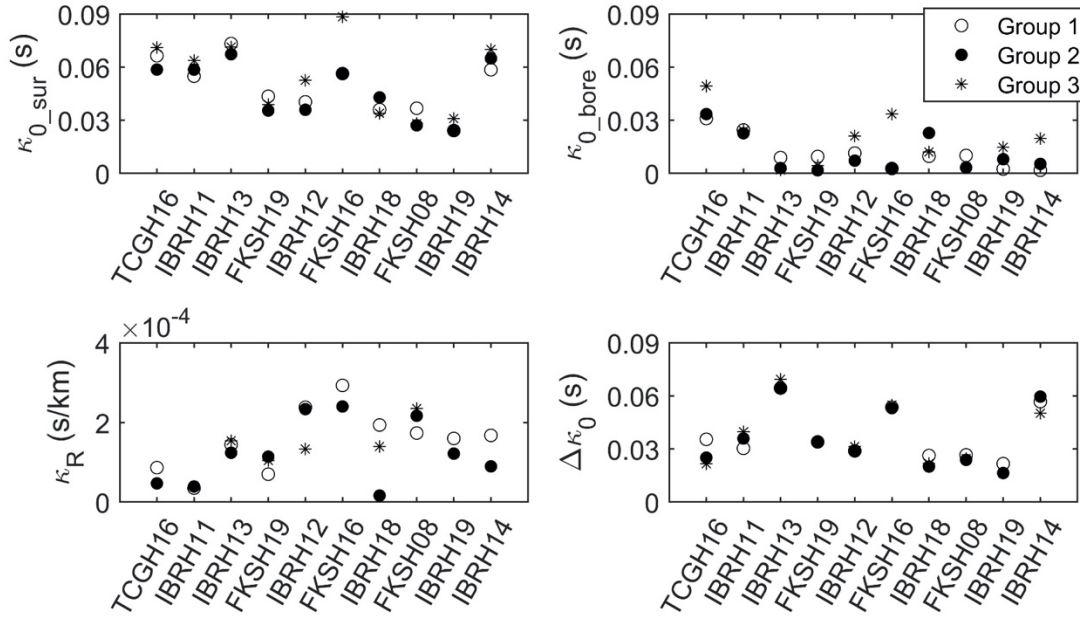


Figure 2.10. Comparisons of κ_0 (at the ground surface and at depth), κ_R , and $\Delta\kappa_0$ (the difference between surface and borehole κ_0) values for different focal depth groups at each station. Groups 1, 2 and 3 consider focal depths of less than 35 km, from 35 to 70 km, and more than 70 km, respectively.

The influence of earthquake type and focal depth is further explored in Figure 2.11, where κ_R , κ_0 and $\Delta\kappa_0$ values estimated only using ACRsh events, and a dataset of records with focal depth less than 35 km (i.e., Group 1) are compared. It should be noted that a negative κ_R value is derived at IBRH11 for the ACRsh datasets, which may be caused by the absence of events for epicentral distance less than 50 km. The average differences of κ_R estimations between these two data sets across the ten stations is 28.43% (neglecting the values at IBRH11), while the corresponding average differences of κ_{0_sur} and $\Delta\kappa_0$ are 8.77% and 4.51%, respectively. The differences in κ_R , κ_{0_sur} , κ_{0_bore} , and $\Delta\kappa_0$ estimates are acceptable, which supports the

incorporation of shallow subduction zone events to a shallow crustal event dataset. Estimates of κ_R and κ_0 for each group and earthquake types at the selected stations are shown in Table S1 (available in the electronic supplement to this article).

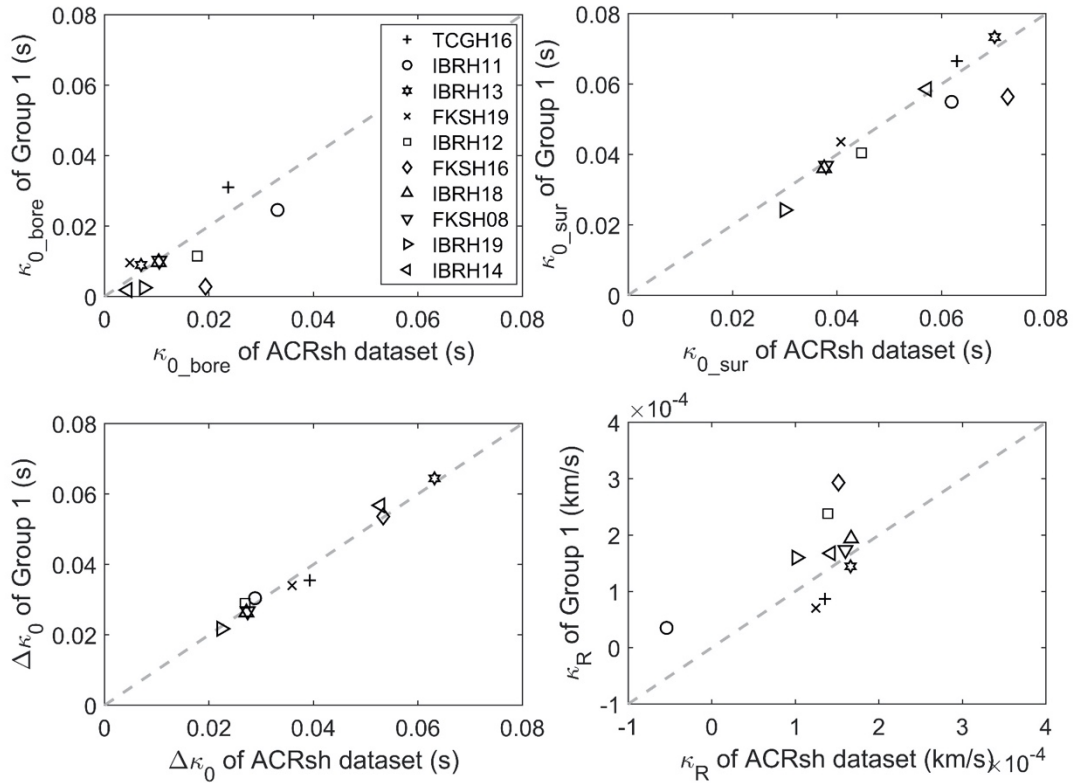


Figure 2.11. Comparisons of κ_0 (at the ground surface and at depth), κ_R , and $\Delta\kappa_0$ (the difference between surface and borehole κ_0) values estimated with ACRsh dataset, and Group 1. Group 1 includes the events with focal depth less than 35 km (which includes both ACRsh and SZintra events).

2.7. Conclusions

Repeatable contributions from path and site terms to the within-station variability in individual estimates of κ_r and site-specific κ_0 were investigated using ten stations from the KiK-net database. Our dataset consisted of linear ground motions with surface PGA less than 0.01 g, M_w larger than 4.0 and epicentral distance less than 150 km. Both active crustal and subduction

earthquakes were used in this work to investigate repeatable contributions from the wave propagation path. Systematic variability on κ_r and κ_0 values stemming from the dataset choice, namely the selection of events based on their focal depth and type of seismicity was evaluated. Contributions to the within-station variability associated with ground motion directionality were also investigated.

The influence of ground motion directionality on the estimates of κ_{r_AS} was studied, and findings from this work revealed that the orientation of ground motion affects estimates of κ_{r_AS} computed on single horizontal components. However, this influence can be removed when calculating the average of two as-recorded horizontal component κ_{r_AS} values. Thus, using the mean of two horizontal κ_{r_AS} values (without considerations of the difference between these two values) is recommended as the representative κ value for each ground motion pair. This is different from previous recommendations to only report κ_{r_AS} values for which differences between the recorded horizontal components is less than 20%. It was also found that the within-station variability in $\Delta\kappa_0$ values (i.e., the difference between κ_0 values at the surface and at depth) associated with directionality effects can be comparable to the between-station variability. This observation highlights the importance of quantifying the within-station variability on κ estimates in a more robust manner. Moreover, our findings support previous research efforts indicating that site amplification effects on κ estimates should be minimized in order to obtain reliable estimates at sites of interest. Systematic contributions from event-azimuths were not observed, while the variability in $\Delta\kappa(\theta)$ estimates with rotation angle was found to be a function of local soil conditions. The influence of ground motion directionality on the parameterization of near-surface attenuation was found to be station-dependent, but further investigation is required to identify relevant correlations between observed ground motion directionality and site properties. Near-

surface seismic attenuation anisotropy could help explain observed variations of $\Delta\kappa(\theta)$ with ground motion orientation. Anisotropy in Q values has been observed from both laboratory experiments (Tao and King, 1990, Kern et al. 1997) and the analysis of earthquake ground motions (Liu et al. 2005). The random distributed cracks near surface could also cause seismic anisotropy (Liu et al. 1993, Liu et al. 2004, Boness and Zoback 2004), which could then influence seismic wave scattering and reflection. The specific geological condition and volcanic environment in Japan also lead to anisotropy in Q (Pei et al. 2009, and Nakano et al. 2015). More generally, a preferred direction of ground motion independent from the expected polarization (based on focal mechanism and location of the events) has also been observed in recorded data from the Whittier Narrows and Loma Prieta earthquakes (Bonamassa et al. 1991, Bonamassa and Vidale 1991). More research on directionality effects is required to elucidate the physical basis for the observed variation of attenuation characteristics of ground motions with orientation.

Different earthquake types were found to lead to different κ_R values. However, it is important to note that the classification of seismicity type is also tied to the focal depth. Selecting a dataset with considerations of systematic variations stemming from varying focal depths and earthquake types is recommended to resolved κ 's path-component, κ_R more reliably. Deep earthquakes can produce multi-wave propagation paths to the site of interest, which could have a more significant influence on κ_R . On the other hand, the incidence angle of seismic waves when the focal depth is shallow could introduce larger within-station variability. Smaller differences in surface and borehole κ_0 values were observed across the datasets used (i.e., different focal depths and/or earthquake types). The lack of variability of $\Delta\kappa_0$ values as a function of source and path effects evidences that $\Delta\kappa_0$ is mainly a function of near-surface attenuation, which supports its site-specific nature also observed in previous research studies.

2.8. Data and Resources

Accelerograms and geotechnical data are obtained from the KiK-net network at <http://www.kyoshin.bosai.go.jp> (last accessed December 2018), collected and distributed by National Research Institute for Earth Science and Disaster Prevention (NIED). The orientations of borehole sensors are available at http://www.hinet.bosai.go.jp/st_info/detail/?LANG=ja (last accessed December 2018). The earthquake information is available F-net network at <http://www.fnet.bosai.go.jp/top.php> (last accessed December 2018). The electronic supplement to this article includes one table, which contains κ -values of different datasets classified by earthquake type and focal depth, and two figures, which provide the additional comparisons to show the influence of ground motion directionality on κ estimations.

CHAPTER 3. EFFECTS OF NONLINEAR SOIL BEHAVIOR ON KAPPA (κ): OBSERVATIONS FROM THE KIK-NET DATABASE

Based on the paper published on Bulletin of the Seismological Society of America:

Ji, C., Cabas, A., Bonilla, L.F. and Gelis, C., 2021. Effects of Nonlinear Soil Behavior on Kappa (κ): Observations from the KiK-Net Database. Bulletin of the Seismological Society of America.

3.1. Abstract

Soil nonlinear behavior is often triggered in soft sedimentary deposits subjected to strong ground shaking and has led to catastrophic damage to civil infrastructure in many past earthquakes. Nonlinear behavior in soils is associated with large shear strains, increased material damping ratio and reduced stiffness. However, most investigations of the high-frequency spectral decay parameter κ , which captures attenuation, have focused on low-intensity ground motions inducing only small shear strains. Because studies of the applicability of the κ -model when larger deformations are induced are limited, this paper investigates the behavior of κ (both κ_r per record and site-specific κ_0 estimates) beyond the linear-elastic regime. Twenty stations from the KiK-net database, with time-average shear wave velocities in the upper 30 m between 213 and 626 m/s, are used in this study. We find that the classification scheme used to identify ground motions that trigger soil nonlinear behavior biases estimates of κ_0 in the linear and nonlinear regimes. A hybrid method to overcome such bias is proposed considering proxies for in situ deformation (via the shear strain index) and ground shaking intensity (via peak ground acceleration). Our findings show that soil nonlinearity affects κ_r and κ_0 estimates, but this influence is station-dependent. Most κ_0 at our sites had a 5-20% increase at the onset of soil nonlinear behavior. Velocity gradients and impedance contrasts influence the degree of soil nonlinearity and its effects on κ_r and κ_0 . Moreover, we observe that other complexities in the

wave propagation phenomenon (e.g., scattering and amplifications in the high-frequency range) impose challenges to the application of the κ_0 -model, including the estimation of negative values of κ_r .

3.2. Introduction

The anelastic attenuation of seismic waves as they travel through sedimentary deposits is a function of the deformations induced, which in turn depend on the material properties (e.g., plasticity of the soil) and the intensity of the ground shaking. Material damping ratio, ξ , is commonly used in geotechnical earthquake engineering to quantify viscous and anelastic energy dissipation in soils subjected to dynamic loading. Empirical models of ξ often have a constant minimum value (known as the minimum shear-strain damping, ξ_{\min}) for small shear strains considered in the linear-elastic regime (e.g., Darendeli, 2001). Yet, values of ξ increase as larger shear strains are induced in soil deposits by stronger ground excitations (Idriss et al. 1978, Seed et al. 1986, Darendeli 2001). The characterization of ξ across a wide range of strains is essential to model the effects of local soil conditions on earthquake ground motions.

The high-frequency spectral decay parameter κ was introduced by Anderson and Hough (1984) based on the Fourier spectrum characteristics of a ground motion's shear-wave window recorded directly in the field, which makes it an observable parameter that quantifies total attenuation (e.g., energy dissipation caused by scattering and anelasticity). Estimates of κ have proven useful in multiple applications, from stochastic modeling of ground motions (Boore 2003) to the development of host-to-target adjustments of ground motion models (e.g., Campbell 2003, Al Atik et al. 2014). The site-specific, distance-independent component of κ , known as κ_0 (Anderson 1991), is defined as a site parameter that captures the attenuation due to the propagation of seismic waves through near-surface materials. The relationship between κ_0 and

ξ_{\min} has been investigated in previous studies (e.g., Cabas et al. 2017; Ktenidou et al. 2015; Xu et al. 2019) for weak motion data, but the quantification of κ and κ_0 beyond the linear-elastic regime remains unsolved.

Most studies on individual estimates of κ (i.e., the value measured from the observed Fourier Amplitude Spectra (FAS) per record following the Anderson and Hough (1984) approach), hereafter referred to as κ_r , and its site-specific component κ_0 have used ground motion records that do not trigger nonlinear behavior at the sites of interest or that are not considered influenced by the site's nonlinear response (e.g., Ktenidou et al. 2013, Van Houtte et al. 2011, Laurendeau et al. 2013, Edwards et al. 2015, Perron et al. 2017, Xu et al. 2019). However, nonlinear soil behavior has often been responsible for increasing the damage potential of strong ground motions in past earthquakes (e.g., Darragh and Shakal, 1991, Trifunac and Todorovska, 1994, Bonilla et al., 2011, Rong et al., 2016). Understanding near-surface attenuation effects in the nonlinear regime is then necessary for a thorough assessment of seismic hazards and risks imposed to civil infrastructure (Anderson and Hough 1984). Hence, this paper investigates the relationships among κ , shear strains and ground motion intensity to understand the behavior of κ at the onset of nonlinear soil behavior.

3.3. Background

The first paper that attempted to connect soils' nonlinear response and κ_r was conducted by Yu et al. (1992), where the authors compared two simulated records: one from a linear site response analysis, and the other from a time-domain nonlinear site response analysis. Yu et al. (1992) observed that the value of κ_r estimated with the Anderson and Hough (1984) approach and corresponding to the motion affected by soil nonlinearity was smaller. However, later studies

found a positive correlation between κ_r (and κ_0), strain amplitudes and the intensity of ground shaking (e.g., Durward et al 1996; Lacave-Lachet et al 2000; Dimitriu et al. 2001).

Durward et al. (1996) found that κ_r values were a function of peak ground velocity (PGV, varying from 0.01 to 1 m/s), which was used as a proxy for deformation. Values of κ_r were computed for more than 60 records observed at 23 sites in the Imperial Valley, California based on the acceleration spectrum approach (Anderson and Hough, 1984). Durward et al. (1996) hypothesized that soil nonlinearity had affected κ_r because higher κ_r values correlated well with higher PGVs. Moreover, Lacave-Lachet et al. (2000) analyzed ground motions from the 1995 Kobe earthquake in Japan (i.e., the main shock and aftershocks), and found that κ_r values increased with increasing peak ground acceleration (PGA). Hence, Lacave-Lachet et al. (2000) proposed to use κ_r to detect the onset of soil nonlinearity. Dimitriu et al. (2001) investigated the dependency between site-specific κ_0 and ground shaking intensity. Values of κ_r for 23 ground motions (i.e., 46 horizontal components with values of κ_r reported for each individual component) were computed at two adjacent sites in Lefkas, western Greece, based on the acceleration spectrum method. Dimitriu et al. (2001) provided evidence that κ_0 was a proxy for soil nonlinearity based on the observed dependency between κ_0 and ground shaking amplitudes, which were represented by mean horizontal acceleration in the S-wave window (MGA), PGA, and PGV. Positive correlations were found between the 46 κ_0 values and MGA, PGA, and PGV in log-scale, while a negative correlation was observed between κ_0 and the site dominant-resonance frequency. However, Van Houtte et al. (2014) identified an opposite correlation between estimates of κ_0 (computed as the individual measured κ_r with epicentral distance less than 30 m) and PGA at hard sites (i.e., with V_{s30} varying from 422 to 1073 m/s) using ground

motions from the 2010-2011 Canterbury earthquake sequence in New Zealand. The authors suggested further investigations to understand the associated physical mechanism.

There are still few and contradicting observations of the effects of nonlinearity on κ_r and κ_0 estimates (Ktenidou et al. 2015). Previous studies only considered a very limited database of ground motions. This paper takes advantage of the unique Japanese Kiban-Kyoshin network (KiK-net), which is rich in high-quality ground motions, to further investigate the effects of soil nonlinearity on κ_r and κ_0 . More specifically, we explore the dependence of κ_r and κ_0 on ground shaking intensity (i.e., weak, moderate or strong ground motions as parameterized by PGA), and on the level of shear strains induced in near-surface materials at 20 KiK-net stations. First, we present the conceptual basis for the relationship between κ , shear strains and ground motion intensity. Then, we describe our database and methods, starting with the identification of an appropriate classification scheme for linear and nonlinear ground motions. The analysis of the effects of ground shaking amplitudes on κ_r at each study site follows. Lastly, we compare the ratio of nonlinear and linear site-specific κ_0 across all selected stations to assess the variation of near-surface attenuation estimates from the linear-elastic to the nonlinear regime.

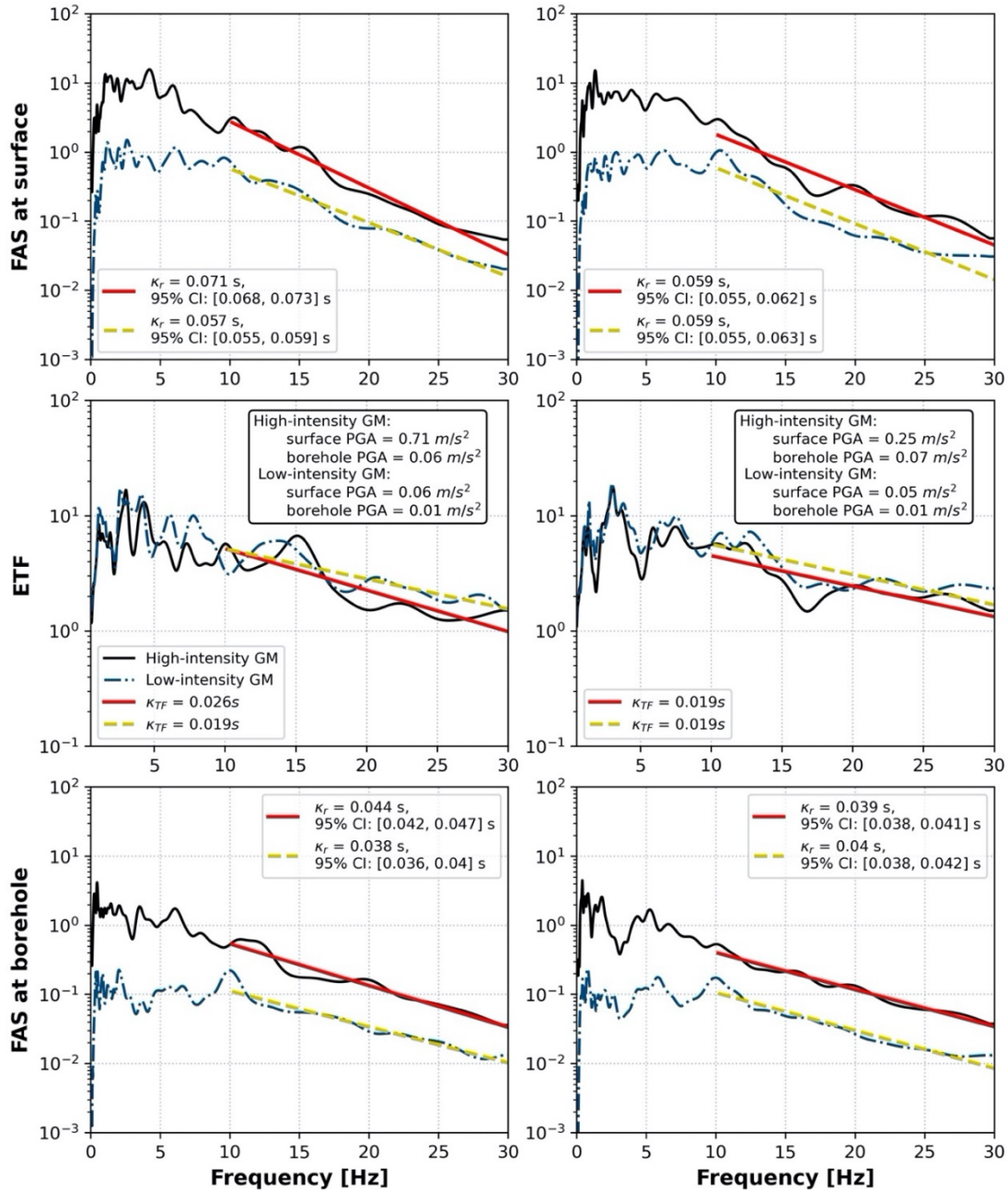


Figure 3.1. Comparisons between a weak and a strong ground motion recorded at FKSH14 ($V_{s30} = 237$ m/s). The M_w and R_c are 4 and 15 km for the low-intensity ground motion, while 5.1 and 15 km for the high-intensity ground motion. The frequency window ([10.05, 30] Hz) applied in this plot is picked manually. The left and right columns correspond to analyses conducted on the horizontal components H_1 and H_2 , respectively. The color version of this figure is available only in the electronic version of this article.

3.4. Conceptual basis for the interpretation of κ beyond the linear-elastic regime

The induced strain level in a given soil layer is a function of the material properties, and the amplitude and frequency content of the incoming wavefield at the site. Stronger ground shaking results in larger-strain responses, which produce an increase in material damping ratio (in combination with a reduction of shear modulus). The short wavelength of high frequency waves allows for multiple cycles of shearing in near-surface sedimentary layers, which makes them more sensitive to the effects of a higher material damping ratio. Thus, we hypothesize that stronger ground shaking inducing larger deformations in sedimentary deposits will affect estimates of the high-frequency spectral decay parameter κ .

Figure 3.1 serves as an example to illustrate this hypothesis. The acceleration FAS and empirical transfer function (ETF) corresponding to a pair of ground motions recorded at depth and at the ground surface at FKSH14 are shown. FKSH14 is one of the 20 KiK-net station analyzed in this work (see Database description). One of the ground motion pairs has a low ground shaking intensity (with a surface PGA of less than 0.1 m/s^2 for both horizontal components), while the other one has a higher ground shaking intensity (with a surface PGA of 0.71 m/s^2 and 0.25 m/s^2 for the H_1 and H_2 components, respectively). Values of κ_r per record are also estimated for both pairs. To minimize the bias from path effects and isolate local site effects on κ_r values per record, the selected weak and strong ground motions in Figure 3.1 correspond to events with similar focal depths, azimuths and epicentral distances (i.e., the focal depths, azimuths and epicentral distances are 5 km, 319° , and 15.04 km, respectively for the low-intensity event, and 5 km, 323° , and 15.79 km, respectively for the high-intensity event). The moment magnitudes of the events associated with the weak and strong ground motions in Figure 3.1 are 4.0 and 5.1, respectively. To reduce the variability associated with the calculation of κ_r

from the acceleration spectrum method, we use the same frequency window for all ground motions (Edwards et al. 2011).

Larger values of κ_r at the ground surface (e.g., 0.071 s for the horizontal component H_1) are obtained for the high-intensity ground motion compared to the corresponding κ_r values for the low-intensity ground motion (e.g., 0.057 s for H_1). Likewise, the high-intensity ground motion results in a larger κ_{TF} (Drouet et al. 2010), which is computed on the decaying portion of the empirical transfer function at high frequencies and is equivalent to $\Delta\kappa$ (i.e., $\kappa_{r_sur} - \kappa_{r_bor}$) estimates when using the same frequency band for calculation purposes. The value of κ_{TF} corresponding to the high-intensity and low-intensity motions are 0.026 s and 0.019 s, respectively. Meanwhile, the ETF corresponding to the high-intensity event shows lower amplifications at higher frequencies (e.g., amplification ranges from 1 to 2 between 15 and 30 Hz for H_1 approximately) than its counterpart for the low-intensity ground motion (i.e., amplification ranges from 2 to 3 between 15 and 30 Hz for H_1 approximately), which reflects the stronger influence of increased material damping ratio on high frequencies.

Values of κ_r and $\Delta\kappa$ (or κ_{TF} in Figure 3.1) are identical for the high- and low-intensity records for the H_2 component. It must be noted that the difference in PGA between the low- and high- intensity surface ground motions is less significant for the H_2 components than that for the H_1 components, while the PGAs at depth are very similar (i.e., the borehole PGAs for the high-intensity motion are 0.06 and 0.07 m/s^2 for H_1 and H_2 components, respectively; the borehole PGAs for the low-intensity motion are 0.01 m/s^2 for both H_1 and H_2 components). This may explain why $\Delta\kappa$ values are the same for the low and high intensity motions in the H_2 component direction. Additionally, this observation also hints that the near-surface attenuation and site effects may be affected by the ground motion directionality as shown by Ji et al. (2020). Finally,

soil nonlinearity is commonly observed at shallower layers (Régnier et al. 2013), and their effects on κ_r at borehole are smaller than at surface. Thus, the κ_r at borehole should be less affected by soil nonlinearity because its nonlinear soil behavior is less likely to be triggered at depth (e.g., the borehole V_s at FKSH14 is 1210 m/s with borehole sensor depth of 147 m). In Figure 3.1, values of κ_r at borehole are similar for the high- and low-intensity motions. The changes in κ_r shown in Figure 3.1 exemplify the need to further investigate the influence of the onset of soil nonlinearity on κ_r as well as the potential implications on κ_0 values at a specific site.

3.5. Database description

In this study, we use ground motions from the KiK-net database, which provides high quality strong ground motions recorded at more than 600 stations installed uniformly across Japan. Each station possesses a pair of sensors, one at the surface and another one at depth that is typically between 100 to 200 m deep. The sampling frequency of the observed acceleration series is either 100 or 200 Hz. The P- and S-wave velocity profiles are measured by downhole PS logging and available at the KiK-net website (see Resources and Data). The earthquake information, including the seismic moment magnitude M_w , focal depth and epicenter location are provided by the broadband seismography network (F-net) catalog. The dataset used in this work was processed by Bahrampouri et al. (2020) with an automated protocol, which corrects the baseline and removes the background noise with a bandpass/high-pass acausal filter. The low-frequency filter corner frequency is determined based on a required value of the (signal+noise)/noise equal to 3, corresponding to a signal-to-noise ratio (SNR) of 2.0 (Boore and Bommer, 2005); this frequency ranges between predetermined minimum and maximum values of 0.05 and 0.5 Hz, respectively. The minimum high-frequency filter corner frequency is

determined for a SNR of 1.0 (Douglas and Boore 2011). The minimum bandpass width is 60% of the range defined from zero to the Nyquist frequency. Further detailed descriptions on the ground motion processing are available in Bahrampouri et al. (2020).

We use surface and borehole records (only horizontal components) in this paper. The criteria applied to select records are as follows: (1) epicentral distance is less than 150 km, (2) the SNR ratio is larger than 3.0 at each frequency from 1.0 to 30 Hz, (3) focal depth is less than 35 km (Ji et al. 2020), and (4) the seismic wave path does not cross the Japanese volcanic belt (Nakano et al. 2015). Thus, twenty stations with more than five nonlinear ground motions (the definition of nonlinear ground motions is described next in the Methods section) are used in this work (with 18 stations having more than 10 nonlinear records and 8 stations having more than 15 nonlinear records, see Table 1). Table 1 provides local soil conditions and the number of ground motions at each selected site. The locations of selected stations are shown in Figure 3.2a, while the magnitude and distance distribution of selected ground motions is provided in Figure 3.2b.

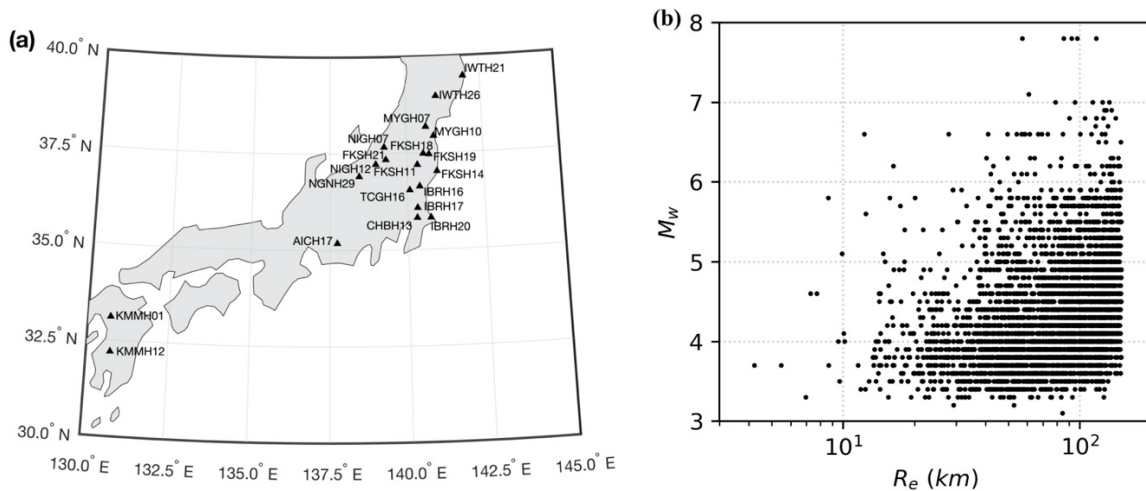


Figure 3.2. (a) Locations of selected Japanese recording stations in this study, and (b) magnitude and distance distribution of selected ground motions.

Table 3.1. Local soil conditions, number of ground motions per dataset, predetermined fixed-frequency bandwidth and thresholds for shear strain index, I_γ at all study sites.

| Station | V_{s30}^1 (m/s) | V_{s0}^2 (m/s) | $V_{s,depth}^3$ (m/s) | Hole Depth (m) | Number of linear records | Number of transitional records | Number of nonlinear records | 1 st resonant frequency (Hz) | Predominant frequency (Hz) | f_1^4 (Hz) | f_2^5 (Hz) | $I_{\gamma,0,l}^6$ (%) | $I_{\gamma,0,t}^7$ (%) |
|---------|----------------------|---------------------|--------------------------|----------------------|-----------------------------------|--------------------------------------|--------------------------------------|--|----------------------------------|-----------------|-----------------|---------------------------|---------------------------|
| AICH17 | 314 | 150 | 2200 | 101 | 23 | 27 | 12 | 4.07 | 4.07 | 12.65 | 25.00 | 0.001 | 0.003 |
| CHBH13 | 235 | 220 | 2920 | 1300 | 139 | 49 | 11 | 1.78 | 1.78 | 8.95 | 25.00 | 0.001 | 0.003 |
| FKSH11 | 240 | 110 | 700 | 115 | 148 | 140 | 26 | 1.51 | 9.98 | 13.97 | 25.00 | 0.001 | 0.003 |
| FKSH14 | 237 | 120 | 1210 | 147 | 114 | 221 | 28 | 1.12 | 4.15 | 10.05 | 25.00 | 0.001 | 0.007 |
| FKSH18 | 307 | 140 | 2250 | 100 | 158 | 103 | 16 | 2.59 | 5.69 | 8.95 | 25.00 | 0.001 | 0.003 |
| FKSH19 | 338 | 170 | 3060 | 100 | 185 | 95 | 21 | 3.27 | 3.27 | 10.05 | 25.00 | 0.001 | 0.003 |
| FKSH21 | 365 | 200 | 1600 | 200 | 60 | 17 | 8 | 3.90 | 3.90 | 12.65 | 25.00 | 0.001 | 0.003 |
| IBRH16 | 626 | 140 | 2050 | 300 | 137 | 81 | 15 | 1.71 | 7.08 | 10.05 | 25.00 | 0.001 | 0.003 |
| IBRH17 | 301 | 90 | 2300 | 510 | 117 | 177 | 18 | 0.93 | 9.30 | 13.01 | 25.00 | 0.001 | 0.007 |
| IBRH20 | 244 | 180 | 1200 | 923 | 133 | 86 | 11 | 0.27 | 0.27 | 8.95 | 25.00 | 0.001 | 0.007 |
| IWTH21 | 521 | 150 | 2460 | 100 | 39 | 24 | 6 | 5.27 | 5.27 | 7.38 | 25.00 | 0.001 | 0.003 |
| IWTH26 | 371 | 130 | 680 | 108 | 79 | 32 | 11 | 2.12 | 10.17 | 14.24 | 25.00 | 0.001 | 0.003 |
| KMMH01 | 575 | 150 | 1900 | 100 | 94 | 24 | 15 | 4.03 | 9.98 | 13.97 | 25.00 | 0.001 | 0.003 |
| KMMH12 | 410 | 210 | 1000 | 123 | 134 | 34 | 11 | 3.27 | 8.17 | 11.44 | 25.00 | 0.001 | 0.003 |
| MYGH07 | 366 | 130 | 740 | 142 | 59 | 39 | 11 | 0.93 | 8.61 | 12.06 | 25.00 | 0.001 | 0.003 |
| MYGH10 | 348 | 110 | 770 | 205 | 229 | 132 | 16 | 0.95 | 10.66 | 14.93 | 25.00 | 0.001 | 0.007 |
| NGNH29 | 465 | 150 | 1040 | 110 | 81 | 38 | 16 | 1.95 | 6.93 | 10.05 | 25.00 | 0.001 | 0.003 |
| NIGH07 | 528 | 200 | 1600 | 106 | 29 | 10 | 11 | 4.12 | 7.08 | 10.05 | 25.00 | 0.001 | 0.003 |
| NIGH12 | 553 | 240 | 780 | 110 | 29 | 9 | 11 | 2.00 | 5.00 | 12.65 | 25.00 | 0.001 | 0.003 |
| TCGH16 | 213 | 80 | 680 | 112 | 112 | 334 | 35 | 1.27 | 4.81 | 11.27 | 25.00 | 0.001 | 0.007 |

¹ V_{s30} : time averaged shear-wave velocity in the top 30 m of the soil profile

² V_{s0} : shear-wave at the ground surface

³ $V_{s,depth}$: shear-wave velocity at the depth of the borehole sensor

⁴ f_1 : the lower frequency limit to estimate individual κ_r

⁵ f_2 : the upper frequency limit to estimate individual κ_r

⁶ $I_{\gamma,0,l}$: the shear-strain index threshold to separate linear and transitional datasets

⁷ $I_{\gamma,0,t}$: the shear-strain index threshold to separate transitional and nonlinear datasets

3.6. Method

3.6.1. Identification of the onset of nonlinearity

Identifying ground motions that trigger soil nonlinear behavior is key to evaluate κ estimates beyond the linear-elastic regime empirically. The shear-strain index ($I_\gamma = PGV/V_s$), which is a proxy for the in-situ deformation, and PGA, which describes the peak amplitude of the ground motion, are commonly used to differentiate linear from nonlinear ground motions (e.g., Xu et al. 2019, Cabas et al. 2017, Wang et al. 2019). Moreover, the correlation between PGA and I_γ has been shown to be an effective proxy to capture in-situ stress-strain relationships. This correlation has been characterized via the classic hyperbolic model, which fits empirical observations (Chandra et al. 2014, 2015, Guéguen et al. 2018). However, there is lack of consensus regarding the sufficiency and efficiency of existing proxies associated with the onset of nonlinear behavior. For example, Xu et al. (2019) assumed that records with I_γ less than 0.01% are linear ground motions, while Cabas et al. (2017) adopted 0.1%. On the other hand, Ktenidou et al. (2013) chose a PGA of 0.1 m/s² as the threshold for linear ground motions. Régnier et al. (2013) conducted a statistical analysis on the KiK-net dataset to understand nonlinear site response at their stations. They characterized linear soil behavior as that associated with motions with a PGA at depth less than 0.1 m/s².

We develop appropriate criteria to identify nonlinear ground motions based on PGA and I_γ . In this paper, the shear-strain index at the surface ($I_{\gamma,0}$) is defined as follows:

$$I_{\gamma,0} = PGV_{rotD50} / V_{s,0} \quad (3.1)$$

where $V_{s,0}$ is the shear-wave velocity at the ground surface, and PGV_{rotD50} is the median PGV for all rotated surface ground motions following the approach of Boore (2010). The use of PGV_{rotD50} rather than the PGV from recorded ground motion horizontal components can minimize

directionality effects. The use of $I_{\gamma,0}$ (Equation 3.1) as an indicator of the onset of soil nonlinearity has some limitations though. First, the selection of single V_s and PGV values to capture the depth-dependent deformation in the profile may underestimate or overestimate the level of nonlinearity experienced across the whole column. Thus, $I_{\gamma,0}$, as defined in Equation (3.1), serves simply as a proxy for a representative shear strain to take place in the sedimentary deposit of interest. Notably, there is no consensus regarding the most appropriate choice of V_s for I_{γ} estimates. For example, V_{s30} is a commonly used site proxy and hence often selected to compute I_{γ} (e.g., Kim et al. 2016, Guéguen et al. 2018). The equivalent V_s measured between two successive sensors with seismic interferometry by deconvolution has also been adopted for I_{γ} estimates (e.g., Chandra et al. 2015, 2016, Wang et al. 2019). Second, values of $I_{\gamma,0}$ are not directly comparable to shear strains measured in the laboratory, not only because I_{γ} is a proxy and not a measured value, but also because the dissipation of seismic energy as captured in the laboratory may not fully represent the attenuation mechanisms taking place in the field (Cabas et al. 2017).

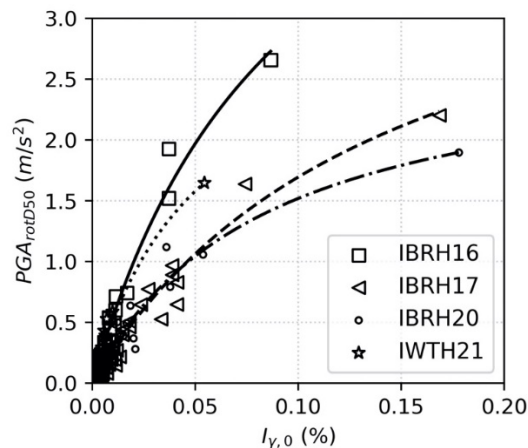


Figure 3.3. Hyperbolic models fitted to observed PGA_{rotD50} and $I_{\gamma,0}$ data at four study sites. The V_{s30} for IBRH16, IBRH17, IBRH20, and IWTH21 are 626, 301, 244, and 521 m/s, respectively.

By applying the classic hyperbolic model to describe the correlation between PGA_{rotD50} and $I_{\gamma,0}$, we find that there is no unique threshold to identify nonlinear ground motions across all study sites. Figure 3.3 provides examples of theoretical hyperbolic fitting curves at four stations (i.e., IBRH16, IBRH17, IBRH20 and IWTH21) with varying V_{s30} values (from 244 to 626 m/s) to demonstrate the limitations associated with using a single parameter to identify nonlinear ground motions at multiple sites. Scatter points represent PGA_{rotD50} and $I_{\gamma,0}$ pairs from recorded ground motions at the sites of interest, while the lines correspond to the fitting curves from the hyperbolic model. It is observed that the same deformation at various sites would be triggered by different levels of ground shaking (e.g., $I_{\gamma,0}$ of 0.05% will be caused by a PGA_{rotD50} around 1 m/s^2 at a NEHRP D site, such as IBRH20 with V_{s30} of 244 m/s, and by a PGA_{rotD50} of 2 m/s^2 at a NEHRP C site, such as IBRH16 with V_{s30} of 626 m/s). On the other hand, if nonlinearity is assumed to be triggered when the PGA_{rotD50} is larger than a predetermined threshold, different levels of $I_{\gamma,0}$ will be associated with the onset of soil nonlinearity. Hence, in this work, we propose a hybrid method (further described in the next section) based on both, the intensity of the excitation and in-situ deformation to classify ground motions.

3.6.2. Linear, transitional, and nonlinear datasets

Surface and borehole ground motions are considered separately herein. Régnier et al. (2013) considered that records with borehole PGA less than 0.1 m/s^2 cannot trigger nonlinear site response at the ground surface. They also observed that soil nonlinearity is mainly triggered at superficial layers. In this study, there are only 3% records with borehole PGA larger than 0.1 m/s^2 . Therefore the borehole records are assumed to remain in the linear-elastic regime (i.e., they do not trigger nonlinear behavior at depth). Surface records are separated into three sub-datasets,

namely linear, transitional (i.e., soil's behavior is between the linear-elastic and nonlinear regimes), and nonlinear ground motions. First, we define a threshold based on $I_{\gamma,0}$ to differentiate linear from transitional records, which is hereafter referred to as $I_{\gamma,0,l}$. Likewise, a transitional threshold, $I_{\gamma,0,t}$, is defined to separate transitional and nonlinear ground motions. The linear $I_{\gamma,0,l}$ threshold is defined as the onset of soil nonlinearity by visual inspections of the corresponding PGA_{rotD50} versus $I_{\gamma,0}$ curve, and corresponds to the point where PGA_{rotD50} values begin to increase at a higher rate with increasing $I_{\gamma,0}$. The transitional $I_{\gamma,0,t}$ threshold captures when the soil nonlinearity becomes more apparent, which corresponds to the point where the second change in slope of the PGA_{rotD50} versus $I_{\gamma,0}$ curve takes place. Figure 3.4 provides an example of the selection of $I_{\gamma,0,t}$ and $I_{\gamma,0,l}$ at station MYGH10. The threshold separating the linear and transitional ground motions is $I_{\gamma,0,l} = 0.001\%$, while the threshold separating transitional and nonlinear ground motions is $I_{\gamma,0,t} = 0.007\%$.

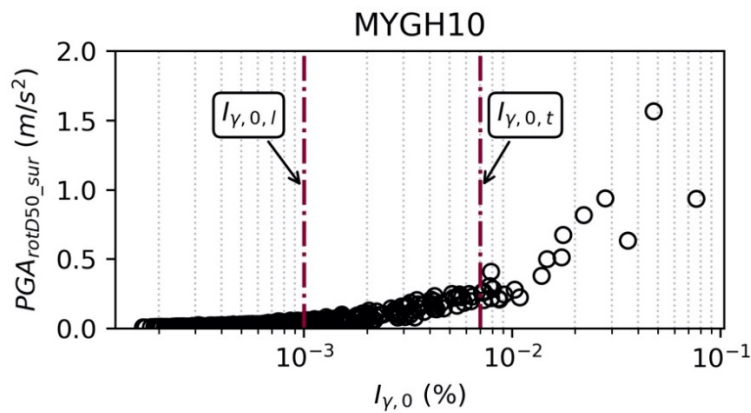


Figure 3.4. Surface PGA_{rotD50} against $I_{\gamma,0}$ at MYGH10 ($V_{s30} = 348$ m/s). The red dot-dashed lines present the linear ($I_{\gamma,0,l}$) and transitional ($I_{\gamma,0,t}$) thresholds for $I_{\gamma,0}$. The color version of this figure is available only in the electronic version of this article.

A maximum PGA_{rotD50} of 0.25 m/s^2 , which is the value adopted by Régnier et al. (2016) to define low-amplitude motions, is chosen as an additional constraint to avoid linear ground motions being erroneously included into the nonlinear dataset. Thus, linear, transitional, and nonlinear datasets are defined as follows:

- Linear ground motions: records with $I_{\gamma,0}$ less than the $I_{\gamma,0,1}$ threshold.
- Nonlinear ground motions: records with (a) $I_{\gamma,0}$ larger than the $I_{\gamma,0,t}$ threshold and (b) PGA_{rotD50} larger than 0.25 m/s^2 .
- Transitional ground motions: records not classified as either linear or nonlinear.

The validity of the proposed linear, transitional, and nonlinear datasets is tested by examining the behavior of the shear modulus, G against $I_{\gamma,0}$ at the study sites. The reduction of G for empirical ground motions is estimated as follows (after Guéguen et al., 2019):

$$\frac{G}{G_{\max}} = \frac{PGA_{rotD50}}{PGV_{rotD50}/V_{s,0}} \left/ \left(\frac{PGA_{rotD50}}{PGV_{rotD50}/V_{s,0}} \right)_{\max} \right. \quad (3.2)$$

The term $\left(\frac{PGA_{rotD50}}{PGV_{rotD50}/V_{s,0}} \right)_{\max}$ is computed from the corresponding average ratio of records with $I_{\gamma,0}$ less than 0.001% , which is the predetermined threshold of $I_{\gamma,0,1}$ for the linear-elastic deformation limit in this work. Figure 3.5 shows the G/G_{\max} versus $I_{\gamma,0}$ curves at all study sites. Even though Figure 3.5 does not directly correspond to laboratory-based curves, it serves as a first order verification of the distinct behavior corresponding to the linear, transitional, and nonlinear ground motions identified with the categorization scheme proposed herein. One challenge when interpreting these data is the characterization of the soil volume being sampled when using I_{γ} , which is related to the frequency band that PGV is acting on. Identified linear

ground motions mainly have G/G_{\max} values around 1 (G/G_{\max} values higher than 1 result from using mean G values as a proxy for G_{\max}), while the ratios corresponding to the nonlinear dataset are generally less than 1 due to the onset of soil nonlinearity. Notably, values of G/G_{\max} associated with the transitional dataset are between the linear and nonlinear datasets. It is not clear whether the site response associated with records identified as transitional could be equivalent to a linear-elastic or a nonlinear response, because associated G/G_{\max} values vary within a single station and across stations. Hence, the characterization as transitional is deemed appropriate herein.

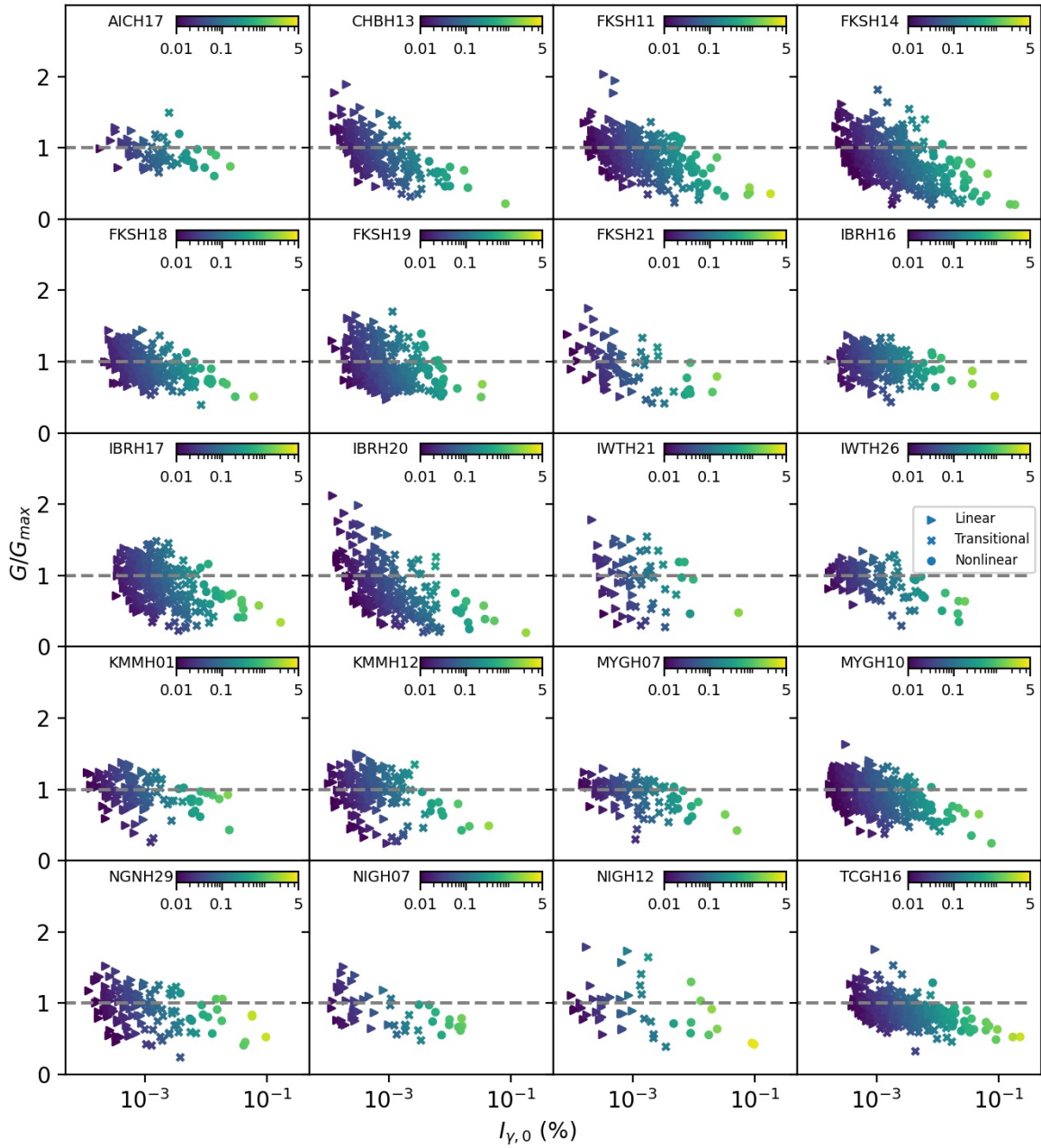


Figure 3.5. G/G_{\max} versus $I_{y,0}$ at study sites. The G_{\max} is computed from the average values of

$$\left(\frac{PGA_{rotD50}}{PGV_{rotD50}/V_{s,0}} \right)$$

for records with $I_{y,0}$ less than 0.001%. The colors represent PGA_{rotD50} values (in units

of m/s^2). The color version of this figure is only available in the electronic version of this article. The

color version of this figure is available only in the electronic version of this article.

3.6.3. κ_{r_AS} estimates

We use the acceleration spectrum approach (Anderson and Hough, 1984) to estimate κ_{r_AS} . To minimize the variability introduced by the selection of the S-wave window, the entire time series is used. Because compatibility with engineering analysis such as geotechnical site response analysis and ground motion models is also desired, and such applications use complete time series, calculating κ_{r_AS} using the entire time series is convenient. Moreover, the differences of κ_{r_AS} values measured from S-wave window and the entire time series are not significant in most cases (Ji et al. 2020). In this study, a subset of randomly selected ground motions is used to further assess potential discrepancies between using the S-wave window relative to the entire time series, and no significant differences are observed. Hence, the entire time histories are used.

The variability in estimates of κ_{r_AS} is a function of the selection of the frequency band (Edwards et al. 2015, Perron et al. 2017) among other factors (Ji et al. 2020, Ktenidou et al. 2013). Moreover, soil nonlinearity affects low and high frequencies differently. The onset of nonlinear soil behavior can influence high frequencies first (Bonilla et al. 2011, Bonilla and Ben-Zion, 2020) because larger shear strains are induced in softer, thinner layers located at shallower depths (i.e., in a profile with increasing stiffness with depth). Hence, we compute κ_{r_AS} based on a pre-determined fixed frequency window ($[f_1, f_2]$). The pre-determined f_1 corresponds to the maximum value between $1.4 f_c$ (where f_c is the earthquake source corner frequency of each record) and $1.4 f_0$ (where f_0 is the site's predominant frequency). Indeed, if f_1 is lower than f_0 , the value of κ_{r_AS} will be biased by the site amplification in the high-frequency range (Parolai and Bindi 2004). On the other hand, the f_c requirement is added to reduce the effects of the earthquake source. The value of f_2 is set to be 25 Hz due to consideration of KiK-net instrument's response (Aoi et al., 2004, Fujiwara et al. 2004, Oth et al. 2011, Laurendeau et al.

2013). These limits ensure a broad frequency bandwidth for κ calculations of at least 10 Hz per record, which reduces potential bias from local amplification effects (Parolai and Bindi, 2004; Ktenidou et al. 2016). The arithmetic average of the resulting κ_{r_AS} estimated from two orthogonal horizontal components is used because it is not affected by the record azimuth and its implementation can reduce the variability in κ_{r_AS} caused by ground motion directionality (Ji et al. 2020). However, a prescribed, fixed-frequency band does not guarantee the most appropriate linear regression for the high-frequency spectral decay in all cases. Thus, we further investigate the performance of the fixed-frequency window and the effects of the frequency band selection for weak and strong ground motion records by comparing individual κ_{r_AS} values estimated from a pre-determined fixed frequency window with their counterparts, κ_{r_auto} , resulting from an automated algorithm which does account for the most appropriate linear regression.

The automated procedure used in this paper follows a similar protocol as those presented in Sonnemann, and Halldorsson (2017) and Pilz et al. (2019), which focus on finding an appropriate frequency band ($[f_1, f_2]$) to describe the linear decay in the high frequency range over a relatively broad frequency window. As part of the automated protocol, the minimum f_l is selected as the maximum value between $1.4f_0$, and $1.4f_c$. To ensure a minimum frequency bandwidth of 10 Hz, the maximum value of f_l is 15 Hz and the minimum f_2 corresponds to $(f_l + 10)$ Hz. With 0.5 Hz increments in f_1 and f_2 , f_1 is varied from the maximum value between $1.4f_0$ and $1.4f_c$ to 15 Hz, while f_2 changes from $(f_l + 10)$ Hz to 25 Hz. Going through all the possible combinations of f_1 and f_2 , the frequency range with the minimum root mean square error over the frequency bandwidth is set as the optimal frequency band. The errors are computed with the following equation after Pilz et al. (2019):

$$P = \frac{RMS}{\sqrt{\Delta f}} \quad (3.3)$$

Where Δf is the frequency bandwidth, and RMS is the root mean square error between the fitting line and smoothed FAS. The FAS is smoothed with the Konno-Ohmachi filter with a coefficient of 40 (Konno and Ohmachi, 1998). It should be noted that this automated procedure returns $\kappa_{r,auto}$ values associated with an appropriate regression for a broad frequency band. However, the changes of the FAS shape in high frequencies caused by site effects or soil nonlinearity (e.g., bumps or multiple linear trends) may not be properly accounted for by the automated algorithm.

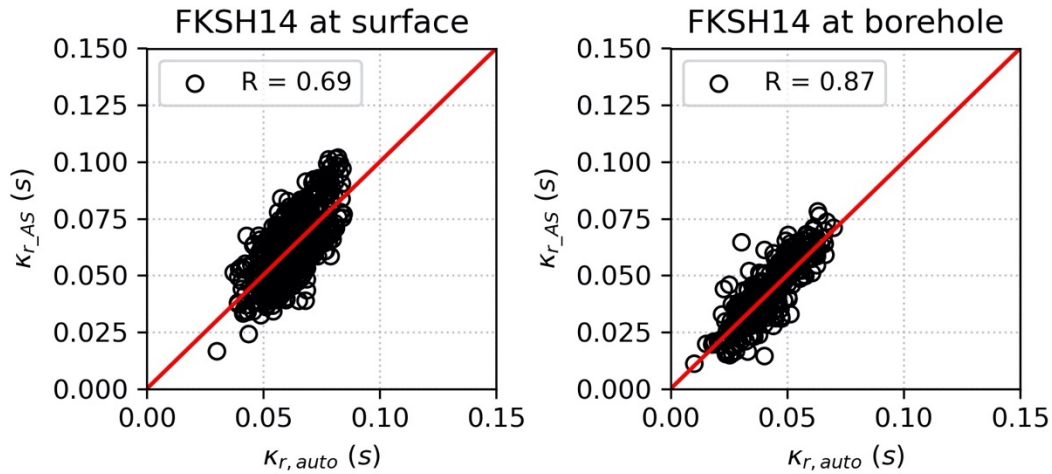


Figure 3.6. Comparisons of individual κ_r estimates from our automated algorithm, $\kappa_{r,auto}$, and the fixed frequency band method, $\kappa_{r,AS}$ at FKSH14 ($V_{s30} = 237$ m/s) for surface (left) and borehole (right) records.

The color version of this figure is available only in the electronic version of this article.

Figure 3.6 compares $\kappa_{r,AS}$ and $\kappa_{r,auto}$ for all selected ground motions at FKSH14, where overall similar $\kappa_{r,AS}$ and $\kappa_{r,auto}$ estimates are observed and discrepancies are more significant at the ground surface than at depth. The remaining stations also show an acceptable agreement between the two methods at the surface and at depth. However, there are few records that show

significant differences between κ_{r_AS} and κ_{r_auto} (e.g., one surface record has κ_{r_AS} of about 0.025 s, while κ_{r_auto} is almost 0.05 s). This reflects the variability of κ_r as a function of the frequency band selected. For example, there are 13% of records at AICH17 showing clear variations with the frequency band selection based on the coefficient of variation (COV) obtained for all frequency windows evaluated by the automatic procedure (i.e., COV larger than 0.15). Differences between κ_{r_AS} and κ_{r_auto} are mainly caused by some empirical FAS shapes, for example, when multiple linear decaying trends are present in the high-frequency range. The latter cannot be captured by the single linear decay assumption within the κ -model. More research is needed to study how more complex wave propagation effects in the high frequency range can be captured. Testing the appropriateness of the κ_r model as introduced by Anderson and Hough (1984) for these cases is outside the scope of this study, but it constitutes an area of relevant future research.

Negative κ_{r_AS} values are excluded from this work. Overall, there are 14 of 20 stations with less than 20% negative κ_{r_AS} values (i.e., arithmetic means of two horizontal components), and 1 of 20 stations with more than 50% negative κ_{r_AS} estimates. To further understand the observed negative κ_{r_AS} values, the corresponding FAS are reinspected. These FAS generally show bumps or multiple linear decays in high frequencies. The pre-determined frequency band used in this study is then not able to capture the linear decay appropriately and leads to negative κ_{r_AS} values. Moreover, amplifications at higher frequencies may also affect estimates of κ_{r_AS} and lead to negative values. The original κ_r model (i.e., the linear decay of FAS in log-linear scale for high frequency ranges per record proposed by Anderson and Hough, 1984), requires the site response at the site of interest to be almost flat in the high frequency range. Complex in-situ site conditions that lead to high frequency amplification (e.g., heterogeneities in the near-surface,

and/or shallow impedance contrasts) can challenge this simple linear decay model. Our observations suggest the need to further explore the limitations and simplified assumptions of the Anderson and Hough (1984) κ_r model for it to be applicable or extended to more complex environments and stronger ground shaking. Accounting for the discrepancies between actual field conditions and assumptions suggested by the Anderson and Hough (1984) κ_r model could reduce the large variability observed in κ_{r_AS} estimates. Further research should focus on evaluating the limitations of the Anderson and Hough (1984) model and its potential modification to capture more complex wave propagation patterns in heterogeneous media, especially near the surface. In this work, such an investigation is not included, but future efforts of the authors envision the assessment of negative κ_{r_AS} estimates observed in this work as a first step to improve the existing κ_r model.

3.6.4. κ_0 -model

κ_{r_AS} is generally modeled with contributions from a site-specific component (κ_0), a path component (κ_R), and a source component (κ_s). The source component, κ_s , is often assumed to be negligible and its contribution is reduced by using a dataset with sufficient records (Van Houtte et al. 2011, Ktenidou et al. 2014). A linear distance-dependency model is commonly applied to capture the path component κ_R , which represents source-to-site effects or regional attenuation (Hough et al. 1988, Anderson, 1991, Ktenidou et al. 2013, Boore and Campbell, 2017). Thus, the most commonly accepted model is described below:

$$\kappa_{r_AS} = \kappa_0 + \kappa_R \times R_e \quad (3.4)$$

where κ_0 and κ_{r_AS} are in units of time (s), κ_R is in units of second per kilometer (s/km) and R_e refers to epicentral distance in km. This model is valid when a unique source-to-site path

is assumed for each record along with a homogeneous and frequency-independent seismic quality factor Q (Knopoff 1964). In this paper, the assumption of a unique source-to-site path is supported by using ground motions with R_e less than 150 km (e.g., Palmer and Atkinson 2020, Cabas et al. 2017, Ktenidou et al. 2013). In addition, ground motions whose travel path crosses Japan's volcanic belt are not included in our database to minimize the likelihood of seismic waves propagating through regions with varying Q values (Pei et al. 2009, Nakano et al. 2015).

The model described by Equation (3.4) is straightforward to apply when only surface linear ground motion datasets are used. However, the incorporation of nonlinear and borehole ground motions adds complexity to the estimation of regional attenuation as captured by κ_R . In this paper, we assume that soil nonlinearity is triggered near the surface, which is consistent with previous studies showing that nonlinear behavior occurs mostly in the superficial soil layers (i.e., Régnier et al., 2013; Bonilla et al., 2019; Qin et al., 2020). Thus, nonlinear soil behavior is treated as a site contribution rather than a path contribution, and we assume the regional attenuation to be identical for linear and nonlinear ground motions recorded at the ground surface and at depth.

Analogous to the formulation suggested by Douglas et al. (2010) for soil and rock sites, we propose a model based on Equation (3.4), which includes linear and nonlinear surface and borehole records:

$$\kappa_{r_AS} = N_1 \kappa_{0_depth} + N_2 \kappa_{0_lin_sur} + N_3 \kappa_{0_nl_sur} + N_4 \kappa_{0_tran_sur} + \kappa_R \times R_e \quad (3.5)$$

where κ_{0_depth} is the site-specific κ_0 at depth (i.e., depth of borehole sensor), and $\kappa_{0_lin_sur}$, $\kappa_{0_tran_sur}$ and $\kappa_{0_nl_sur}$ are the site-specific linear, transitional and nonlinear κ_0 at the surface. The coefficients N_1 , N_2 , N_3 , and N_4 are defined as follows:

$$N_1 = \begin{cases} 1 & \text{for dataset at depth} \\ 0 & \text{otherwise} \end{cases}$$

$$N_2 = \begin{cases} 1 & \text{for linear dataset at surface} \\ 0 & \text{otherwise} \end{cases}$$

$$N_3 = \begin{cases} 1 & \text{for nonlinear dataset at surface} \\ 0 & \text{otherwise} \end{cases}$$

$$N_4 = \begin{cases} 1 & \text{for transitional dataset at surface} \\ 0 & \text{otherwise} \end{cases}$$

The parameter N_4 in Equation (3.5) only takes a value of 1 when ground motions classified as transitional are considered independently and not as part of the linear or nonlinear datasets. That means that when transitional ground motions are excluded from analysis (i.e., AP1, see Table 3.2) or included into either the linear (i.e., AP2, see Table 3.2) or nonlinear (i.e., AP3, see Table 3.2) datasets, the coefficient N_4 will be equal to zero.

Table 3.2. Ground motion datasets constructed via alternative approaches (AP1 to AP4) explored in this study to implement the κ_0 -model.

| Approach | $\kappa_{0_lin_sur}^*$ | $\kappa_{0_nl_sur}^\dagger$ | $\kappa_{0_tran_sur}^{\dagger\dagger}$ | $\kappa_{0_depth}^\S$ | κ_0 -model |
|----------|----------------------------------|-------------------------------------|--|------------------------|-------------------|
| AP1 | Linear dataset | Nonlinear dataset | -- | Borehole dataset | Equation (3.5) |
| AP2 | Linear and transitional datasets | Nonlinear dataset | -- | Borehole dataset | Equation (3.5) |
| AP3 | Linear dataset | Nonlinear and transitional datasets | -- | Borehole dataset | Equation (3.5) |
| AP4 | Linear dataset | Nonlinear dataset | Transitional datasets | Borehole dataset | Equation (3.5) |

* $\kappa_{0_lin_sur}$: the surface site-specific κ_0 for linear dataset

† $\kappa_{0_nl_sur}$: the surface site-specific κ_0 for nonlinear dataset

†† $\kappa_{0_tran_sur}$: the surface site-specific κ_0 for transitional dataset

§ κ_{0_depth} : the site-specific κ_0 at depth

3.7. Results and Discussion

3.7.1. Effects of soil nonlinearity on empirical κ_{r_AS}

First, we study the influence of soil nonlinearity on κ_{r_AS} estimates per record at each site. It should be noted that soil nonlinearity is commonly triggered at shallower soil layers (Régnier et al. 2013), so we only focus on surface records in this section. Figure 3.7 depicts calculated κ_{r_AS} values at the surface against the corresponding $I_{\gamma,0}$ values at FKSH14 ($V_{s30} = 237$ m/s) and MYGH10 ($V_{s30} = 348$ m/s). As described in Equation (3.4), κ_{r_AS} is affected by both local site conditions and path effects in the context of a linear-elastic deformation analysis. Hence, the colorbar in Figure 3.7 represents varying epicentral distances, and the sizes of markers represent the corresponding PGA_{rotD50} . An overall increasing trend of κ_{r_AS} with increasing intensity of ground shaking (either evidenced by increased PGA or $I_{\gamma,0}$ values) is observed at FKSH14 for events that share similar epicentral distances. A slightly decreasing trend is observed for short-distance records with R_e less than about 50 km and high PGA_{rotD50} . However, κ_{r_AS} values corresponding to those shorter distance and higher PGA_{rotD50} events (i.e., the largest circles in Figure 3.7a) are larger than their counterparts for low-intensity motions (i.e., the smallest circles in Figure 3.7a) regardless of the R_e . To the best knowledge of the authors, this observation has not been reported before and could be associated with the depth of influence of κ_r . Variations in κ due to strong nonlinear effects may be a function of a more significant contribution of the site to the overall attenuation, which may not be necessarily the case for smaller amplitude events. There might be several mechanisms of attenuation combined, and their contributions as captured by κ need to be further investigated. Similar trends are observed at other seven sites with V_{s30} less than 400 m/s, which include AICH17, CHBH13, FKSH11, IBRH20, IWTH26, MYGH07, and TCGH16, and at KMMH12 with V_{s30} greater than 400 m/s.

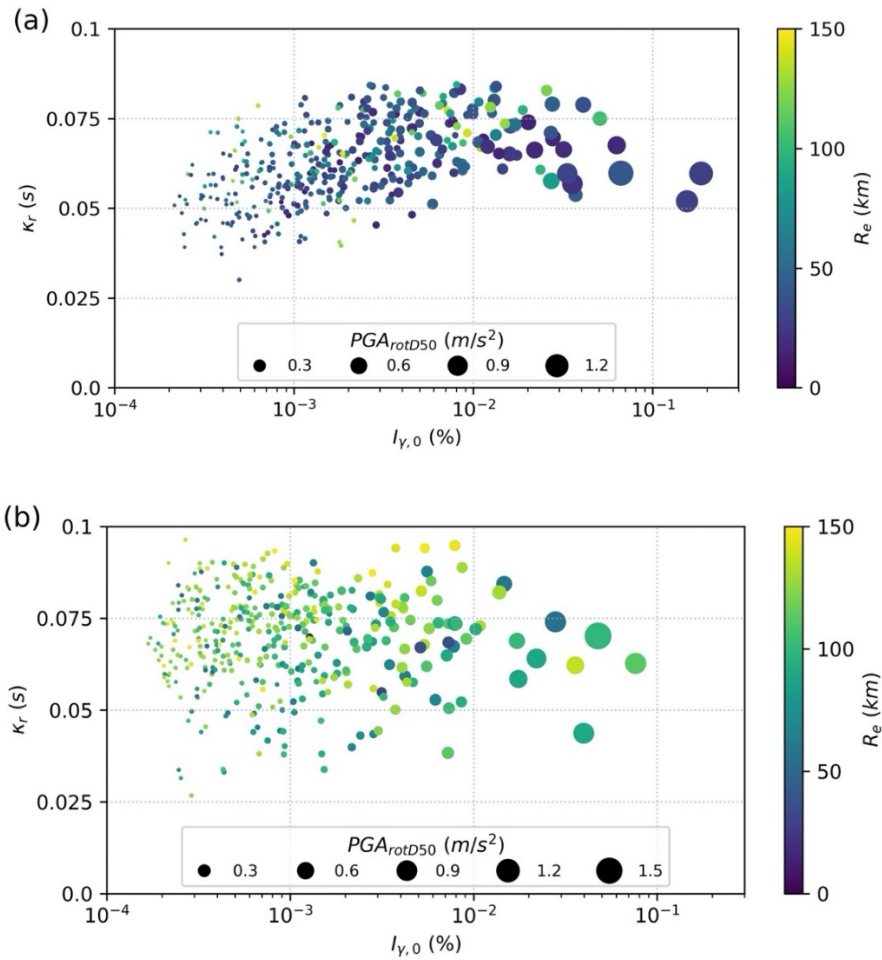


Figure 3.7. Surface κ_{r_AS} estimates and their corresponding PGA_{rotD50} , $I_{\gamma,0}$ and R_e values for selected ground motions recorded at (a) FKSH14 ($V_{s30} = 237$ m/s) and (b) MYGH10 ($V_{s30} = 348$ m/s). Different colors represent varying epicentral distances per record, and the size of markers indicate the corresponding PGA_{rotD50} . The color version of this figure is only available in the electronic version of this article. The color version of this figure is available only in the electronic version of this article.

The increasing κ_{r_AS} trend with increasing PGA_{rotD50} and $I_{\gamma,0}$ is not as significant at MYGH10 (Figure 3.7b), which has relatively stiffer site conditions than FKSH14. Either no correlation or a slightly decreasing trend is found at other stiff sites with V_{s30} greater than 400 m/s (i.e., FKSH21, NIGH12, NGNH29, NIGH07, KMMH01, and IBRH16), and at four softer

sites with V_{s30} between 300 and 400 m/s (i.e., IWTH21, FKSH18, FKSH19, and IBRH17). We note that the number of available nonlinear records for the R_e ranges at the sites where the decreasing trend is observed is rather limited. Additional nonlinear records at those sites are necessary (i.e., stronger intensity ground motions) to further evaluate the contributing factors to a potential decreasing trend in κ_{r_AS} values. However, in general, we observe that positive correlations between κ_{r_AS} and the intensity of ground shaking are more significant at softer sites (e.g., TCGH16 with V_{s30} of 213 m/s) than at stiffer sites (e.g., KMMH12 with V_{s30} of 408 m/s). These data support that the onset of soil nonlinearity can affect κ_{r_AS} estimates, but such influence is station-dependent. The level of soil nonlinearity can be unique at each site (for a similar intensity of ground shaking) because of the characteristics of shallow geologic structures (e.g., differences in velocity gradients and seismic impedance contrasts) and the location of low shear-wave velocity layers. Thus, subsurface conditions can play a key role on the effects of nonlinearity on κ_{r_AS} . We observe the same patterns shown in Figure 3.7 when using our results from the automated procedure to compute κ_{r_auto} .

3.7.2. Effects of soil nonlinearity on the empirical κ_0 -model

Linear, transitional, and nonlinear ground motion datasets are used in this section to evaluate the κ_0 -model beyond the linear-elastic regime. We explore four approaches (i.e., AP1 to AP4) to incorporate records within the transitional dataset into the κ_0 -model presented in Equation (3.5). Table 2 summarizes how the identified linear, transitional, and nonlinear datasets are used to estimate $\kappa_{0_lin_sur}$ and $\kappa_{0_nl_sur}$.

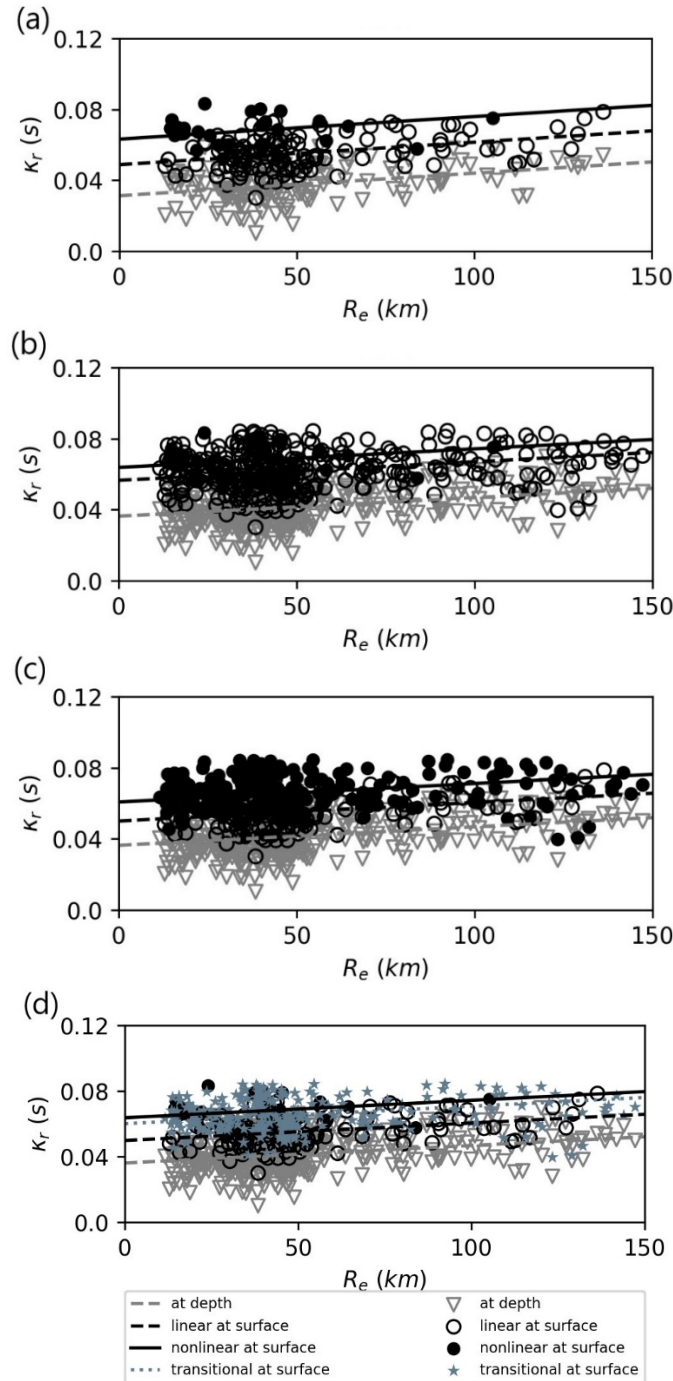


Figure 3.8. κ_0 -model at FKSH14 ($V_{s30} = 237$ m/s) from datasets defined by (a) AP1, which only considers the linear and nonlinear datasets, (b) AP2, where transitional records are included as part of the linear dataset, (c) AP3, where transitional records are included as part of the nonlinear dataset, and (d) AP4, where the linear, transitional, and nonlinear datasets are considered separately. The color version of this figure is only available in the electronic version of this article.

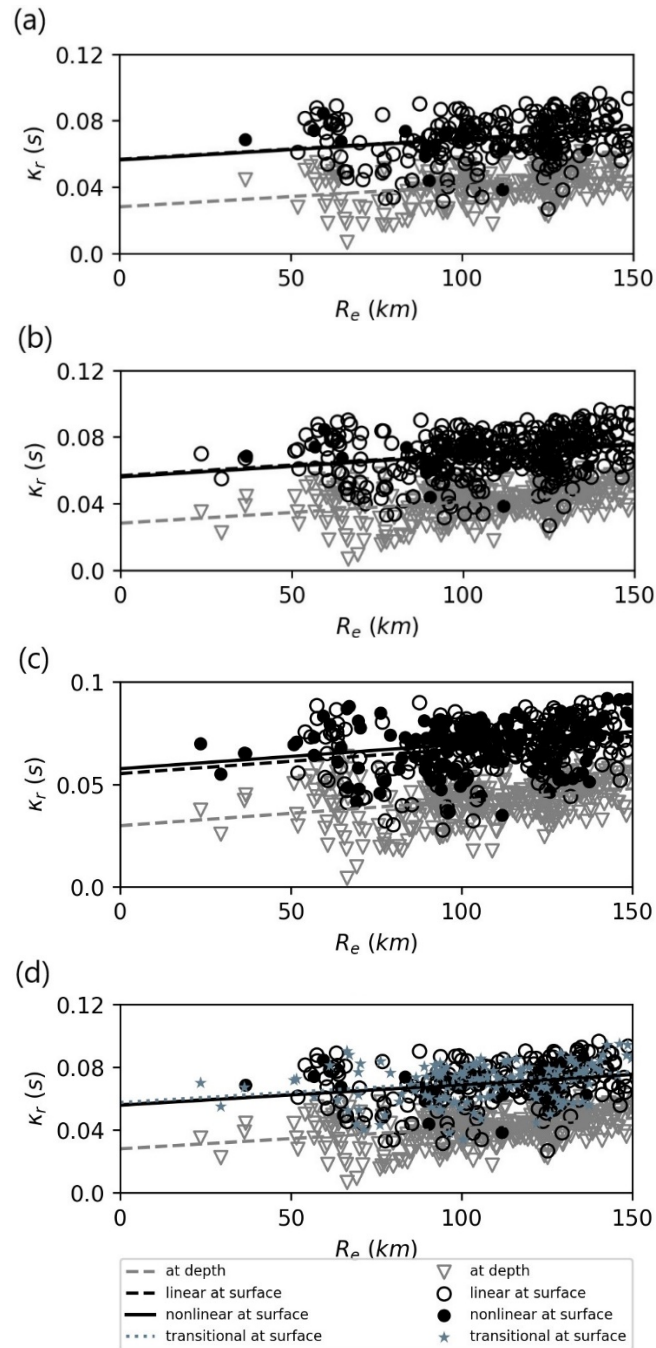


Figure 3.9. κ_0 -model at MYGH10 ($V_{s30} = 348$ m/s) with datasets defined by: (a) AP1, which only considers the linear and nonlinear datasets, (b) AP2, where transitional records are included as part of the linear dataset, (c) AP3, where transitional records are included as part of the nonlinear dataset, and (d) AP4, where the linear, transitional, and nonlinear datasets are considered separately. The color version of this figure is available only in the electronic version of this article.

Figures 3.8 and 3.9 present the resulting κ_0 models from each approach at FKSH14 and MYGH10, respectively. Figure 3.8 shows that κ_{r_AS} and κ_0 values corresponding to the nonlinear ground motions (regardless of the selected approach to construct the nonlinear dataset) are larger than their linear counterparts at FKSH14. However, results at the stiffer station presented in Figure 3.9 show little disagreement between κ_{r_AS} and κ_0 values corresponding to the linear and nonlinear motions (regardless of the approach to construct each dataset).

Table 3.3. Site-specific κ_0 values obtained from different dataset definitions at stations FKSH14 and MYGH10.

| | Approach | $\kappa_{0_lin_sur}^*$ (s) | $\kappa_{0_nl_sur}^\dagger$ (s) | $\kappa_{0_tran_sur}^\ddagger$ (s) |
|---------------|--------------------|------------------------------|-----------------------------------|--------------------------------------|
| FKSH14 | AP1 | 0.0488 | 0.0633 | -- |
| | AP2 | 0.0565 | 0.0638 | -- |
| | AP3 | 0.0500 | 0.0607 | -- |
| | AP4 | 0.0499 | 0.0638 | 0.0602 |
| | Maximum difference | 15.83% | 5.10% | |
| MYGH10 | AP1 | 0.0567 | 0.0563 | -- |
| | AP2 | 0.0568 | 0.0560 | -- |
| | AP3 | 0.0559 | 0.0572 | -- |
| | AP4 | 0.0560 | 0.0558 | 0.0575 |
| | Maximum difference | 1.56% | 2.53% | |

* $\kappa_{0_lin_sur}$: the surface site-specific κ_0 for linear dataset

† $\kappa_{0_nl_sur}$: the surface site-specific κ_0 for nonlinear dataset

‡ $\kappa_{0_tran_sur}$: the surface site-specific κ_0 for transitional dataset

Variations in $\kappa_{0_lin_sur}$ estimates are observed as a function of the approach considered to construct the linear datasets (see specific values in Table 3 for FKSH14 and MYGH10, the results for other selected stations are available in the electronic supplement). Similarly, variations in $\kappa_{0_nl_sur}$ values are also found across the different approaches to define the nonlinear datasets. At FKSH14 (Figure 3.8), $\kappa_{0_lin_sur}$ estimates are more variable as a function of the dataset

definitions (with a maximum difference of 15.83% across approaches AP1 to AP4), compared to $\kappa_{0_nl_sur}$ values (with a maximum difference of 5.10%). In addition, Figure 3.8 (d) shows that data points corresponding to the transitional dataset are more compatible with their counterparts within the nonlinear dataset, which may indicate that at FKSH14, the level of nonlinearity induced by the transitional dataset is closer to that induced by the ground motions in the nonlinear dataset. Other study sites such as AICH17 ($V_{s30} = 314$ m/s) and IWTH21 ($V_{s30} = 521$ m/s) also show that $\kappa_{0_lin_sur}$ estimates are more sensitive to dataset selections. In contrast, variations of $\kappa_{0_lin_sur}$ and $\kappa_{0_nl_sur}$ across datasets at MYGH10 (Figure 3.9) are small, with maximum differences of only 1.56% and 2.53%, respectively. Large differences in $\kappa_{0_nl_sur}$ estimates across datasets are observed at eight sites, but the limited number of nonlinear records at some of those sites may be the main contributing factor (e.g., there are only six nonlinear records at IWTH21, which results in a maximum difference of 47.05% for $\kappa_{0_lin_sur}$ and 11.17% for $\kappa_{0_nl_sur}$). Adding transitional records to either the linear or the nonlinear dataset at such sites can bias the regression model. In general, differences in the κ_0 -model as a function of the selected dataset are observed in 45% of our study sites (with differences in $\kappa_{0_lin_sur}$ or $\kappa_{0_nl_sur}$ values greater than 10%). This is a relevant observation because it demonstrates the importance of selecting appropriate ground motions even for typical κ_0 estimations (i.e., in the linear-elastic regime) at a given site.

Our findings suggest that the development of a κ_0 -model beyond the linear-elastic regime requires an evaluation of the definition of what constitutes linear and nonlinear ground motion datasets. The identification of transitional ground motion datasets in this study allows us to assess which records provide estimates of κ_{T_AS} that are closer to either the linear or the nonlinear behavior at different sites. Differences in behavior triggered by the records within the transitional

database may be caused by unique local site conditions (i.e., the level of soil nonlinearity developed at each site) or by limitations of the simplified definition used herein to classify transitional records (i.e., as a function of PGA and I_γ). Identifying appropriate linear and nonlinear datasets for κ_{r_AS} estimations requires further research to provide consistent models of near-surface attenuation that can more effectively be implemented from small to large shear strains. However, the site-specific response at a site of interest may impose challenges in determining appropriate dataset classifications based on a simple, generalized criterion.

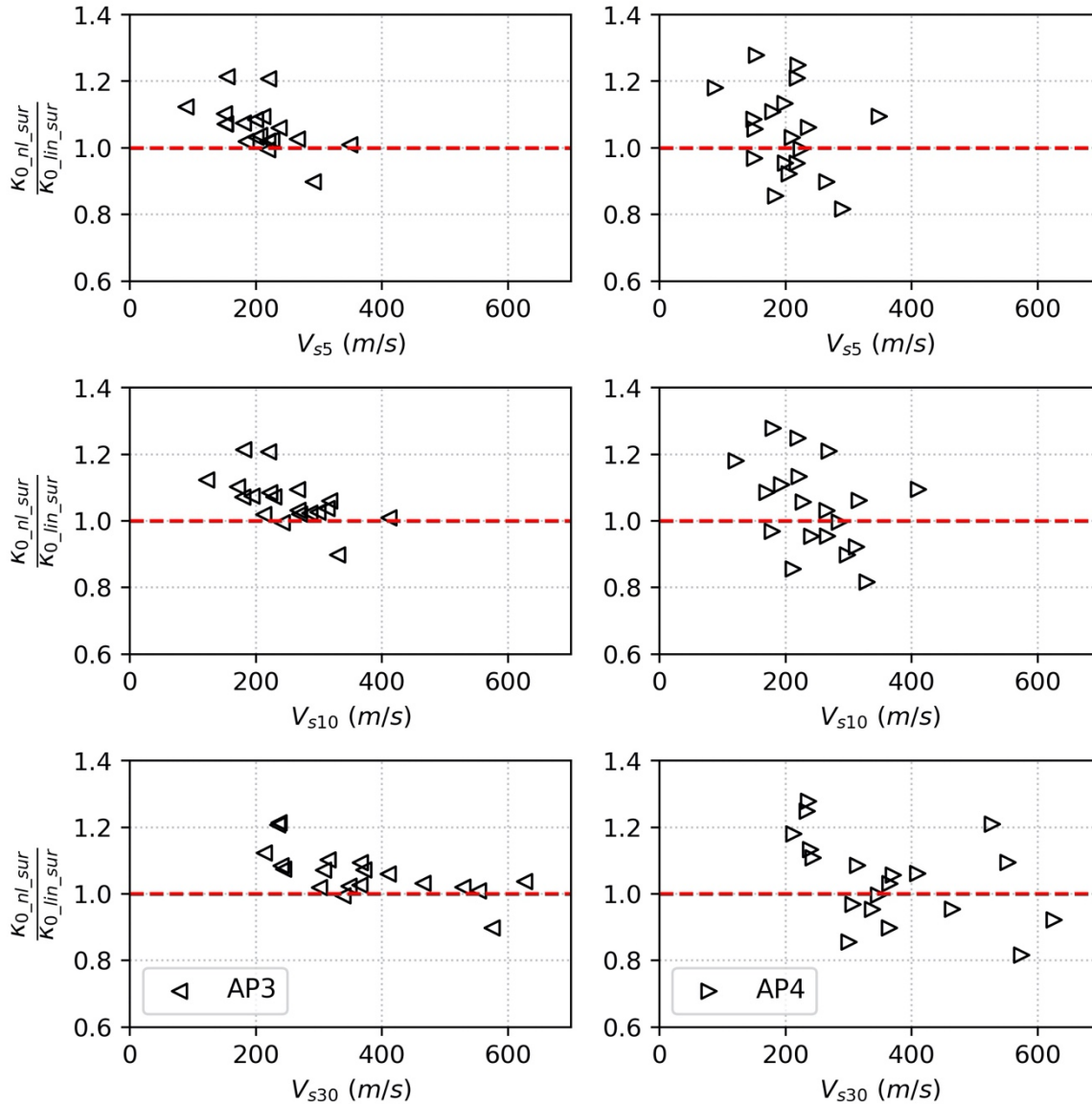


Figure 3.10. Ratio of $\kappa_{0_nl_sur}/\kappa_{0_lin_sur}$ at study sites estimated using the dataset definitions based on AP3 (left panel) and AP4 (right panel) against to V_{s5} , V_{s10} , and V_{s30} . The color version of this figure is available only in the electronic version of this article.

Figure 3.10 provides ratios of $\kappa_{0_nl_sur}/\kappa_{0_lin_sur}$ at the 20 study sites against the corresponding time-average V_s value in the top 5 m (V_{s5}), 10 m (V_{s10}), and 30 m (V_{s30}). The ratios are computed based on the AP3 and AP4 approaches to construct linear and nonlinear datasets (Table 2). Larger ratios are observed at softer sites regardless of the dataset chosen (i.e.,

AP3 and AP4) for the κ_0 -model. Differences between κ_0 values in the linear and nonlinear regimes seem to be reconciled at sites with higher V_{s5} (> 300 m/s), V_{s10} (> 300 m/s) and V_{s30} (> 400 m/s) values, where the ratios fluctuate more closely around unity particularly when using AP3. The trend of increasing ratios of $\kappa_{0_nl_sur}/\kappa_{0_lin_sur}$ with softer site conditions is better captured by V_{s5} and V_{s10} than by V_{s30} , because soil nonlinearity is more likely triggered at shallower and softer layers (Régnier et al. 2013). Hence, lower V_s layers may dominate soil nonlinearity effects on κ_0 . Thus, site proxies that can characterize such near-surface layers may be more informative when evaluating nonlinear soil effects on κ_0 .

When grouping transitional and nonlinear ground motions (i.e., AP3), most stations result in ratios of $\kappa_{0_nl_sur}/\kappa_{0_lin_sur}$ larger than one, which can be interpreted as the signature of soil nonlinearity on the near-surface attenuation estimates (i.e., near-surface attenuation increases with increasing deformations as soil nonlinearity is triggered). These findings are consistent with the behavior of material damping ratio observed in dynamic laboratory testing of soils (i.e., increased damping ratio with increasing shear strain; Darendeli 2001; Menq 2003; Ishibashi and Zhang 1993). When treating linear, transitional, and nonlinear datasets independently (i.e., AP4), there are 12 sites with ratios larger than one. The instances where ratios of $\kappa_{0_nl_sur}/\kappa_{0_lin_sur}$ are lower than one may result from the limited nonlinear records available at those sites coupled with the uncertainties associated with $\kappa_{0_lin_sur}$ (e.g., Ji et al., 2020).

Overall, the variations observed in the $\kappa_{0_nl_sur}/\kappa_{0_lin_sur}$ ratio support our hypothesis that soil nonlinearity plays a role on the estimates of near-surface attenuation from recorded ground motions. This effect is station-dependent, and further research is needed to identify the most appropriate parameter or vector of parameters capable of capturing the influence of nonlinear soil behavior on near-surface attenuation. Moreover, the relatively weaker correlation between

V_{s30} and the $\kappa_{0_nl_sur}/\kappa_{0_lin_sur}$ ratio evidences the challenges in connecting site conditions and soil nonlinearity via a single site parameter. Multiple parameters that can describe attenuation and impedance effects from the shallow and deep geologic structures should be investigated. The $\kappa_{0_nl_sur}/\kappa_{0_lin_sur}$ ratio corresponding to IWTH21 ($V_{s30} = 521$ m/s) is not shown in Figure 3.10 because it is very large (i.e., approximately 1.8). This observation may result from uncertainties associated with κ_{r_AS} values propagating to estimates of κ_0 when the fixed frequency band approach is applied for all records without consideration of the optimal linear decay trend. In fact, the corresponding $\kappa_{0_nl_sur}/\kappa_{0_lin_sur}$ ratio when implementing the automated procedure is approximately 0.90 for this station. Finally, Figure 3.10 shows less scatter in $\kappa_{0_nl_sur}/\kappa_{0_lin_sur}$ ratios when using datasets defined by AP3. In addition, using AP3 results in ratios either larger than one or approaching one for most stations (i.e., only FKSH19 and KMMH01 results in a ratio lower than unity), which is consistent with our conceptual basis for increased attenuation with the onset of nonlinear soil behavior. Therefore, we adopt the AP3 approach (which includes transitional records into nonlinear dataset) to evaluate predictions of near-surface attenuation in the next section of this paper.

3.7.3. Effects of soil nonlinearity on predicted near-surface attenuation

Site-specific $\kappa_{0_lin_sur}$ or $\kappa_{0_nl_sur}$ values from Equation (3.5) allow for the comparison of empirical estimates of near-surface attenuation, but these two parameters represent the average attenuation of all records in linear and nonlinear regimes. Thus, in this section, we introduce the predicted near-surface attenuation at zero-distance (κ_{0_pred}), which is expected to capture the attenuation contributed by the superficial soil layers per event by removing the path contributions from κ_{r_sur} . κ_{0_pred} is modeled as:

$$\kappa_{0_pred} = \kappa_{r_AS_sur} - R_e \bullet \kappa_R \quad (3.6)$$

where $\kappa_{r_AS_sur}$ refers to the individual κ_{r_AS} value for a surface ground motion, and the path-component, κ_R , corresponds to the values derived with Equation (3.5) at each site of interest. We assume that by removing the effect of the path-component κ_R from $\kappa_{r_AS_sur}$ values per record, the remaining κ_{0_pred} becomes an approximation to the attenuation contributed by the shallower sedimentary deposits per event. Thus, we can explore how the near-surface attenuation changes with the various input ground motion amplitudes at the site of interest.

Figure 3.11 provides comparisons between κ_{0_pred} , ground shaking intensity, and deformation as captured by PGA_{rotD50} and $I_{\gamma,0}$ at FKSH14 and MYGH10. Both colors and sizes of markers represent the PGA_{rotD50} values per record. The red dashed-lines result from a local regression model characterizing the κ_{0_pred} versus $I_{\gamma,0}$ data. Triangles and circles represent the linear and nonlinear ground motions (identified with AP3), respectively. Values of κ_{0_pred} first increase and then decrease with increasing PGA_{rotD50} and $I_{\gamma,0}$ at FKSH14. This behavior is also observed at other 7 sites (i.e., AICH17, CHBH13, FKSH11, IWTH26, KMMH12, MYGH07, TCGH16). Even with the decreasing trend for large $I_{\gamma,0}$, κ_{0_pred} is still generally higher than its counterpart in the linear regime (i.e., the means of linear and nonlinear κ_{0_pred} are 0.050 sec and 0.0605 sec, respectively). Overall, κ_{0_pred} values at FKSH14 corresponding to larger deformations and higher PGA_{rotD50} are larger than those corresponding to weaker ground motions. In contrast, only a weak correlation to the intensity of ground shaking and deformation in situ is observed at MYGH10. These results are consistent with our estimations of κ_r shown in Figure 3.7. Soil nonlinear behavior can influence near-surface attenuation as captured by κ_r and κ_0 , and local site conditions may play a key role in this process. The remaining approaches

explored in this study (i.e., AP1, AP2, and AP4) provide similar results as those shown in Figure 3.11.

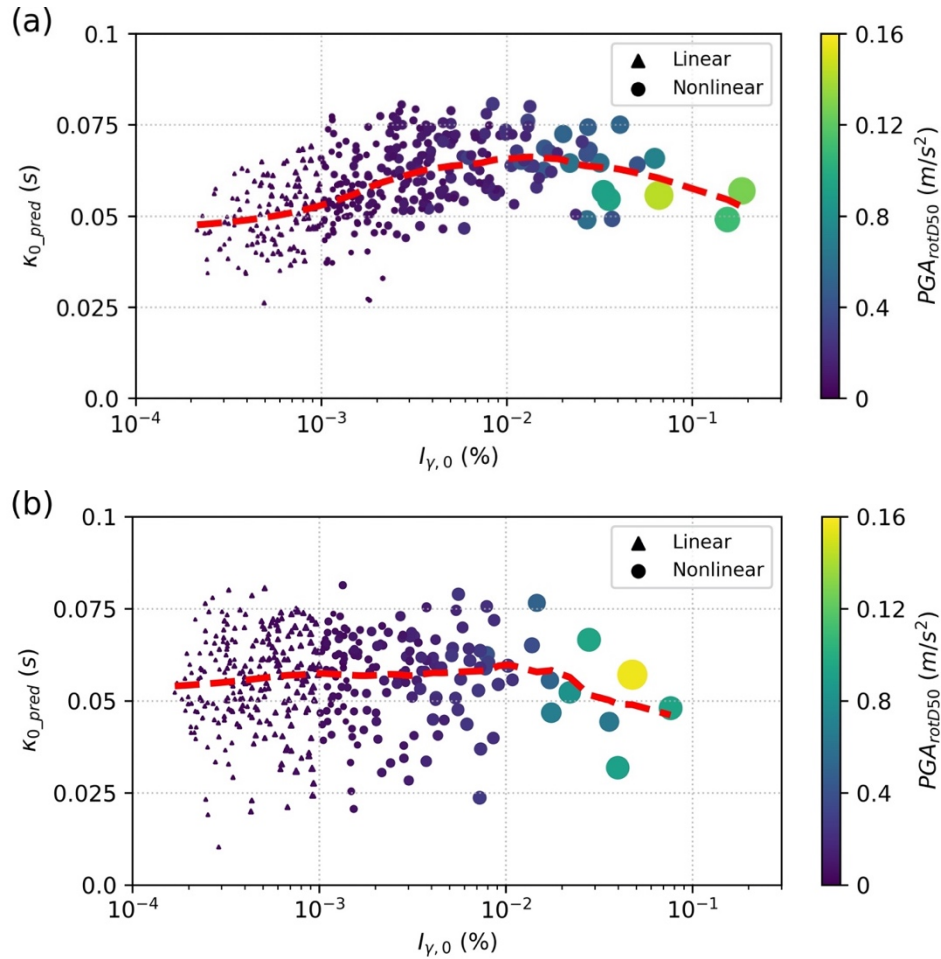


Figure 3.11. Estimated surface κ_{0_pred} and their corresponding ground shaking intensity and in situ deformation characterized by PGA_{rotD50} and $I_{\gamma,0}$, respectively at (a) FKSH14 ($V_{s30} = 237$ m/s) and (b) MYGH10 ($V_{s30} = 348$ m/s). Both, the color and the size of markers represent varying PGA_{rotD50} values. Triangles and circles represent the linear and nonlinear datasets defined by AP3. The red dashed lines depict the local regression model based on the κ_{0_pred} and $I_{\gamma,0}$ data. The color version of this figure is only available in the electronic version of this article. The color version of this figure is available only in the electronic version of this article.

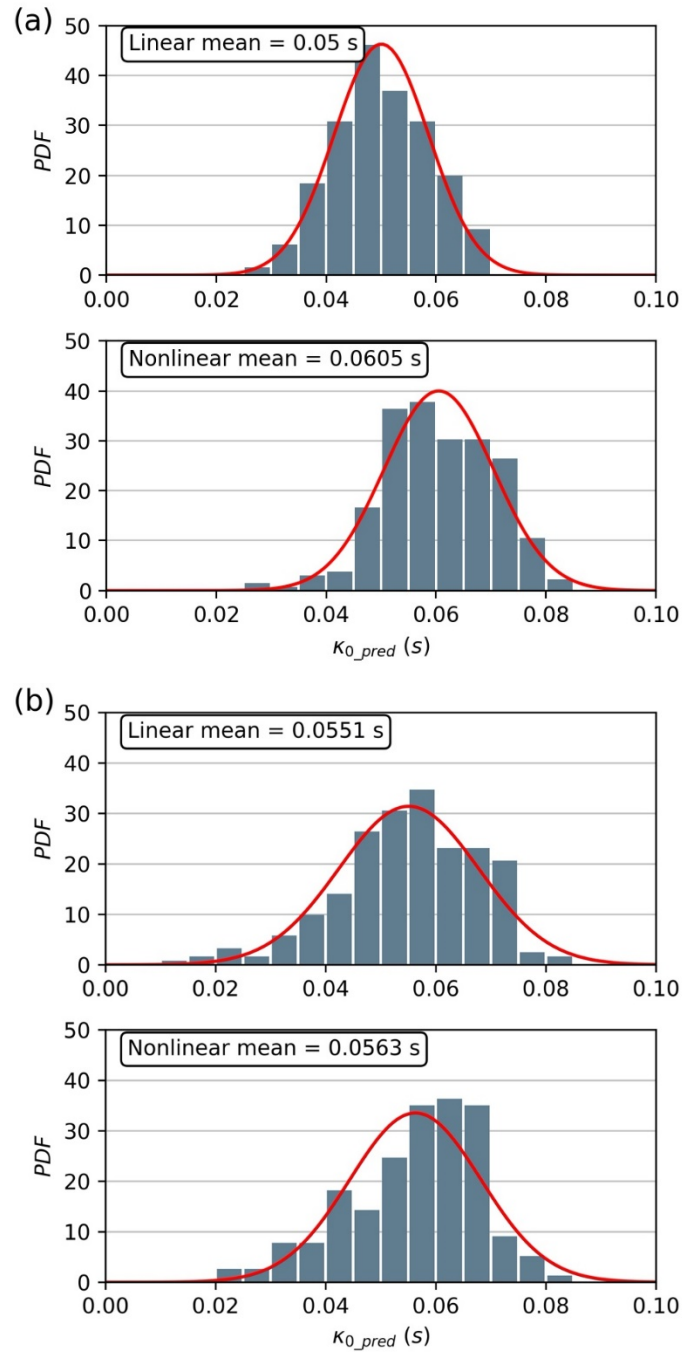


Figure 3.12. Observed distribution of κ_{0_pred} at (a) FKSH14 ($V_{s30} = 237$ m/s) and (b) MYGH10 ($V_{s30} = 348$ m/s) for the linear and nonlinear datasets. The red lines depict the theoretical probability density function (PDF) fitted with a Gaussian distribution. The color version of this figure is available only in the electronic version of this article.

Table 3.4. T-test results for κ_{0_pred} values estimated with linear and nonlinear datasets defined by AP3 (which includes records categorized as transitional into the nonlinear dataset).

| Station | V_{s30}^* (m/s) | p-value | Statistically different |
|---------|----------------------|--|-------------------------|
| | | Linear κ_{0_pred} vs. nonlinear $\kappa_{0_pred}^\dagger$ | |
| AICH17 | 314 | 10.37% | -- |
| CHBH13 | 235 | <0.01% | Yes |
| FKSH11 | 240 | 1.07% | Yes |
| FKSH14 | 237 | <0.01% | Yes |
| FKSH18 | 307 | 2.36% | Yes |
| FKSH19 | 338 | 57.66% | -- |
| FKSH21 | 365 | 47.12% | -- |
| IBRH16 | 626 | 13.80% | -- |
| IBRH17 | 301 | 55.92% | -- |
| IBRH20 | 244 | 5.97% | -- |
| IWTH21 | 521 | 9.23% | -- |
| IWTH26 | 371 | 0.62% | Yes |
| KMMH01 | 575 | 0.32% | Yes |
| KMMH12 | 410 | 3.38% | Yes |
| MYGH07 | 366 | 0.04% | Yes |
| MYGH10 | 348 | 34.13% | -- |
| NGNH29 | 465 | 72.74% | -- |
| NIGH07 | 528 | 88.97% | -- |
| NIGH12 | 553 | 66.61% | -- |
| TCGH16 | 213 | <0.01% | Yes |

* V_{s30} : time averaged shear-wave velocity in the top 30 m of the soil profile

† The transitional dataset is included into the nonlinear dataset (i.e., datasets following the criteria of AP3).

Figure 3.12 compares the probability distribution of κ_{0_pred} values from the linear and nonlinear datasets (AP3 case) at FKSH14 and MYGH10. The resulting κ_{0_pred} values are fitted with a Gaussian distribution and the corresponding probability density functions (PDFs) are represented by red lines. A shift to the right (i.e., toward larger κ_{0_pred} values) of the theoretical PDF is observed at FKSH14 as ground motions from the linear and nonlinear datasets are

considered. The mean κ_{0_pred} estimates change from 0.05 s for the linear dataset to 0.0605 s for the nonlinear dataset at FKSH14 (i.e., a difference of 21%). In contrast, the variation of mean κ_{0_pred} between linear and nonlinear datasets at MYGH10 is 2%. Most of our study sites have either a significant increase in their mean κ_{0_pred} when using the nonlinear dataset (i.e., an increase of more than 20%) or only a slight increase. There are only 4 stations that show a decrease in their mean κ_{0_pred} values with respect to the linear dataset when using the nonlinear one (i.e., FKSH19, KMMH01, NIGH07, and NIGH12). Statistical hypothesis tests (i.e., t-test) are conducted to analyze whether there is a statistically significant difference between the means of linear and nonlinear κ_{0_pred} distributions. Considering a critical value of 5%, p-values at each station are shown in Table 4. Nine out of 20 stations display statistically significant differences between their mean κ_{0_pred} corresponding to the linear and nonlinear datasets. Table 3.4, Figures 3.11 and 3.12 show that soil nonlinear behavior can affect κ_{0_pred} at the sites selected in this study, although this influence is station-dependent. At the stations that display apparent effects of nonlinearity on κ , an increasing trend in predicted near-surface attenuation with increasing ground shaking intensity and/or increasing deformation is observed.

3.8. Conclusions

In this work, we investigated the influence of soil nonlinear behavior on κ_{r_AS} values per record and site-specific κ_0 estimates at 20 stations selected from the KiK-net database. To avoid potential bias on our results due to the calculation process, we also examined the effects of the frequency band selection on κ_{r_AS} estimates, and the differences between using the S-wave window or the entire time series FAS. We compared results from a predetermined fixed-frequency window approach with an automated procedure that considers multiple frequency

windows. The latter is capable of finding the optimal frequency band per record for all records at each site. The selection of a common, fixed and broader frequency band for κ_{r_AS} estimations reduced the scatter and bias in the data, while providing reasonable estimations of κ_{r_AS} . On the other hand, values of κ_{r_AS} computed from the S-wave window FAS were reasonably similar to their counterparts based on the entire time series FAS. Hence, the analyses presented in this paper were conducted with κ_r values estimated by the fixed-frequency band approach and the FAS corresponding to the entire time series.

A consistent identification of ground motions that trigger nonlinear behavior in sedimentary deposits is also necessary to quantify near-surface attenuation beyond the linear-elastic regime. Based on the examination of an in-situ stress-strain proxy, namely the correlation between PGA_{rotD50} and $I_{\gamma,0}$, we found that the variation of shear strains with ground shaking intensity at the onset of nonlinear soil behavior is site-specific. A unique threshold for a single parameter, whether it is PGA_{rotD50} or $I_{\gamma,0}$, was not able to capture the onset of soil nonlinearity at our study sites in a consistent manner across all sites. Hence, we proposed a hybrid method to classify linear and nonlinear ground motions considering both, PGA_{rotD50} and $I_{\gamma,0}$, which resulted in linear, transitional, and nonlinear datasets at each site.

Increasing κ_{r_AS} values with increasing PGA_{rotD50} or $I_{\gamma,0}$ for ground motions with similar epicentral distances were observed at about half of our study sites. This trend was more consistently observed at softer sites. Additionally, we found that κ_0 -models could be biased by the definition of linear and nonlinear ground motion datasets. Hence, we studied the effects of ground motion categorization and proposed a hybrid classification scheme for linear and nonlinear records. We defined transitional ground motions as those associated with soil behavior between the linear-elastic and nonlinear regimes. Even though more research is necessary to

define robust classification schemes for linear and nonlinear ground motions, we observed that including the transitional motions into the nonlinear dataset reduced the variability associated with κ estimations at our study sites.

Our results also revealed differences between $\kappa_{0_lin_sur}$ (i.e., κ_0 corresponding to the linear-elastic regime) and $\kappa_{0_nl_sur}$ (i.e., κ_0 for the nonlinear regime) at most sites when implementing the κ_0 -model using ground motions classified by AP3 (which includes transitional records into the nonlinear dataset). Such differences were more prevalent among softer sites. Site parameters such as V_{s5} , V_{s10} , and V_{s30} were used in this study to investigate the influence of soil conditions on the effects of nonlinearity on κ_0 . Considering that high frequencies have short wavelengths, and that nonlinear soil behavior is triggered in low velocity layers more often located at a shallow depth, site proxies such as V_{s5} and V_{s10} may be more informative than V_{s30} when assessing effects of nonlinearity on κ . For instance, large V_{s30} values do not imply that all near-surface layers have a large V_s . The ratio of $\kappa_{0_nl_sur}$ and $\kappa_{0_lin_sur}$ decreases and approaches one for increasing V_{s5} , V_{s10} , and V_{s30} , when using the AP3 method to define nonlinear ground motion datasets.

The hypothesis posed and tested in this paper focused on the effects of ground shaking intensity on induced shear strains in sedimentary deposits and associated consequences on the attenuation experienced by seismic waves (particularly in the high frequency range). In general, we find that soil nonlinear behavior can affect estimates of κ_{r_AS} and κ_0 , but our results show that this influence is station-dependent. This is reasonable because the wave propagation of short wavelength waves is highly affected by heterogeneities in the soil or rock, local geologic structures, and topography. Moreover, the level of soil nonlinearity can be distinct at a given site (even when site parameterizations such as V_{s30} are similar and the considered intensity of ground

shaking is also similar) because of the complexities of the in situ subsurface conditions (e.g., differences in velocity gradients and seismic impedance contrasts). We note that 2D/3D site effects may affect ground motions recorded at six of our stations. The influence of soil nonlinearity on κ values computed at these stations (i.e., AICH17, CHBH13, FKSH21, IBRH20, KMMH01, KMMH12; based on the classification of Thompson et al. 2012 and Pilz and Cotton 2019) may be masked by the combined effects of wave scattering and topographic effects. Further research is necessary to evaluate the contributions of the aforementioned mechanisms on κ estimates at stations subjected to 2D/3D site effects. Likewise, future work should focus on collecting and analyzing additional strong ground motion data to identify local site conditions more conducive to generate significant changes in near-surface attenuation as captured by κ_0 when nonlinear soil behavior is triggered.

Complexities in the wave propagation phenomenon driven by scattering effects and amplification in the high-frequency range can result in negative estimates of κ_r . In this study, we obtained negative κ_{r_AS} estimates when multiple linear decaying trends, bumps, and high frequency amplifications affected the corresponding FAS spectral shape. The identification of multiple linear decays in the high-frequency range supports previous work on the bias in κ_{r_AS} associated with the selection of the frequency band. The bumps and amplifications in the high frequencies present in the FAS of some of the ground motions in our database hint that the site response may not be approximately flat within the frequency range of interest for κ_{r_AS} calculation. Considering that a flat site response is one of the assumptions of the Anderson and Hough (1984) κ_r model, further research is needed to overcome this limitation at sites where this is not the case. This work not only provides evidence of the need to understand and quantify κ in both, the linear and nonlinear regimes, but it also presents the limitations of the current κ_r model

when it comes to characterizing attenuation when conditions deviate from the original assumptions embedded in the Anderson and Hough (1984) model.

3.9. Data and Resources

Accelerograms and geotechnical data are downloaded from the KiK-net network at <http://www.kyoshin.bosai.go.jp> (last accessed May 2020). The earthquake information is available from F-net network at <http://www.fnet.bosai.go.jp/top.php> (last accessed May 2020). The supplemental material to this article includes two tables and three figures. The tables provide the κ_0 -model results when using the datasets defined by AP1, AP2, AP3, and AP4, and the κ_{0_pred} results estimated with datasets defined by AP3. The three sets of figures presented depict the results corresponding to our 20 stations as follows:

- Surface PGA_{rotD50} against $I_{\gamma,0}$ (i.e., results analogous to those presented in Figure 3.4 for MYGH10).
- Surface κ_{r_AS} estimates and their corresponding PGA_{rotD50} , $I_{\gamma,0}$ and R_e values for selected ground motions at each study site (i.e., results analogous to those presented in Figure 3.7 for FKSH14 and MYGH10).
- Estimated surface κ_{0_pred} and their corresponding ground shaking intensity and in situ deformation characterized by PGA_{rotD50} against $I_{\gamma,0}$, respectively (i.e., results analogous to those presented in Figure 3.11 for FKSH14 and MYGH10).

CHAPTER 4. VARIABILITY IN KAPPA: CONTRIBUTIONS FROM THE COMPUTATION PROCEDURE

Based on the conference paper accepted by 2022 Geo-Congress:

Ji, C., Cabas, A., Bonilla, L.F. and Gelis, C., Variability in kappa: contributions from the computation procedure, 2022 Proceedings from ASCE GeoCongress 2022, Charlotte, North Carolina (accepted).

4.1. Abstract

Kappa (κ_r), the high-frequency spectral decay parameter, has been gaining popularity in the engineering seismology field for more than forty years, but it was not until recently that κ_r has been used for geotechnical earthquake engineering applications. For instance, κ_r has been used in site-specific seismic hazard analysis and site response analysis. Values of κ_r capture high-frequency attenuation at short rupture distances. However, the high variability and uncertainty associated with its calculation has hindered its application more broadly in geotechnical engineering analyses. The uncertainties in κ_r may stem from either the poor understanding of the physics behind this parameter or the oversimplified computation procedure. Variability due to the computation procedure can be minimized with the implementation of a standardized and robust calculation process. In this work, we evaluate the variability in κ_r introduced during the calculation procedure by the selection of the frequency band and discuss potential causes for negative κ_r values. We note that the classic κ_r model may be an oversimplification of complex wave propagation phenomena, and the divergence between its assumptions and actual site conditions require further investigation.

4.2. Introduction

The systematic contribution of near-surface local geologic structures to ground motion characteristics is commonly referred to as site effects. Site effects are a complex function of the incident ground motion, dynamic properties of the materials and their densities, stratigraphy (including the location of the water table), and topographic features (Kaklamanos et al., 2021). Site effects are often parameterized by using V_{s30} , the time-averaged shear-wave velocities for the top 30 m, in ground motion models. However, it has long been recognized that V_{s30} has some limitations in capturing the complexity of expected changes in ground motions due to local soil conditions. For instance, other site parameters such as the depth to the top of a layer with V_s of 1,000 m/s or 2,500 m/s (i.e., $Z_{1.0}$, and $Z_{2.5}$, respectively) have also been proposed to complement V_{s30} . Anderson and Hough (1984) introduced an empirical parameter, κ_r , to describe the linear decay trend of the acceleration S-wave Fourier Amplitude Spectrum (FAS) in high frequencies in log-linear scale (see Figure 4.1). The site-specific component κ_0 captures the near-surface attenuation at specific sites (Ktendiou et al. 2013, Cabas et al. 2017). Recent studies have shown the advantages of site-specific κ_0 , as it is able to adjust ground motion models (GMM) from host to target regions, within the framework of nonergodic probabilistic seismic hazard analysis (PSHA). Additionally, κ_0 has been used in the development of synthetic ground motions (e.g., Campbell 2003, Cabas and Rodriguez-Marek 2017). Therefore, the computation of robust estimates of site-specific κ_0 for a given site of interest is critical to enable its future implementation in multiple geotechnical earthquake engineering analyses in practice.

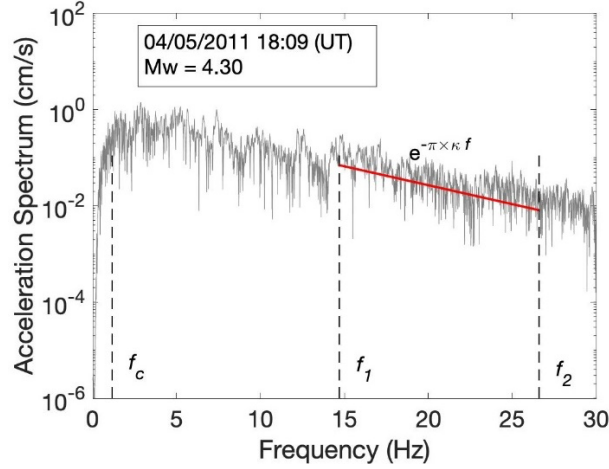


Figure 4.1. Example of κ_r estimate for a ground motion observed at a KiK-net station (IBRH20). Depicted f_1 and f_2 correspond to the range of frequencies where the linear decay of the spectrum is used for the computation of κ_r . The f_1 and f_2 are selected manually in this case to illustrate the computation of κ_r . f_c refers to the corner frequency of the corresponding event.

Three assumptions are suggested by Anderson and Hough (1984) κ_r model, which are (1) the earthquake source acceleration spectrum is flat above the corner frequency, (2) the seismic quality factor Q (Knopoff, 1964) is frequency independent, and (3) the local site response is almost flat in high frequencies. Anderson (1991) investigated the potential correlation between the apparent κ_r per record and source-to-site distances. A linear distance-dependency model was recommended because it can fit the observed data with statistic robustness. However, it should be clarified that there is no physics-based reason to expect a linear relationship between κ_r values and source-to-site distances (Boore and Campbell 2017). Thus, the apparent κ_r is usually decomposed into a source-component (i.e., κ_S), path-component (i.e., $\widetilde{\kappa}_R$, a function of distance), and a site-specific component (i.e., κ_0). The κ_r -model is often simplified to be a linear distance-dependency model as below.

$$\kappa_r = \kappa_S + \widetilde{\kappa}_R + \kappa_0 = \kappa_0 + \kappa_R \times R \quad (4.1)$$

There are large uncertainties and significant scatter associated with κ_0 , which ultimately hinder its implementation in seismic hazard analysis. Considering the lack of understanding of the physics behind κ_0/κ_r and the user-biased computation procedure for κ_r estimates, the variability observed in site-specific κ_0 values are mainly due to (1) the oversimplified linear-distance dependency of the κ_r model and (2) the large variability in empirical κ_r values per record. Therefore, a more comprehensive distance-dependency model is required to derive a robust estimate of κ_0 . Meanwhile, the absence of a uniform computation procedure for κ_r and the differences between the real in situ site conditions and simplifications embedded in the Anderson and Hough (1984) κ_r model also result in the large scatter of κ_r per record.

The objective of this work is to discuss the challenges associated with the implementation of the simplified Anderson and Hough (1984) κ_r model for sites conditions commonly found in the field. Complex in situ conditions limit the compliance with the Anderson and Hough (1984) κ_r model assumptions. Particularly, site amplification effects and scattering of the wavefield due to heterogenous soil layers deviate from the assumptions of the κ_r model (i.e., Anderson and Hough (1984) assumed a flat site response in the high frequencies, in other words, no high frequency amplification of the ground motion due to local soil conditions). In this study, the potential causes for negative κ_r values and the effect of frequency band selections are analyzed using two stations from the Japanese Kiban-Kyoshin network (KiK-net, Aoi et al., 2004, Fujiwara et al. 2004) as case studies.

4.3. Methods

The KiK-net dataset is used in this work, which is rich in high-quality ground motions recorded at more than 600 stations installed uniformly across Japan. Each station has a pair of

sensors, one at the surface and another one at borehole with typical depths between 100 to 200 m. Sampling frequency of the instruments is 100 or 200 Hz, and body wave velocity profiles for each station are measured by downhole PS logging. The earthquake information, such as the seismic moment magnitude, location of the epicenter, and focal depth, are compiled from the moment tensor solutions provided by the broadband seismography network (F-net) catalog. In this article, two stations (i.e., AICH17 and FKSH19) are analyzed (see Table 1 for the corresponding site information). AICH17 and FKSH19 have increasing V_s profiles with depth, and a strong impedance contrast at 40 m depth is observed at FKSH19. At each station, the ground motions are selected based on the following criteria: (1) epicentral distances less than 150 km, (2) focal depths less than 35 km (Ji et al. 2020), (3) source-to-site paths do not go through the Japanese volcanic belt, and (4) signal-to-noise (SNR) ratio larger than 3.0 from 1 to 30 Hz. No additional constraints are used to limit the intensity of ground motions (e.g., no thresholds to peak ground acceleration values or shear strain index are used). All the ground motions are processed by Bahrapouri et al. (2021) with an automated protocol.

Table 4.1. Site information for the selected KiK-net stations

| Station | V_{s30}^1 (m/s) | $V_{s,depth}^2$ (m/s) | Hole Depth (m) | Number of ground motions | Fundamental frequency (Hz) | Predominant frequency (Hz) |
|---------|-------------------|-----------------------|----------------|--------------------------|----------------------------|----------------------------|
| AICH17 | 314 | 2200 | 101 | 78 | 4.07 | 4.07 |
| FKSH19 | 338 | 3060 | 100 | 440 | 3.27 | 3.27 |

¹ V_{s30} : the time averaged shear-wave velocity for the top 30 m.

² $V_{s,depth}$: the shear-wave velocity at the borehole sensor's depth.

The classic acceleration spectrum (AS) approach (Anderson and Hough, 1984) shown in Figure 4.1 is used to estimate κ_r , which is hereafter referred to as κ_{r_AS} . However, instead of manually selecting a frequency range for the calculation of κ_r , a moving frequency window ($[f_i,$

f_2] is used to study the influence of the frequency band selection. The minimum width of the frequency window is 10 Hz. Values of f_l (i.e., the beginning of the frequency window) are selected as the maximum among three values: (1) $1.4 f_c$ (where f_c is the earthquake's corner frequency of the corresponding event, estimated with the Brune 1970, 1971 model), (2) $1.4 f_0$ (where f_0 is the predominant site frequency), and (3) 15 Hz. Meanwhile, the value of f_2 changes from (f_l+10) Hz to 25 Hz. The 25 Hz is set to avoid bias from KiK-net instrument's response (Aoi et al., 2004, Fujiwara et al. 2004, Oth et al. 2011, Laurendeau et al. 2013). The increments of f_l and f_2 considered in our algorithm are equal to 0.5 Hz. This procedure covers several possible frequency bands per record. Following the algorithm proposed by Sonnemann and Halldorsson (2017) and Pilz et al. (2019), the optimal frequency band has the minimum root mean square error (RMS) over the frequency bandwidth where it is computed:

$$P = \frac{RMS}{\sqrt{\Delta f}} \quad (4.2)$$

Where Δf is the frequency window width, and RMS is the error between the fitting line and the smoothed FAS, which is estimated with the Konno-Ohmachi filter with a coefficient of 40 (Konno and Ohmachi, 1998).

4.4. Results and discussions

First, the influence of the selected frequency band on κ_r estimates is studied. Considering that the Anderson and Hough (1984) κ_r model assumes a frequency-independent Q, different frequency bands should not play an important role on κ_r estimates. However, previous studies have shown that this is not the case (e.g., Edwards et al. 2015; Mayor et al. 2018; Haendel et al. 2020).

Figure 4.2 shows the variations of κ_{r_AS} with all possible frequency bands at FKSH19 and AICH17. The blue circles represent the κ_{r_AS} computed with the optimal frequency band (i.e., the minimum P values from Eq. 2). The error bars indicate the mean of all possible κ_{r_AS} values (i.e., black, solid circle) +/- the corresponding standard deviation per horizontal component. Large variations of κ_{r_AS} are observed at both, FKSH19 and AICH17, and the influence of frequency band selections on κ_{r_AS} estimates is more significant at FKSH19.

For most of the selected ground motions, the κ_{r_AS} with minimum P value is outside the error bar. Figure 4.2 provides evidence of the limitations of the classic κ_r model by showing the high variability in κ_{r_AS} values as a function of the frequency band selection. This observation suggests that the variability in κ_r values with frequency may not be negligible at certain sites, which could introduce biases when implementing the Anderson and Hough (1984) model. For instance, a systematic bias in κ_{r_AS} for H₂ component is observed at FKSH19 (Figure 4.2). The κ_{r_AS} estimates corresponding to the minimum P values (i.e., blue circles in Figure 4.2) are generally below the error bar for the H₂ component, which is not the case for the H₁ and H₂ components at AICH17.

To explore this systematic bias in the H₂ component, the FAS and the corresponding empirical transfer function (ETF) are inspected. Figure 4.3 provides an example ground motion observed at FKSH19. The solid lines are the smoothed FAS with the Konno-Ohimachi filter (Konno and Ohimachi, 1998), and the red dashed lines show the optimal frequency band with the minimum P values computed from Eq. 2. In Figure 4.3, the κ_{r_AS} values are 0.0575 s and 0.0097 s for surface H₁ and H₂, respectively. There are bumps and multiple linear decay trends in high frequencies. A flat spectrum trend (i.e., no significant decay or increase in amplitude with frequency) begins at 20 Hz for the H₁ component, where the ETF appears flat. A rapid decay

happened around 14 Hz for the H₂ component, and the moving frequency window detects smaller errors between the linear fitting line and smoothed FAS over a relatively broader range in higher frequencies (i.e., more than 15 Hz). The FAS has a relatively flat shape in that frequency range, which results in a smaller κ_{r_AS} value.

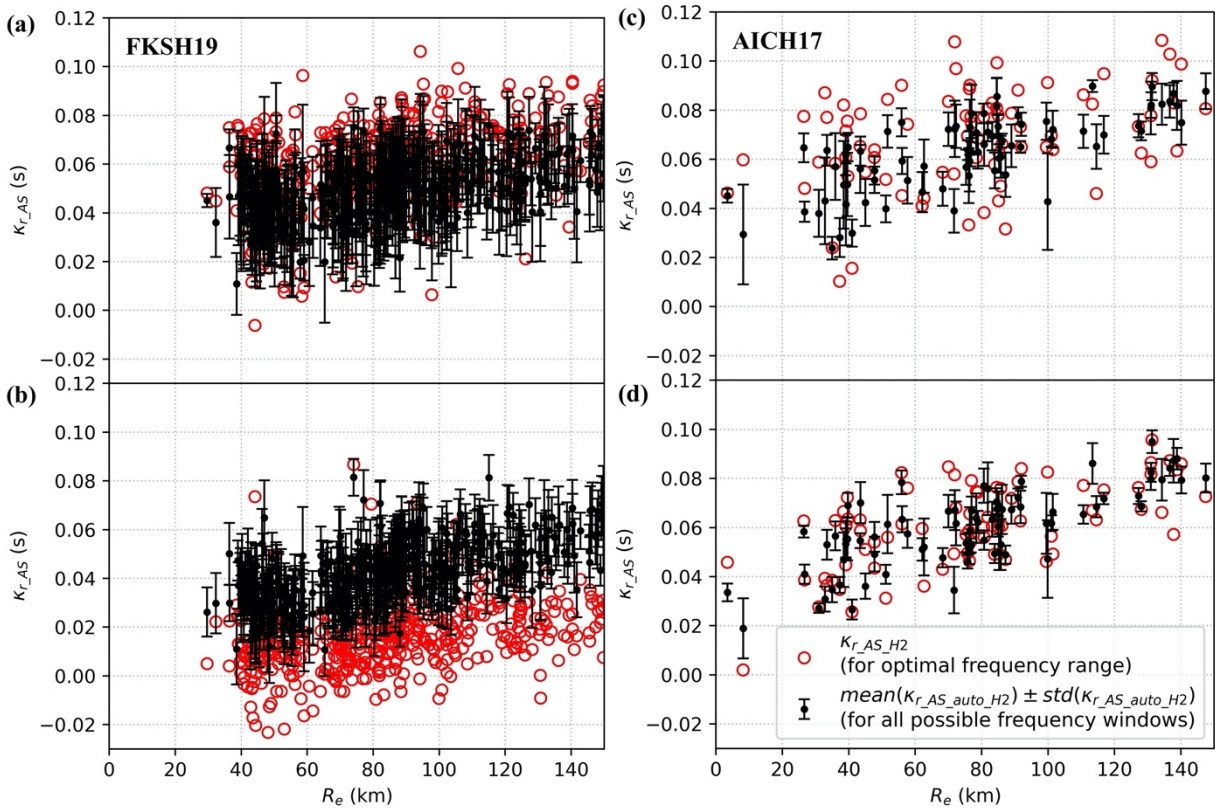


Figure 4.2. The effects of frequency band selection on κ_{r_AS} estimates at (a) FKSH19 for H₁, (b) FKSH19 for H₂, (c) AICH17 for H₁, and (d) AICH17 for H₂.

A similar trend is also found for most of the other ground motions at FKSH19. The systematic bias of κ_{r_AS} for the H₂ components could result from soil anisotropy in the field driving differences in the ETF for different ground motion orientations. Site effects have been recently studied in the context of their influence on ground motion directionality (Ramos-Sepulveda and Cabas 2021), but further research in this area is still needed. The assumption used

in the Anderson and Hough (1984) κ_r model regarding a flat site response at high frequencies is not always valid, particularly when there are shallow impedance contrasts and heterogeneities that can scatter the wavefield within the site profile. Picking a frequency band for κ_{r_AS} estimates above the predominant frequency of the site can mitigate this bias. Additionally, Parolai and Bindi (2004) suggested to use a broad frequency band to compute κ_{r_AS} to reduce site effects on κ_{r_AS} estimates. In practice, however, the instrument's response, the earthquake corner frequency, the site's predominant frequency, and the usable frequency range governed by the signal-to-noise ratio (SNR) limit the frequency range that can be used for κ_{r_AS} calculations. Thus, it is necessary to further explore the classic Anderson and Hough (1984) κ_r model to identify which assumptions can be modified and how so that more complex wave propagation phenomena can be captured. Such investigation could enable the implementation of the κ_r model in site response analysis (e.g., Cabas and Rodriguez-Marek 2018; Xu and Rathje 2021; Gann et al. 2022).

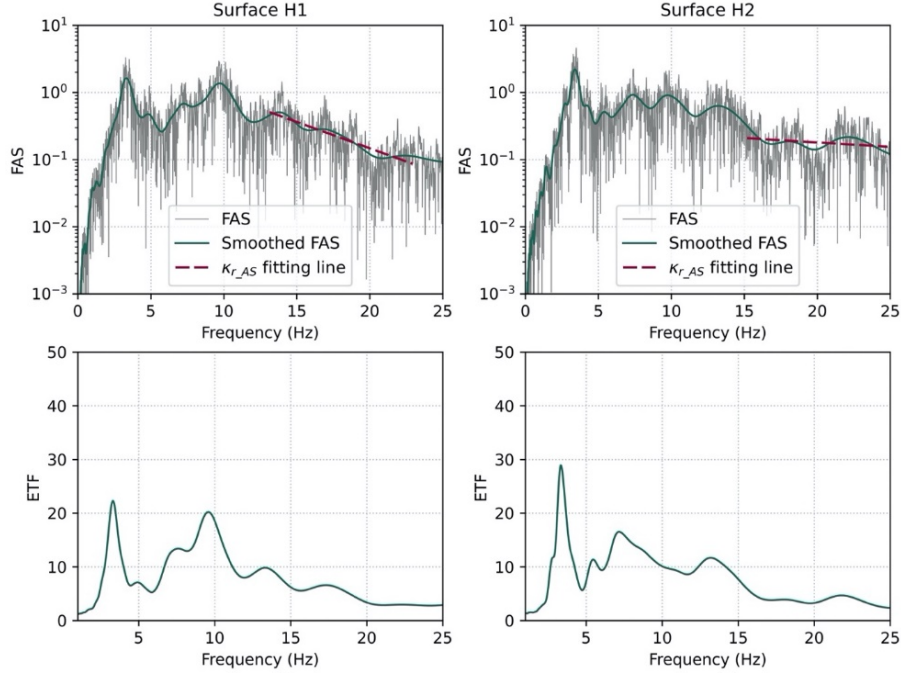


Figure 4.3. Example ground motion for surface κ_{r_AS} estimates and the corresponding ETF of two orthogonal horizontal components. This event was observed at FKSH19 on December 31, 2002 (UT). The seismic moment magnitude (M_w) is 4.3, the focal depth is 35 km, the epicentral distance is 82 km and the azimuth is 124°.

Negative values of κ_{r_AS} are also obtained for some records at both study sites, but mostly for the H₂ recorded components at FKSH19 as shown in Figure 4.2. In theory, κ_{r_AS} could take any value if it is analyzed through the lens of the mathematical computation of the slope of the FAS in the high frequency range (i.e., an observable, empirical parameter). However, when κ_{r_AS} is understood as a seismic attenuation parameter that captures a physics-based phenomenon in the field, negative κ_{r_AS} estimates are not easily explained in terms of energy dissipation. Figure 4.4 shows a ground motion at FKSH19 with a surface negative κ_{r_AS} value.

In Figure 4.4, the surface κ_{r_AS} values are 0.0381 s and -0.0094 s for the H₁ and H₂ components, respectively, while the borehole κ_{r_AS} values are -0.0094 s and 0.0022 s. At FKSH19, there are 41 out of 440 ground motions with negative surface κ_{r_AS} values

corresponding to the H_2 component, and 112 out of 440 ground motions with negative borehole κ_{r_AS} values. On the other hand, there are only 86 and 1 ground motions with negative borehole and surface κ_{r_AS} values for H_1 component, respectively. As Figure 4.4 shows, the borehole FAS is almost flat at high frequencies. And the H_2 surface FAS shows increasing amplitudes over the optimal frequency window (i.e., the one with minimum P value) due to high-frequency site amplifications (Figure 4.4d) that counteract attenuation effects. A relatively strong V_s impedance contrast observed at 40 m depth, where the V_s changes from 960 m/s to 3060 m/s, could help explain negative κ_{r_AS} values. The down-going wave effect can bias and affect κ_{r_AS} estimates at borehole (Chandra et al. 2015, Bonilla and Ben-Zion 2021).

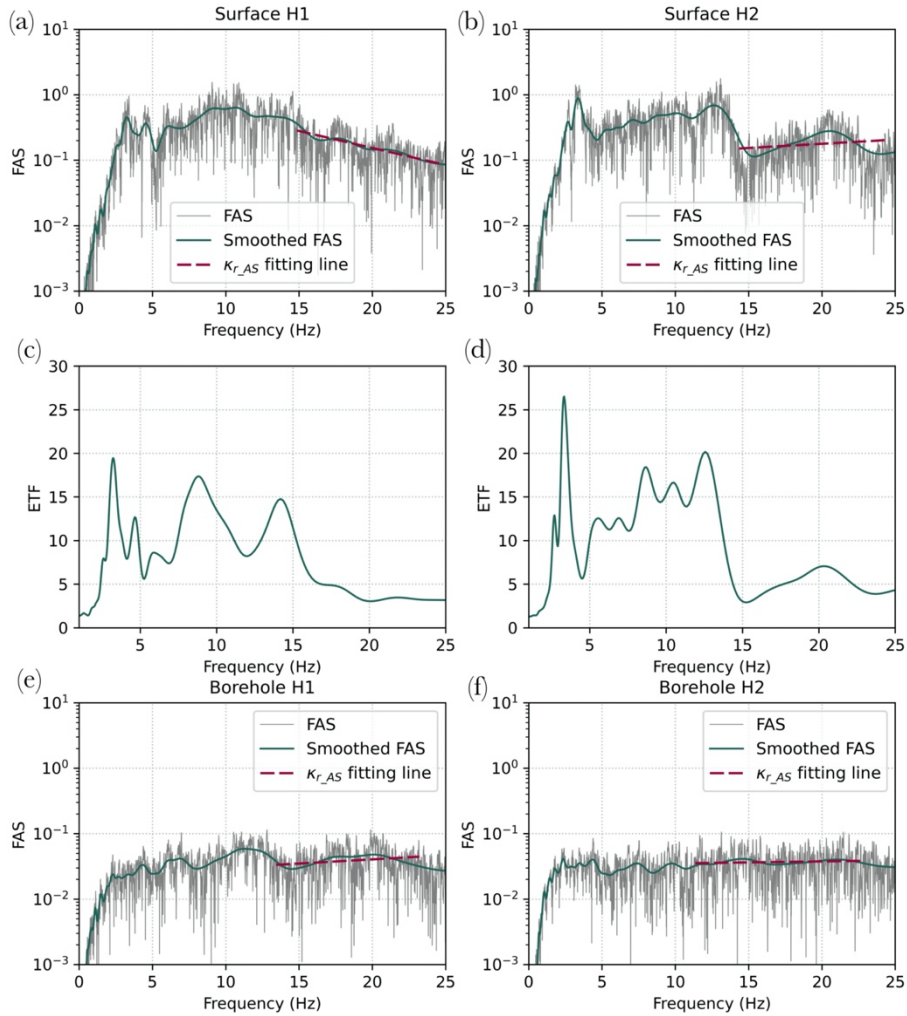


Figure 4.4. Example ground motions at FKSH19 with negative κ_{r_AS} estimates. (a) and (b) are FAS corresponding to the H₁ and H₂ recorded components at the ground surface, (c) and (d) present the empirical transfer function (ETF) computed using the surface and borehole records at the site for the H₁ and H₂ components, respectively, (e) and (f) depict the FAS corresponding to the borehole H₁ and H₂ recorded components. The ground motions depicted here are associated with a seismic event recorded on June 11, 2011 (UT). The corresponding seismic moment magnitude (M_w) is 3.7, the focal depth is 58 km, the epicentral distance is 48 km and the azimuth is 116°.

Although there is no consensus in the seismological community regarding the origin of such negative values, negative κ_{r_AS} values merit more attention and discussion as they can bias the estimation of site-specific κ values (i.e., κ_0) and affect their application in ground motion

models, site response analysis, or seismic hazard assessments. Negative κ_{r_AS} values at depth in this case result from the FAS having an almost flat spectral shape at high frequencies. At FHS19, the V_s at depth is 3060 m/s (see Table 1), which suggests the presence of a low-attenuating medium (e.g., very hard, crystalline rock with a high seismic quality factor Q). Resulting negative values in this case are then a mathematical artifact of the computation of κ_{r_AS} values at an effectively flat portion of the FAS. Visual inspection and judgement are required to fully understand the sources of observed deviations from the classic κ_r model, and to provide more accurate assessments of the contributions of shallow geologic structures to the attenuation experienced at a site.

4.5. Conclusions

This paper discusses the variability associated with values of κ_r per record, which can affect the estimation of site-specific κ_0 values and their application in geotechnical earthquake engineering analysis. The still evolving understanding of the physics behind κ_r and the highly user-orientated computation process are primary sources of the observed variability and epistemic uncertainty. Assumptions embedded into the classic κ_r linear model introduced by Anderson and Hough (1984) may also introduce bias in κ_r estimates for complex wavefields that cannot be accurately simplified or represented by the current κ_r model. In this paper, we first study the influence of the selected frequency band on κ_r by quantifying the variations in κ_r estimated with a moving frequency window. Our findings suggest that there is a significant effect of the selected frequency band on κ_r , which supports previous studies on the limitations of assuming a frequency-independent Q in the Anderson and Hough (1984) model. Additionally, negative κ_r values are discussed and associated with pronounced site effects at high frequencies.

Higher mode amplifications and/or complex shapes of FAS are often found at stations with ground motions associated with negative κ_r values. The presence and meaning of negative κ_r values are not captured in or explained by the Anderson and Hough (1984) model because it is assumed that the site response is almost flat in high frequencies. The aforementioned limitation of this classic model may require modifications to accommodate more complex wave propagation phenomena especially near the surface due to local site effects.

Although the sources of variability in κ_r may be coupled and difficult to decompose (e.g., Ktenidou et al. 2013, Edwards et al. 2015, Ji et al. 2020), studies that focus on the contributors to the observed scatter can shed light on future research directions to enable the implementation of this parameter in geotechnical earthquake engineering analysis. For instance, Haendel et al. (2020) introduced a frequency-dependent Q model to explore an alternative formulation they called the zeta-model, to the classic κ_r model. Previous studies have investigated κ within the linear-elastic regime (e.g., Cabas et al. 2017, Xu et al. 2019), while our understanding of the correlation between ground motion intensities and κ for larger-strain events is still limited (e.g., Xu and Rathje 2021, Ji et al., 2021). Current linear distance-dependency models to separate the path and site-specific components of κ_r may need modifications that can accommodate more complex phenomena. These topics are deserving of further exploration to improve the robustness of κ_r and κ_0 estimates and their use in engineering seismology and geotechnical earthquake engineering.

CHAPTER 5. A DESIGNSAFE GROUND MOTION DATABASE FOR CALIFORNIA

Based on paper to be submitted to the Earthquake Spectra: Ji, C., Cabas, A., Kottke, A. and Pilz, M., A DesignSafe Ground Motion Database for California. (in preparation)

5.1. Abstract

This paper presents a ground motions database for California for California available at the cyberinfrastructure of DesignSafe (DSGM-CA) and its close surroundings (i.e., areas near the border with Nevada, Oregon, and Arizona) between 1999 and 2021 by 74 different networks and data centers. This dataset includes earthquakes with magnitudes larger than 1.3 and focal depths less than 40 km. Ground motion records and events included in this dataset are collected and processed with an automated protocol developed by the USGS, which is known as the gmprocess toolkit. Path measures such as rupture distance and epicentral distance are computed. Spectral accelerations, duration metrics, Arias intensity, and other ground motion intensity measures are provided for records that pass the quality assurance check performed by the gmprocess toolkit. Additionally, site metadata are provided, including wave velocity information (from proxy-based time-averaged shear-wave velocity for the top 30 m, V_{s30} , and from P- and S- wave measured velocity profiles when available), predominant frequency measured from microtremor-based horizontal-to-vertical ratios, and site-specific κ_0 values computed from multiple ground motions recorded at each station. In total, 131670 ground motions observed at 1623 stations from 1253 earthquakes are included in this database with magnitudes ranging from 1.3 to 7.2 and distances ranging from 0.24 to 335 km.

5.2. Introduction

Recorded ground motions are necessary to fully understand the nature of earthquakes and their effects on civil infrastructure and society at large. The increase of ground motion records

worldwide allows the seismological and engineering community to improve empirical characterizations of seismic hazards; from developing more robust ground motion models (GMMs), to more accurately quantifying complex wave propagation effects such as the ones resulting from nonlinear soil behavior or basin effects. Moreover, proper recording, processing, and archiving of ground motion records play an essential role in modern seismology and earthquake engineering. One relevant example is Japan's national strong motion network, Kiban Kyoshin Network (KiK-net), with the same type of instruments to record real-time earthquakes in Japan after the 1995 Hyogoken-Nanbu (Kobe) earthquake (Aoi et al. 2004).

One of the challenges for researchers studying ground motions recorded in the most seismically active regions in the US, such as west coast, is that there is not a single seismic network with the same type of instruments uniformly deployed across those regions. For instance, in California, available ground motion recording stations are operated by different networks (e.g., USGS Northern California Network, NC; California Strong Motion Instrumentation Program, CE). Hence, ground motions are usually recorded by various types of sensor (e.g., broadband high gain accelerometers or extremely short period seismometers) and archived by different data providers (e.g., the IRIS Data Management Center). Additionally, geotechnical information (e.g., soil profiles) and site parameters (such as the time-averaged shear-wave velocity for the top 30 m, V_{s30}) are not available or not well documented at all recording stations. Therefore, a more homogeneous ground motion database which includes site information can enable more research with ground motions recorded in highly seismic regions in the US. The NGA-West2 database (Ancheta et al., 2013) hosts a large number of ground motions from shallow tectonic earthquakes worldwide, and for California it only includes Earthquakes from 1998 to 2011 with magnitudes ranging from 3 to 5.5.

The overarching goal of this work is to create a database of ground motions from earthquakes contributing to the seismic hazard of various regions in the US west coast that can be easily updated as more ground motions in those areas are recorded. In pursuit of that goal, this paper aims to (1) compile and process events primarily in California and some in neighbor states from 1999 to 2021 using the U.S. Geologic Survey (USGS) gmprocess toolkit to process the corresponding ground motions, and (2) provide a dataset of site parameters for seismic stations included in the database. The USGS developed gmprocess as python toolkit to process ground motions with an automatic and uniform protocol (Hearne et al. 2019, Rekoske et al. 2020), which can be used to efficiently process a large number of records. This ground motion dataset for California can be accessed via DesignSafe, which is a cyberinfrastructure providing closed-based tools to manage, retrieve, publish and analysis datasets (Rathje et al., 2017). Moreover, significant recent events in the region are included in this new database, hereafter referred to as the DSGM-CA database, such as the 2003 San Simeon, California earthquake, 2019 Ridgecrest, California earthquake and the 2020 Monte Cristo, Nevada earthquake. The authors envision that future expansions of this database will include more events from Nevada, Utah, Idaho, and Arizona. The quality of the ground motions included in this database is assessed via multiple algorithms to screen processed ground motions. Commonly used site parameters such as V_{s30} , P- and S-wave velocity profiles, and the site's predominant frequency (i.e., the frequency corresponding to the peak horizontal-to-vertical ratio, HVSR) are compiled from publicly accessible databases hosted by the USGS and the University of California, Los Angeles (UCLA). The site-specific component of the high frequency attenuation parameter kappa (Anderson and Hough 1984), known as κ_0 (Anderson 1991), is computed with an in-house code

(Ji et al. 2021). This database will be the first one, to the authors knowledge, to compute and report values of κ_0 per station.

5.3. Ground motion database

This database can be separated into two sets as a function of the signal processing used via the USGS gmprocess toolkit. Different criteria were applied to select earthquake events (e.g., magnitude) and ground motions (e.g., sampling rate) to construct each set of ground motions which result in datasets DSGM-CA-P1 and DSGM-CA-P2.

5.3.1. Earthquake and ground motion selection

Earthquakes included in DSGM-CA-P1 and DSGM-CA-P2 are queried from the USGS Comprehensive Catalog (ComCat, Guy et al. 2015). Dataset P1 includes earthquakes that happened in or near California (e.g., in Nevada) from 1 Jan 2001 to 31 Dec 2020 with magnitudes larger than 4.0 and focal depths less than 35 km. On the other hand, dataset P2 includes events that occurred from 13 Jan 1999 to 09 Jul 2021 with magnitudes larger than 1.3 and focal depths less than 37 km. Thus, there are 1253 earthquakes included in DSGM-CA database, where 409 events are included in both datasets P1 and P2, 212 events are only included in dataset P1, and 632 events only included in dataset P2. Various magnitude types (e.g., seismic moment magnitude M_w or local magnitude M_l) are included since the commonly used M_w was not always reported by the different networks used in this study. The earthquake source information in DSGM-CA database is based on the information archived in ComCat up to July 2021, which is subject to changes. Details on potential changes to the source information can be accessed with event ID (which is provided in the flatfile) via ComCat.

The USGS gmprocess toolkit queries major data providers (e.g., IRIS Data Management Center, the North California Earthquake Data Center, and Southern California Earthquake Data Center) to search and download ground motions with specific filtering criteria. The screening criteria used for Dataset P1 includes: (1) a minimum sampling frequency of 50 Hz, (2) source-to-site distance less than 150 km, (3) availability of two horizontal components, and (4) availability of broadband and high broadband accelerometer or high gain seismometer sensors. Meanwhile, the screening criteria used for Dataset P2 includes: (1) a minimum sampling frequency of 20 Hz, (2) source-to-site distances up to 300 km, (3) availability of two horizontal and one vertical components, and (4) availability of accelerometers or high gain seismometer sensors. The instrument responses are required for all ground motions to remove its effect on ground motion characteristics, and only surface ground motions are processed in this work.

Table 5.1. Summary of ground motion screening criteria and processing using with USGS gmprocess toolkit.

| | DSGM-CA-P1 | DSGM-CA-P2 |
|----------------------------|---|--|
| Source characteristics | Event occurred from 1 Jan 2001 to 31 Dec 2020 | Event occurred from 13 Jan 1999 to 09 Jul 2021 |
| | Magnitude > 4.0 | Magnitude > 1.3 |
| | Focal depth < 35 km | Focal depth < 40 km |
| Path characteristics | Distance < 150 km | Distance < 300 km |
| Instrument characteristics | Sampling frequency > 50 Hz | Sampling frequency > 20 Hz |
| | Ground motion channels include BH, HH, BN, and HN | Ground motion channels include HN, BN, HH, BH, and EH ¹ |
| | Two horizontal components included | Two horizontal components and one vertical component included |

Table 5.1 (continued).

| | | |
|--|---|---|
| Ground motion screening and processing | Free-field station | Free-field station |
| | Accelerometer is preferred for collocated sensors | Accelerometer is preferred for collocated sensors |
| | N/A | Amplitude checks to avoid clipping ³ |
| | Baseline corrections: demean and linear detrend | Baseline corrections: demean and linear detrend |
| | Both side Hann taper with width of 0.05 s is applied | Both side Hann taper with width of 0.05 s is applied |
| | Butterworth highpass/lowpass filter with order of 5 is applied ² | Butterworth highpass/lowpass filter with order of 5 is applied |
| | processed ground motion is trimmed 3 sec before the onset of signal | processed ground motion is trimmed 2 sec before the onset of signal |
| | SNR is checked from earthquake corner frequency up to 5 Hz | SNR is checked from earthquake corner frequency up to 5 Hz |
| | Minimum of 0.1 zero crossing rate | Minimum of 0.1 zero crossing rate ⁴ |
| Waveform metrics output | PGA; PGV, 5% damped PSA; duration measures ⁵ | PGA; PGV, 5% damped PSA; duration measures; Arias Intensity |

¹The channel codes follow the Standard for the Exchange of Earthquake Data (SEED) channel naming. The first letter is the band code indicating the sampling rate and response band of the instrument. The second letter presents the instrument type. For the band code, B, H, and Z represent the Broad Band, High Broad Band, and Extremely Short Period, respectively. On the other hand, the instrument code H refers to high gain seismometer and N is accelerometer.

² The highpass and lowpass frequencies for each record are available in the final flatfile included as an electronic supplement to this dataset.

³ Clipping often is a concern for geophones.

⁴ The rate of signal changes from positive to negative or negative to positive per second

⁵PGA: peak ground acceleration; PGV: peak ground velocity; Sa: 5% damped Pseudo-Spectral acceleration.

5.3.2. Automated ground motion processing

The ground motion processing of DSGM-CA P1 and P2 was conducted using similar procedures as shown in Table 1. Some of the common processing steps are described next. First, the non-free-field sensors (i.e., sensors attached to a larger structure) are excluded and a minimum of 0.1 zero crossing rate is chosen to screen the time series. The mean and linear trend are removed to correct the baseline. A correction for the instrument's response is applied. The

main difference between the ground motion processing for datasets P1 and P2 is that DSGM-CA-P1 trimmed the processed ground motion later than dataset P2 resulting in longer tails of the processed time series in DSGM-CA-P1.

The quality of ground motions in DSGM-CA P1 and P2 was controlled by signal-to-noise ratio SNR (i.e., only use ground motions with $SNR > 3.0$ between the earthquake's corner frequency and 5 Hz). The earthquake's corner frequency is computed from Brune (1970, 1971) model with stress drop of 10 bars and crustal shear wave velocity of 3.7 km. However, if the computed corner frequency is less than 0.1 Hz or larger than 2.0 Hz, 0.1 or 2.0 Hz will be reset as the minimum frequency range to screen SNR, respectively. The screening for record maximum amplitude with units of counts (rather than physical units) was only conducted for dataset P2 to avoid signal clipping (see Table 1). The aforementioned evaluations of the quality of the signals in each dataset were performed via the USGS gmprocess toolkit automatically. Additionally, the median of the geometric PGA values measured from as-recorded orthogonal horizontal components rotated with all potential angles (PGArotD50, Boore 2010) was used as a proxy to identify outliers within the DSGM-CA database. A threshold of 98 m/s^2 (i.e., 10g) was set to get rid of problematic records.

5.4. Overview of processed ground motions

In total, there are 131670 ground motions observed at 1623 stations from 1253 earthquakes available in DSGM-CA database. Figure 1 shows the location of earthquakes and stations. Among the 1253 earthquakes, 409 events and 13584 ground motions are both included in dataset P1 and P2 (see Figure 2). The duplicated ground motions included in datasets P1 and P2 are provided in the flatfile available on DesignSafe, where a note is added to indicate the

corresponding dataset. Figure 3 shows the distribution of magnitude, distance and PGArrotD50 of records in this work. The magnitude of seismic events included in DSGM-CA database varies from 1.3 to 7.2, and the epicentral distances range from 0.24 to 335 km. Approximately 94% of the records have PGArrotD50 less than 0.1 m/s^2 .

To evaluate the differences between the processed ground motion in datasets P1 and P2 from the variations in processing protocols, PGArrotD50 and PGVrotD50 are compared for the duplicated records in datasets P1 and P2. Figure 4 shows that the differences in PGArrotD50 and PGVrotD50 for the same record included in both datasets are negligible. There are more than 99% duplicated records with differences in PGArrotD50 for the same ground motion being less than 1%. Visual inspections were also performed for three randomly selected earthquakes (i.e., about 100 associated ground motions) to screen the acceleration time series and the corresponding FAS. Again, a good agreement was observed for the duplicated ground motions.

The processed ground motions are stored as an Adaptable Seismic Data Format (ASDF, Krischer et al. 2016), and are archived in the container of Hierarchical Data Format version 5 (HDF5) for each earthquake event. The raw ground motion, processed ground motion, earthquake information, station and waveforms metrics, and important intermediate results are grouped by station in HDF5 files. Each ASDF HDF5 file contains (1) Earthquake information (labelled QuakeML in HDF5 file), (2) ground motion records (processed and raw) and the corresponding instrument information at each station (labelled Waveforms), (3) waveform/station metrics, parameters involved for record processing, and important intermediate results (labelled AuxilliaryData), and (4) provenance information following Krischer et al. (2015). More details about the layout of ASDF particularly for the outcomes of USGS gmprocess toolkit are explained in Krischer et al. (2016) and Rekoske et al. (2020).

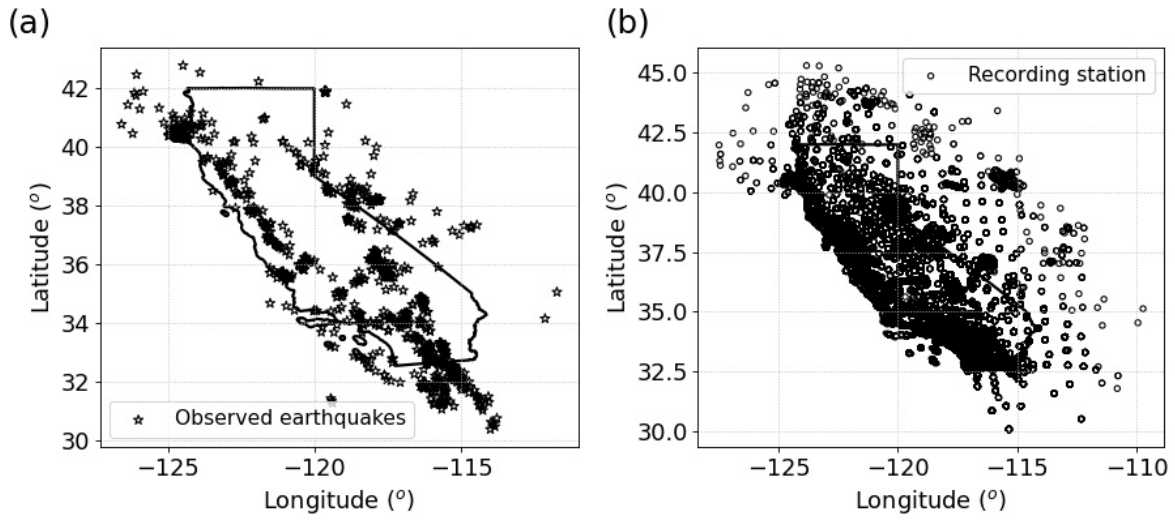


Figure 5.1. Location of (a) earthquake epicenters and (b) ground motion recording stations included in DSGM-CA database.

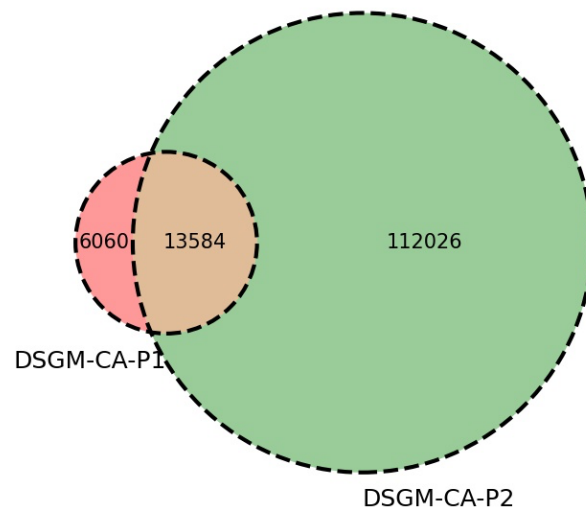


Figure 5.2. Distribution of ground motions included in datasets DSGM-CA-P1 and DSGM-CA-P2.

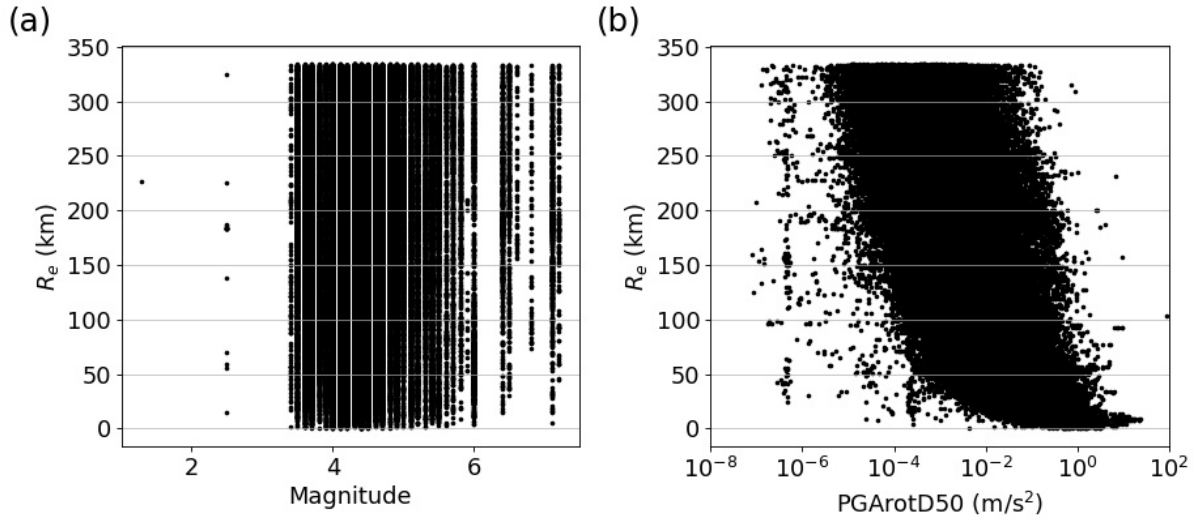


Figure 5.3. Distribution of epicentral distance, magnitude and PGArrotD50 for all records in this work.

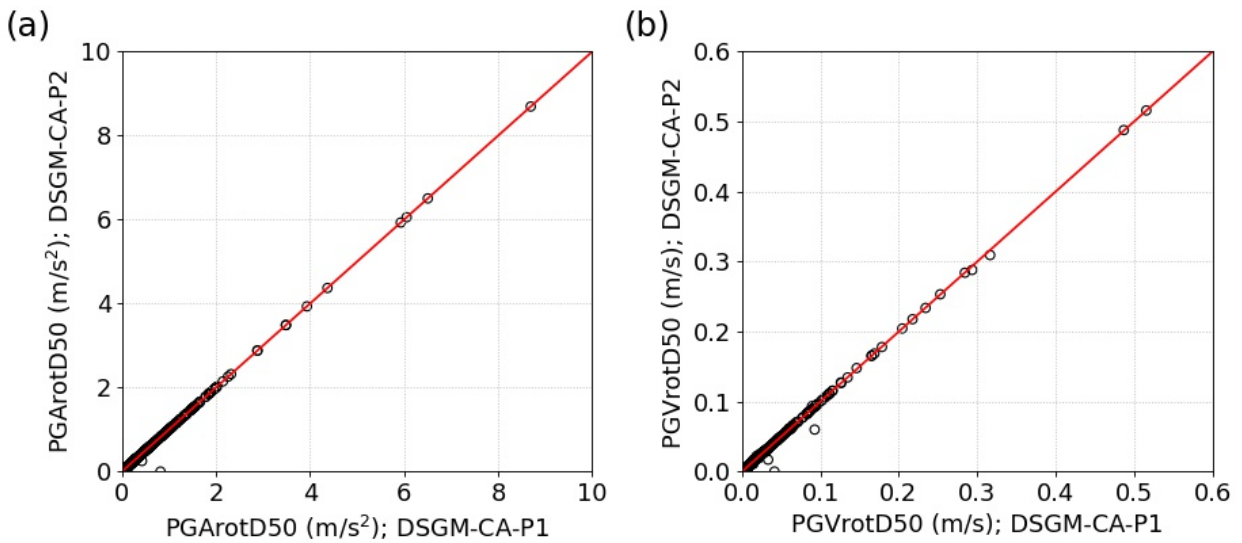


Figure 5.4. Comparisons of (a) PGArrotD50 and (b) PGVrotD50 for duplicated records included in DSGM-CA-P1 and DSGM-CA-P2.

5.5. Site database

We collect shear wave velocity, V_s , compressional wave velocity, V_p , and HVSR values from multiple data providers and include them in DSGM-CA database. Site specific κ_0 values estimated with the whole record (e.g., Cabas et al. 2017; Ji et al., 2020; Mayor et al. 2018; Xu et

al. 2019) and the S-wave window only (e.g., Anderson and Hough 1984) are provided at stations with more than 5 ground motion records suitable for κ computations (i.e., the ground motions pass the record quality checks described later). In general, the site metadata consist of proxy-based and measured V_{s30} (based on geology- and topography-informed proxies by Thompson et al. 2014), V_p and V_s profiles, HVSR information, and site-specific κ_0 values when available.

5.5.1. V_s and V_p dataset and profiles

The S- and P-wave velocities are provided by USGS V_s global model and dataset (Allen and Wald, 2009, Heath et al., 2020, Wald and Allen, 2007, Yong et al., 2015, Thompson et al. 2014), and the UCLA Velocity Profile Database (VSPDB, Kwak et al. 2021). The USGS V_s models and data possess a global proxy-based V_{s30} map and computed V_{s30} values from measured V_s profiles at 4389 sites in the United States (McPhillips et al. 2020). UCLA VSPDB is a global dataset that includes measured V_p or V_s values and wave velocity profiles (Kwak et al. 2021). In this work, a subset of USGS data and the UCLA VSPDB dataset is prepared for California and nearby regions, including (1) proxy-based V_{s30} retrieved from USGS proxy-based V_{s30} model retrieved at the locations of ground motion recording stations in this work, (2) estimated V_{s30} form measured V_s profiles either from USGS dataset or UCLA VSPDB, and (3) measured V_p or V_s profiles from the UCLA VSPDB.

The proxy-based V_{s30} is available at 4911 stations included in this database, and ranges from 11 to 2197 m/s. Values of V_{s30} in water-covered areas is assumed to be 600 m/s. There are 2031 values of V_{s30} based on measured V_s profiles from USGS at stations in or near California ranging from 106 to 2073 m/s. Usually, V_{s30} values are not obtained from measured V_s profiles at the same location of the ground motion recording stations. The distances between any two V_{s30}

measurement sites and ground motion recording stations are computed based on their latitudes and longitudes. With the computed distances, only 107 (out of 2031) V_{s30} values from measured V_s profiles located at ground motion recording stations, which the distance between the V_{s30} measurement site and ground motion recording station is 0 m, in this dataset are identified. Future expansions of the database will include V_{s30} values calculated from measured V_s profiles at nearby sites. Figure 5 shows the location of V_s profiles measured by the USGS (blue circles), and the 107 ground motion recording stations that have a USGS measured V_s profile and corresponding V_{s30} . Most of the stations with available V_s data are located in Southern California (red dots in Figure 5.5).

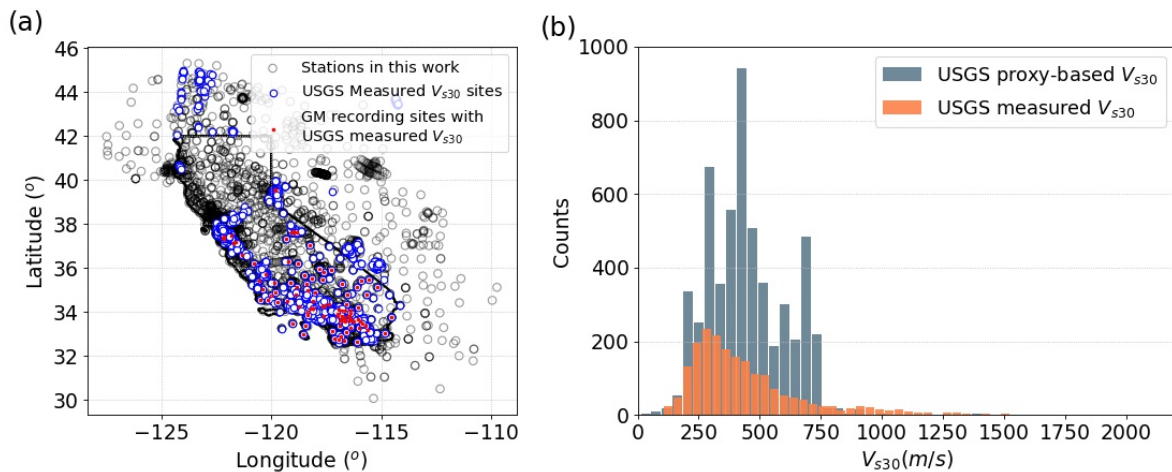


Figure 5.5. (a) Location of recording station used in this work along with available V_s measured profiles, (b) Comparison of the distribution of proxy-based V_{s30} values and their counterparts from measured V_s in the field.

The UCLA VSPDB is a global database providing values of V_{s30} , S- and P-wave velocity profiles. A subset including 347 measured V_{s30} values is extracted from the UCLA VSPDB with field methods (e.g., seismic cone penetration test SCPT, multi-channel analysis of surface waves, MASW, and spectral analysis of surface waves, SASW). Only 29 out of 347 V_{s30}

values within the UCLA VSPDB correspond to ground motion recording station included in DSGM-CA database. The stations with measured V_s or V_p velocity profiles are shown in Figure 6. 1000 stations in UCLA VSPDB have V_s profiles, but only 34 out of those 1000 correspond to recording station locations. Similarly, 587 sites have V_p profiles, but only 6 out of those 587 sites are associated with ground motion recording stations. As shown in Figure 6, UCLA VSPDB stations are mainly located in Southern California and the Bay area.

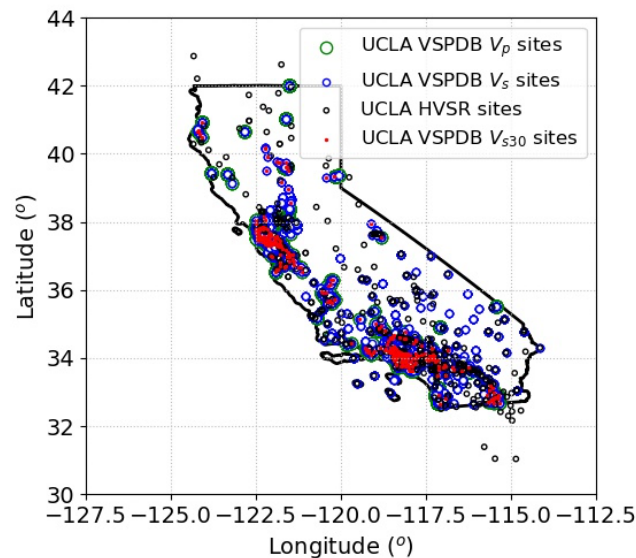


Figure 5.6. Locations of UCLA VSPDB stations included DSGM-CA database. The red dots depict the UCLA VSPDB V_{s30} values from measurements at stations in California; green and blue circles indicate the UCLA VPDB locations where V_p and V_s profiles are available in California, respectively, and the black circles show the location of HVSR measurements from the UCLA VPDB database.

5.5.2. Predominate frequency

The UCLA HVSR database (Wang et al. 2021) provides microtremor-based HVSR data, and the site's predominant frequency (i.e., the frequency corresponding to the maximum

amplitude of the HVSR) is selected with a peak identification algorithm (Wang et al. 2021). A subset of the UCLA HVSR database is extracted, and only the stations with a clearly identified peak frequency are included in DSGM-CA database. Thus, 585 locations with HVSR data are selected from the UCLA HVSR database, but only 81 of them correspond to ground motion recording stations included in this work (see Figure 5.6).

5.5.3. Site-specific κ_0 values

Recently, the site-specific κ_0 started to serve as a site parameter to characterize local site conditions because its capacity to capture near-surface attenuation, which is important for site-specific seismic hazard analysis and site response analysis. However, to authors' knowledge, there is no dataset that publishes site-specific κ_0 . DSGM-CA database provides the site specific κ_0 values for the stations that pass the specific filtering criteria. The classic calculation approach by Anderson and Hough (1984) using the acceleration spectrum (AS) is used herein to compute values of κ_r per horizontal component of ground motion. The average of two horizontal component κ_r values are set as the representative values per record to minimize the effect of ground motion directionality (Ji et al. 2020). A linear regression model as a function of epicentral distance is used to compute values of κ_0 per station as a measure of near-surface attenuation (Cabas et al. 2017). We provide both, site-specific κ_0 computed with the entire time series (which is favored by engineers) and values of κ_0 corresponding to the S-wave window (which is more commonly used in engineering seismology). The onset of the S-wave window is chosen as one sec before the maximum recorded horizontal amplitude. The 5%-75% ground motion significant duration, which intends to capture the body wave energy (Bommer et al. 2009), is set to be the length of the S-wave window per record. Site-specific κ_0 values estimated with the entire time series and the S-wave window follow the same computation procedure.

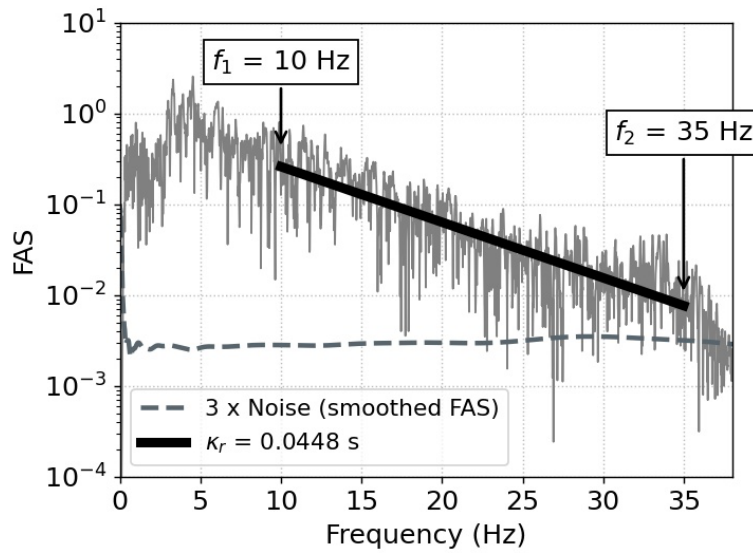


Figure 5.7. An example ground motion for κ_r computation. This ground motion was recorded at NC.MCO from a 2020 Mw 4.6 earthquake in Bodie, California.

Ground motions with epicentral distances less than 150 km, magnitudes larger than 4.5, focal depths less than 35 km and sampling frequencies larger than 50 Hz are used in this work. The PGA values for both horizontal components are less than 0.1 m/s^2 to avoid potential effects of soil nonlinearity (Ji et al. 2021). The usable frequency range is determined based on values of SNR larger than 3.0. The same frequency range is applied for the two horizontal components per record. The lower limit of the selected frequency window is either larger than 10 Hz, which is an equivalent corner frequency for an event with magnitude of 3.5 and stress drop of 10 MPa (Hanks and Kanamori 1979; Edwards et al. 2015), or the minimum usable frequency. The upper limit of frequency band is the minimum value between 35 Hz and the maximum usable frequency. The minimum width of frequency band is set to 10 Hz to improve the robustness of the regression (Ktenidou et al. 2013). Figure 5.7 provides an example ground motion observed at NC.MCO from a 2020 Mw 4.6 earthquake in Bodie, California. The frequency band ([10, 35]

Hz) is applied for this record to compute κ_r , which has the SNR larger than 3.0 and width more than 10 Hz.

A linear distance-dependency model, $\kappa_r = \kappa_0 + R_e \times \kappa_R$, is applied to compute the site-specific κ_0 per station. Sites with more than five κ_r values and an epicentral distance range larger than 75 km for those records are considered suitable for site-specific κ_0 evaluations. Ideally, a larger number of datapoints would benefit the quality of the regression (Ktenidou et al. 2013), but a very limited number of stations in this study had more than five adequate records for κ_r calculations.

Finally, there are 574 stations with site-specific κ_0 estimated from the entire time series, which are mainly located in southern California and the Bay area (Figure 5.8), while 499 sites with site-specific κ_0 values based on S-wave window are provided. The standard deviations and 95% confidence intervals for the path-component kappa associated with regional attenuation (known as κ_R ; the slope of the linear regression of κ_r values and epicentral distances, $\kappa_r = \kappa_0 + R_e \times \kappa_R$) and site-specific κ_0 are included as an electronic supplement. Negative κ_R and κ_0 values are observed at some sites (e.g., 73 stations have negative κ_R computed with the entire time series), which may be caused by (1) statistical uncertainties due to the limited number of usable ground motions per site, (2) the oversimplified linear-distance dependency model, which cannot separate site-specific κ_0 and path-components appropriately (Ji et al. 2021), and (3) uncertainty in κ_r estimates due to multiple factors such as the user-biased computation procedure, site effects in high frequencies, and the limitation and simplification of Anderson and Hough (1984) κ_r model (Ktenidou et al. 2013, Edwards et al. 2015, Ji et al., 2020, 2021, 2022a).

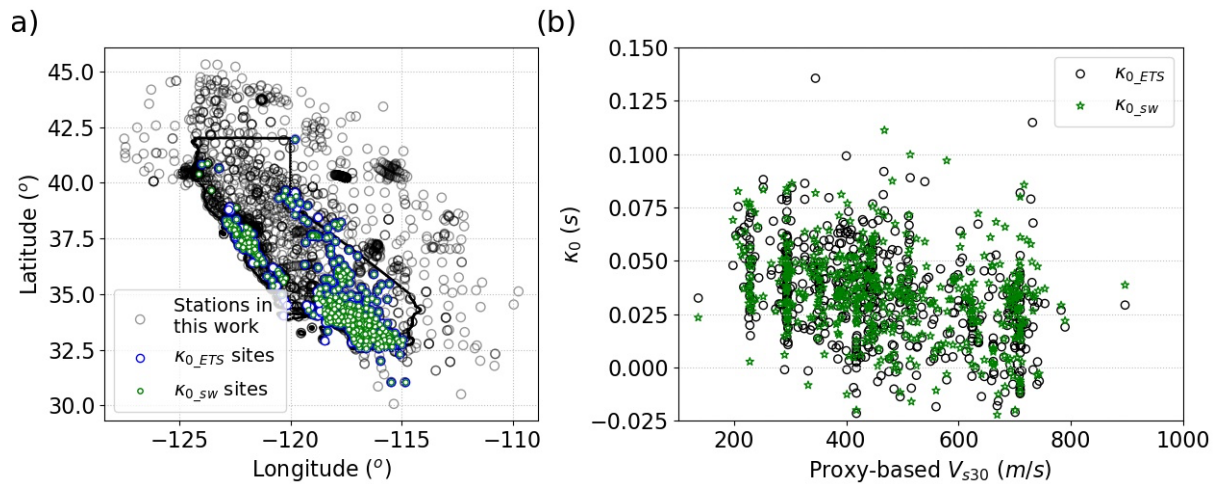


Figure 5.8. (a) Location of stations with site-specific κ_0 values in California and nearby regions, and (b) relationship between entire time series- and S-wave-based κ_0 values with proxy-based V_{s30} at selected stations within this DSGM-CA database.

5.6. Station and waveform metrics

Path measures for each ground motion (e.g., source-to-site distances) and waveform metrics or intensity measures (e.g., response spectrum) are computed with the USGS gmprocess toolkit. Path measures include epicentral, hypocentral, rupture distances (i.e., the closest distance to the rupture plane) and its variance, Joyner-Boore distance and its variance. The derived waveform metrics include PGA, PGV, PGARotD50, PGVrotD50, and PSA are also computed with USGS gmprocess toolkit. The station and waveform metrics are tabulated in the final faltfile attached to this dataset, and complete results are also accessible via HDF5 files per record.

5.7. Summary

A database including ground motions observed in or near California from 1999 to 2021 is provided, which consists of 131670 ground motions observed at 1623 stations from 1253

earthquakes (with magnitudes from 1.3 to 7.2). A site catalog for California is prepared by collecting and reorganizing the available information from USGS (Allen and Wald, 2009; Heath et al., 2020, Wald and Allen, 2007, Yong et al., 2015, Thomas et al. 2014) and UCLA VSPDB (Kwak et al. 2021). The site parameter database (or site metadata) includes (1) proxy-based and estimated V_{s30} values from measured V_s profiles, and V_s/V_p velocity profiles from the USGS V_s data and models as well as from the UCLA VSPDB, (2) site's predominant frequency measured from HVSr data provided by the UCLA HVSr database, and (3) site-specific κ_0 estimated with the entire time series or S-wave windows using an in-house algorithm described in detail in Ji et al. (2021, 2022b, c). The path measures including multiple source-to-site distances and derived ground motion waveform metrics are also included in DSGM-CA. Table 2 summarizes the major parameters involved in DSGM-CA dataset.

Raw and processed ground motions, and other important intermediate information are archived in HDF5 files with the format of ASDF per earthquake event, which are accessible via DesignSafe Platform (the link to access will be updated later). Beside the ground motion records, ground motion and station information are stored as comma-separated values file and attached to this dataset. We provide tabulated files as follows:

1. A complete flatfile with the basic ground motion information (e.g., event ID, time, magnitude, focal depth observed station name, sampling rate, distance, PGA and PGV, USGS proxy-based V_{s30}).
2. A file with PGArrotD50, PGVrotD50, and PSA results.
3. A USGS measured V_{s30} table with the notes if it is a ground motion recording station or not.

4. A UCLA VSPDB V_{s30} measured V_{s30} table with the notes if it is a ground motion recording station or not.
5. A UCLA VSPDB V_s profile table with the notes if it is a ground motion recording station or not.
6. A UCLA VSPDB V_p profile table with the notes if it is a ground motion recording station or not.
7. A UCLA VSPDB HVSR profile table with the notes if it is a ground motion recording station or not.
8. A table documenting the site-specific κ_0 estimated with the entire time series and S-wave window, as well as the corresponding standard deviation and 95% confidence interval of site-specific κ_0 .

Table 5.2. Major information included in this dataset

| | Parameters |
|---------------------|---|
| Station information | Network, station code, station name, and sensor channel Station latitude, longitude, and elevation Proxy-based V_{s30} , and measured V_{s30} , V_p , V_s profiles for applicable stations Predominate frequency for applicable stations Site-specific κ_0 estimated with entire time series or S-wave windows for applicable stations |
| Event information | Magnitude and the corresponding type provided by data provider Focal depth, and epicenter location |
| Record information | Back azimuth Epicentral, hypocentral, rupture and Joyner-Boore distances |

CHAPTER 6. VARIABILITY IN KAPPA (κ_r) ESTIMATED WITH CODA WAVES FOR CALIFORNIA

Based on paper submitted to the 4th International. Conference on Performance-based Design in Earthquake. Geotechnical Engineering (PBD-IV) in Beijing, China:

Ji, C., Cabas, A., Pilz, M. and Kottke, A., Variability in kappa (κ_r) estimated with coda waves for California (under review)

6.1. Abstract

Characterizing and quantifying the effects of local soil conditions are essential for site-specific seismic hazard assessment and site response analysis. The high-frequency spectral decay parameter κ_r and its site-specific component, κ_0 , have gained popularity due to their abilities to characterize near-surface attenuation in situ. Values of κ_0 for rock conditions are of particular interest for site-specific seismic hazard analysis for critical facilities. However, ground motions (GM) recorded at sites underlain by stiff soils or rocks are scarce, which limits the computation of κ_0 values via the classic acceleration spectrum method. Recent research has found that κ values computed using the coda wave of a GM (i.e., the multiple-scattered wave that is less sensitive to the earthquake source and local site effects) can capture regional variations of the attenuation of hard rock materials regardless of the subsurface conditions near the surface. However, there are still large uncertainties in κ estimates based on the coda wave per GM, κ_{r_coda} , associated with the absence of consistent guidelines for the computation procedure and a user-orientated GM processing protocol. This work uses California GMs to examine the variability associated with the computation process of κ_{r_coda} , including the choice of onset of the coda wave and its duration. The objective of this paper is to understand and quantify the variabilities in κ values based on coda waves, which has potentially large implications in its applicability in future ground motion models.

6.2. Introduction

Site-specific seismic assessment and site response analysis require the quantification of the effects of local soil columns on ground motions (GMs), which are a complex function of multiple factors (e.g., the depth to bedrock, the stiffness of the materials, and damping, Kaklamanos et al. 2021). Commonly used site parameters such as the time-averaged shear wave velocity for the top 30 m, V_{s30} , are not able to capture comprehensive effects from shallow and deep soil layers. High-frequency attenuation parameter kappa (κ), which was proposed to describe the linear spectral decay of Shear-wave (S-wave) Fourier Amplitude Spectrum (FAS) in log-linear scale (Anderson and Hough 1984), and its site-specific component κ_0 have been shown to capture near-surface attenuation although there is no agreement about the soil depth captured by κ_0 (Cabas et al. 2017, Ktenidou et al. 2015, 2017). However, the classic acceleration spectrum (AS) approach for κ estimations have limitations for hard-rock sites because of the scarcity of records and potential bias from site amplification in high frequencies. The appropriate characterization of site effects at hard-rock sites is critical for the definition of reference stations, which can enable host-to-target evaluations among seismically active and inactive regions and allow the applicability of ground motion models (GMM) from soft to stiff and hard rock sites (Hashash et al. 2014).

The coda wave, which results from the scattering of S-waves by the heterogeneous lithosphere (Aki and Chouet. 1975, Biswas and Aki 1984, Herraiz and Espinosa 1987), is affected by the Earth's crust properties and it can capture regional attenuation characteristics associated with hard-rock sites (Mayor et al. 2018, Pilz et al. 2019). For example, a regional pattern of the site-specific κ_0 computed with coda waves, κ_{0_coda} , for rock conditions has been observed in Europe (Pilz et al. 2019). However, there are still uncertainties and significant

variability in the κ_r (i.e., κ value measured directly from FAS per record) and κ_0 (Ktenidou et al. 2013, Ji et al, 2020) estimations. Additionally, κ_r computed with coda waves, which is denoted as κ_{r_coda} , is also affected by the definition of the coda wave (i.e., its onset and duration). The objective of this work is to investigate and quantify the influence of the selection of the coda wave onset selection and duration on κ_{r_coda} estimates using GMs from a recording station in California, USA.

6.3. Methods

A Garner Valley Downhole Array (GVDA) station operated by UC Santa Barbara Engineering Seismology network (SB) is selected to explore the variability in κ_{r_coda} associated with the coda wave window pickup. The V_{s30} at the station is 281.5 m/s. Twelve GMs with sampling frequency of 200 Hz are included in this work, which are observed from the events with magnitude larger than 4.0, epicentral distance less than 150 km, and focal depth less than 35 km. The earthquakes involved in this work are queried from the USGS Comprehensive Catalog (ComCat, Guy et al. 2015), and the event IDs are available in Table 1. Although the seismic moment magnitude (M_w) is preferred, other available types of magnitude are used in ComCat query (e.g., local magnitude M_l). Figure 6.1 shows the location of station SB.GVDA, locations of the epicenters of selected earthquakes, and the shear-wave velocity profile at SB.GVDA (Kwak et al., 2021).

Processing of the GMs was performed with USGS gmprocess (Hearne et al. 2019), which is a Python toolkit for GM retrieving and processing. The gmprocess toolkit processes GMs with an automatic protocol and a quality assurance check (Rekoske et al. 2020). The trend and instrument response are corrected per record, and a bandpass filter is applied to remove the

noise. The processed GMs are trimmed 3 sec prior to the P-wave arrival. The usable frequency band (with signal-to-noise ratio (SNR) larger than 3.0) is at least 10 Hz (for each horizontal component). All records have peak ground acceleration (PGA) less than 0.5 m/s^2 to minimize soil nonlinear behavior effects.

The onset of the coda wave should be selected after the end of the S-wave window and the acceleration time series amplitude decay becomes regular. The lapse time, which is twice the S-wave travel time, has been commonly used as the onset of coda wave in previous studies (Sato and Fehler 1998, Biswas and Aki 1984). However, the origin time of earthquake is not available or not reliable for the trimmed GMs in this work. Hence, an equivalent model for the onset of the coda wave proposed (Pilz et al. 2019, Perron et al. 2018) is used in this work:

$$T_c = 2.3 \times (T_s + T_p) + T_s \quad (6.1)$$

where T_c is the onset of the coda wave, T_s and T_p are the onsets of the S-wave and P-wave, respectively. T_s is set to be 1 sec before the maximum horizontal amplitude (Pilz et al. 2019). Visual inspection is necessary to ensure that wave phases are identified appropriately.

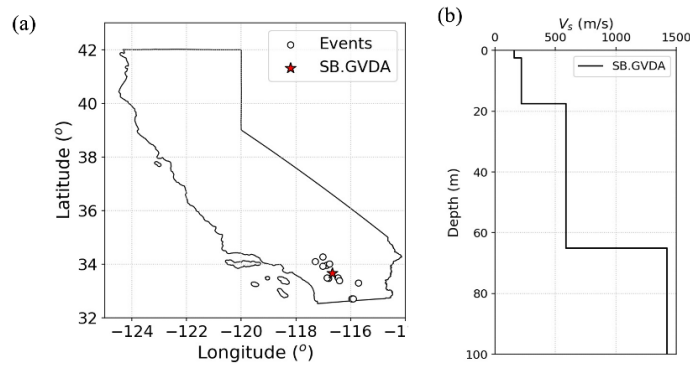


Figure 6.1. (a) Location of SB.GVDA and observed earthquakes, and (b) shear-wave velocity profile at SB.GVDA

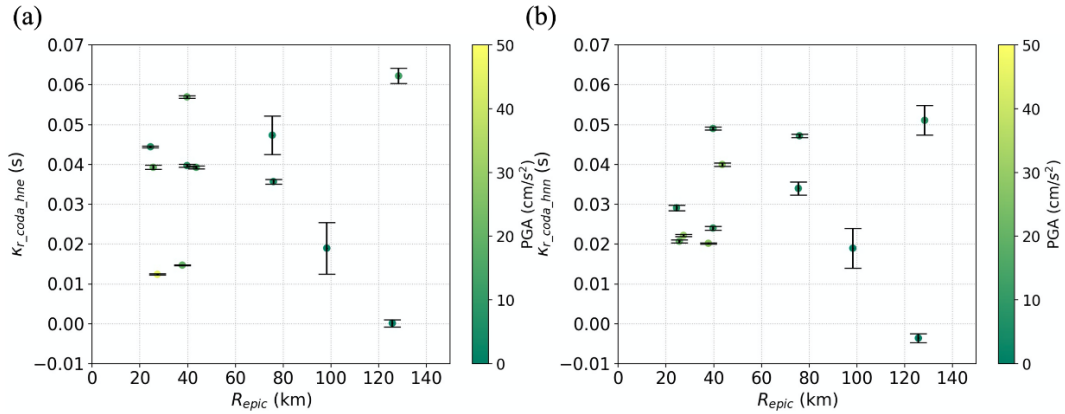


Figure 6.2. Variations of κ_{r_coda} with coda wave durations at SB.GVDA for (a) NS and (b) EW component. The dots show the mean estimate of κ_{r_coda} estimated from coda windows with potential durations, the error bars represent the corresponding σ_κ , and marker colors show the PGA per horizontal component.

To study the influence of coda wave durations on κ_{r_coda} estimates, the onset of coda (i.e., T_c) is fixed and the duration is increased with increments of 1 s. To investigate the effect of coda wave onset, the width of the coda window is fixed to be 20 s and the onset of the coda wave is increased with the interval of 1 s. κ_{r_coda} estimates per horizontal component are computed with the classic AS approach (Anderson and Hough 1984). The same frequency band for the κ_{r_coda} computation is used for coda waves with all possible durations or coda onsets per record to minimize the bias associated with frequency band selections (Perron et al. 2018). The fixed frequency band ($[f_1, f_2]$) is selected with the following criteria: (1) SNR is larger than 3.0, (2) the higher frequency limit is less than 35 Hz with support of visual inspections, and (3) the lower limit of the frequency band is larger than 10 Hz, which is the earthquake corner frequency for magnitude of 3.5 and stress drop of 10 MPa (Hanks and Kanamori 1979). The ordinary least square regression is applied to the FAS over the selected frequency band to compute κ_{r_coda} .

6.4. Results and discussions

The variation in κ_{r_coda} estimates as a function of coda wave durations is shown in Figure 6.1 and Table 6.1. There are at least five coda windows with various widths analyzed per horizontal component. The influence of the coda wave duration on κ_{r_coda} estimates is insignificant for nine out of twelve GMs at the site of interest. The other three records are associated with higher standard deviations (σ_{κ}) for at least one horizontal component. The marker colors represent the corresponding PGA values, and there is no pattern observed between the κ_{r_coda} variations and PGA. To further evaluate the observed scatter in the data, two earthquake GMs, one that is significantly affected by the coda duration, and another one that is not, are selected to inspect their acceleration time series and FAS shapes.

Table 6.1. Variability in κ_{r_coda} as a function of the coda wave durations and coda wave onset for the selected GMs at SB.GVDA

| Event ID | Magnit ude ¹ | R _{epic} (km) | Influence of coda duration | | | | Influence of coda onset | | | |
|------------|-------------------------|------------------------|---------------------------------|------------------------------------|--------------------|-----------------------|-------------------------|-----------------------|--------------------|-----------------------|
| | | | EW component | | NS component | | EW component | | NS component | |
| | | | μ_{κ} ² (s) | σ_{κ} ³ (s) | μ_{κ} (s) | σ_{κ} (s) | μ_{κ} (s) | σ_{κ} (s) | μ_{κ} (s) | σ_{κ} (s) |
| ci15296281 | M _n 4.7 | 27 | 0.0124 | 0.0001 | 0.0222 | 0.0002 | 0.0222 | 0.0026 | 0.0234 | 0.0036 |
| ci37510616 | M _w 4.4 | 38 | 0.0147 | 0.0001 | 0.0202 | 0.0001 | 0.0349 | 0.0069 | 0.0235 | 0.0026 |
| ci37701544 | M _w 4.3 | 98 | 0.0190 | 0.0065 | 0.0190 | 0.0050 | 0.0151 | 0.0156 | 0.0184 | 0.0100 |
| ci14746172 | M _l 4.3 | 126 | 0.0002 | 0.0009 | - | 0.0011 | 0.0056 | 0.0034 | 0.0111 | 0.0017 |
| ci38167848 | M _w 4.5 | 40 | 0.0397 | 0.0004 | 0.0240 | 0.0005 | 0.0124 | 0.0023 | 0.0152 | 0.0012 |
| ci15520985 | M _w 4.6 | 75 | 0.0473 | 0.0048 | 0.0340 | 0.0017 | 0.0328 | 0.0113 | 0.0335 | 0.0016 |
| ci10701405 | M _w 4.5 | 40 | 0.0570 | 0.0003 | 0.0490 | 0.0003 | 0.0487 | 0.0142 | 0.0476 | 0.0074 |
| ci10370141 | M _w 4.5 | 76 | 0.0357 | 0.0006 | 0.0472 | 0.0004 | 0.0380 | 0.0035 | 0.0482 | 0.0076 |
| ci10530013 | M _l 4.3 | 44 | 0.0393 | 0.0004 | 0.0400 | 0.0004 | 0.0223 | 0.0055 | 0.0284 | 0.0050 |
| ci38245496 | M _w 4.4 | 24 | 0.0444 | 0.0002 | 0.0291 | 0.0007 | 0.0518 | 0.0028 | 0.0489 | 0.0112 |
| ci14403732 | M _l 4.1 | 26 | 0.0393 | 0.0005 | 0.0207 | 0.0003 | 0.0385 | 0.0039 | 0.0314 | 0.0066 |
| ci14745580 | M _w 5.7 | 128 | 0.0622 | 0.0019 | 0.0511 | 0.0037 | 0.0278 | 0.0044 | 0.0312 | 0.0051 |

¹M_w: seismic moment magnitude; M_n: Non-standard magnitude method; M_l: local magnitude.

² μ_{κ} : the mean of κ_{r_coda} estimates

³ σ_{κ} : the standard deviation of κ_{r_coda} estimates

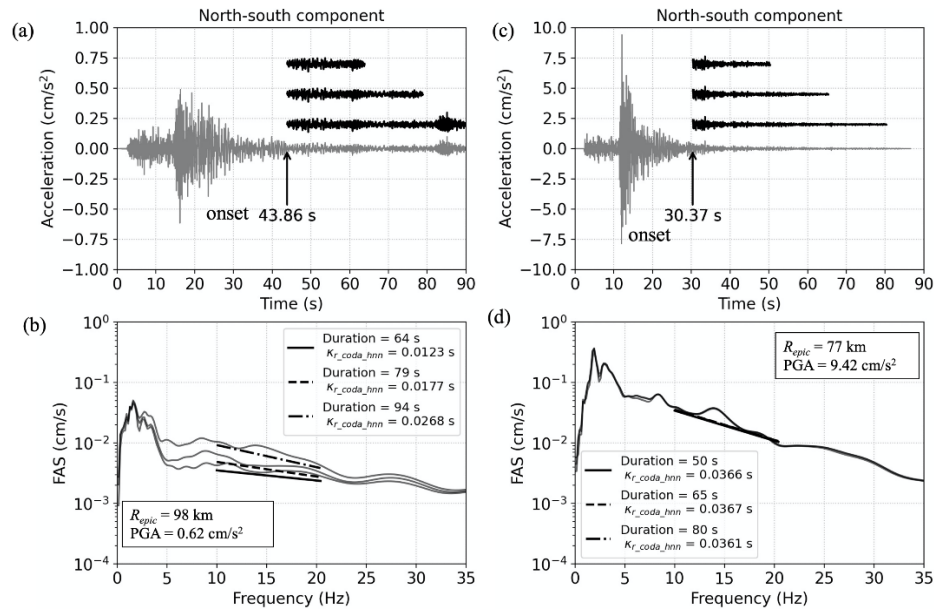


Figure 6.3. Illustrations of coda duration influence on κ_{r_coda} estimates with example GMs (NS component). Three coda windows with different durations are determined with the same onset, and the corresponding FAS and κ_{r_coda} values are plotted (bottom). (a) and (b) are observed from event ci37701544, (c) and (d) are from event ci10370141.

Figure 6.3 shows the acceleration time series and FAS of two example earthquake GMs, where one of them corresponds to event with R_{epic} of 98 km and M_w of 4.3 and the other one to the event with R_{epic} of 77 km and M_w of 4.5. Significant influence of the coda wave window duration (Figure 6.3a) is observed in Figure 6.3b. The σ_{κ} of κ_{r_coda} estimates based on different coda wave window widths is 0.0050 s for the north-south (NS) component shown in Figure 6.3a. In contrast, the σ_{κ} of κ_{r_coda} estimates for the GM shown in Figure 6.3c (event with R_{epic} of 77 km and M_w of 4.5) is 0.0004 s, and little variation of its FAS is observed in Figure 6.3d. Variations in spectral shape observed in Figure 6.3b may be caused by the presence of larger amplitudes of waves at the end of time series (see Figure 6.3a, which could be an artifact due to the noise or disturbance. Figure 6.3c and d provide evidence that the duration of the coda wave

window does not affect κ_{r_coda} estimates significantly (e.g., the FAS shapes are almost the same in high frequencies). Hence, if appropriate GM quality controls are put in place during the processing protocol (including visual inspection to discard GMs with uncommon waveforms), the effect of the selected duration of the coda wave window should have a negligible effect on κ_{r_coda} calculations.

The influence of the onset of the coda wave on κ_{r_coda} estimates is discussed in this section. Table 6.1 and Figure 6.4 show the variations in κ_{r_coda} estimates with the change of three selected onset of the coda wave (i.e., the coda wave onset estimated with Equation (6.1) is increased with increments of 1 sec). The duration of the coda wave window has been fixed to 20 sec for these analyses to isolate the effects of the selected onset. Compared with Figure 6.2, the selection of the onset of the coda wave plays an important role on κ_{r_coda} values. All the selected GMs show a larger σ_{κ} of κ_{r_coda} values resulting from the assumption of different coda windows for at least one horizontal component. No relationship between computed σ_{κ} and PGA or Repic is observed in Figure 6.4. Figure 6.5 shows the time series and FAS for the same GMs displayed in Figure 6.4. Comparing spectral shapes in Figure 6.3 (d) and Figure 6.5 (d) shows that the FAS displays significant changes in high frequencies as a function of the selected onset of the coda wave window.

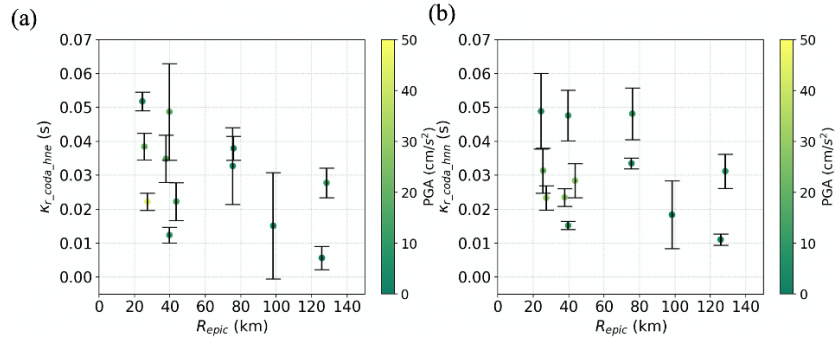


Figure 6.4. Variations of κ_{r_coda} with coda wave onset selections at SB.GVDA for (a) NS and (b) EW component. The dots show the mean estimate of κ_{r_coda} estimates with all moving coda window, the error bars represent the corresponding standard deviation, and marker colors show the PGA per horizontal component.

Earlier onset times, such as $T_c = 30$ s in Figure 6.5b may capture more energetic portions of the time series (e.g., some of S-waves and surface waves), which results in larger amplitude FAS. Further investigation is required to develop recommendations for selections of coda wave onset window to minimize potential bias in κ_{r_coda} values.

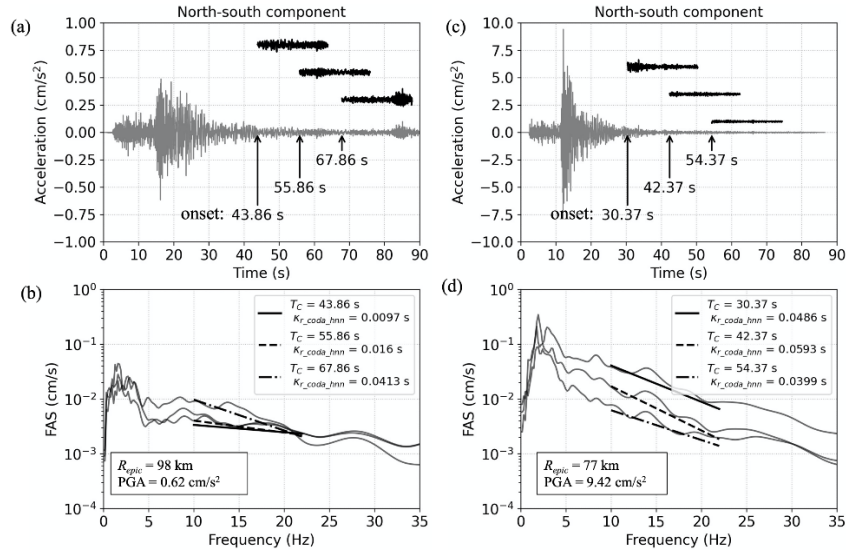


Figure 6.5. Variations of κ_{r_coda} with coda wave onset at SB.GVDA for NS (left) and EW (right) component. The dots show the mean estimate of κ_{r_coda} estimated from coda windows with different start times, the error bars represent the corresponding standard deviation, and marker colors show the PGA per horizontal component.

6.5. Conclusions

This paper studied the influence of the computation procedure on κ_{r_coda} values, particularly the selection of the coda wave window onset and duration. Using a recording station in California (i.e., the Garner Valley Downhole Array) and twelve GMs recordings, the effects of the onset of the coda wave window and its duration were analyzed. We found that, generally, the effect of the coda wave onset selection on κ_{r_coda} estimates were prominent. In contrast, the influence of coda wave durations was negligible. The early stage of coda wave was governed by the angular dependence of scattering and is sensitive to the source radiation pattern, but the latter coda waves are dominated by the multiple scattering of S-waves (Sato and Fehler 1998, Biswas and Aki 1984). Thus, the selection of the coda wave onset implies the explicit consideration (or

lack thereof) of the influence of multiple scattering waves of S-wave and disturbance by surface waves.

Thus, we conclude that identifying the appropriate coda wave is critical for a robust κ_{r_coda} computation. Picking later onsets of the coda wave than the lapse time (i.e., twice the S-wave travel time) could help avoid the potential influence of surface waves. However, the lower amplitude of late portions of the seismogram usually has lower SNR and narrower usable frequency ranges, which introduces additional difficulties for analyses in the Fourier domain (e.g., for κ studies). Since there is no consensus on wave phase identifications yet, the resulting uncertainties in κ_{r_coda} caused by coda wave selection remain unavoidable and require further investigation.

CHAPTER 7. SITE-SPECIFIC NEAR-SURFACE ATTENUATION ESTIMATED WITH CODA WAVES

Based on paper to be submitted to the Bulletin of the Seismological Society of America:

Ji, C., Cabas, A., Pilz, M. and Kottke, A., Site-specific near-surface attenuation estimated with coda waves, Bulletin of the Seismological Society of America (in preparation).

7.1. Abstract

Characterizing attenuation properties of near-surface materials is relevant to advance our understanding of site effects and assess site-specific seismic hazards. Attenuation properties of hard rocks are of particular interest for host-to-target adjustments. The high-frequency spectral attenuation parameter (κ_r) as well as its site-specific component (κ_0) have been the subject of many recent studies because of their ability to describe near surface attenuation. However, the quantification of the contribution of shallow and deep geologic structures to κ_0 values remains a challenge. Analyses of coda waves have shown their independence from earthquake source and local, shallow site conditions, which makes coda waves good candidates to explore attenuation properties of deeper geologic structures (i.e., rock sites). The objective of this work is to compute κ_r and κ_0 with coda waves and evaluate their ability to capture site-specific near-surface attenuation properties associated with hard rock conditions. In this study, we use earthquake ground motions from California and nearby regions to compare values of κ_r and κ_0 based on the acceleration spectrum approach using the entire time series, the S-wave window, and the coda wave window. Although only a limited database of linear ground motions is used in this work, our findings show that κ_0 values from coda waves can describe attenuation properties at stiffer and/or rock sites. The relationship between the κ_r and κ_0 values obtained for different types of waves at softer sites may be obscured by the presence of amplification effects at high frequencies.

7.2. Introduction

There are a few approaches that aim to account for the influence of local site conditions on the estimated seismic hazard at a site of interest. Often, they involve probabilistic seismic hazard analysis (PSHA) performed for reference rock conditions, and a deterministic adjustment to account for site effects. Systematic contributions of the site of interest to the ground motion can be estimated if multiple recordings exist at such location, or if the effects of shallow deposits and deeper geologic structures (i.e. the bedrock) can be accurately modeled. The effect of local site conditions on the characteristics of ground motions is a complex function of multiple factors, such as the depth to bedrock, the stiffness of the materials, and damping (i.e., attenuation properties). Due to soils' nonlinear behavior, seismic site response is also dependent on the level of ground shaking. Multiple parameters have been considered in the literature as site response predictors, mostly based on their ability to capture the aforementioned key properties of the site. Values of the average shear wave velocity over the top 30 m of the site (V_{s30}) provide a measure of the stiffness of near surface materials, while site-specific κ values (i.e., κ_0), as proposed by Anderson and Hough (1984), represent near-surface attenuation characteristics at a site (Ktenidou et al., 2013; 2015, Cabas et al., 2017).

In recent decades, the high-frequency spectral decay parameter κ_r has been used to adjust ground motion models (GMMs) and constrain high frequencies for simulated ground motions (e.g., Boore 2003, Cabas et al., 2015; Laurendeau et al. 2013; Cabas and Rodriguez-Marek 2017). Uncertainty in the estimation of κ_r is still large though (Ktenidou et al., 2014; Ji et al., 2020), and it has important implications for seismic risk assessments; especially at rock sites, where the estimation of the attenuation or damping in the profile is vital to assessing appropriate levels of high-frequency ($> \sim 5$ Hz) design motions. Site attenuation controls the scaling from

soft to hard rock at high frequencies (Cotton et al., 2006), as it governs ground motion characteristics in the high-frequency range at short site-source distances, where crustal damping effects are small (Hashash et al., 2014). This is especially relevant for low-attenuating hard rock sites, where the high-frequency components of the ground motion can be underestimated (Perron et al., 2017). Consequently, adjusting the GMMs to hard-rock conditions is sensitive to κ_0 (Ktenidou et al., 2016). For instance, the Pegasus Refinement Project (Biro and Renault 2012) demonstrated how κ_0 corrections from soft-rock to hard-rock conditions can lead to differences up to a factor of 3 in the high-frequency range of the response spectrum (Ktenidou et al., 2016). Additionally, the estimations of κ_0 values for rock stations at seismically inactive regions are limited by the number of available ground motion and the applicability of the classic approach to compute κ_r from the FAS of recorded ground motions (e.g., Laurendeau et al. 2013; Van Houtte et al., 2014).

Different methodologies to compute κ_0 values or estimate them based on other site parameters such as V_{s30} populate the literature (Ktenidou et al. 2014). Recently, Pilz et al. (2019) captured κ_0 representative of reference rock regional scales by linking individual values of κ and the properties of multiple-scattered coda waves. Coda waves result from the backscattering of body waves due to the presence of heterogeneities of the lithosphere (Aki 1969), averaging the effects of heterogeneities found between the earthquake source and recording stations (Tucker and King 1984, Wang and Shearer 2019). Previous studies have quantified the attenuation of coda waves by means of the seismic quality factor Q (Knopoff 1964), which is hereafter referred to as Q_c . The influences of local site condition and earthquake source characteristics on Q_c are limited and neglectable, which makes them relatively stable within a given region (Aki and Chouet 1975, Rautian and Khalturin 1978, Fehler and Sato 2003, Pilz et al. 2019). Coda

attenuation Q_c , is frequency-dependent and highly affected by the tectonic setting of the region under consideration (Aki and Chouet 1975, Adams and Abercrombie 1998, Mayor et al. 2018).

The objective of this paper is to test the hypothesis that κ estimated with coda waves captures attenuation properties of deep geologic structures within a profile of interest, which can improve characterizations of reference site conditions for site-specific PSHA and host-to-target adjustments to GMMs. A new strong motion database for California and nearby regions called the DSGM-CA database (Ji et al 2022c; in preparation), which includes earthquakes that happened between 1999 and 2021 is used in this study. Values of site-specific κ_0 computed with the entire time series (ETS), the S-wave window (SW) and coda waves are provided at 113 stations using the classic acceleration spectrum approach (Anderson and Hough, 1984) to test the ability of coda waves to describe site-specific attenuation for reference rock conditions at a regional scale. First, this paper summarizes the characteristics of the ground motion database used, followed by a description of the κ_r and κ_0 computation corresponding to different wave types at selected stations. Comparisons among the different κ_r and κ_0 values across multiple local site conditions in the region of study (i.e., California) are then presented, and the benefits and limitations of using coda waves to characterize attenuation properties of deep geologic structures are discussed.

7.3. Database description

A recently created strong ground motion database including events from California and nearby regions between 1999 and 2021 is used in this work (Ji et al 2022a; in preparation). Ground motions in the DSGM-CA database (Ji et al 2022c; in preparation) were processed automatically with the USGS gmprocess toolkit (Hearne et al. 2019). The details regarding the

screening criteria of ground motions and signal processing are described in Ji et al (2022; in preparation; see Chapter 6). The earthquake source and ground motion information (e.g., magnitude and focal depth) are retrieved from the USGS Comprehensive Catalog (ComCat; Guy et al., 2015; last accessed July 2021).

A subset of ground motions from the DSGM-CA database (Ji et al 2022c; in preparation) is selected for this study based on the following screening criteria: (1) epicentral distances less than 150 km, (2) sampling frequency larger than 50 Hz, (3) magnitudes greater than 4.0, (4) the median of geometric mean peak ground acceleration, PGA, values measured from as-recorded orthogonal horizontal components rotated with all potential angles (PGArotD50, Boore 2010) is less than 25 cm/s^2 to avoid soil nonlinearity effects (Ji et al. 2021), and (5) more than five records are available at each site that passed quality checks to ensure the robustness of κ_r estimates (described in the next section). The implementation of the aforementioned criteria results in 113 suitable stations for our study, where the corresponding ground motions also pass visual inspection quality checks about the correlations between κ_r and distance captured by linear distance-dependency model to compute κ_0 . Figure 7.1 shows the locations of selected stations, which are mainly in Southern California.

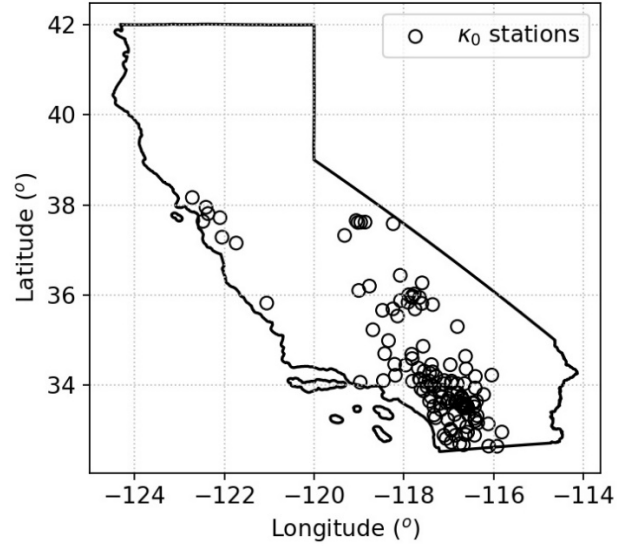


Figure 7.1. Locations of ground motion recording stations selected for κ_r and κ_0 calculations in this study.

7.4. Method

We compute κ values from the entire time series (ETS), the S-wave window (SW) and the coda wave using robust linear regressions to fit the linear trend of the acceleration FAS spectrum. In this section, the determination of the S-wave and coda wave windows is described. The computation procedure and the associated quality check for κ_r values per record, as well as the separation of site-specific κ_0 per site using the classical linear distance-dependency model (Anderson 1991) are also outlined.

7.4.1. Seismic phase windowing

The onset of the S-wave window (T_s) is set to be 1 s before the absolute maximum horizontal amplitude (Pilz et al. 2019). Visual inspections of randomly selected ground motions are implemented to ensure that the T_s is picked appropriately. The maximum and minimum durations of the S-wave window are 30 s and 3 s (Ktenidou et al. 2013), respectively. At least 2 s

are left between the end of the S-wave window and the onset of the coda wave window to avoid the overlap between S-wave and coda window

The onset of the coda-wave window is equivalent to the lapse time, which corresponds to twice of the S-wave travel time between earthquake source and ground motion receiver (Aki 1969, Sato and Fehler 1998). However, the lapse time is not always reliable or available. Perron et al. (2017) proposed an alternative model to estimate the onset of the coda wave (T_c) as a function of T_s and the onset of the P-wave (T_p) as shown below:

$$T_c = 2.3 \times (T_s + T_p) + T_s \quad (7.1)$$

Ji et al. (2022b; Chapter 6) demonstrated that the duration of the coda wave window does not have a strong influence on the resulting κ_r and κ_0 values, but the onset of the coda waves does. Hence, the duration of the coda wave is fixed to be 20 s per record in this study (Pilz et al. 2019). Figure 7.2 provides an example ground motion observed at site NC.MCO from an earthquake with magnitude of 4.6, epicentral distance of 48 km, and focal depth of 9 km to illustrate the selection of the coda wave window. The S-wave and the coda wave windows are highlighted in blue and black coarser lines, respectively.

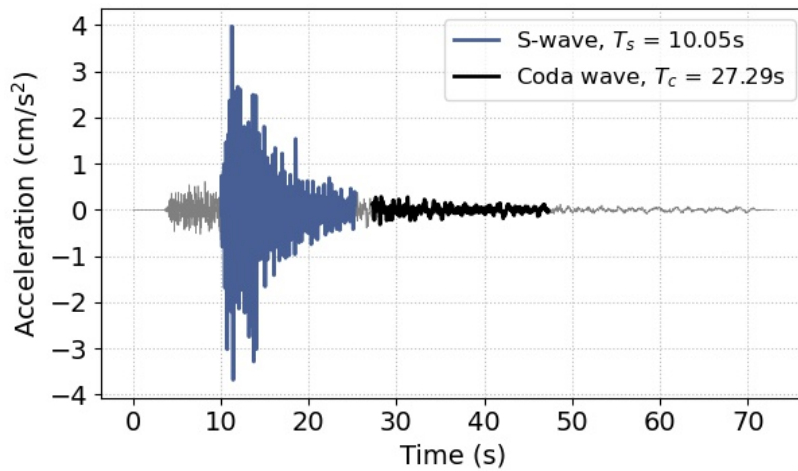


Figure 7.2. An example record to illustrate the seismic wave phase windowing used in this study. This ground motion was recorded at NC.MCO from a 2020 M_w 4.6 earthquake in Bodie, California.

7.4.2. Estimations of κ

κ values corresponding to the entire time series (κ_{r_ets}), the S-wave window, (κ_{r_sw}), and the coda wave window, (κ_{r_coda}) are computed with the classic acceleration spectrum approach (Anderson and Hough 1984). A robust linear regression is applied to fit the linear decay of the unsmoothed acceleration FAS per horizontal component. The arithmetic average of two κ_r values estimated from the orthogonal horizontal components is used for each record to minimize potential ground motion directionality effects (Ji et al., 2020). The same frequency band is applied for all the FAS (i.e., two horizontal ETS FAS, two horizontal SW FAS, and two horizontal coda FAS) to avoid potential bias from the frequency band selection (Perron et al 2017; Edwards et al 2015). The fixed frequency band ($[f_1, f_2]$) is determined based on the usable frequency range, which is defined via signal-to-noise ratios (SNRs) larger than 3.0, within the frequency range between 10 and 35 Hz. The lower limit f_1 is the maximum value among (1) 10 Hz and (2) the minimum frequency with SNR larger than 3.0 for the aforementioned six FAS plots. The upper limit f_2 is the minimum value among (1) 35 Hz and (2) the maximum frequency with SNR larger than 3.0 for the six FAS under consideration. The minimum width of the fixed frequency band is set up to be 10 Hz.

A thorough record screening is implemented to ensure the ground motions used for κ_r computations have high SNRs, and the S-wave and coda wave windows are adequately identified. Thus, four types of errors are identified:

- Error type I-1: Coda wave window less than 20 s.
- Error type I-2: the onset of the S-wave or the coda wave cannot be identified.
- Error type II-1: usable frequency range is less than 10 Hz for any FAS under consideration for a single record (i.e., ETS, SW or coda FAS).

- Error type II-2: fixed frequency band is less than 10 Hz.

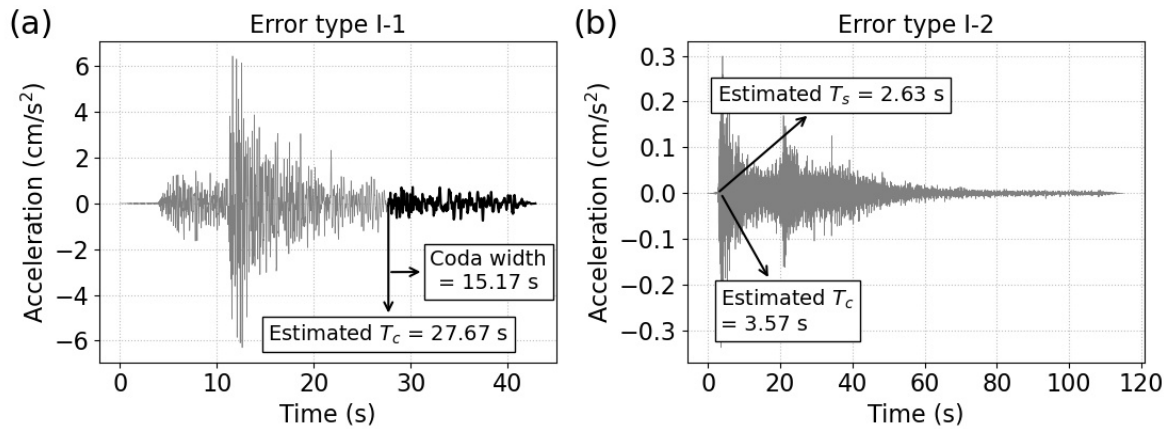


Figure 7.3. Example of (a) Error I-1 and (b) I-2 in ground motions at stations CE.54428 and RE.FRNT, respectively. These ground motions correspond to a 2020 Mw 4.6 earthquake in Bodie, California, and epicentral distances of 53 and 143 km.

Figure 7.3 provides examples for Error types I-1 and I-2 for ground motions observed at stations CE.54428 and RE.FRNT. For the Error type I-1, the onset of coda wave estimated with Equation (7.1) is 27.67 s, and the duration corresponding to the available coda window is 15 s, which is less than the minimum requirement of 20 s. For Error type I-2, it is difficult to identify T_s and T_c . The T_s (i.e., 1 s before the horizontal maximum amplitude) is 2.63 s, which leads to an estimated T_c of 3.57 s. The auto-picked T_s and T_c cannot capture the onset of the S-wave and the coda wave. There are about 50% ground motions included in DSGM-CA database identified as Error types I-1 or I-2.

Examples for Error types II-1 and II-2 for FAS computed based on the ETS (Figure 7.4c and 7.4d) and the coda window (Figure 7.4e and 7.4f) are shown in Figure 7.4. For the Error type II-1, the usable frequency range for coda FAS is narrower than its counterpart corresponding to the ETS. On the other hand, the width of the fixed frequency band for the ground motion

observed at NC.MDH is only 5 Hz (i.e., the Error type II-2). More than 90% ground motions from DSGM-CA dataset are excluded from this work, which highly reduce the availability of records. It could be fixed by improving Usable frequencies for each ground motion horizontal component shown in Figure 7.4 are provided as a function of their SNRs. The minimum frequency for κ_r calculations is set up as 10 Hz, while the maximum frequency corresponds to 15.39 Hz (see Figure 7.4c). This frequency range (i.e., 10-15.39 Hz) is then fixed for all κ_r calculations corresponding to the different types of waves considered in this study.

Figure 7.5 presents an example of κ_{r_ets} , κ_{r_sw} , and κ_{r_coda} computations for a ground motion recorded at station NC.MCO (i.e., the same time series shown in Figure 7.2). The green, blue, and black lines are the fitting lines to the linear decay over the fixed frequency band selected in this case (i.e., 10 Hz to 23.3 Hz). The amplitude of the coda FAS is generally lower than that of the ETS and the S-wave as expected. Similar κ_r values corresponding to the ETS, the S-waves and coda waves are obtained (i.e., 0.0552 s for κ_{r_ETS} , 0.0595 s for κ_{r_sw} , and 0.0532 s for κ_{r_coda}). The proxy-based V_{s30} at this site is 358 m/s (Thompson et al. 2014).

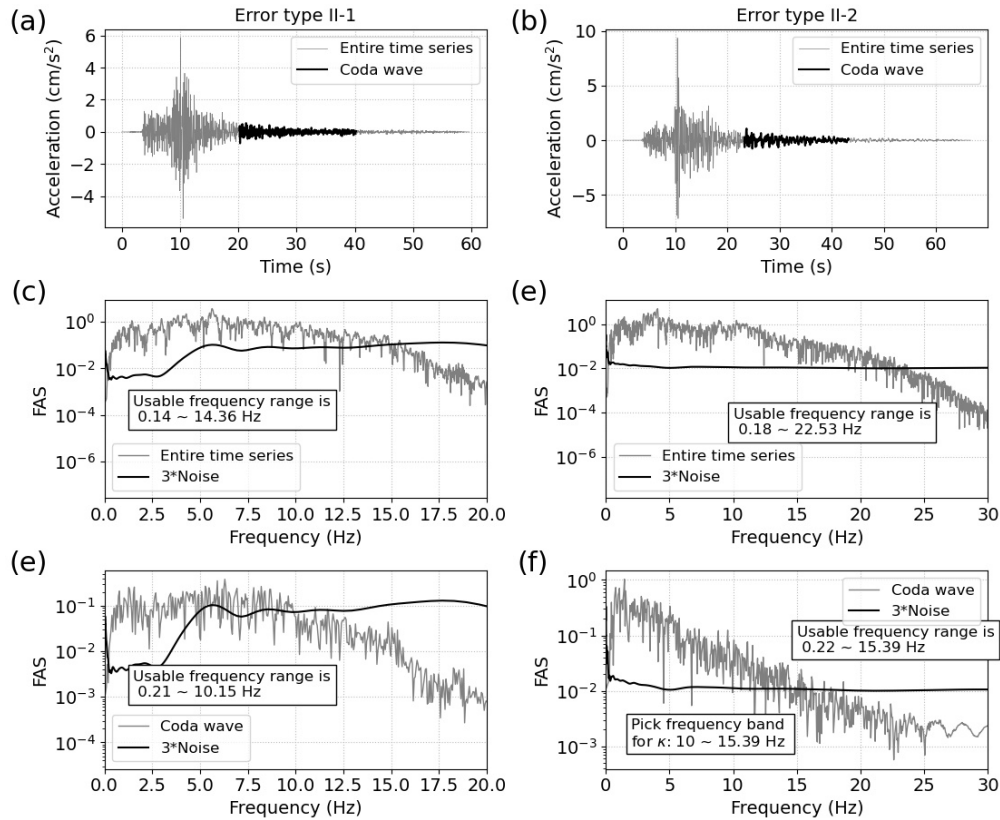


Figure 7.4. Examples of Errors II-1 and II-2 identified in ground motions at stations CE.55157 and NC.MDH. These ground motions correspond to a 2020 Mw 4.6 earthquake in Bodie, California and epicentral distances of 36 and 52 km. The (B) acceleration time series, and the corresponding (c) ETS FAS and (e) coda FAS is east-west component at CE.55157. The (b) acceleration time series, and the corresponding (e) ETS FAS and (f) coda FAS is east-west component at NC.MDH

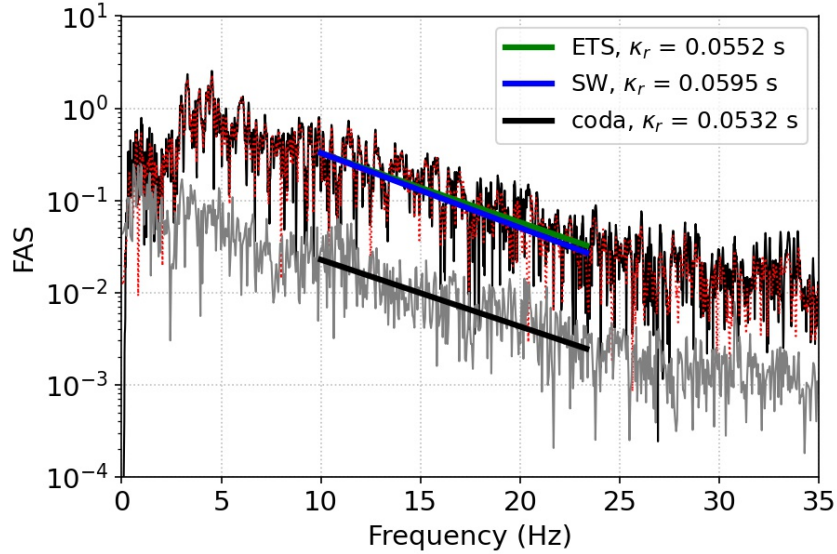


Figure 7.5. An example record for κ_{r_ets} , κ_{r_sw} , and κ_{r_coda} computations. This ground motion is observed at site NC.MCO from a 2020 earthquake with M_w of 4.6. The thin black line shows the ETS FAS, the red dash line is the SW FAS, and the gray line presents the coda FAS.

The classic linear distance-dependency model proposed for kappa (Anderson 1991), $\kappa_r = \kappa_0 + R_e \times \kappa_R$, individual κ_r values are presented as a function of the contributions from a site-specific component (κ_0) and a path component (κ_R). The term R_e refers to epicentral distance in km. A robust linear regression is applied independently to κ_{r_ets} , κ_{r_sw} , and κ_{r_coda} estimates per ground motion pair to fit the linear distance-dependency model. Thus, we find κ_{0_ets} , κ_{0_sw} , and κ_{0_coda} as the corresponding site-specific attenuation components. The path component κ_R is not constrained to be the same for κ_{r_ets} , κ_{r_sw} , and κ_{r_coda} datasets, although it could be assumed that seismic waves considered herein travel through the same ray path from earthquake source to the recording stations.

The seismic quality factor Q (Knopoff 1964) is often used in stochastic modeling (Boore 2003) to represent geometric attenuation. Generally, κ_{r_ets} includes the total attenuation (i.e., scattering, and intrinsic attenuation), while κ_{r_sw} captures the attenuation of the most energetic

part of the ground motion (i.e., the S-waves). The appropriate total Q_t , or S-wave Q_s models are expected to be able to capture the attenuation that takes place during the propagation of seismic waves through the Earth's crust (Ktenidou et al. 2015, Cabas et al. 2017). However, different estimates of Q may correspond to different seismic wave types. Sharma et al. (2007) used ground motion data recorded in Koyna region, India, and found that Q_s is less than Q_c for frequencies below 4 Hz, and Q_s is larger than Q_c for frequencies larger than 4 Hz with. In contrast, Parvez et al. (2012) found that Q_s was less than Q_c for the entire frequency range in the NW-Himalayas. The correlation between Q_s and Q_c models might be frequency- and region-dependent. Considering the relationship between Q and κ_R (e.g., Campbell 2009; Ktenidou et al. 2015; Cabas et al. 2017), we assume that the path component κ_R , should be different for each seismic wave type. Therefore, we relax the constraints for the path component κ_R (i.e., the slope in the linear distance-dependency model) and perform the linear regression for κ_{r_ets} , κ_{r_sw} , and κ_{r_coda} datasets, separately.

7.5. Discussion and Conclusions

First, we compare the individual κ_r values computed with each type of wave window (i.e., ETS, SW and coda windows). There are no systematic trends between κ_{r_ets} and κ_{r_coda} or between κ_{r_sw} , and κ_{r_coda} based on our data. At some stations, κ_{r_coda} values are generally smaller than κ_{r_ets} and κ_{r_sw} values (e.g., station AZ.USGCB; proxy-based $V_{s30} = 399$ m/s, Thompson et al., 2014), and κ_{r_coda} values are generally larger than κ_{r_ets} and κ_{r_sw} values at other stations such as site AZ.CRY, with proxy-based V_{s30} of 624 m/s (Thompson et al., 2014). The κ_{r_ets} , κ_{r_sw} , and κ_{r_coda} datasets for all selected stations are plotted in Figure 7.6 to show the general trend (or lack thereof) among κ_{r_ets} , κ_{r_sw} , and κ_{r_coda} .

Second, the correlations between site-specific κ_0 and other site parameters are explored. Ground motion recording stations in California are operated and maintained by different networks and organizations, hence there is no uniform database of the corresponding site parameters for these sites. Additionally, the measured sites for site parameters (e.g., V_{s30}) are often not collocated with ground motion recording stations. Therefore, a comprehensive subsurface characterization for seismic stations in California is still missing. In this work, the USGS global proxy-based V_{s30} model is used to gain some insights on the local soil conditions in the region. This proxy-based V_{s30} model is based on the work by Thompson et al. (2014). Figure 7.7 shows the comparisons between κ_{0_ets} , κ_{0_sw} , or κ_{0_coda} and USGS proxy-based V_{s30} . The red circles, green triangles, and gray stars present the κ_{0_ets} , κ_{0_sw} , or κ_{0_coda} for the selected 113 stations in this work. Significant scatter is observed from Figure 7.7. Most κ_0 values decrease with increasing proxy-based V_{s30} , but around 700 m/s, multiple deviations for such trend are observed.

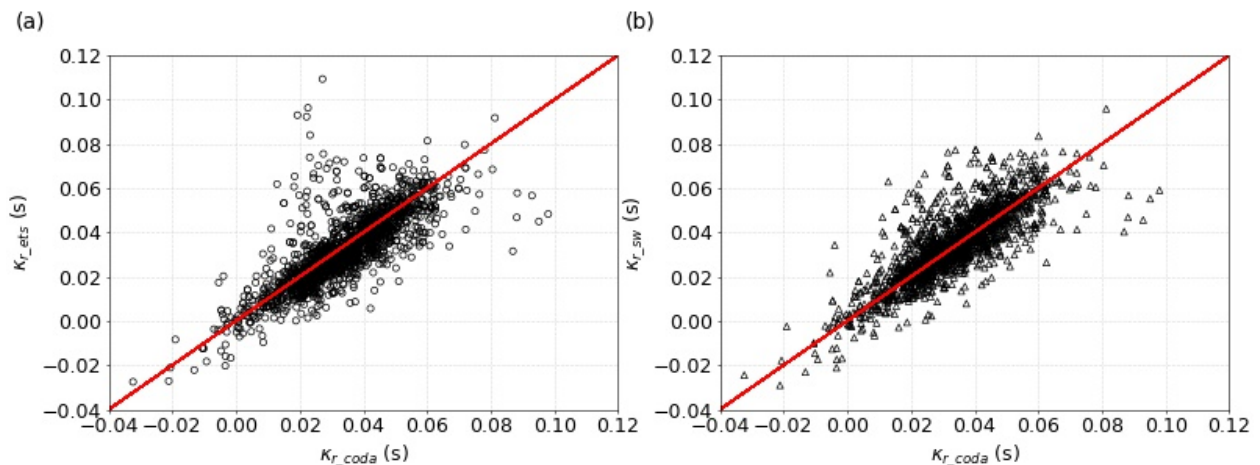


Figure 7.6. Comparisons between (a) κ_{r_ets} and κ_{r_coda} and (b) κ_{r_sw} and κ_{r_coda} datasets, which includes all ground motions observed at the 113 stations with more than 5 suitable records in this work.

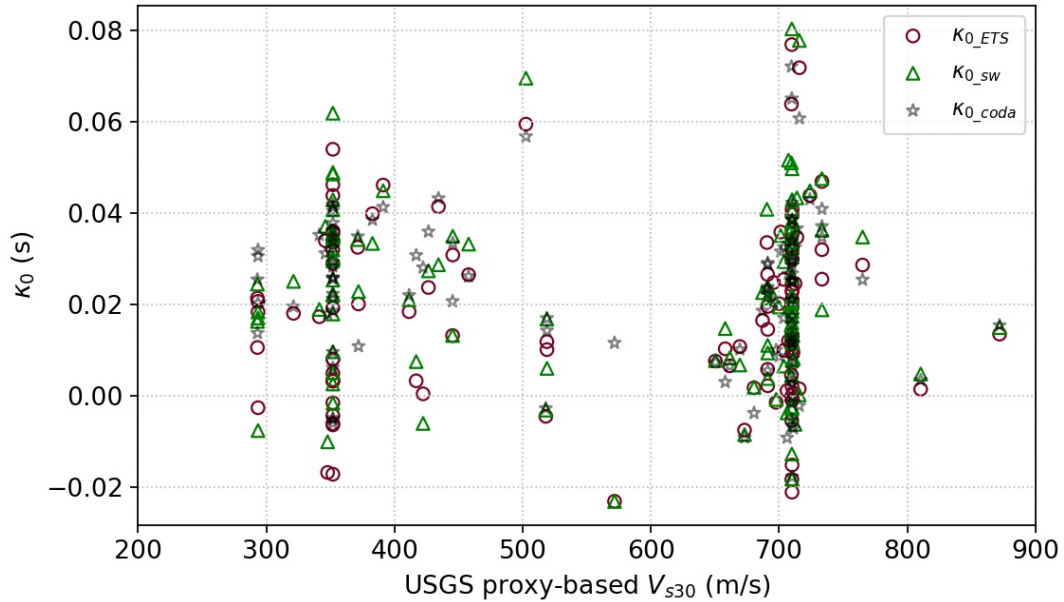


Figure 7.7. Comparisons between site-specific κ_0 and USGS proxy-based V_{s30}

The previously selected 113 stations are separated into three groups based on the USGS proxy-based V_{s30} to evaluate potential bias in our findings as a result of the shallow geologic structures:

- group 1: stations with USGS proxy-based V_{s30} less than 360 m/s (30 sites found)
- group 2: stations with USGS proxy-based V_{s30} between 360 and 700 m/s (32 sites included)
- group 3: stations with USGS proxy-based V_{s30} more than 700 m/s (51 sites included)

Figure 7.8 shows the comparisons between κ_{0_ets} and κ_{0_coda} or between κ_{0_sw} , and κ_{0_coda} for the sites grouped by USGS proxy-based V_{s30} values. At softer sites (i.e., group 1 stations), κ_{0_coda} is larger than κ_{0_ets} , and the correlation between κ_{0_sw} and κ_{0_coda} is not clear. Site amplification at softer sites may be responsible for smaller κ_{0_ets} values. Amplification resonances in the high frequency range may obscure the attenuation effects in that frequency range. Unfortunately, a comprehensive description of the subsurface conditions at the selected

sites in this study was not available by the time of completion of this work. Hence, the presence of site response resonances at high frequencies cannot be confirmed. For group 2 sites, κ_{0_coda} values are generally larger than κ_{0_ets} and κ_{0_sw} . However, better agreements for κ_{0_ets} and κ_{0_coda} or between κ_{0_sw} , and κ_{0_coda} are observed for group 3 stations (i.e., stiff and rock sites), which provides evidence that κ_{0_coda} could capture the attenuation properties of reference rock sites.

In this work, κ values for reference rock conditions using coda waves are explored. The classic acceleration spectrum approach (i.e., Anderson and Hough, 1984) was used to compute individual κ_{r_ets} , κ_{r_sw} , and κ_{r_coda} values per record for the entire time series, the S-wave and the coda window at selected 113 stations. The site-specific κ_0 values are estimated with the linear distance-dependency model (Anderson 1991). The path components κ_R values for κ_{r_ets} , κ_{r_sw} , and κ_{r_coda} datasets are not assumed to be the same and hence, computed separately. We first compare κ_r values estimated with different wave windows. However, no correlations or systematic patterns are observed among κ_{r_ets} , κ_{r_sw} , and κ_{r_coda} . Then, the USGS proxy-based V_{s30} values were used as site parameters to further explore the connections between site-specific κ_0 and local soil conditions. A better agreement between κ_{0_coda} and κ_{0_ets} or κ_{0_sw} is observed for stiffer sites (i.e., the stations with USGS proxy-based V_{s30} larger than 700 m/s). This finding suggests that the κ_{0_coda} can describe the site-specific attenuation properties of reference rock sites, which is critical for the determinations of site-specific κ_0 for reference sites. Additionally, the variations between κ_{0_coda} and κ_{0_ets} or κ_{0_sw} at softer sites hint that local site amplification may bias the characterization of attenuation in the high-frequencies. Further research is needed to quantify local site effects on different seismic wave phases over different frequencies.

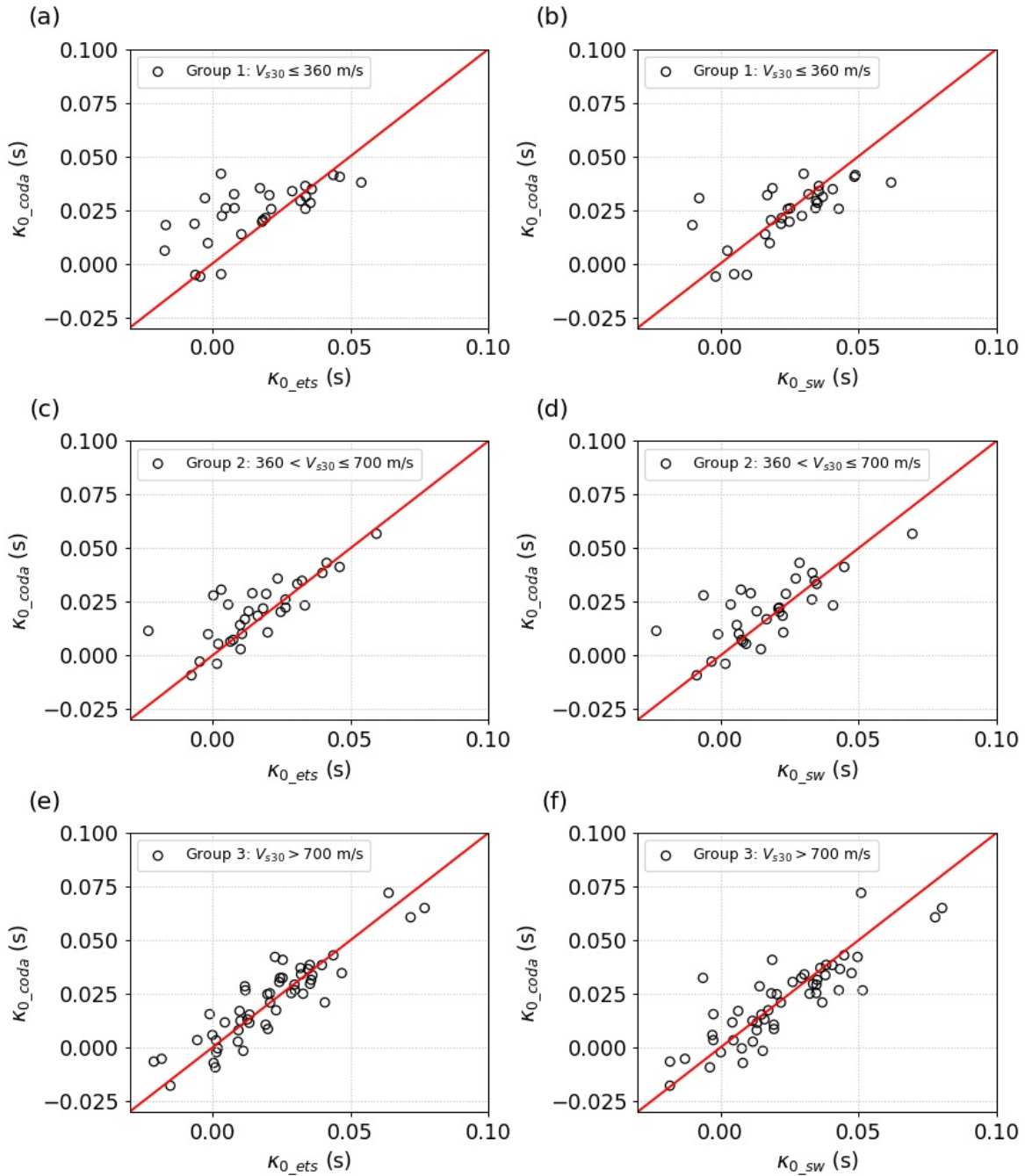


Figure 7.8. Comparisons among κ_{0_ets} , κ_{0_sw} , and κ_{0_coda} values across different V_{s30} -based groups. The stations are grouped using USGS proxy-based V_{s30} values. Group 1 includes the stations with USGS proxy-based V_{s30} less than 360 m/s (a and b), group 2 includes the stations with USGS proxy-based V_{s30} between 360 and 700 m/s (c and d), and group 3 includes the stations with USGS proxy-based V_{s30} more than 700 m/s (e and f).

7.6. Limitations of this work and future research directions

There are still larger uncertainties in the estimation of κ_r values per record. For example, the determination of the coda onset can change the estimations of κ_{r_coda} significantly for the same record (Ji et al 2022). This variability will be investigated via a parametric study in future iterations of this work. Additionally, multiple linear decay trends are observed in the FAS of some records (especially for coda FAS), which contradicts the assumptions of the classical κ_r model proposed by Anderson and Hough (1984) that κ_r is frequency-independent and that there is a unique decaying slope. Second, the lack of available ground motions for coda κ computations (e.g., there are only 113 stations in California with more than five usable ground motions for κ studies). Insufficient number of motions at each station reduces the robustness of site-specific κ_0 values estimated with the oversimplified linear distance-dependency model. Finally, the commonly used linear distance-dependency model cannot separate the site-specific κ_0 and path component κ_R appropriately for some cases. For example, the linear distance-dependency model may not be valid for regions with significant changes in Q . Therefore, an alternative, improved and more flexible model should be developed to account for this challenge and estimate more reliable site-specific κ_0 and path components κ_R .

CHAPTER 8. CONCLUSIONS AND FUTURE WORK

8.1. Conclusions

This work focuses on the characterization and parameterization of site-specific near-surface attenuation with the high-frequency spectral decay parameter κ . The factors that could affect the variability and uncertainty in κ are identified and analyzed, which will enable computations of a more robust site-specific κ_0 at sites of interest. This chapter summarizes the main findings and conclusions of this work.

8.1.1. Within-station variability in κ

A framework of within-station variability in κ is developed, and a logic-tree is provided to illustrate the components that will affect within-station variability. In this chapter, the influence of ground motion directionality and dataset selections are studied. The main findings can be summarized as follows:

- The within-station variability in κ_0 is significant at some sites, which could mask the actual correlations between site-specific κ_0 and site parameters (i.e., between-station variability). Not properly quantifying within-station variability may hinder the application of site-specific κ_0 as a site proxy to parameterize site-specific attenuation in seismic hazard assessment and other applications.
- Ground motion directionality can affect the variability of κ_r at a given station, but this effect could be minimized by using the arithmetic average of two horizontal κ_r as the representative value of a record.
- The earthquake type and focal depth can affect the path component κ_R . A more significant influence on path component κ_R was observed from deep events with

multi-wave propagation paths, and shallow earthquake with larger incidence angle of seismic waves.

8.1.2. Effects of soil nonlinearity on κ

The soil nonlinearity effects on κ_r and site-specific κ_0 are studied and the ability of κ to reflect the onset of soil nonlinearity and its variations is quantified for different site conditions.

The results and discussions from this work can be summarized as follows:

- A conceptual model is proposed to connect the site-specific κ_0 , soil damping ratio, soil deformations and input motion intensity, which could serve as a fundamental model to explore the physics behind κ theoretically.
- Soil nonlinearity can affect both, κ_r and site-specific κ_0 , but this influence is station-dependent.
- For the stations that show their κ values are highly affected by soil nonlinearity, the values of κ_r and predicated κ_0 generally show an increase trend with the increase of PGA or shear-strain index.

8.1.3. Coda wave and κ

The site-specific near-surface attenuation for California estimated with coda waves and characterized by κ_{0_coda} is investigated. Limited by the availability of ground motions in California, only preliminary analysis is presented and findings are summarized as follows:

- Variability in κ_r values estimated with entire time series, S-wave, and coda wave windows are observed. Generally, the differences between κ_{r_ets} and κ_{r_sw} are

insignificant for most records. But the potential correlations between κ_{r_coda} and κ_{r_ets} or κ_{r_sw} are still unclear.

- A better agreement between κ_{0_coda} and κ_{0_ets} or κ_{0_sw} is observed at hard sites, which hints the ability of κ_{0_coda} to capture the pattern of near-surface attenuation for reference rock conditions.

8.2. Limitations and Future work

8.2.1. Soil nonlinearity and κ

Despite we observed that the soil nonlinearity can affect both κ_r and site-specific κ_0 , and this influence is station-dependent, the characteristics and features of the site that will result in a strong influence of soil nonlinear behavior on κ are still not well understood.

This unresolved problem may be caused by multiple factors. First, an efficient way to identify linear and nonlinear ground motions is required. In this work, the shear-strain index (a proxy for soil deformation) and PGA (a measure of input shaking level) are selected to identify nonlinear records with visual inspection per site. This process can be improved to make it more systematic and less subjective. Second, a study of site properties is critical to identify the characteristics of sites whose κ is more sensitive to soil nonlinearity. Third, the assumptions of Anderson and Hough (1984) κ_r model are oversimplified and hard to be satisfied in practice, which can introduce bias to the κ_r estimates. Thus, improvements or even an alternative model is required to compute more reliable κ_r . Finally, to further understand the soil nonlinearity effects on κ_r and pursue in depth studies of the physics behind κ , the correlation of κ_r and site-specific κ_0 with soil dynamic properties such as damping ratio is worth further exploring.

8.2.2. Coda wave and κ for California

There are still a few unresolved issues and questions related to κ values estimated with coda waves for California. First, there are still large uncertainties in κ_{r_coda} and κ_{0_coda} estimates, although the variability in κ_{r_coda} caused by the selection of coda wave were studied in Chapter 6. The lack of understanding of (a) the coda attenuation in both regional and local scales, and (b) the similarities and differences among attenuation mechanisms for coda and S-waves need further investigation. Also, the correlation between local site conditions and site-specific κ_{0_coda} is not evident, and better agreements between site-specific κ_{0_coda} and κ_{0_ets} or κ_{0_sw} at sites with USGS proxy-based V_{s30} larger than 700 m/s should be compared with observations at other stiff sites. The true correlation between site-specific κ_{0_coda} and κ_{0_ets} or κ_{0_sw} could be masked by (a) the discrepancies between the actual V_{s30} in the field and the proxy-based V_{s30} , and (b) the deficiencies of the linear distance-dependency model commonly used to quantify site-specific κ_0 . Finally, a map depicting regional attenuation in California in terms of κ does not exist yet, and it is envisioned to be constructed as a next step based on the work presented in this dissertation. However, the locations and coverage of the selected 113 sites in this work do not provide enough spatial coverage of the region to be able to develop such κ map. Thus, the limitations of the analyses presented in Chapter 7 can be summarized as (1) the availability of limited ground motions suitable for κ_{r_coda} calculations across California (and nearby states), and (2) the oversimplified linear distance-dependency model to compute site-specific κ_0 and path component κ_R .

To address the limited availability of ground motions, a few improvements could be helpful. First, the installation of more ground motion recording stations should be pursued, which will offer tangible mid- and long-term benefits. Second, signal processing protocols could be

revised to avoid discarding good quality ground motions. For example, the DSGM-CA with 131,670 ground motions observed at 1,623 stations is used, but there are only 113 sites with more than 5 ground motions that passed record selection criteria targeting κ_0 calculations. There are 39,355 ground motions selected from 131,670 records based on their magnitude, distance, PGArrotD50 and sampling frequency for κ_r computation. Figure 8.1 shows the distribution of ground motions for these 39,355 ground motions, and there are only 2,996 ground motions observed at 998 stations that passed the quality check for κ computation. The inner pie chart shows the distribution of four types of error observed in records for κ computation. The outside ring indicates the portion of records from DSGM-CA P1 or P2 (see Chapter 7) within each type of errors. It is observed that half of the motions are excluded from this work die to Error type I-1, and it can be solved by re-processing these motions and keeping longer tails for the trimmed motion (to guarantee enough duration of the coda window). Meanwhile, modifying the computation procedure and the selection of frequency bands for the computation of κ is also expected to increase the number of suitable ground motions in this work.

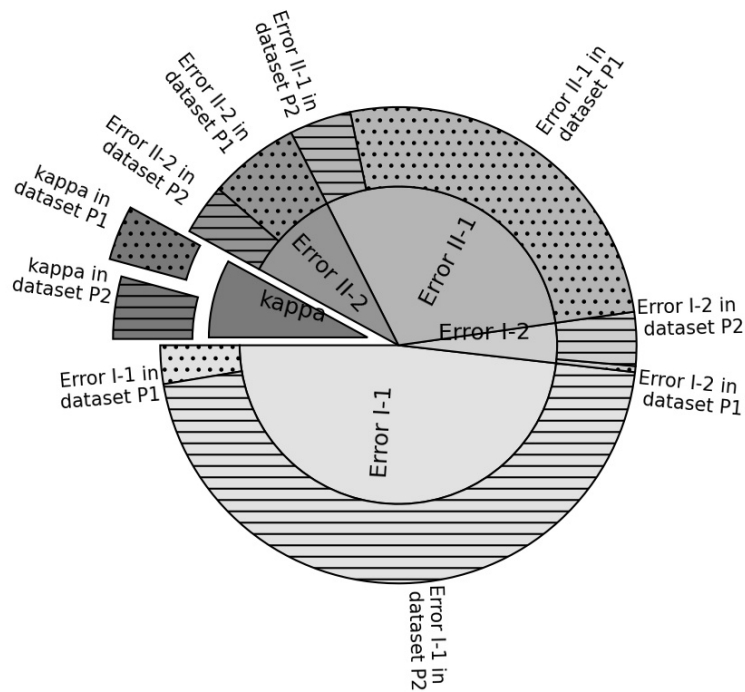


Figure 8.1. Distribution of ground motions for different error types. The patches of lines present the motions included in DSGM-CA P1, and the dot patches presents the motion from DSGM-CA P2 (see Chapter 7 for more details on the composition of the database).

Strict thresholds were put in place to improve the robustness of the empirical regressions (e.g., the simplified linear-distance dependency model requires at least five records with κ values; sites with less than 5 κ_r datapoints were discarded). Meanwhile, the distance range for motions per stations was also constrained to be larger than 30 km and visual inspections were applied. Although there were 2996 ground motions with κ values observed at 998 stations, there were 475 and 185 sites with one or two ground motions (see Figure 8.2). To include more stations, an alternative approach for linear distance dependency κ model is required. Q values have been used to estimate the path component κ_R estimates in previous studies (e.g., Ktenidou et al. 2015, Cabas et al. 2017, Van Houtte et al. 2018). Q-informed κ_R is expected to capture the

regional attenuation, to avoid the limitation of the statistical regression, and to allow the stations with only three or four motions to be considered in the analysis. It should be noted that the selection of an appropriate Q value (total Q, scattering Q, S-wave Q or coda Q) and incorporating 2D or 3D Q models into regional attenuation models are not trivial tasks and they will require further investigation.

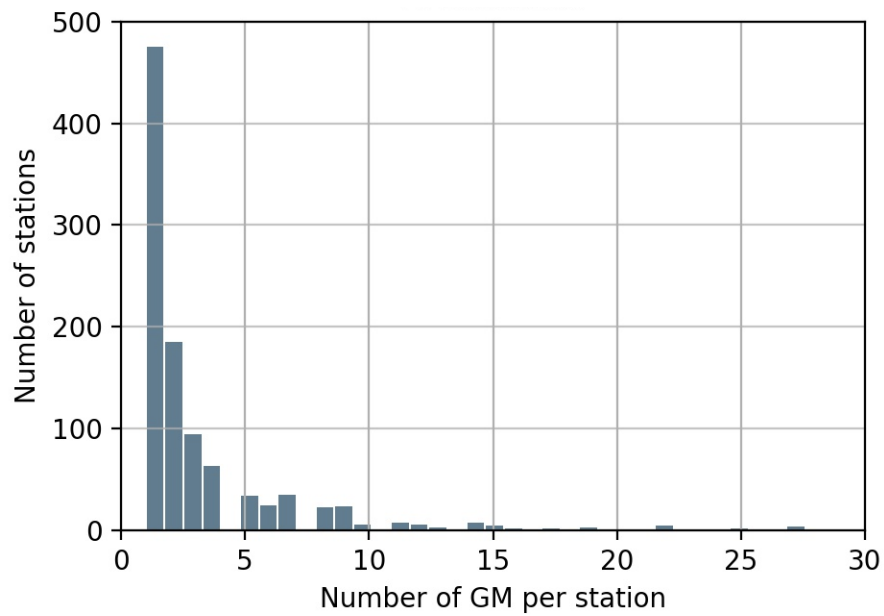


Figure 8.2. Histogram for the number of ground motions with κ values per station.

REFERENCES

- Adams, D. A., & Abercrombie, R. E. (1998). Seismic attenuation above 10 Hz in southern California from coda waves recorded in the Cajon Pass borehole. *Journal of Geophysical Research: Solid Earth*, 103(B10), 24257-24270.
- Aki, K. (1969). Analysis of the seismic coda of local earthquakes as scattered waves. *Journal of geophysical research*, 74(2), 615-631.
- Aki, K., & Chouet, B. (1975). Origin of coda waves: source, attenuation, and scattering effects. *Journal of geophysical research*, 80(23), 3322-3342.
- Aki, K. (1980). Attenuation of shear-waves in the lithosphere for frequencies from 0.05 to 25 Hz. *Physics of the Earth and Planetary Interiors*, 21(1), 50-60.
- Al Atik, L., Abrahamson, N., Bommer, J. J., Scherbaum, F., Cotton, F., & Kuehn, N. (2010). The variability of ground-motion prediction models and its components. *Seismological Research Letters*, 81(5), 794-801.
- Al Atik, L., Kottke, A., Abrahamson, N., & Hollenback, J. (2014). Kappa (κ) scaling of ground-motion prediction equations using an inverse random vibration theory approach. *Bulletin of the Seismological Society of America*, 104(1), 336-346.
- Anderson, J. G., & Hough, S. E. (1984). A model for the shape of the Fourier amplitude spectrum of acceleration at high frequencies. *Bulletin of the Seismological Society of America*, 74(5), 1969-1993.
- Anderson, J.G., (1991). A preliminary descriptive model for the distance dependence of the spectral decay parameter in southern California. *Bulletin of the Seismological Society of America*, 81(6), pp.2186-2193.

- Ancheta, T. D., Darragh, R. B., Stewart, J. P., Seyhan, E., Silva, W. J., Chiou, B. S., & Donahue, J. L. (2013). Peer nga-west2 database.
- Allen, T. I., & Wald, D. J. (2009). On the use of high-resolution topographic data as a proxy for seismic site conditions (VS 30). *Bulletin of the Seismological Society of America*, 99(2A), 935-943.
- Aoi, S., Kunugi, T., & Fujiwara, H. (2004). Strong-motion seismograph network operated by NIED: K-NET and KiK-net. *Journal of Japan association for earthquake engineering*, 4(3), 65-74.
- Aoi, S., Kunugi, T., Nakamura, H., & Fujiwara, H. (2011). Deployment of new strong motion seismographs of K-NET and KiK-net. In *Earthquake data in engineering seismology* (pp. 167-186). Springer, Dordrecht.
- Baltay, A. S., Hanks, T. C., & Abrahamson, N. A. (2017). Uncertainty, variability, and earthquake physics in ground-motion prediction equations. *Bulletin of the Seismological Society of America*, 107(4), 1754-1772.
- Bahrampouri, M., Rodriguez-Marek, A., Shahi, S., & Dawood, H. (2021). An updated database for ground motion parameters for KiK-net records. *Earthquake Spectra*, 37(1), 505-522.
- Biasi, G. P., and K. D. Smith (2001). Site Effects for Seismic Monitoring Stations in the Vicinity of Yucca Mountain, Nevada, MOL20011204.0045, a report prepared for the US DOE/ University and Community College System of Nevada (UCCSN) Cooperative Agreement.
- Biro, Y., & Renault, P. (2012, September). Importance and impact of host-to-target conversions for ground motion prediction equations in PSHA. In *Proc. of the 15th World Conference on Earthquake Engineering* (pp. 24-28).

- Biswas, N. N., & Aki, K. (1984). Characteristics of coda waves: central and southcentral Alaska. *Bulletin of the Seismological Society of America*, 74(2), 493-507.
- Bonilla, L. F., Tsuda, K., Pulido, N., Régnier, J., & Laurendeau, A. (2011). Nonlinear site response evidence of K-NET and KiK-net records from the 2011 off the Pacific coast of Tohoku Earthquake. *Earth, planets and space*, 63(7), 785-789.
- Bonilla, L. F., Guéguen, P., & Ben-Zion, Y. (2019). Monitoring coseismic temporal changes of shallow material during strong ground motion with interferometry and autocorrelation. *Bulletin of the Seismological Society of America*, 109(1), 187-198.
- Bonilla, L. F., & Ben-Zion, Y. (2021). Detailed space–time variations of the seismic response of the shallow crust to small earthquakes from analysis of dense array data. *Geophysical Journal International*, 225(1), 298-310.
- Boness, N. L., & Zoback, M. D. (2004). Stress-induced seismic velocity anisotropy and physical properties in the SAFOD Pilot Hole in Parkfield, CA. *Geophysical Research Letters*, 31(15).
- Boore, D. M. (2003). Simulation of ground motion using the stochastic method. *Pure and applied geophysics*, 160(3), 635-676.
- Boore, D. M., Watson-Lamprey, J., & Abrahamson, N. A. (2006). Orientation-independent measures of ground motion. *Bulletin of the seismological Society of America*, 96(4A), 1502-1511.
- Boore, D. M. (2010). Orientation-independent, nongeometric-mean measures of seismic intensity from two horizontal components of motion. *Bulletin of the Seismological Society of America*, 100(4), 1830-1835.

- Boore, D. M., & Campbell, K. W. (2017). Adjusting central and eastern North America ground-motion intensity measures between sites with different reference-rock site conditions. *Bulletin of the Seismological Society of America*, 107(1), 132-148.
- Bommer, J. J., & Abrahamson, N. A. (2006). Why do modern probabilistic seismic-hazard analyses often lead to increased hazard estimates?. *Bulletin of the Seismological Society of America*, 96(6), 1967-1977.
- Bommer, J. J., Stafford, P. J., & Alarcón, J. E. (2009). Empirical equations for the prediction of the significant, bracketed, and uniform duration of earthquake ground motion. *Bulletin of the Seismological Society of America*, 99(6), 3217-3233.
- Bonamassa, O., & Vidale, J. E. (1991). Directional site resonances observed from aftershocks of the 18 October 1989 Loma Prieta earthquake. *Bulletin of the Seismological Society of America*, 81(5), 1945-1957.
- Bonamassa, O., Vidale, J. E., Houston, H., & Schwartz, S. Y. (1991). Directional site resonances and the influence of near-surface geology on ground motion. *Geophysical Research Letters*, 18(5), 901-904.
- Brune, J. N. (1970). Tectonic stress and the spectra of seismic shear waves from earthquakes. *Journal of geophysical research*, 75(26), 4997-5009.
- Brune, J. N. (1971). Correction to tectonic stress and the spectra of seismic shear waves from earthquakes. *J. geophys. Res.*, 76(20), 5002.
- Cabas, A., & Rodriguez-Marek, A. (2017). VS- κ 0 correction factors for input ground motions used in seismic site response analyses. *Earthquake Spectra*, 33(3), 917-941.

- Cabas, A., Rodriguez-Marek, A., & Bonilla, L. F. (2017). Estimation of site-specific kappa (κ_0)-consistent damping values at KiK-net sites to assess the discrepancy between laboratory-based damping models and observed attenuation (of seismic waves) in the field. *Bulletin of the Seismological Society of America*, 107(5), 2258-2271.
- Cabas, A., & Rodriguez-Marek, A. (2018). Toward Improving Damping Characterization for Site Response Analysis. In *Geotechnical Earthquake Engineering and Soil Dynamics V: Seismic Hazard Analysis, Earthquake Ground Motions, and Regional-Scale Assessment* (pp. 648-657). Reston, VA: American Society of Civil Engineers.
- Campbell, K. W. (2003). Prediction of strong ground motion using the hybrid empirical method and its use in the development of ground-motion (attenuation) relations in eastern North America. *Bulletin of the Seismological Society of America*, 93(3), 1012-1033.
- Campbell, K. W. (2009). Estimates of shear-wave Q and κ_0 for unconsolidated and semiconsolidated sediments in Eastern North America. *Bulletin of the Seismological Society of America*, 99(4), 2365-2392.
- Cotton, F., Scherbaum, F., Bommer, J. J., & Bungum, H. (2006). Criteria for selecting and adjusting ground-motion models for specific target regions: Application to central Europe and rock sites. *Journal of Seismology*, 10(2), 137-156.
- Chandra, J., Guéguen, P. and Bonilla, L.F., (2014). Application of PGV/VS proxy to assess nonlinear soil response—from dynamic centrifuge testing to Japanese K-NET and KiK-net data. In *Second European Conference on Earthquake Engineering and Seismology*, Istanbul Aug (pp. 25-29).

- Chandra, J., Guéguen, P., Steidl, J. H., & Bonilla, L. F. (2015). In situ assessment of the $G-\gamma$ curve for characterizing the nonlinear response of soil: Application to the Garner Valley downhole array and the wildlife liquefaction array. *Bulletin of the Seismological Society of America*, 105(2A), 993-1010.
- Chandra, J., Gueguen, P., & Bonilla, L. F. (2016). PGA-PGV/Vs considered as a stress-strain proxy for predicting nonlinear soil response. *Soil dynamics and earthquake engineering*, 85, 146-160.
- Darendeli, M. B. (2001). Development of a new family of normalized modulus reduction and material damping curves. The university of Texas at Austin.
- Darragh, R. B., & Shakal, A. F. (1991). The site response of two rock and soil station pairs to strong and weak ground motion. *Bulletin of the Seismological Society of America*, 81(5), 1885-1899.
- Dawood, H. M., Rodriguez-Marek, A., Bayless, J., Goulet, C., & Thompson, E. (2016). A flatfile for the KiK-net database processed using an automated protocol. *Earthquake Spectra*, 32(2), 1281-1302.
- Douglas, J., Gehl, P., Bonilla, L. F., & Gélis, C. (2010). A κ model for mainland France. *Pure and applied geophysics*, 167(11), 1303-1315.
- Douglas, J., & Boore, D. M. (2011). High-frequency filtering of strong-motion records. *Bulletin of Earthquake Engineering*, 9(2), 395-409.
- Dimitriu, P., Theodulidis, N., Hatzidimitriou, P., & Anastasiadis, A. (2001). Sediment non-linearity and attenuation of seismic waves: a study of accelerograms from Lefkas, western Greece. *Soil dynamics and earthquake engineering*, 21(1), 63-73.

- Durward, J. A., Boore, D. M., Joyner, W. B., Durward, J. A., Boore, D. M., & Joyner, W. B. (1996). The amplitude dependence of high-frequency spectral decay: constraint on soil nonlinearity. In Proc, of the International Workshop on Site Response Subjected to Strong Earthquake Motions (pp. 82-103).
- Drouet, S., Cotton, F., & Guéguen, P. (2010). V_{s30} , κ , regional attenuation and M_w from accelerograms: Application to magnitude 3–5 French earthquakes. *Geophysical Journal International*, 182(2), 880-898.
- Edwards, B., Ktenidou, O. J., Cotton, F., Abrahamson, N., Van Houtte, C., & Fäh, D. (2015). Epistemic uncertainty and limitations of the κ_0 model for near-surface attenuation at hard rock sites. *Geophysical Journal International*, 202(3), 1627-1645.
- Fehler, M., & Sato, H. (2003). *Coda*. *Pure and applied geophysics*, 160(3), 541-554.
- Fujiwara, H., Aoi, S., Kunugi, T., & Adachi, S. (2004). Strong-motion Observation Networks of NIED: K-NET and KiK-net. *Cosmos Report*.
- Garcia, D., Wald, D. J., & Hearne, M. G. (2012). A global earthquake discrimination scheme to optimize ground-motion prediction equation selection. *Bulletin of the Seismological Society of America*, 102(1), 185-203.
- Gann, C., Ji, C., and Cabas A. (2022) Kappa-compatible Damping for Nonlinear Site Response Analysis. Proceedings from ASCE GeoCongress 2022, Charlotte, North Carolina (accepted)
- Guy, M. R., Patton, J. M., Fee, J., Hearne, M., Martinez, E. M., Ketchum, D. C., ... & Schwarz, S. (2015). National Earthquake Information Center systems overview and integration. US Department of the Interior, US Geological Survey.

- Guéguen, P., Bonilla, L. F., & Douglas, J. (2019). Comparison of soil nonlinearity (in situ stress–strain relation and G/G max reduction) observed in strong-motion databases and modeled in ground-motion prediction equations. *Bulletin of the Seismological Society of America*, 109(1), 178-186.
- Haendel, A., Anderson, J. G., Pilz, M., & Cotton, F. (2020). A frequency-dependent model for the shape of the Fourier amplitude spectrum of acceleration at high frequencies. *Bulletin of the Seismological Society of America*, 110(6), 2743-2754.
- Hanks, T. C., & Kanamori, H. (1979). A moment magnitude scale. *Journal of Geophysical Research: Solid Earth*, 84(B5), 2348-2350.
- Hashash, Y. M., Kottke, A. R., Stewart, J. P., Campbell, K. W., Kim, B., Moss, C., ... & Silva, W. J. (2014). Reference rock site condition for central and eastern North America. *Bulletin of the Seismological Society of America*, 104(2), 684-701.
- Herraiz, M., & Espinosa, A. F. (1987). Coda waves: a review. *Pure and applied geophysics*, 125(4), 499-577.
- Hearne, M., E. M. Thompson, H. Schovanec, J. Rekoske, B. T. Aagaard, and C. B. Worden (2019). USGS automated ground motion processing software, USGS Software Release, doi: 10.5066/P9ANQXN3.
- Heath, D. C., Wald, D. J., Worden, C. B., Thompson, E. M., & Smoczyk, G. M. (2020). A global hybrid VS 30 map with a topographic slope–based default and regional map insets. *Earthquake Spectra*, 36(3), 1570-1584.
- Hough, S. E., Anderson, J. G., Brune, J., Vernon III, F., Berger, J., Fletcher, J., ... & Baker, L. (1988). Attenuation near Anza, California. *Bulletin of the Seismological Society of America*, 78(2), 672-691.

- Idriss, I. M., Dobry, R., & Singh, R. D. (1978). Nonlinear behavior of soft clays during cyclic loading. *Journal of the Geotechnical Engineering Division*, 104(12), 1427-1447.
- Ishibashi, I., & Zhang, X. (1993). Unified dynamic shear moduli and damping ratios of sand and clay. *Soils and foundations*, 33(1), 182-191.
- Ji, C., Cabas, A., Cotton, F., Pilz, M., & Bindi, D. (2020). Within-station variability in kappa: Evidence of directionality effects. *Bulletin of the Seismological Society of America*, 110(3), 1247-1259.
- Ji, C., Cabas, A., Bonilla, L. F., & Gelis, C. (2021). Effects of Nonlinear Soil Behavior on Kappa (κ): Observations from the KiK-Net Database. *Bulletin of the Seismological Society of America*. doi: <https://doi.org/10.1785/0120200286>
- Ji, C., Cabas, A., Bonilla, L.F. and Gelis, C. (2022a), Variability in kappa: contributions from the computation procedure, 2022 Proceedings from ASCE GeoCongress 2022, Charlotte, North Carolina (accepted).
- Ji, C., Cabas, A., Pilz, M. and Kottke, A. (2022b), Variability in kappa (κ_r) estimated with coda waves for California, 2022 4th International. Conference on Performance-based Design in Earthquake. *Geotechnical Engineering (PBD-IV)* in Beijing, China (under review).
- Ji, C., Cabas, A., Kottke, A. and Pilz, M. (2022c), A DesignSafe Ground Motion Database for California, *Earthquake Spectrum* (in preparation).
- Kaklamanos, J., Cabas, A., Parolai, S., & Guéguen, P. (2021). Introduction to the Special Section on Advances in Site Response Estimation. *Bulletin of the Seismological Society of America*, 111(4), 1665-1676.

- Kwak D.Y.; Ahdi S.K.; Wang P.; Zimmaro P.; Brandenberg S.J.; Stewart J.P.: Web portal for shear wave velocity and HVSR databases in support of site response research and applications. UCLA Geotechnical Engineering Group. DOI:10.21222/C27H0V, last accessed 2021/10/02.
- Kern, H., Liu, B., & Popp, T. (1997). Relationship between anisotropy of P and S wave velocities and anisotropy of attenuation in serpentinite and amphibolite. *Journal of Geophysical Research: Solid Earth*, 102(B2), 3051-3065.
- Kuehn, N. M., Abrahamson, N. A., & Walling, M. A. (2019). Incorporating nonergodic path effects into the NGA-West2 ground-motion prediction equations. *Bulletin of the Seismological Society of America*, 109(2), 575-585.
- Knopoff, L., (1964). *Q. Rev. Geophysics*, 2, no. 4, 625-660.
- Konno, K., & Ohmachi, T. (1998). Ground-motion characteristics estimated from spectral ratio between horizontal and vertical components of microtremor. *Bulletin of the Seismological Society of America*, 88(1), 228-241.
- Ktenidou, O. J., Gélis, C., & Bonilla, L. F. (2013). A study on the variability of kappa (κ) in a borehole: Implications of the computation process. *Bulletin of the Seismological Society of America*, 103(2A), 1048-1068.
- Ktenidou, O. J., Cotton, F., Abrahamson, N. A., & Anderson, J. G. (2014). Taxonomy of κ : A review of definitions and estimation approaches targeted to applications. *Seismological Research Letters*, 85(1), 135-146.
- Ktenidou, O. J., Abrahamson, N. A., Drouet, S., & Cotton, F. (2015). Understanding the physics of kappa (κ): Insights from a downhole array. *Geophysical Journal International*, 203(1), 678-691.

- Ktenidou, O. J., Abrahamson, N., Darragh, R., & Silva, W. (2016). A methodology for the estimation of kappa (κ) from large datasets, example application to rock sites in the NGA-East database, and implications on design motions. PEER Report 2016, 1.
- Krischer, L., Megies, T., Barsch, R., Beyreuther, M., Lecocq, T., Caudron, C., & Wassermann, J. (2015). ObsPy: A bridge for seismology into the scientific Python ecosystem. *Computational Science & Discovery*, 8(1), 014003.
- Krischer, L., Smith, J., Lei, W., Lefebvre, M., Ruan, Y., de Andrade, E. S., ... & Tromp, J. (2016). An adaptable seismic data format. *Geophysical Supplements to the Monthly Notices of the Royal Astronomical Society*, 207(2), 1003-1011.
- Kotha, S. R., Cotton, F., & Bindi, D. (2019). empirical Models of shear-Wave Radiation pattern Derived from Large Datasets of Ground-shaking observations. *Scientific reports*, 9(1), 1-11.
- Laurendeau, A., Cotton, F., Ktenidou, O. J., Bonilla, L. F., & Hollender, F. (2013). Rock and stiff-soil site amplification: Dependency on VS 30 and kappa (κ 0). *Bulletin of the Seismological Society of America*, 103(6), 3131-3148.
- Lacave-Lachet, C., Bard, P. Y., Gariel, J. C., & Irikura, K. (2000). Straightforward methods to detect non-linear response of the soil. Application to the recordings of the Kobe earthquake (Japan, 1995). *Journal of seismology*, 4(2), 161-173.
- Liu, E., Crampin, S., Queen, J. H., & Rizer, W. D. (1993). Velocity and attenuation anisotropy caused by microcracks and macrofractures in a multiazimuth reverse VSP. *Canadian Journal of Exploration Geophysics*, 29(1), 177-188.
- Liu, Y., Teng, T. L., & Ben-Zion, Y. (2004). Systematic analysis of shear-wave splitting in the aftershock zone of the 1999 Chi-Chi, Taiwan, earthquake: shallow crustal anisotropy and

- lack of precursory variations. *Bulletin of the Seismological Society of America*, 94(6), 2330-2347.
- Liu, Y., Teng, T. L., & Ben-Zion, Y. (2005). Near-surface seismic anisotropy, attenuation and dispersion in the aftershock region of the 1999 Chi-Chi earthquake. *Geophysical Journal International*, 160(2), 695-706.
- Mayor, J., Bora, S. S., & Cotton, F. (2018). Capturing regional variations of hard-rock κ_0 from coda analysis. *Bulletin of the Seismological Society of America*, 108(1), 399-408.
- Mayor, J., Traversa, P., Calvet, M., & Margerin, L. (2018). Tomography of crustal seismic attenuation in Metropolitan France: Implications for seismicity analysis. *Bulletin of Earthquake Engineering*, 16(6), 2195-2210.
- McPhillips, D., Herrick, J. A., Ahdi, S., Yong, A. K., & Haefner, S. (2020). Updated compilation of VS 30 data for the United States. US Geol. Surv. Data Release.
- Menq, F. Y. (2003). Dynamic properties of sandy and gravelly soils. The University of Texas at Austin.
- Nakano, K., Matsushima, S., & Kawase, H. (2015). Statistical properties of strong ground motions from the generalized spectral inversion of data observed by K-NET, KiK-net, and the JMA Shindokei network in Japan. *Bulletin of the Seismological Society of America*, 105(5), 2662-2680.
- Oth, A., Parolai, S., & Bindi, D. (2011). Spectral analysis of K-NET and KiK-net data in Japan, Part I: Database compilation and peculiarities. *Bulletin of the Seismological Society of America*, 101(2), 652-666.

- Parolai, S., & Bindi, D. (2004). Influence of soil-layer properties on k evaluation. *Bulletin of the Seismological Society of America*, 94(1), 349-356.
- Parolai, S., Bindi, D., & Pilz, M. (2015). k_0 : The role of Intrinsic and Scattering Attenuation. *Bulletin of the Seismological Society of America*, 105(2A), 1049-1052.
- Parolai, S. (2018). κ_0 : Origin and usability. *Bulletin of the Seismological Society of America*, 108(6), 3446-3456.
- Parvez, I. A., Yadav, P., & Nagaraj, K. (2012). Attenuation of P, S and coda waves in the NW-Himalayas, India. *International Journal of Geosciences*, 3(01), 179.
- Perron, V., Hollender, F., Bard, P. Y., Gélis, C., Guyonnet-Benaize, C., Hernandez, B., & Ktenidou, O. J. (2017). Robustness of kappa (κ) measurement in low-to-moderate seismicity areas: Insight from a site-specific study in Provence, France. *Bulletin of the Seismological Society of America*, 107(5), 2272-2292.
- Perron, V., Laurendeau, A., Hollender, F., Bard, P. Y., Gélis, C., Traversa, P., & Drouet, S. (2018). Selecting time windows of seismic phases and noise for engineering seismology applications: A versatile methodology and algorithm. *Bulletin of Earthquake Engineering*, 16(6), 2211-2225.
- Pei, S., Cui, Z., Sun, Y., Toksöz, M. N., Rowe, C. A., Gao, X., ... & Morgan, F. D. (2009). Structure of the upper crust in Japan from S-wave attenuation tomography. *Bulletin of the Seismological Society of America*, 99(1), 428-434.
- Pilz, M., & Fäh, D. (2017). The contribution of scattering to near-surface attenuation. *Journal of Seismology*, 21(4), 837-855.

- Pilz, M., & Cotton, F. (2019). Does the one-dimensional assumption hold for site response analysis? A study of seismic site responses and implication for ground motion assessment using KiK-Net strong-motion data. *Earthquake Spectra*, 35(2), 883-905.
- Pilz, M., Cotton, F., Zaccarelli, R., & Bindi, D. (2019). Capturing regional variations of hard-rock attenuation in Europe. *Bulletin of the Seismological Society of America*, 109(4), 1401-1418.
- Qin, L., Ben-Zion, Y., Bonilla, L. F., & Steidl, J. H. (2020). Imaging and monitoring temporal changes of shallow seismic velocities at the Garner Valley near Anza, California, following the M7. 2 2010 El Mayor-Cucapah earthquake. *Journal of Geophysical Research: Solid Earth*, 125(1), e2019JB018070.
- Ramos-Sepulveda, M. and Cabas, A. (2021), Site Effects on Ground Motion Directionality: Lessons Learned from Case Studies in Japan, *ASCE Journal of Soil Dynamics and Earthquake Engineering*, Volume 147, 106755
<https://doi.org/10.1016/j.soildyn.2021.106755>
- Rathje, E. M., Dawson, C., Padgett, J. E., Pinelli, J. P., Stanzione, D., Adair, A., ... & Mosqueda, G. (2017). DesignSafe: New cyberinfrastructure for natural hazards engineering. *Natural Hazards Review*, 18(3), 06017001.
- Rodriguez-Marek, A., Rathje, E. M., Bommer, J. J., Scherbaum, F., & Stafford, P. J. (2014). Application of single-station sigma and site-response characterization in a probabilistic seismic-hazard analysis for a new nuclear site. *Bulletin of the Seismological Society of America*, 104(4), 1601-1619.
- Rautian, T. G., & Khalturin, V. I. (1978). The use of the coda for determination of the earthquake source spectrum. *Bulletin of the Seismological Society of America*, 68(4), 923-948.

- Rekoske, J. M., Thompson, E. M., Moschetti, M. P., Hearne, M. G., Aagaard, B. T., & Parker, G. A. (2020). The 2019 Ridgecrest, California, earthquake sequence ground motions: Processed records and derived intensity metrics. *Seismological Research Letters*, 91(4), 2010-2023.
- Régnier, J., Cadet, H., Bonilla, L. F., Bertrand, E., & Semblat, J. F. (2013). Assessing nonlinear behavior of soils in seismic site response: Statistical analysis on KiK-net strong-motion data. *Bulletin of the Seismological Society of America*, 103(3), 1750-1770.
- Régnier, J., Cadet, H., & Bard, P. Y. (2016). Empirical quantification of the impact of nonlinear soil behavior on site response. *Bulletin of the Seismological Society of America*, 106(4), 1710-1719.
- Rong, M., Wang, Z., Woolery, E. W., Lyu, Y., Li, X., & Li, S. (2016). Nonlinear site response from the strong ground-motion recordings in western China. *Soil Dynamics and Earthquake Engineering*, 82, 99-110.
- Sato, H., & Fehler, M. (1998). *Scattering and attenuation of seismic waves in heterogeneous earth*.
- Sharma, B., Teotia, S. S., & Kumar, D. (2007). Attenuation of P, S, and coda waves in Koyna region, India. *Journal of Seismology*, 11(3), 327-344.
- Silva, W. J., and R. Darragh (1995). *Engineering Characterization of Earthquake Strong Ground Motion Recorded at Rock Sites*, Palo Alto, Electric Power Research Institute, TR-102261.
- Seed, H. B., Wong, R. T., Idriss, I. M., & Tokimatsu, K. (1986). Moduli and damping factors for dynamic analyses of cohesionless soils. *Journal of geotechnical engineering*, 112(11), 1016-1032.

- Sonnemann, T., & Halldorsson, B. (2017, June). Towards an automated kappa measurement procedure. In International Conference on Earthquake Engineering and Structural Dynamics (pp. 39-52). Springer, Cham.
- Tao, G., & King, M. S. (1990, October). Shear-wave velocity and Q anisotropy in rocks: A laboratory study. In International Journal of Rock Mechanics and Mining Sciences & Geomechanics Abstracts (Vol. 27, No. 5, pp. 353-361). Pergamon.
- Thompson, E. M., Baise, L. G., Tanaka, Y., & Kayen, R. E. (2012). A taxonomy of site response complexity. *Soil Dynamics and Earthquake Engineering*, 41, 32-43.
- Thompson, E. M., Wald, D. J., & Worden, C. B. (2014). A V_{S30} map for California with geologic and topographic constraints. *Bulletin of the Seismological Society of America*, 104(5), 2313-2321.
- Trifunac, M. D., & Todorovska, M. I. (1996). Nonlinear soil response—1994 Northridge, California, earthquake. *Journal of geotechnical engineering*, 122(9), 725-735.
- Tucker, B. E., & King, J. L. (1984). Dependence of sediment-filled valley response on input amplitude and valley properties. *Bulletin of the seismological society of america*, 74(1), 153-165.
- Van Houtte, C., Drouet, S., & Cotton, F. (2011). Analysis of the origins of κ (kappa) to compute hard rock to rock adjustment factors for GMPEs. *Bulletin of the Seismological Society of America*, 101(6), 2926-2941.
- Van Houtte, C., Ktenidou, O. J., Larkin, T., & Holden, C. (2014). Hard-site κ_0 (kappa) calculations for Christchurch, New Zealand, and comparison with local ground-motion prediction models. *Bulletin of the Seismological Society of America*, 104(4), 1899-1913.

- Van Houtte, C., Ktenidou, O. J., Larkin, T., & Holden, C. (2018). A continuous map of near-surface S-wave attenuation in New Zealand. *Geophysical Journal International*, 213(1), 408-425.
- Wald, D. J., & Allen, T. I. (2007). Topographic slope as a proxy for seismic site conditions and amplification. *Bulletin of the Seismological Society of America*, 97(5), 1379-1395.
- Wang, P., Zimmaro, P., Gospe, T., Ahdi, S. K., Yong, A., & Stewart, J. P. (2021). Horizontal-to-vertical spectral ratios from California sites: Open-source database and data interpretation to establish site parameters. California Geological Survey.
- Wang, W., & Shearer, P. M. (2019). An improved method to determine coda-Q, earthquake magnitude, and site amplification: Theory and application to southern California. *Journal of Geophysical Research: Solid Earth*, 124(1), 578-598.
- Wu, H., Masaki, K., Irikura, K., & Sánchez-Sesma, F. J. (2017). Application of a simplified calculation for full-wave microtremor H/V spectral ratio based on the diffuse field approximation to identify underground velocity structures. *Earth, Planets and Space*, 69(1), 1-18.
- Xu, B., Rathje, E. M., Hashash, Y., Stewart, J., Campbell, K., & Silva, W. J. (2020). κ_0 for soil sites: Observations from Kik-net sites and their use in constraining small-strain damping profiles for site response analysis. *Earthquake Spectra*, 36(1), 111-137.
- Xu, B., & Rathje, E. M. (2021). The effect of soil nonlinearity on high-frequency spectral decay and implications for site response analysis. *Earthquake Spectra*, 37(2), 686-706.
- Yong, A., Thompson, E. M., Wald, D. J., Knudsen, K. L., Odum, J. K., Stephenson, W. J., & Haefner, S. (2016). Compilation of V S30 data for the United States (No. 978). US Geological Survey.

Yu, G., Anderson, J. G., & Siddharthan, R. A. J. (1993). On the characteristics of nonlinear soil response. *Bulletin of the Seismological Society of America*, 83(1), 218-244.

Zalachoris, G., & Rathje, E. M. (2015). Evaluation of one-dimensional site response techniques using borehole arrays. *Journal of Geotechnical and Geoenvironmental Engineering*, 141(12), 04015053.

APPENDICES

Appendix A: Supplementary Material for Chapter 2

This file contains one table and two figures. Table A. 1 provides the site-specific κ_0 values at borehole and surface, path-component κ_R , and the corresponding standard derivations from the regression used to estimate κ_0 (σ) at the study sites with maximum likelihood statistic regression. All records at each station are classified by earthquake type or focal depth. Figure A.1 compares the event azimuth and θ_{\max} . Figure A. 2 shows the differences between $\kappa_{r_AS_ave}$ (the average of two horizontal κ_{r_AS} estimated from the as-recorded components) and $\kappa_{r_AS_mean}$ (the mean of all rotated κ_{r_AS}), and the color indicates the differences between $\kappa_{r_AS_H1}$ and $\kappa_{r_AS_H2}$.

Table A. 1. Estimated κ -values along with the corresponding earthquake type and depth at each selected station

| Station Name | κ values | Earthquake type | | | | Earthquake depth | | |
|--------------|------------------------|-----------------|---------|---------|---------|------------------|------------|--------|
| | | ACRsh | ACRde | SZintra | SZinter | <35km | 35 ~ 70 km | >70 km |
| IBRH14 | Record Number | 35 | 4 | 27 | 50 | 67 | 40 | 9 |
| | κ_R (s/km) | 0.00014 | - | 0.00003 | 0.00010 | 0.00017 | 0.00009 | - |
| | κ_{0_bore} (s) | 0.0044 | 0.0143 | 0.0146 | 0.0068 | 0.0018 | 0.0054 | 0.0197 |
| | κ_{0_sur} (s) | 0.0572 | 0.0664 | 0.0693 | 0.0680 | 0.0586 | 0.0650 | 0.0700 |
| | $\Delta\kappa_0$ (s) | 0.0528 | 0.0521 | 0.0547 | 0.0612 | 0.0568 | 0.0596 | 0.0503 |
| | σ^* | 0.0079 | 0.0048 | 0.0110 | 0.0105 | 0.0095 | 0.0107 | 0.0112 |
| IBRH19 | Record Number | 88 | 14 | 68 | 63 | 112 | 87 | 34 |
| | κ_R (s/km) | 0.00010 | 0.00027 | 0.00011 | 0.00010 | 0.00016 | 0.00012 | - |
| | κ_{0_bore} (s) | 0.0076 | 0.0021 | 0.0082 | 0.0112 | 0.0025 | 0.0080 | 0.0148 |
| | κ_{0_sur} (s) | 0.0299 | 0.0118 | 0.0258 | 0.0288 | 0.0242 | 0.0245 | 0.0311 |
| | $\Delta\kappa_0$ (s) | 0.0224 | 0.0096 | 0.0176 | 0.0176 | 0.0217 | 0.0165 | 0.0163 |
| | σ^* | 0.0086 | 0.0056 | 0.0071 | 0.0080 | 0.0084 | 0.0074 | 0.0075 |

Table A.1 (continued).

| | | | | | | | | |
|--------|------------------------|---------|---------|---------|---------|---------|---------|--------------|
| | Record Number | 71 | 23 | 71 | 79 | 97 | 124 | 23 |
| FKSH08 | κ_R (s/km) | 0.00016 | 0.00020 | 0.00025 | 0.00018 | 0.00017 | 0.00022 | 0.00024 |
| | κ_{0_bore} (s) | 0.0105 | 0.0075 | 0.0008 | 0.0081 | 0.0101 | 0.0033 | 0.0036 |
| | κ_{0_sur} (s) | 0.0379 | 0.0331 | 0.0276 | 0.0295 | 0.0368 | 0.0272 | 0.0282 |
| | $\Delta\kappa_0$ (s) | 0.0274 | 0.0256 | 0.0268 | 0.0214 | 0.0267 | 0.0239 | 0.0246 |
| | σ^* | 0.0097 | 0.0097 | 0.0100 | 0.0085 | 0.0095 | 0.0095 | 0.0099 |
| | Record Number | 38 | 6 | 22 | 18 | 52 | 24 | 8 |
| IBRH18 | κ_R (s/km) | 0.00017 | 0.00170 | 0.00015 | 0.00016 | 0.00019 | 0.00002 | 0.00014 |
| | κ_{0_bore} (s) | 0.0104 | -0.1037 | 0.0126 | 0.0149 | 0.0097 | 0.0228 | 0.0121 |
| | κ_{0_sur} (s) | 0.0375 | -0.0832 | 0.0330 | 0.0383 | 0.0361 | 0.0429 | 0.0339 |
| | $\Delta\kappa_0$ (s) | 0.0272 | 0.0205 | 0.0205 | 0.0234 | 0.0263 | 0.0201 | 0.0219 |
| | σ^* | 0.0107 | 0.0042 | 0.0091 | 0.0087 | 0.0102 | 0.0084 | 0.0073 |
| | Record Number | 55 | 0 | 27 | 33 | 64 | 45 | 6 |
| FKSH16 | κ_R (s/km) | 0.00015 | NA | 0.00011 | 0.00024 | 0.00029 | 0.00024 | - 0.00003 |
| | κ_{0_bore} (s) | 0.0193 | NA | 0.0189 | 0.0050 | 0.0028 | 0.0030 | 0.0335 |
| | κ_{0_sur} (s) | 0.0727 | NA | 0.0702 | 0.0572 | 0.0564 | 0.0561 | 0.0884 |
| | $\Delta\kappa_0$ (s) | 0.0533 | NA | 0.0513 | 0.0522 | 0.0536 | 0.0531 | 0.0549 |
| | σ^* | 0.0102 | NA | 0.0113 | 0.0110 | 0.0110 | 0.0119 | 0.0077 |
| | Record Number | 51 | 16 | 52 | 51 | 81 | 68 | 21 |
| IBRH12 | κ_R (s/km) | 0.00014 | 0.00019 | 0.00018 | 0.00038 | 0.00024 | 0.00023 | 0.00013 |
| | κ_{0_bore} (s) | 0.0178 | 0.0123 | 0.0155 | -0.0064 | 0.0115 | 0.0072 | 0.0211 |
| | κ_{0_sur} (s) | 0.0447 | 0.0384 | 0.0448 | 0.0262 | 0.0404 | 0.0359 | 0.0526 |
| | $\Delta\kappa_0$ (s) | 0.0269 | 0.0261 | 0.0294 | 0.0327 | 0.0289 | 0.0287 | 0.0315 |
| | σ^* | 0.0114 | 0.0091 | 0.0116 | 0.0110 | 0.0117 | 0.0097 | 0.0126 |
| | Record Number | 46 | 0 | 65 | 49 | 82 | 68 | 10 |
| FKSH19 | κ_R (s/km) | 0.00012 | NA | 0.00012 | 0.00008 | 0.00007 | 0.00011 | 0.00010 |
| | κ_{0_bore} (s) | 0.0048 | NA | 0.0014 | 0.0075 | 0.0096 | 0.0018 | 0.0045 |
| | κ_{0_sur} (s) | 0.0407 | NA | 0.0351 | 0.0400 | 0.0436 | 0.0355 | 0.0390 |
| | $\Delta\kappa_0$ (s) | 0.0359 | NA | 0.0337 | 0.0325 | 0.0340 | 0.0338 | 0.0345 |
| | σ^* | 0.0119 | NA | 0.0076 | 0.0097 | 0.0106 | 0.0089 | 0.0063 |

Table A.1 (continued).

| | | | | | | | | |
|--------|------------------------|--------------|---------|--------------|---------|---------|---------|--------------|
| | Record Number | 45 | 20 | 59 | 62 | 87 | 81 | 18 |
| IBRH13 | κ_R (s/km) | 0.00017 | 0.00060 | 0.00015 | 0.00006 | 0.00014 | 0.00012 | 0.00015 |
| | κ_{0_bore} (s) | 0.0070 | -0.0464 | 0.0031 | 0.0144 | 0.0089 | 0.0030 | 0.0020 |
| | κ_{0_sur} (s) | 0.0702 | 0.0201 | 0.0683 | 0.0797 | 0.0734 | 0.0674 | 0.0714 |
| | $\Delta\kappa_0$ (s) | 0.0632 | 0.0665 | 0.0652 | 0.0653 | 0.0645 | 0.0644 | 0.0694 |
| | σ^* | 0.0126 | 0.0065 | 0.0116 | 0.0132 | 0.0122 | 0.0114 | 0.0105 |
| | Record Number | 60 | 6 | 35 | 36 | 75 | 54 | 8 |
| IBRH11 | κ_R (s/km) | - 0.00005 | 0.00019 | 0.00007 | 0.00013 | 0.00004 | 0.00004 | - 0.00003 |
| | κ_{0_bore} (s) | 0.0331 | 0.0219 | 0.0181 | 0.0132 | 0.0245 | 0.0227 | 0.0241 |
| | κ_{0_sur} (s) | 0.0619 | 0.0518 | 0.0548 | 0.0511 | 0.0550 | 0.0586 | 0.0638 |
| | $\Delta\kappa_0$ (s) | 0.0288 | 0.0299 | 0.0368 | 0.0379 | 0.0304 | 0.0360 | 0.0397 |
| | σ^* | 0.0129 | 0.0099 | 0.0101 | 0.0117 | 0.0127 | 0.0114 | 0.0100 |
| | Record Number | 46 | 7 | 22 | 27 | 57 | 37 | 8 |
| TCGH16 | κ_R (s/km) | 0.00014 | 0.00056 | 6.25E- 05 | 0.00013 | 0.00009 | 0.00005 | - 0.00006 |
| | κ_{0_bore} (s) | 0.02365 | 0.00384 | 0.03564 | 0.02866 | 0.0310 | 0.0335 | 0.0494 |
| | κ_{0_sur} (s) | 0.06293 | 0.03381 | 0.0632 | 0.05075 | 0.0665 | 0.0587 | 0.0711 |
| | $\Delta\kappa_0$ (s) | 0.03928 | 0.02996 | 0.02756 | 0.02209 | 0.0355 | 0.0251 | 0.0216 |
| | σ^* | 0.01033 | 0.01695 | 0.00878 | 0.00966 | 0.0103 | 0.0105 | 0.0061 |

¹ACRsh: shallow active crustal events;

²ACRde: deep active crustal events;

³SZintra: subduction zone intraslab events;

⁴SZinter: subduction zone interface events;

* σ : Standard derivations from the regression used to estimate κ_0 .

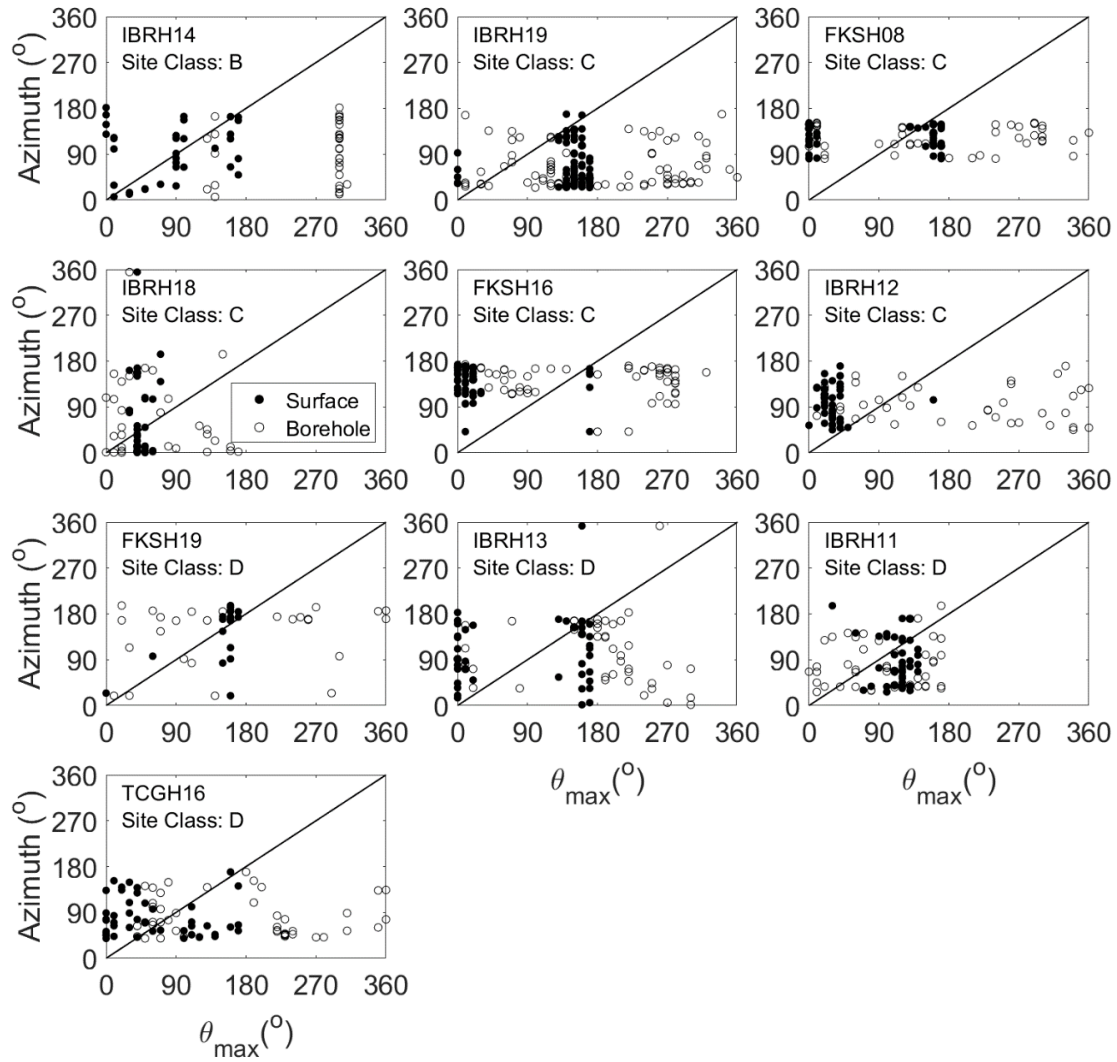
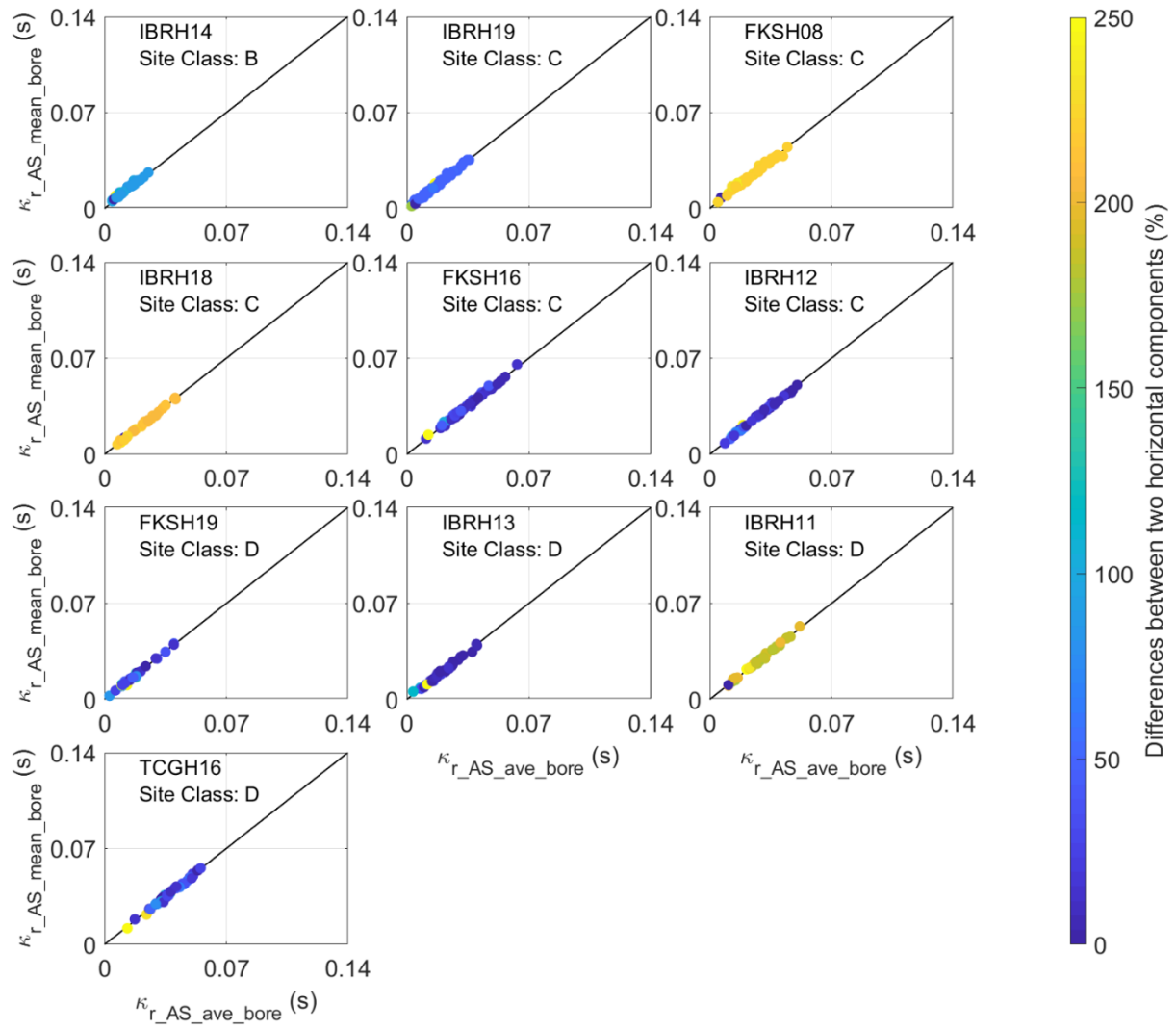


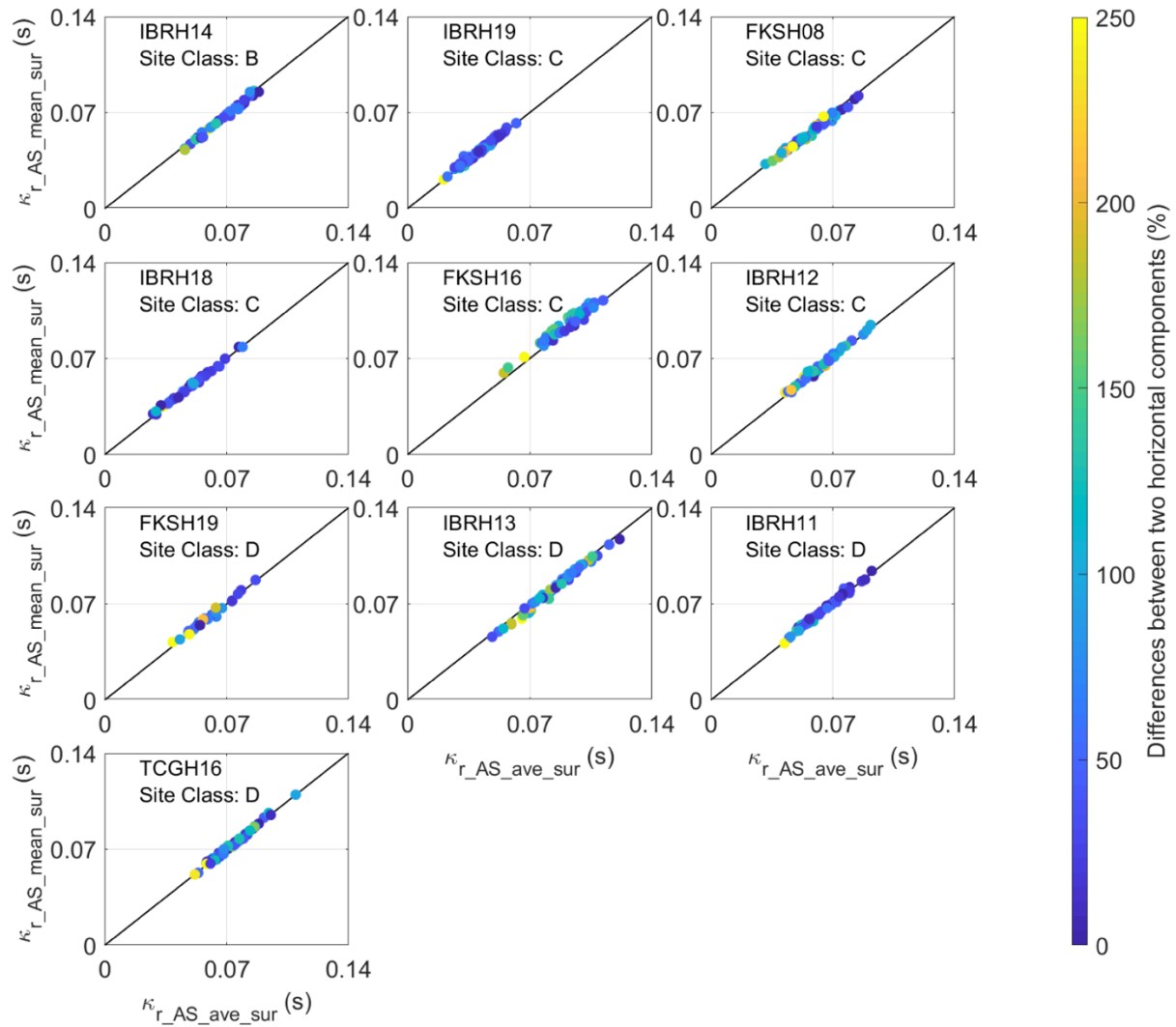
Figure A. 1. Comparison between source-to-site azimuth and rotation angle corresponding to the maximum $\kappa_{T,AS,ROT}$ (θ_{max}) calculated from borehole and surface records at the selected stations.

Figure A. 2. Comparisons between $\kappa_{r_AS_ave}$ and $\kappa_{r_AS_mean}$ at selected stations: (a) the results at borehole, and (b) the data at surface. The colors represent the difference between κ_{r_AS} estimated from two as-recorded borehole horizontal components. The solid line provides the 1:1 correlation reference between $\kappa_{r_AS_ave}$ and $\kappa_{r_AS_mean}$, and the colors indicate the differences between $\kappa_{r_AS_H1}$ and $\kappa_{r_AS_H2}$ computed from as-recorded horizontal components. $\kappa_{r_AS_mean}$ is the mean values of all $\kappa_{r_AS_ROT}$ for each record, and $\kappa_{r_AS_ave}$ is the arithmetic average of two as-recorded horizontal component values.

(a)



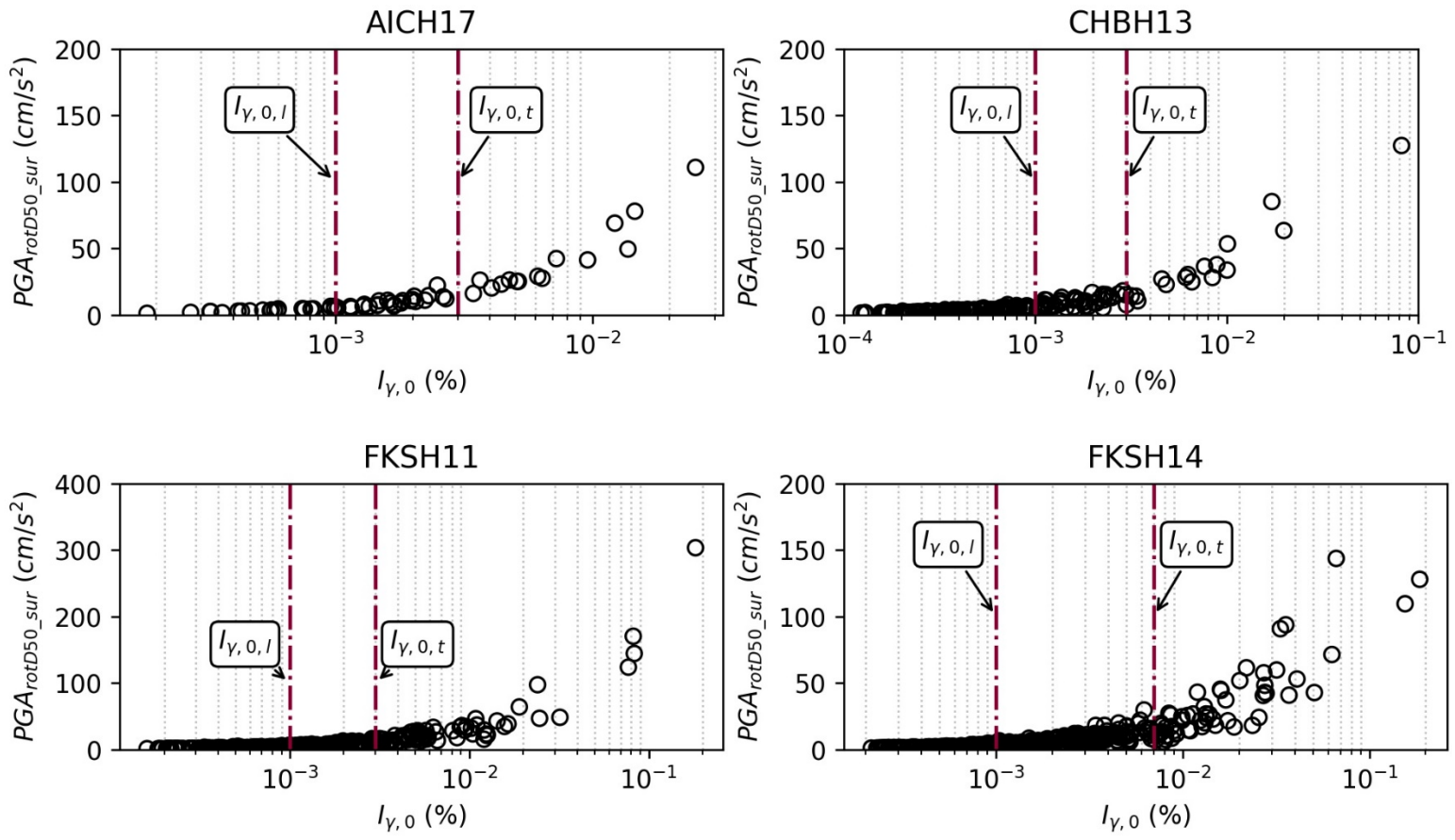
(b)

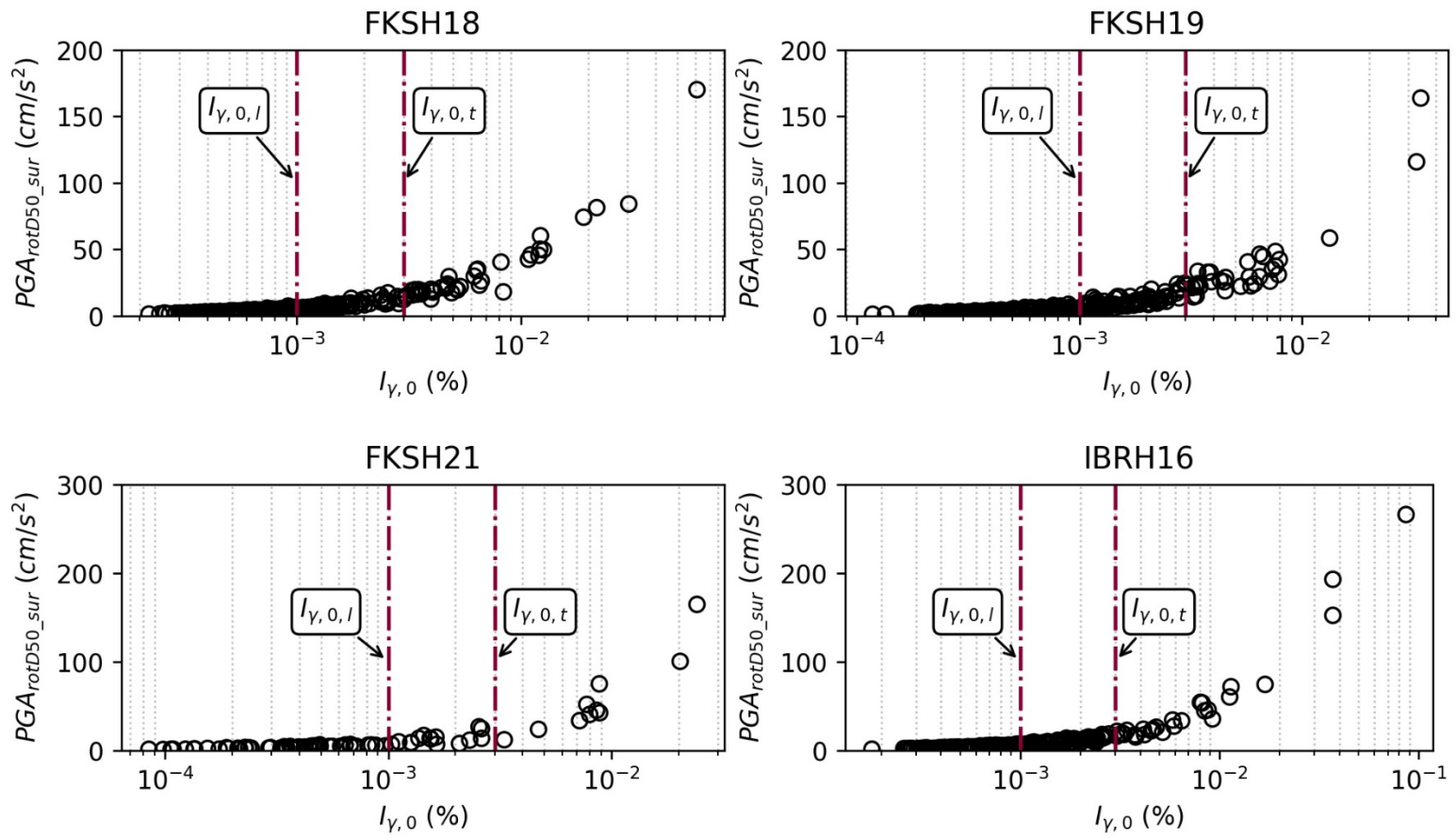


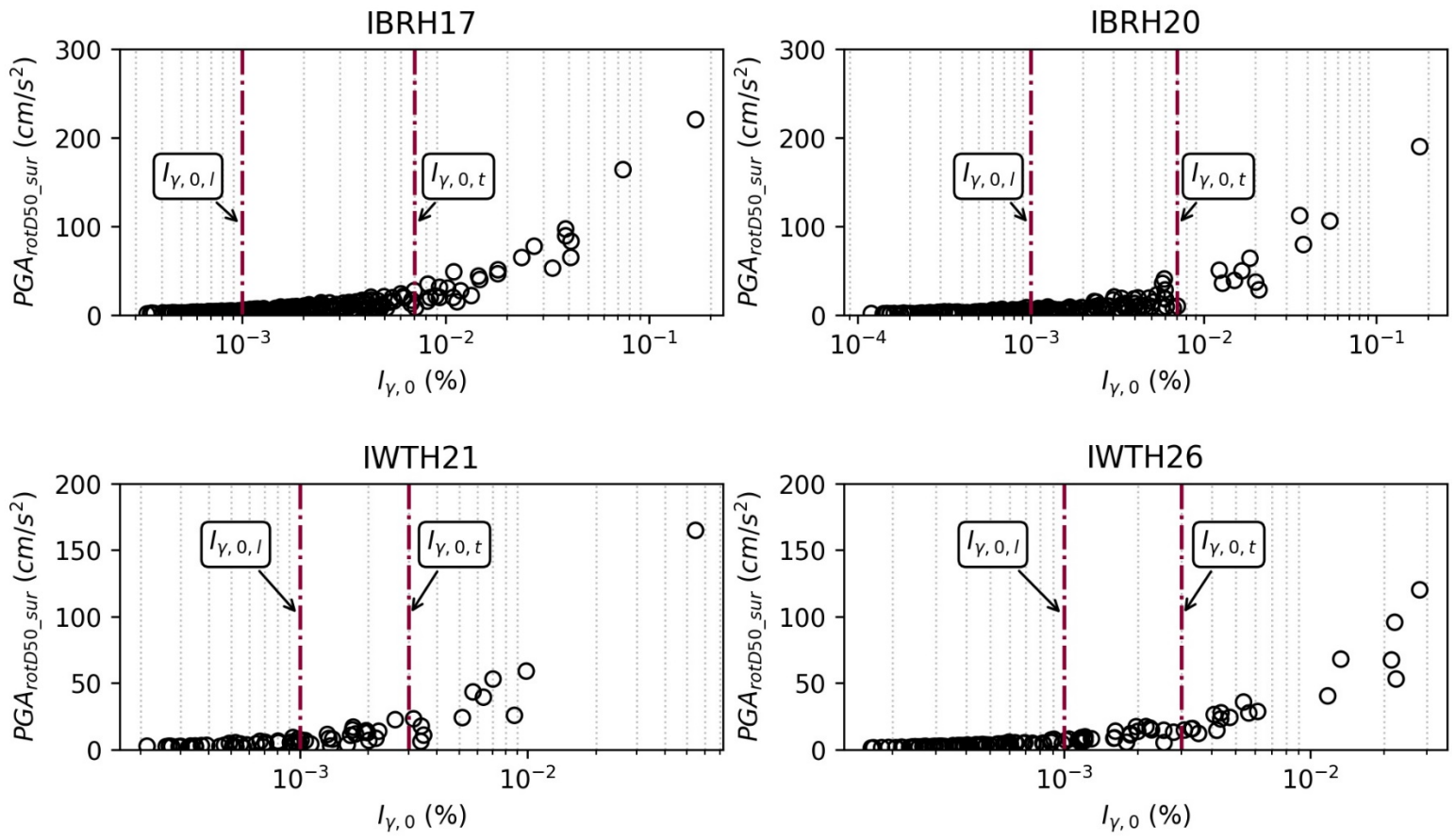
Appendix B: Supplementary Material for Chapter 3

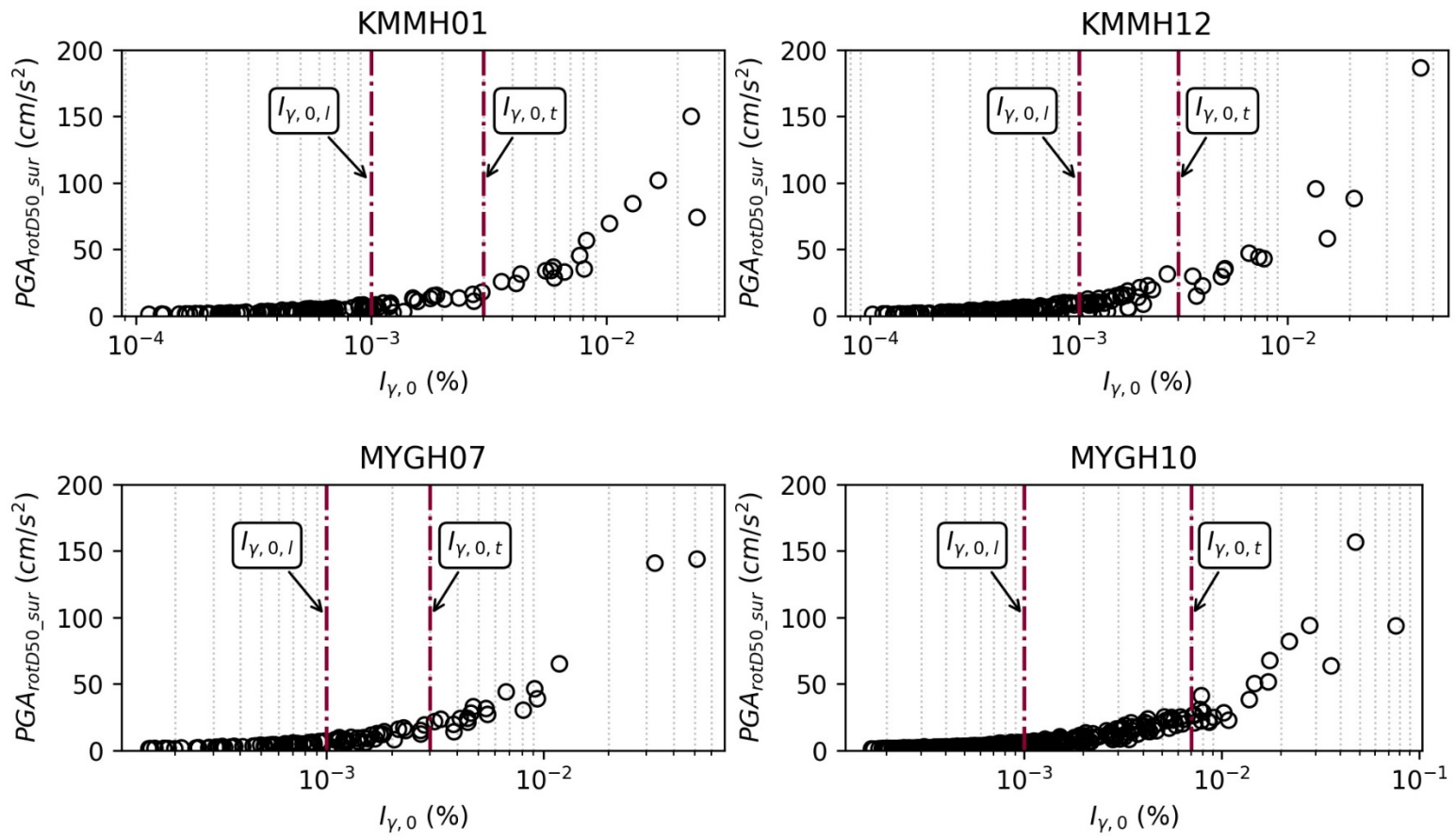
This file contains three sets of figures and two tables. Figure B.1 corresponds to Figure 3.4 in this article, which presents the surface PGA_{rotD50} against $I_{\gamma,0}$ at selected 20 stations. Figure B.2 corresponds to Figure 3.7, which depicts the relationship between surface κ_{r_AS} estimates and ground shaking intensities at the studied sites. Figure B.3 corresponds to Figure 3.11 in this article, which indicates the correlations between surface κ_{0_pred} and ground shaking intensities at the studied stations. Table B.1 provides the results of the implementation of the κ_0 -model with the datasets defined by AP1, AP2, AP3, and AP4. The averages of surface κ_{0_pred} , which are estimated with AP3, and their standard derivations are also included in Table B.2.

Figure B. 1. Surface PGA_{rotD50} against $I_{\gamma,0}$ at the studied stations. The dashed lines represent the linear and transitional thresholds of $I_{\gamma,0}$.









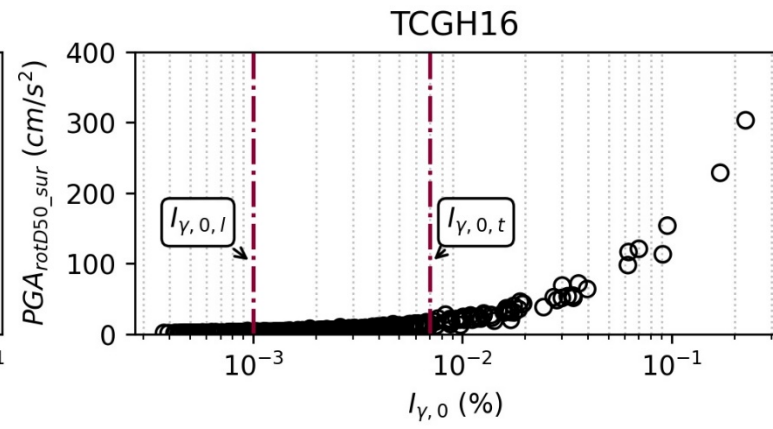
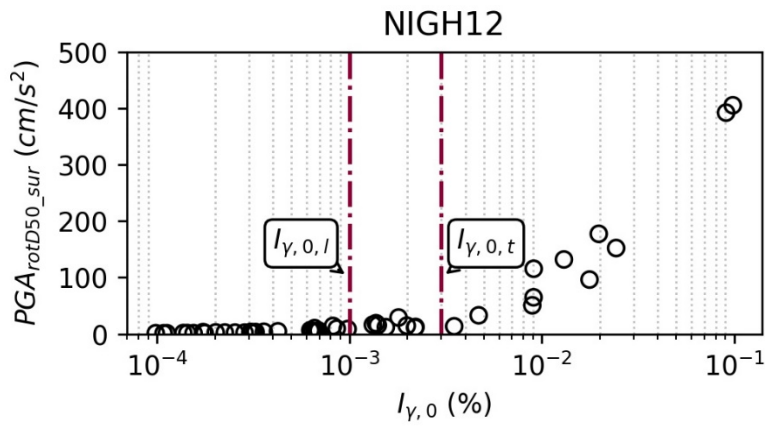
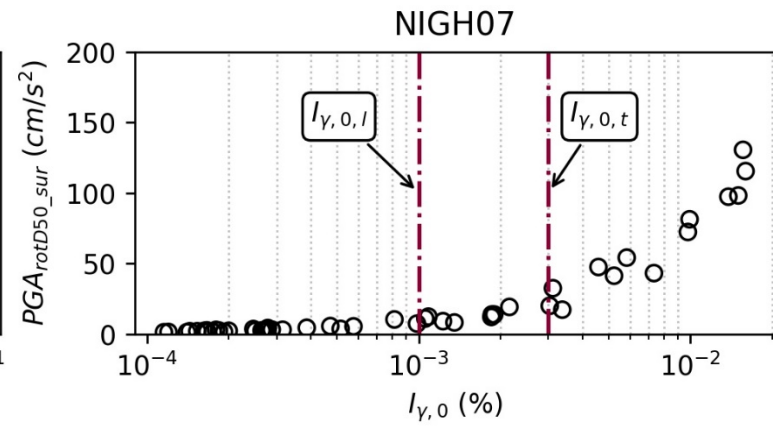
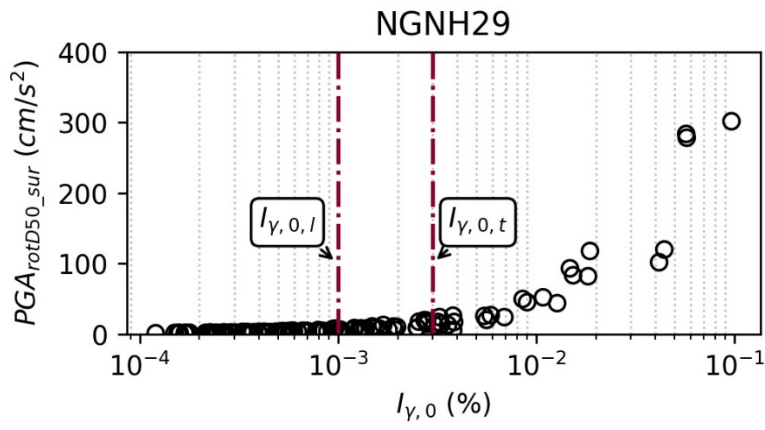
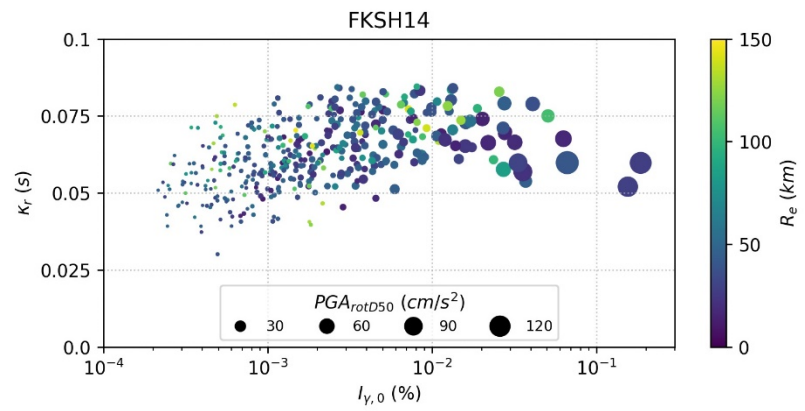
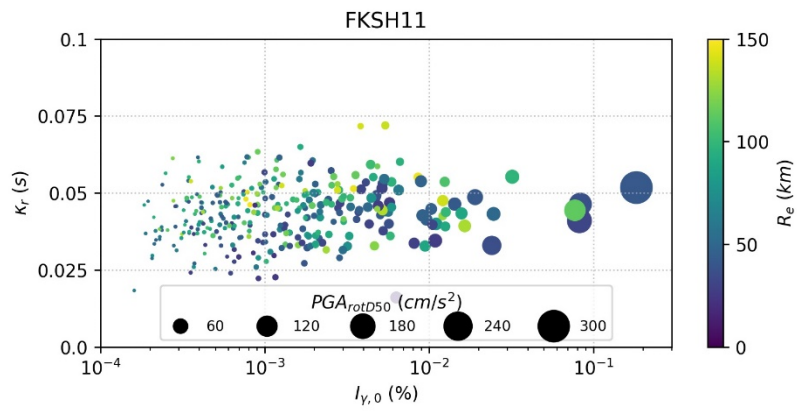
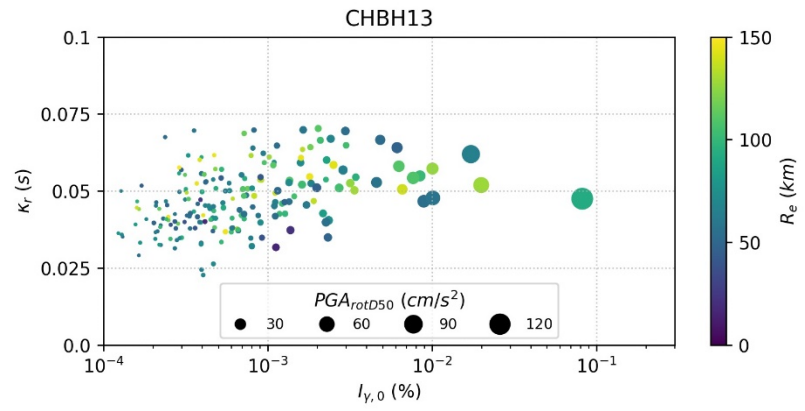
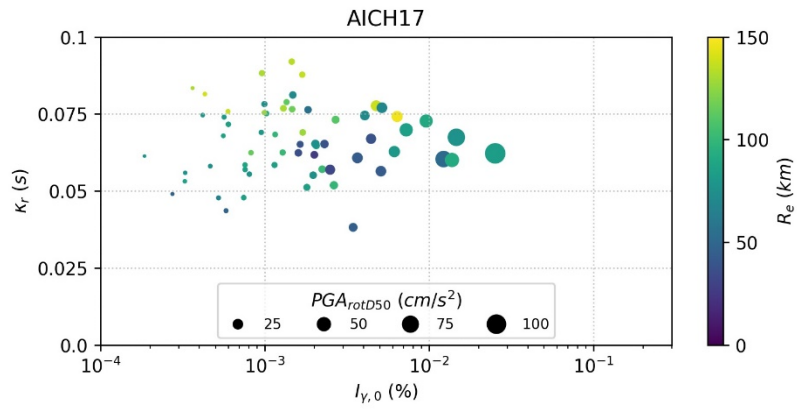
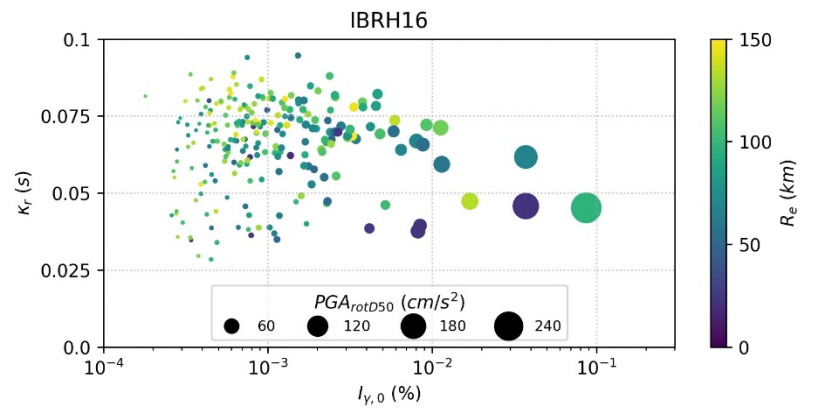
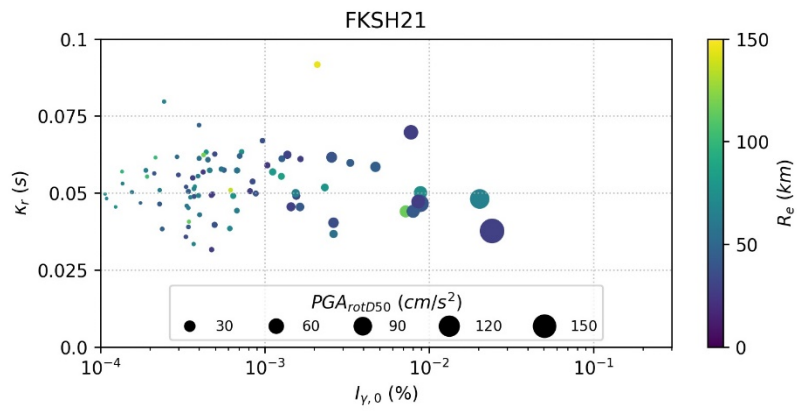
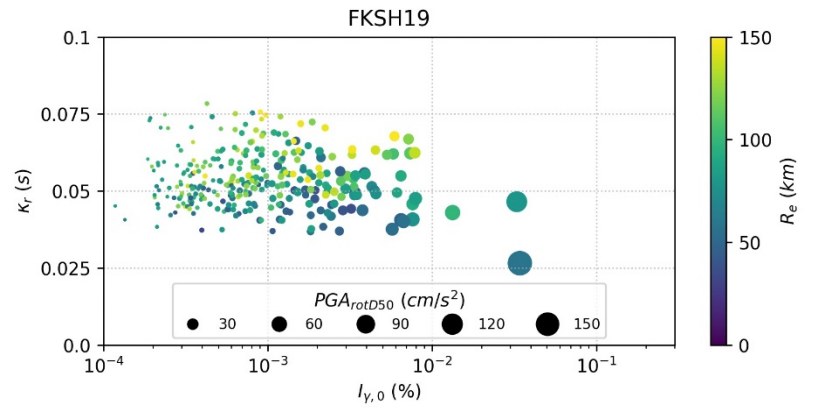
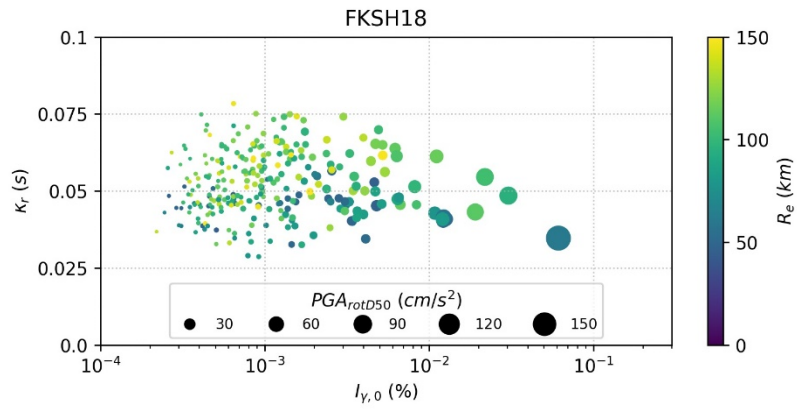
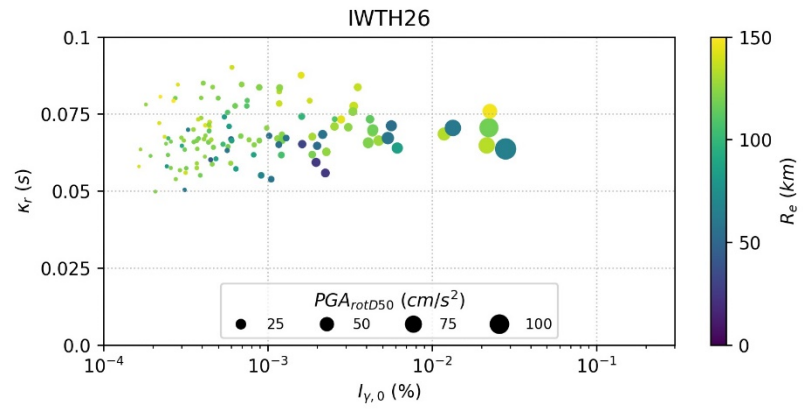
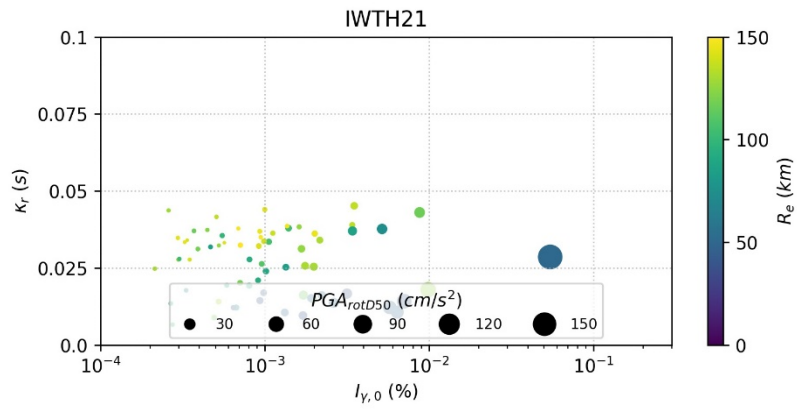
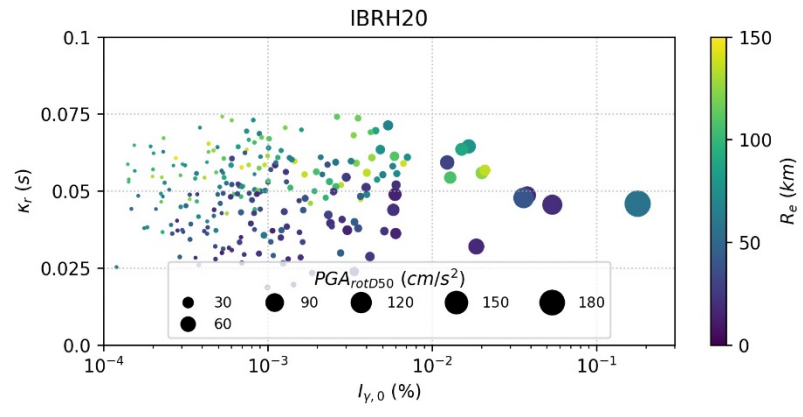
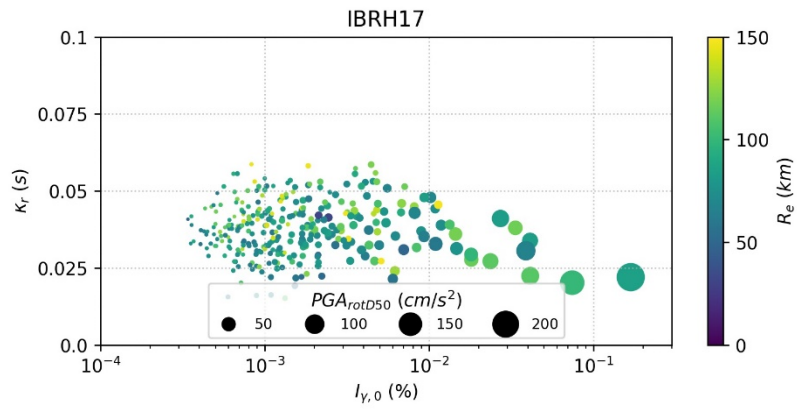
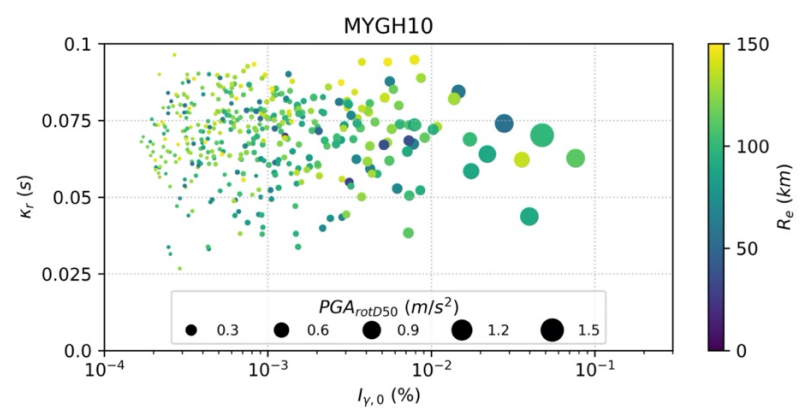
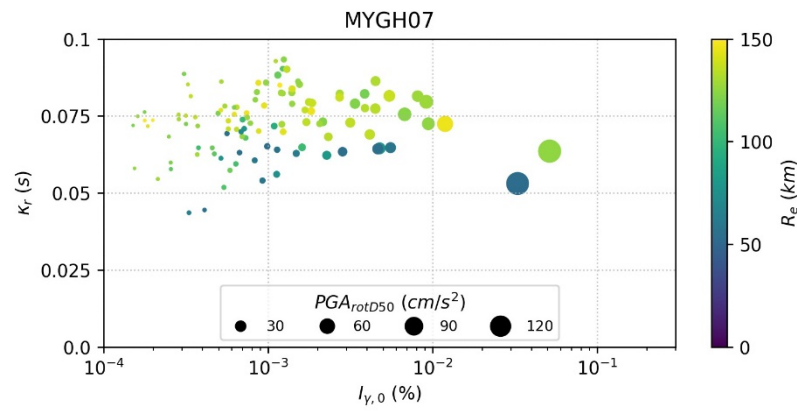
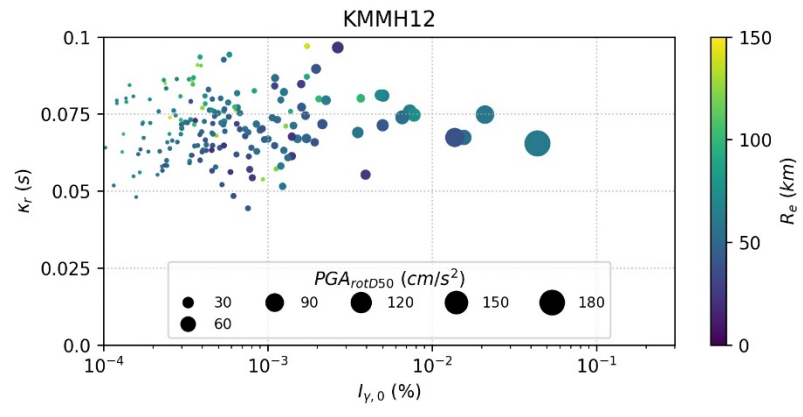
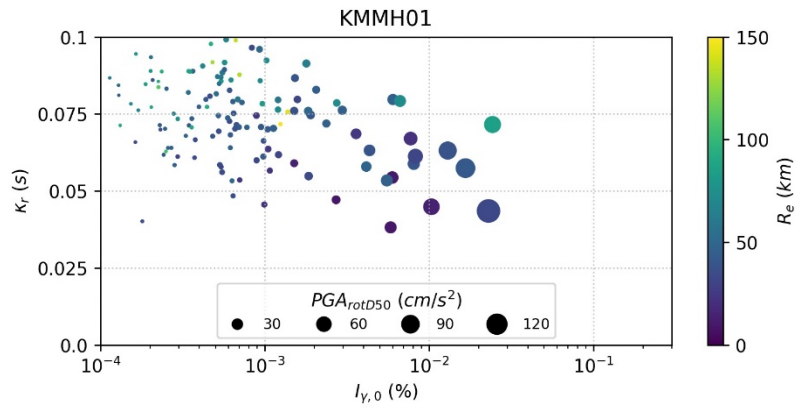


Figure B. 2. Relationship between surface κ_{r_AS} estimates and ground shaking intensities at the studied sites. Different colors illustrate epicentral distances per record, and the sizes of markers represent the corresponding PGA_{rotD50} .









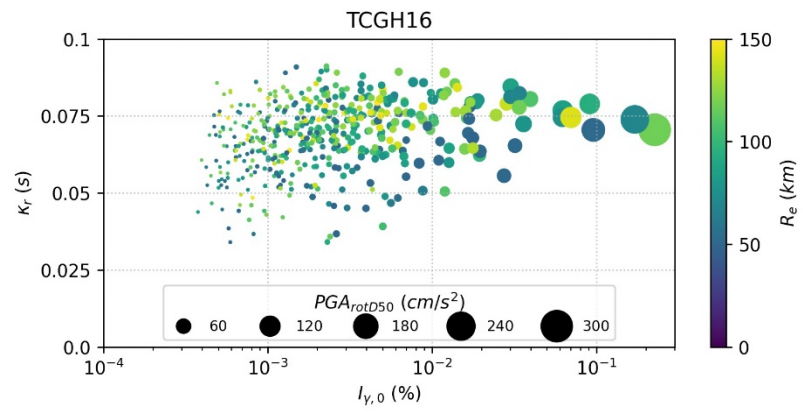
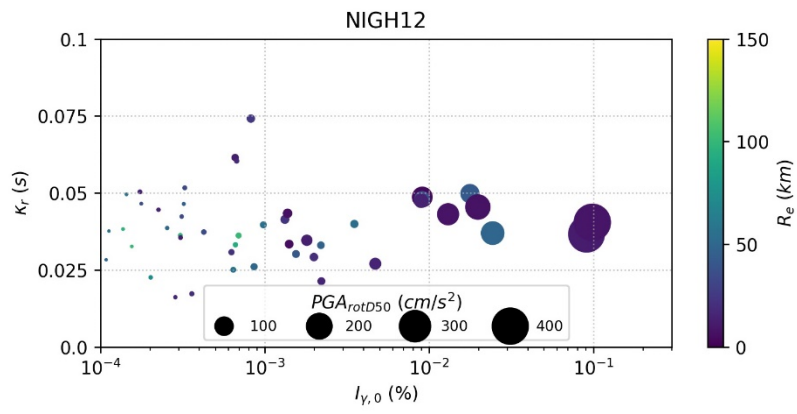
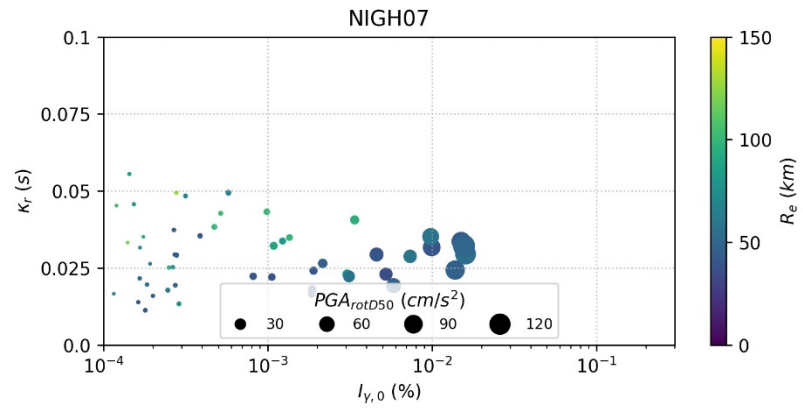
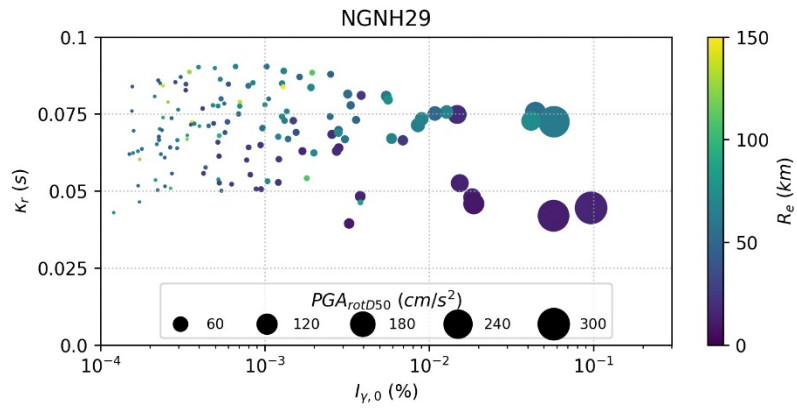
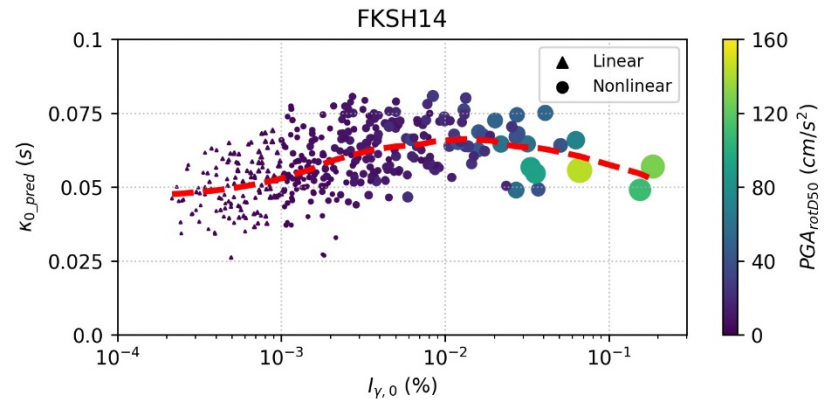
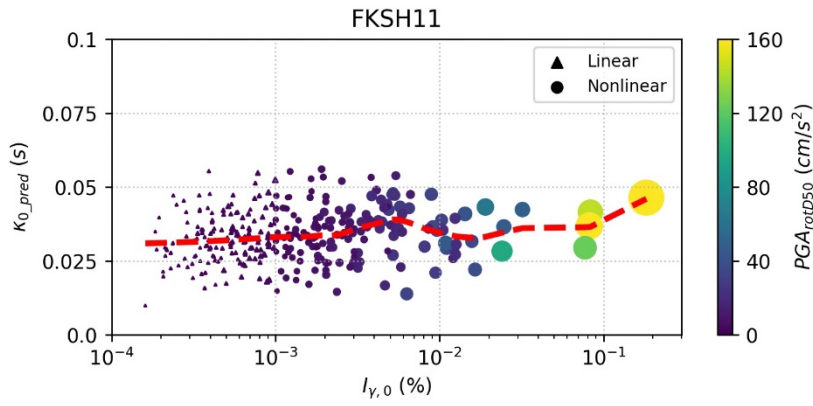
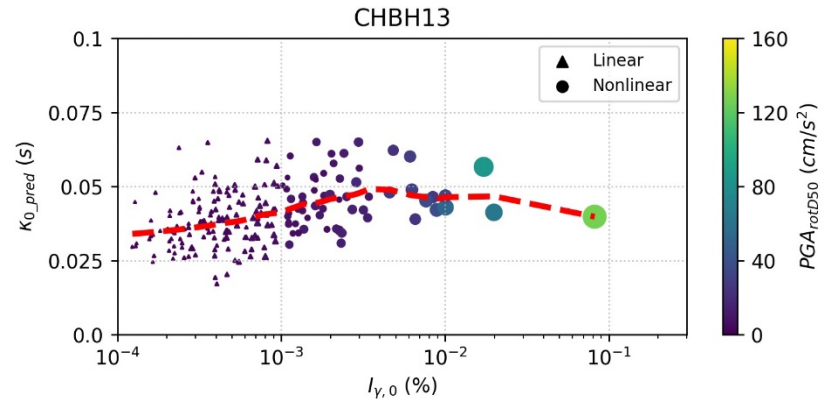
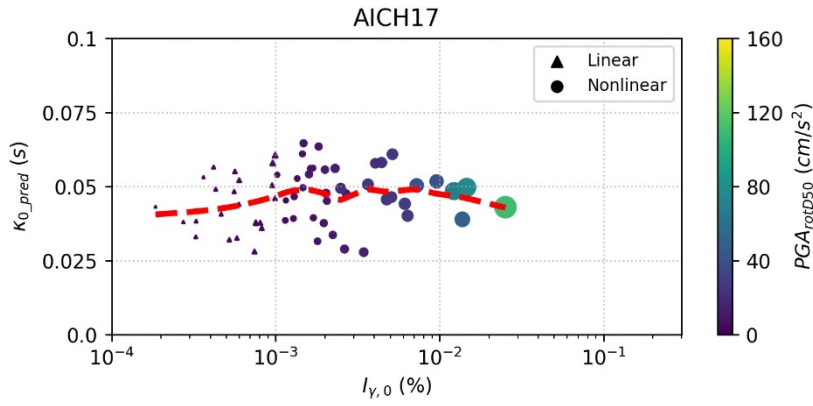
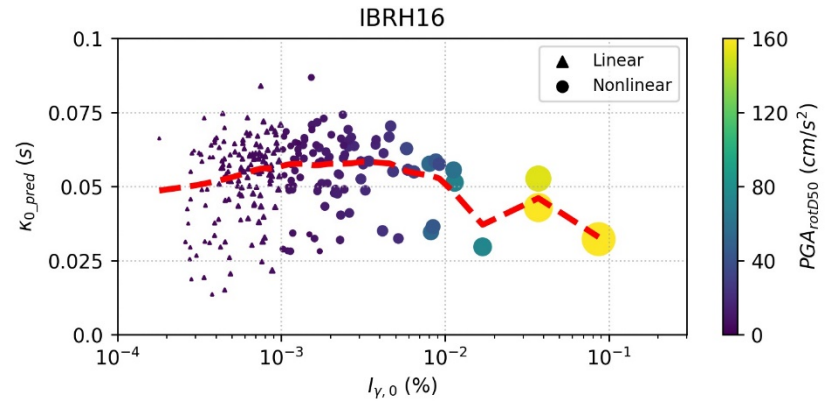
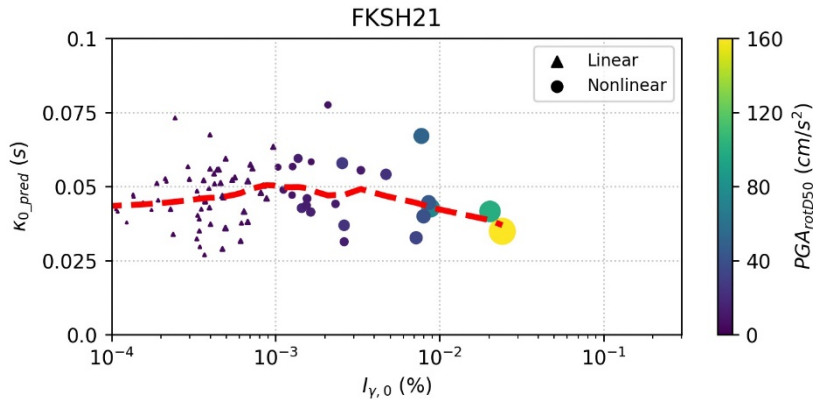
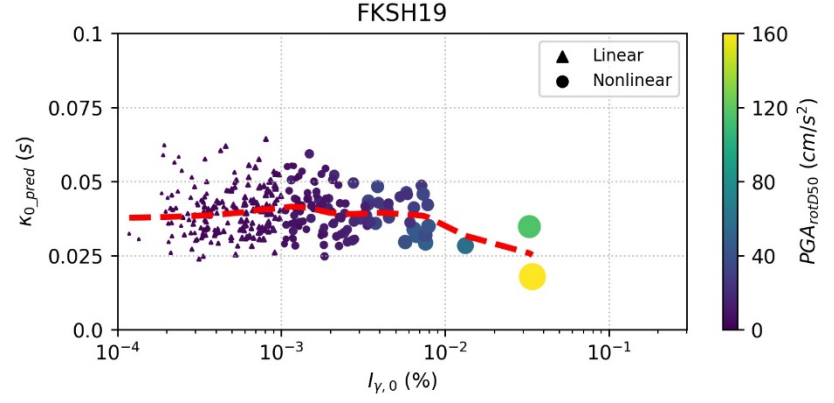
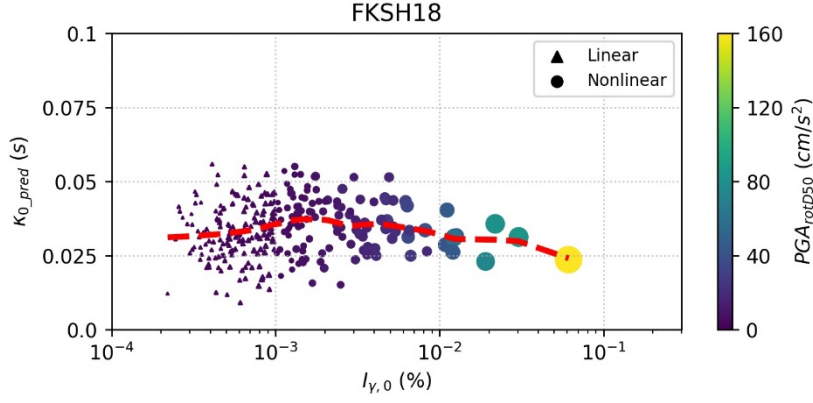
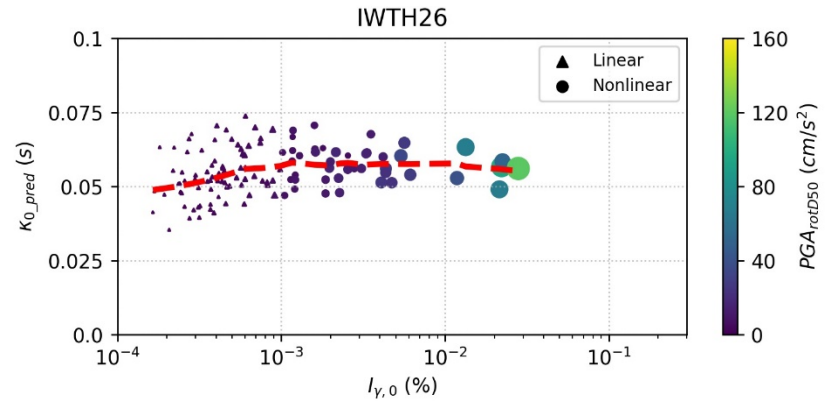
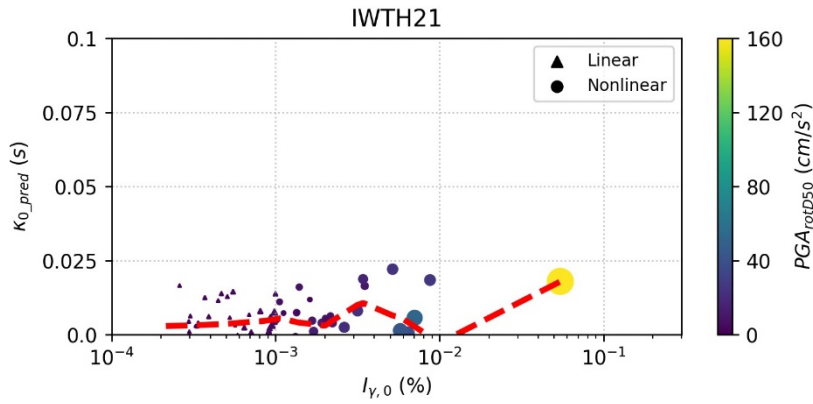
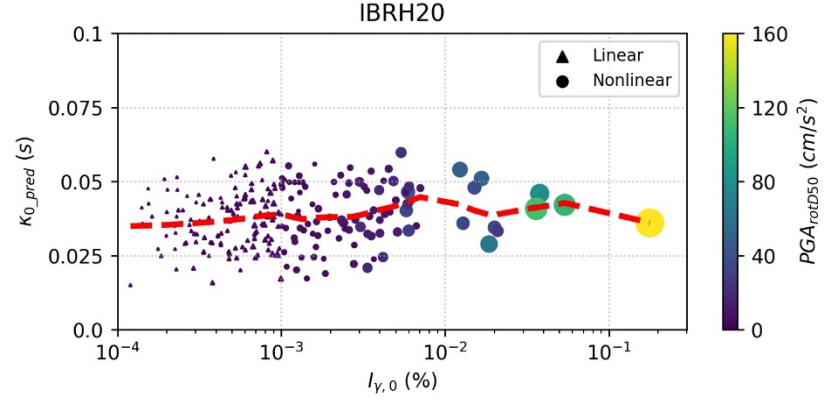
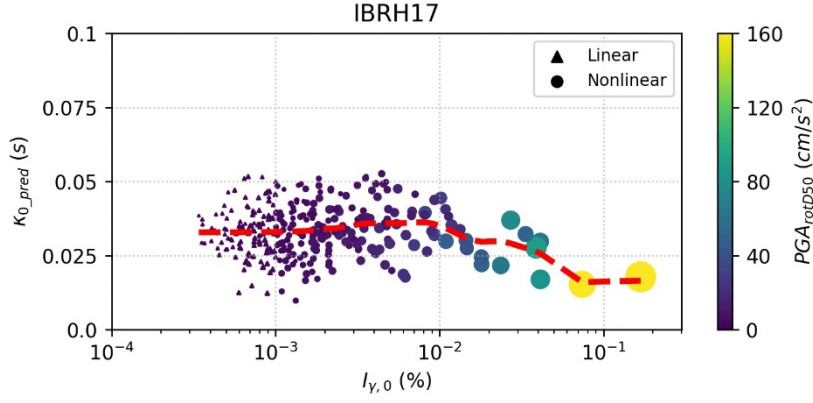
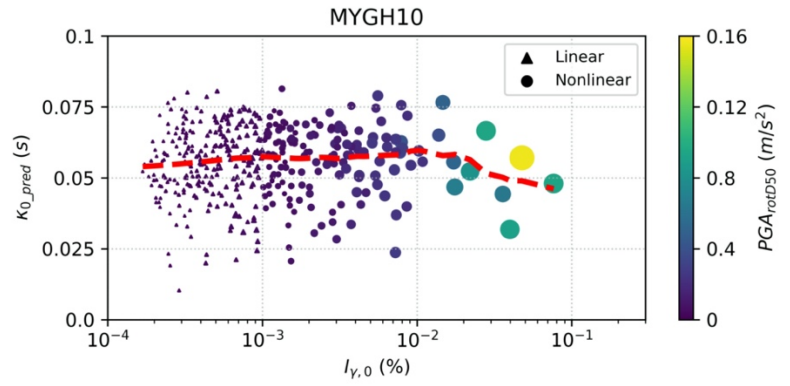
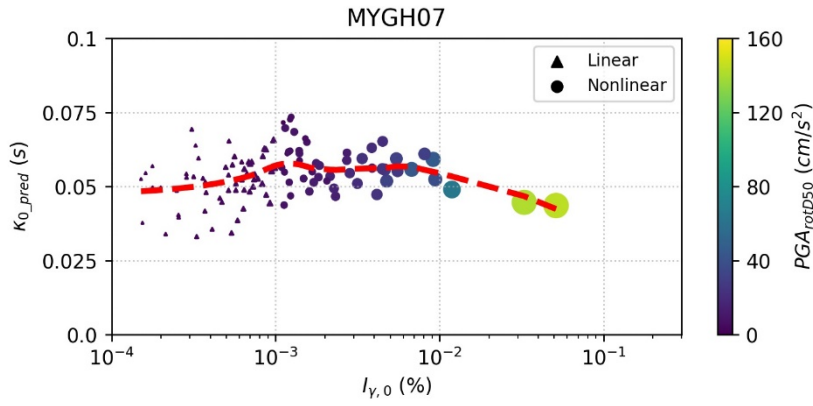
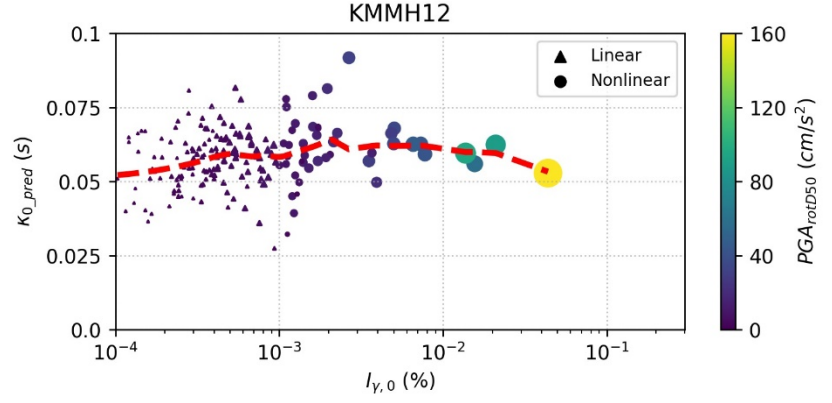
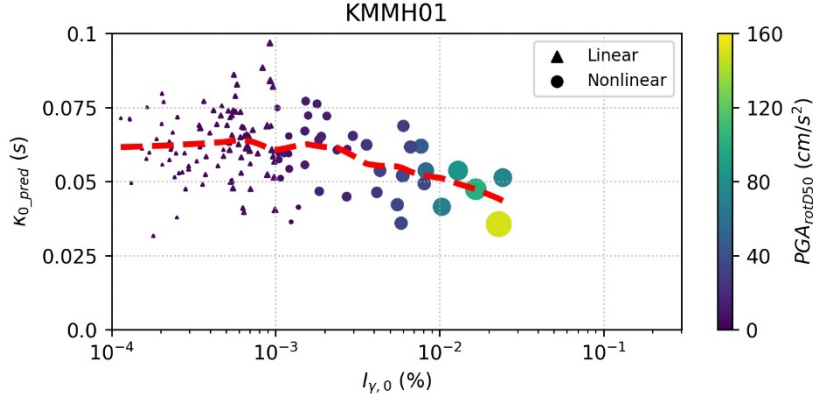


Figure B. 3. Correlations between surface κ_{0_pred} and ground shaking intensities at studied sites. At each site, both colors and sizes of markers present the corresponding PGA_{rotD50} values. The triangle and circles depict linear and nonlinear datasets defined by AP3, respectively. The red dashed-lines indicate the trend between κ_{0_pred} and $I_{y,0}$ as determined by a local regression model.









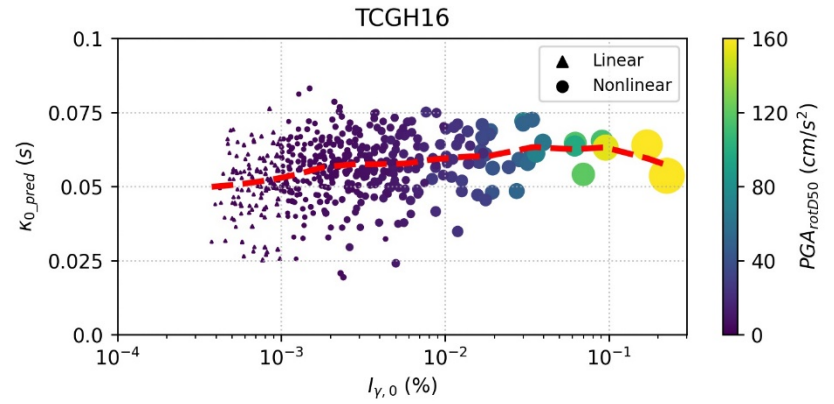
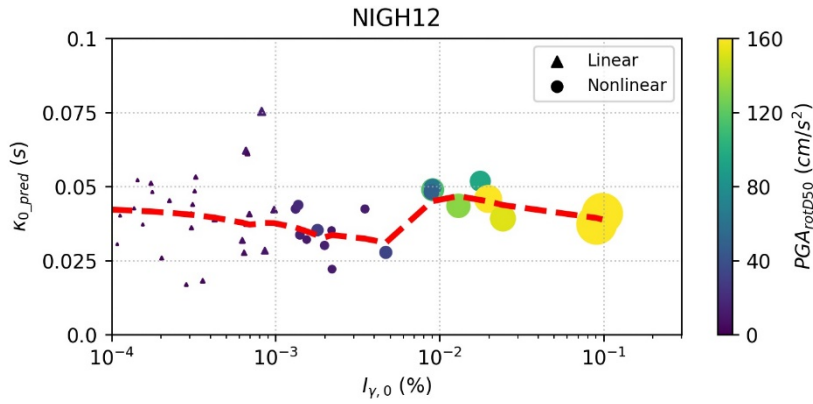
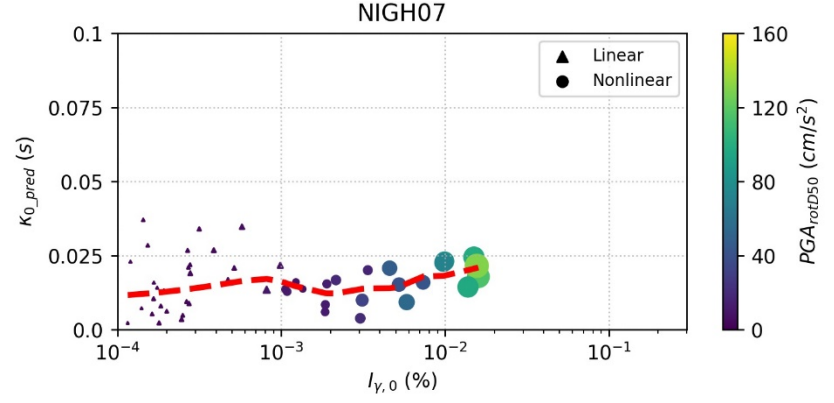
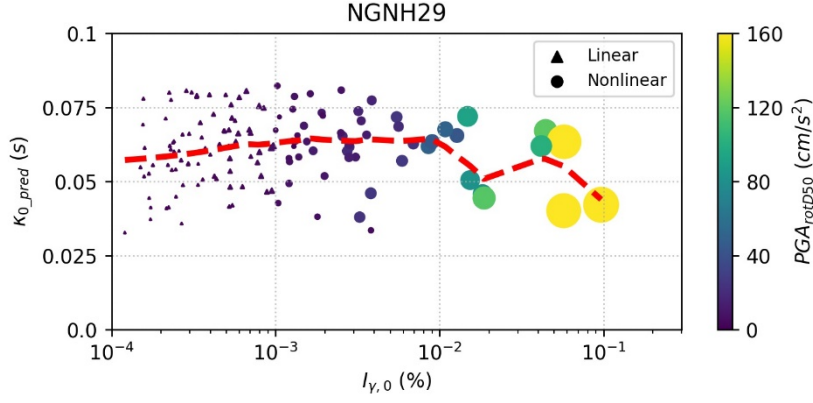


Table B. 1. κ_0 -model estimated with datasets defined by AP1, AP2, AP3 and AP4.

| Station | V_{s30} (m/s) | AP1 | | | | AP2 | | | |
|---------|--------------------|------------------------|------------------------------|---------------------------------|--------------------------------|------------------------|------------------------------|---------------------------------|--------------------------------|
| | | κ_R^1 (km/s) | $\kappa_{0_depth}^2$ (s) | $\kappa_{0_lin_sur}^3$ (s) | $\kappa_{0_nl_sur}^4$ (s) | κ_R^1 (km/s) | $\kappa_{0_depth}^2$ (s) | $\kappa_{0_lin_sur}^3$ (s) | $\kappa_{0_nl_sur}^4$ (s) |
| AICH17 | 314 | 0.00028 | 0.0027 | 0.0392 | 0.0432 | 0.00023 | 0.0085 | 0.0464 | 0.0477 |
| CHBH13 | 235 | 0.00007 | 0.0140 | 0.0386 | 0.0480 | 0.00009 | 0.0138 | 0.0390 | 0.0465 |
| FKSH11 | 240 | 0.00012 | 0.0152 | 0.0328 | 0.0368 | 0.00013 | 0.0159 | 0.0333 | 0.0364 |
| FKSH14 | 237 | 0.00013 | 0.0313 | 0.0488 | 0.0633 | 0.00010 | 0.0363 | 0.0565 | 0.0638 |
| FKSH18 | 307 | 0.00016 | 0.0022 | 0.0348 | 0.0335 | 0.00018 | 0.0021 | 0.0348 | 0.0325 |
| FKSH19 | 338 | 0.00014 | 0.0057 | 0.0405 | 0.0385 | 0.00015 | 0.0052 | 0.0398 | 0.0379 |
| FKSH21 | 365 | 0.00008 | 0.0102 | 0.0473 | 0.0425 | 0.00009 | 0.0092 | 0.0473 | 0.0416 |
| IBRH16 | 626 | 0.00014 | 0.0083 | 0.0539 | 0.0499 | 0.00013 | 0.0093 | 0.0562 | 0.0507 |
| IBRH17 | 301 | 0.00005 | 0.0097 | 0.0328 | 0.0280 | 0.00005 | 0.0115 | 0.0337 | 0.0283 |
| IBRH20 | 244 | 0.00017 | 0.0198 | 0.0368 | 0.0409 | 0.00017 | 0.0212 | 0.0379 | 0.0410 |
| IWTH21 | 521 | 0.00021 | - 0.0029 | 0.0032 | 0.0054 | 0.00021 | - 0.0013 | 0.0047 | 0.0056 |
| IWTH26 | 371 | 0.00010 | 0.0322 | 0.0553 | 0.0581 | 0.00011 | 0.0320 | 0.0555 | 0.0571 |
| KMMH01 | 575 | 0.00027 | 0.0167 | 0.0611 | 0.0502 | 0.00024 | 0.0188 | 0.0623 | 0.0513 |
| KMMH12 | 410 | 0.00022 | 0.0217 | 0.0563 | 0.0599 | 0.00021 | 0.0230 | 0.0579 | 0.0608 |
| MYGH07 | 366 | 0.00014 | 0.0255 | 0.0546 | 0.0559 | 0.00016 | 0.0252 | 0.0542 | 0.0535 |
| MYGH10 | 348 | 0.00012 | 0.0280 | 0.0567 | 0.0563 | 0.00013 | 0.0282 | 0.0568 | 0.0560 |
| NGNH29 | 465 | 0.00013 | 0.0196 | 0.0615 | 0.0584 | 0.00014 | 0.0196 | 0.0622 | 0.0580 |
| NIGH07 | 528 | 0.00023 | 0.0099 | 0.0142 | 0.0171 | 0.00023 | 0.0094 | 0.0133 | 0.0171 |
| NIGH12 | 553 | - 0.00003 | 0.0228 | 0.0388 | 0.0420 | - 0.00001 | 0.0204 | 0.0366 | 0.0417 |
| TCGH16 | 213 | 0.00013 | 0.0177 | 0.0524 | 0.0614 | 0.00015 | 0.0189 | 0.0550 | 0.0597 |

Table B. 1 (continued).

| Station | AP3 | | | | AP4 | | | | |
|---------|------------------------|---|--|---|------------------------|---|--|---|---|
| | κ_R^1 (km/s) | κ_0^{depth} ² (s) | $\kappa_0^{\text{lin_sur}}$ ³ (s) | $\kappa_0^{\text{nl_sur}}$ ⁴ (s) | κ_R^1 (km/s) | κ_0^{depth} ² (s) | $\kappa_0^{\text{lin_sur}}$ ³ (s) | $\kappa_0^{\text{nl_sur}}$ ⁴ (s) | $\kappa_0^{\text{tran_sur}}$ ⁵ (s) |
| AICH17 | 0.00023 | 0.0083 | 0.0437 | 0.0482 | 0.00023 | 0.0083 | 0.0437 | 0.0474 | 0.0486 |
| CHBH13 | 0.00008 | 0.0144 | 0.0377 | 0.0455 | 0.00008 | 0.0143 | 0.0377 | 0.0470 | 0.0451 |
| FKSH11 | 0.00013 | 0.0159 | 0.0322 | 0.0349 | 0.00013 | 0.0159 | 0.0321 | 0.0364 | 0.0345 |
| FKSH14 | 0.00010 | 0.0363 | 0.0500 | 0.0607 | 0.00011 | 0.0362 | 0.0499 | 0.0638 | 0.0602 |
| FKSH18 | 0.00018 | 0.0016 | 0.0331 | 0.0355 | 0.00018 | 0.0018 | 0.0333 | 0.0322 | 0.0362 |
| FKSH19 | 0.00015 | 0.0051 | 0.0396 | 0.0394 | 0.00015 | 0.0052 | 0.0397 | 0.0379 | 0.0399 |
| FKSH21 | 0.00010 | 0.0090 | 0.0462 | 0.0474 | 0.00010 | 0.0089 | 0.0461 | 0.0414 | 0.0499 |
| IBRH16 | 0.00013 | 0.0087 | 0.0543 | 0.0563 | 0.00013 | 0.0089 | 0.0545 | 0.0503 | 0.0576 |
| IBRH17 | 0.00005 | 0.0114 | 0.0329 | 0.0335 | 0.00005 | 0.0115 | 0.0330 | 0.0282 | 0.0342 |
| IBRH20 | 0.00017 | 0.0211 | 0.0369 | 0.0396 | 0.00017 | 0.0211 | 0.0369 | 0.0409 | 0.0394 |
| IWTH21 | 0.00021 | - 0.0017 | 0.0033 | 0.0060 | 0.00021 | - 0.0016 | 0.0034 | 0.0055 | 0.0061 |
| IWTH26 | 0.00012 | 0.0315 | 0.0535 | 0.0574 | 0.00012 | 0.0315 | 0.0535 | 0.0565 | 0.0577 |
| KMMH01 | 0.00024 | 0.0190 | 0.0630 | 0.0566 | 0.00024 | 0.0190 | 0.0631 | 0.0515 | 0.0603 |
| KMMH12 | 0.00021 | 0.0229 | 0.0573 | 0.0607 | 0.00021 | 0.0229 | 0.0572 | 0.0608 | 0.0606 |
| MYGH07 | 0.00016 | 0.0251 | 0.0517 | 0.0566 | 0.00016 | 0.0256 | 0.0522 | 0.0538 | 0.0581 |
| MYGH10 | 0.00013 | 0.0279 | 0.0559 | 0.0572 | 0.00013 | 0.0280 | 0.0560 | 0.0558 | 0.0575 |
| NGNH29 | 0.00015 | 0.0193 | 0.0606 | 0.0625 | 0.00015 | 0.0194 | 0.0607 | 0.0579 | 0.0644 |
| NIGH07 | 0.00022 | 0.0102 | 0.0150 | 0.0153 | 0.00022 | 0.0095 | 0.0142 | 0.0172 | 0.0120 |
| NIGH12 | - 0.00002 | 0.0210 | 0.0384 | 0.0387 | - 0.00002 | 0.0209 | 0.0382 | 0.0418 | 0.0346 |
| TCGH16 | 0.00014 | 0.0193 | 0.0509 | 0.0572 | 0.00015 | 0.0191 | 0.0508 | 0.0599 | 0.0567 |

¹ κ_R : path-component of κ ² κ_0^{depth} : site-specific κ_0 at borehole³ $\kappa_0^{\text{lin_sur}}$: site-specific κ_0 at surface estimated with linear dataset⁴ $\kappa_0^{\text{nl_sur}}$: site-specific κ_0 at surface estimated with nonlinear dataset⁵ $\kappa_0^{\text{tran_sur}}$: site-specific κ_0 at surface estimated with transitional dataset

Table B. 2. Average and standard derivation of κ_0_pred values for surface linear and nonlinear datasets.

| Station | V_{s30} (m/s) | Linear dataset [#] | | Nonlinear dataset* | |
|---------|--------------------|---------------------------------|--------------------------------|---------------------------------|--------------------------------|
| | | mean(κ_0_pred) (s) | std(κ_0_pred) (s) | mean(κ_0_pred) (s) | std(κ_0_pred) (s) |
| AICH17 | 314 | 0.0438 | 0.0091 | 0.0478 | 0.0091 |
| CHBH13 | 235 | 0.0381 | 0.0091 | 0.0458 | 0.0086 |
| FKSH11 | 240 | 0.0324 | 0.0084 | 0.0349 | 0.0088 |
| FKSH14 | 237 | 0.0500 | 0.0086 | 0.0605 | 0.0100 |
| FKSH18 | 307 | 0.0330 | 0.0093 | 0.0355 | 0.0089 |
| FKSH19 | 338 | 0.0401 | 0.0081 | 0.0396 | 0.0075 |
| FKSH21 | 365 | 0.0463 | 0.0091 | 0.0481 | 0.0108 |
| IBRH16 | 626 | 0.0523 | 0.0138 | 0.0549 | 0.0122 |
| IBRH17 | 301 | 0.0330 | 0.0080 | 0.0335 | 0.0088 |
| IBRH20 | 244 | 0.0369 | 0.0093 | 0.0394 | 0.0099 |
| IWTH21 | 521 | 0.0027 | 0.0078 | 0.0060 | 0.0081 |
| IWTH26 | 371 | 0.0539 | 0.0083 | 0.0575 | 0.0058 |
| KMMH01 | 575 | 0.0631 | 0.0114 | 0.0565 | 0.0111 |
| KMMH12 | 410 | 0.0570 | 0.0092 | 0.0609 | 0.0105 |
| MYGH07 | 366 | 0.0514 | 0.0081 | 0.0568 | 0.0073 |
| MYGH10 | 348 | 0.0551 | 0.0127 | 0.0563 | 0.0119 |
| NGNH29 | 465 | 0.0608 | 0.0127 | 0.0615 | 0.0116 |
| NIGH07 | 528 | 0.0156 | 0.0105 | 0.0153 | 0.0055 |
| NIGH12 | 553 | 0.0407 | 0.0129 | 0.0394 | 0.0078 |
| TCGH16 | 213 | 0.0503 | 0.0111 | 0.0568 | 0.0100 |

[#]Linear dataset defined by AP3

*Nonlinear dataset defined by AP